UNIVERSITY OF OKLAHOMA

GRADUATE COLLEGE

THE USE OF POLARIMETRIC RADAR DATA FOR INFORMING NUMERICAL WEATHER PREDICTION MODELS

A DISSERTATION

SUBMITTED TO THE GRADUATE FACULTY

in partial fulfillment of the requirements for the

Degree of

DOCTOR OF PHILOSOPHY

By

JACOB TAYLOR CARLIN
Norman, Oklahoma
2018

THE USE OF POLARIMETRIC RADAR DATA FOR INFORMING NUMERICAL WEATHER PREDICTION MODELS

A DISSERTATION APPROVED FOR THE
SCHOOL OF METEOROLOGY

BY

Dr. Guifu Zhang, Chair

Dr. Alexander Ryzhkov, Co-chair

Dr. Jidong Gao, Co-chair

Dr. Xuguang Wang

Dr. Howie Bluestein

Dr. Nathan Goodman

Acknowledgments

First and foremost, I owe my deepest gratitude to my advisors, Alexander Ryzhkov and Jidong Gao, without whom I would not be where I am today. They have always kept my best interest in mind and have provided countless opportunities for me to share my work and grow as a scientist. Their mentorship, accessibility, and patience remain exemplary for one's graduate school advisor(s), and I remain thankful that they took a chance on me. I hope to one day be half the scientist they've shown themselves to be.

I would also like to thank the other members my committee – Guifu Zhang, Xuguang Wang, Howie 'Cb' Bluestein, and Nathan Goodman – for their willingness to serve on my committee and the thoughtful and insightful feedback and discussions they have provided me over the years. Thanks are also due to Jeff Snyder for serving as a *de facto* advisor to me for both technical and scientific guidance.

Navigating the graduate school process was made so much easier by the School of Meteorology staff: Celia Jones, Nancy Campbell, Becky Steely, Marcia Pallutto, Shelby Hill, and Christie Upchurch. Thanks are also due to the OU Supercomputing Center for Education and Research, whose support and facilities made this work possible; Keli Pirtle and Kevin Manross, for overseeing my internship at the NSSL years ago and starting me down the dual-polarization radar path; John Krause, for his technical expertise in processing radar data; Ted Mansell, Alexander Khain, Yunheng Wang, Gerry Creager, Charles Kuster, and Matt Kumjian for their technical assistance and informative discussions; Tonia Rollins, Colleen Hickman, Mike Jain, Tanya Riley, Jamie Foucher, Tracy Reinke, and Randy Peppler for their administrative support; and Pamela Heinselman, Terry Schuur, and Dušan Zrnić for their friendly discussions and life advice that always made working in the office a pleasure.

I owe so much to the amazing friends I've made throughout my time in graduate school who have made this journey an exciting and fun one and who I have learned so

much from: Elizabeth DiGangi, Nick Szapiro, Lee Carlaw, Chris Riedel, Ariel Cohen, James Russell, Amanda Murphy, Jon Labriola, Laura Labriola, Sean Waugh, and Manda Chasteen. Grillfests and the camping and trips taken with Alan and Sandy Shapiro, Lou Wicker, Evgeni Fedorovich and Petra Klein will undoubtedly remain a highlight of my graduate school years. I am also particularly grateful to Sam Lillo (for putting up with me as a roommate for so many years), Jessica Erlingis Lamers and Katie Wilson (for advice that always kept me grounded), and Elizabeth Smith (for always keeping it real... and agreeing to routine bubble tea trips).

My expressions of gratitude would be incomplete without acknowledging Jacob Hofer, who has stuck by my side through this entire journey and met countless hours of ranting, coding frustrations, and restless nights with steadfast love and support. I could not have done this without you.

Funding for this work came from the U.S. Department of Energy Atmospheric System Research Grant DE-SC0014295, the U.S. Department of Energy Atmospheric System Research Grant ER65459, National Science Foundation Grant AGS-1341878, and from the NOAA/Office of Oceanic and Atmospheric Research under NOAA – The University of Oklahoma Cooperative Agreement NA11OAR4320072.

Finally, I would like to thank my family. From sending me to weather camp and driving me to job shadow at the National Weather Service to buying me countless meteorology books and a weather station to record my own weather observations, as well as supporting me in my decision to move thousands of miles away to pursue my dreams, their early and unwavering support has undoubtedly led me to where I am today.

Table of Contents

List of Tables

List of Figures

Abstract

The explicit prediction of convective storms using storm-scale models has recently become a reality. Radar data is a crucial source of information about the microphysical and kinematic properties of convection at the storm-scale. Whereas assimilation studies have primarily focused on radial velocity and reflectivity, much less has been done to investigate how dual-polarization radar data, and the enhanced microphysical information it offers, may inform storm-scale models.

This study employs a suite of microphysical and numerical weather prediction models, coupled to a polarimetric radar operator, to study how dual-polarization radar data may be used in conjunction with storm-scale models. The commonly-used polarimetric variables are defined, and a review of existing microphysical, wind, moisture, and thermodynamic retrieval and radar data assimilation techniques is presented for reflectivity, radial velocity, and dual-polarization data. Using a one-dimensional spectral bin model, the efficacy of reflectivity-based retrievals of hydrometeor mixing ratios in rain/hail mixtures, and the potential benefits of dual-polarization data, is assessed. A one-dimensional model of the melting layer is presented and used to study the impact of the environment on polarimetric brightband characteristics, the potential for polarimetric thermodynamic retrievals in the melting layer, and the potential microphysical causes of "sagging" brightband signatures. Predicated on a connection between Z_{DR} column characteristics and the latent heating rate within convective updrafts, a novel method for assimilating Z_{DR} columns using a cloud analysis is developed, with results indicating positive impacts compared to reflectivity-based cloud analysis techniques. Future work ideas and an outlook for the near future is presented.

Chapter 1

Introduction

The roots of radar meteorology lie in the wake of World War II, when radars being used for military applications were observed to detect precipitation. Immediately thereafter, radar meteorology rapidly advanced, and has since become an integral part of meteorological observing and warning operations and a primary source of data to further understanding of atmospheric phenomena. The first nationwide network of weather radars in the United States used for operational meteorology purposes was the Weather Surveillance Radar - 1957 (WSR-57) network, which only provided coarse reflectivity (Z). The introduction of the upgraded Weather Surveillance Radar - 1988 Doppler (WSR-88D) network, which was deployed nationwide through the mid-1990s, revolutionized the field by providing radial wind information in addition to Z, along with enhanced resolution and volumetric scans. This enabled great advancements in severe weather warnings, with improved lead time (primarily due to increased probability of detection) of tornadoes and fewer fatalities compared to before the upgrade (Simmons and Sutter 2005).

Alongside observing systems like radar, numerical weather prediction (NWP) models have developed over the last century to become an integral part of both research applications and operational forecasting. These models integrate the equations of motions from an initial state to some future state and have advanced significantly since their initial formulations. Bauer et al. (2015) has described the advancements in NWP models as a "quiet revolution... [whose impacts are] among the greatest of any area of physical science". In addition to improved understanding of the physical processes represented in NWP models, much of this advancement is attributed to the increasing availability of observations and to data assimilation techniques (Rabier 2005), which seek to integrate

observations into NWP models. NWP models have historically been run with relatively coarse grid spacings that do not allow for the resolving of small-scale processes. Instead, they have relied on parameterization schemes to assess and implement the bulk effect of physical processes within the grid volume. For example, instead of actually simulating the motions within a convective storm, convective parameterization schemes produce precipitation and adjust the thermodynamic environment in a given grid volume to that which would be achieved post-convection.

As computing power increased, studies that investigated the explicit processes within simulated cumulus clouds (e.g., Ogura 1963; Orville 1965; Steiner 1973) and thunderstorms (e.g., Miller and Pearce 1974; Klemp and Wilhelmson 1978; Weisman and Klemp 1982) began to be performed. These modeled storms were sometimes compared to observations of real storms to evaluate the model and derive insight into the physical processes behind occurring convection (e.g., Klemp et al. 1981; Wilhelmson and Klemp 1981). However, in a seminal paper, Lilly (1990) challenged the meteorological community to begin pursuing explicit *forecasts* of observed convection. In addition to the availability of increased computing power, part of his motivation for believing this to be an achievable goal was the then-impending WSR-88D network. Since then, much progress has been made in the development of so-called convection-allowing models (CAMs), which explicitly resolve convective processes and motions and do not rely upon convective parameterization schemes. Whereas most CAMs are still only being used in a research context, some, such as the High Resolution Rapid Refresh (HRRR) model (e.g., Benjamin et al. 2009, 2011), have recently been adopted for operational use.

Owing to the continual improvement of CAMs and the inherent limit to lead time afforded to warnings based on detection of tornado precursors, the National Oceanic and Atmospheric Administration's (NOAA) National Severe Storms Laboratory (NSSL) is investigating the potential for a paradigm shift known as Warn-on-Forecast (Stensrud

et al. 2009, 2013). In this approach, forecasters would incorporate forecasts from an ensemble of CAMs to issue probablistic forecasts and warnings well in advance of the formation of traditional precursors of severe weather with the hope of appreciably extending the lead time for severe weather warnings. The project is still in its nascent stages, with much research still being done on data assimilation strategies for radar (e.g., Wheatley et al. 2015) and satellite (e.g., Jones et al. 2016) data, the impact of horizontal grid spacing (e.g., Potvin and Flora 2015), and even the sociological impacts of tornado warning lead times in excess of one hour (Hoekstra et al. 2011). Recently, however, a prototype Warn-on-Forecast system was used by forecasters at the National Weather Service office in Norman, Oklahoma for the first time to provide approximately 90 min of advance notice of an impending tornado threat in Elk City, Oklahoma, with tornado sirens sounded 30 min in advance (National Oceanic and Atmospheric Administration 2017). These early successes are encouraging and provide a motivation for continued research.

Whereas increased computing power, the increasing availability of observations, and improved data assimilation methods are all contributing to the advancement of CAMs, many challenges remain owing to the strong nonlinearities present at the convective-scale, continued uncertainty about how to properly parameterize various physical processes, and the general lack of observations dense enough to define the atmospheric state at such fine resolutions. Any system of CAMs that will be used operationally to forecast convection will necessarily rely on the assimilation of radar data. Doppler radar is the only source of data of sufficient spatial and temporal resolution to fully resolve convective systems in time and space, and as such is a crucial component of reducing the spin-up time of convection in a modeling system compared to a so-called "cold-start". Principally, the assimilation of radar data has been limited to radial velocity and Z. However, to achieve a balanced storm in a model that is able to be sustained, information about the temperature, moisture, and wind perturbations and the hydrometeor

contents of different precipitation species within the storm must be established. Many approaches exist for accomplishing this (discussed further in section 2.3), but difficulties exist with defining multiple state variables from solely Z and/or radial velocity.

The latest upgrade to the WSR-88D network was to add dual-polarization capability. Although radar polarimetry has been utilized for research applications for decades, the completion of the upgrade in 2013 has resulted in an unprecedented amount of polarimetric observations. In contrast to single-polarization radars, dual-polarization radars transmit and receive orthogonally-polarized electromagnetic waves from which information about a target's size, shape, orientation, and composition can be garnered (e.g., Kumjian 2013a). In addition to Z, commonly measured variables include differential reflectivity, co-polar correlation coefficient, and differential phase shift. Dual-polarization radar data have contributed to significant advancements in our understanding of precipitation microphysics, with a number of ubiquitous signatures identified related to specific microphysical processes (e.g., Kumjian 2012). Additionally, dual-polarization data have been successfully leveraged for a number of applications including, but not limited to, updraft detection (e.g., Brandes et al. 1995; Kumjian and Ryzhkov 2008; Picca et al. 2010; Kumjian et al. 2012, 2014; Snyder et al. 2015), attenuation correction (e.g., Bringi et al. 1990; Testud et al. 2000; Snyder et al. 2010), quantitative precipitation estimation (e.g., Zrnić and Ryzhkov 1996; Ryzhkov et al. 2005a,b; Tabary et al. 2011), hydrometeor classification (e.g., Lim et al. 2005; Park et al. 2009; Snyder et al. 2010; Al-Sakka et al. 2013; Thompson et al. 2014), tornado debris detection (e.g., Ryzhkov et al. 2005c; Schultz et al. 2012b,a; Bodine et al. 2013, 2014; van den Broeke and Jauernic 2014; Snyder and Ryzhkov 2015), and the identification (e.g., Heinselman and Ryzhkov 2006) and size discrimination (e.g., Ryzhkov et al. 2013a,b) of hail.

Despite the advantages and additional information that radar polarimetry offers, it remains unclear how to best incorporate these data into NWP models and, in particular, CAMs. The goal of this work is to investigate the potential for dual-polarization radar

data to aid CAMs and offer improvements over what is currently available from Z alone for both analyzing and forecasting convection. More specifically, this work will investigate the efficacy of using dual-polarization observations to retrieve hydrometeor content and thermodynamic information within precipitation and the impacts of assimilating this information using a suite of microphysical and NWP models coupled to a polarimetric radar operator. Chapter 2 provides an overview of radar polarimetry as well as current microphysical and thermodynamic retrieval and radar data assimilation techniques. The various models and tools used in this work are described in Chapter 3. In Chapter 4, the use of Z for the retrieval of hydrometeor content (in the context of assimilation into NWP models) is examined and compared to those from polarimetric data using both observations and a simple model of melting hail. In Chapter 5, the potential for dual-polarization data to provide information about the diabatic heating rate in updrafts (using differential reflectivity columns) and the cooling rate within stratiform precipitation (using polarimetric brightband signatures) is examined. As a follow-up, Chapter 6 explores a novel approach of assimilating differential reflectivity columns into CAMs and the impact it has on short-term forecasts. Finally, Chapter 7 offers a summary of the conclusions from this work as well as an outlook for future work.

Chapter 2

Background and Motivation

2.1 Radar Variables

The most widely-used radar variables, and those relevant to this work, are briefly described below. For a further review of weather radar polarimetry, see Zrnić and Ryzhkov (1999), Kumjian (2013a,b,c), and Zhang (2016).

2.1.1 Reflectivity Factor (Z)

The most commonly-used and well-known radar variable is the radar reflectivity factor (Z). The radar reflectivity factor at either horizontal (h) or vertical (v) polarization is defined most generally as (Doviak and Zrnić 1993; Ryzhkov et al. 2011)

$$Z_{h,v} = \frac{\lambda^4}{\pi^5 |K_w|^2} \int_0^\infty \sigma_{h,v}(D) N(D) dD \tag{2.1}$$

where λ is the radar wavelength, $|K_w|^2$ is the squared dielectric factor related to the dielectric constant for water ε_w by

$$|K_w|^2 = \left| \frac{(\varepsilon_w - 1)}{(\varepsilon_w + 2)} \right|^2 \approx 0.93, \tag{2.2}$$

$N(D)$ is the particle size distribution (PSD), and $\sigma_{h,v}(D)$ is the radar cross section of a particle with equivolume diameter D at polarization h or v, given by

$$\sigma_{h,v}(D) = 4\pi \left| f_{a,b}^{(\pi)}(D) \right|^2 \tag{2.3}$$

where, for oblate spheroids, $f_{a,b}^{(\pi)}(D)$ is the backscattering amplitude of size D along its axis of rotation (a) and the orthogonal axis (b). For an uncanted particle with its axis of rotation aligned with the vertical, a and b correspond to the v and h polarization planes, respectively. The exact scattering amplitudes of particles of any size can be

found according to the Mie scattering equations (Mie 1908). However, for particles with diameters much smaller than the radar wavelength, the Rayleigh approximation can be invoked, in which $f_{a,b}^{(\pi)}(D)$ is equal to

$$f_{a,b}^{(\pi)}(D) = f_{a,b}^{(0)}(D) = \frac{\pi^2 D^3}{6\lambda^2}\xi \tag{2.4}$$

where $f_{a,b}^{(0)}(D)$ is the forward scattering amplitude, and where ξ is a parameter related to the shape of the particle given by

$$\xi = \frac{1}{L_{a,b} + \dfrac{1}{\varepsilon - 1}} \tag{2.5}$$

where, for oblate spheroids,

$$L_a = \frac{1+f^2}{f^2}\left(1 - \frac{\arctan f}{f}\right), \tag{2.6}$$

$$L_b = \frac{1 - L_a}{2}, \tag{2.7}$$

and

$$f = \sqrt{\frac{b^2}{a^2} - 1}, \tag{2.8}$$

and where ε is the dielectric constant of the scattering material. For spherical particles, Eq. (2.4) reduces to

$$f_{a,b}^{(\pi)}(D) = f_{a,b}^{(0)}(D) = \frac{\pi^2 D^3}{2\lambda^2}\frac{\varepsilon - 1}{\varepsilon + 2}, \tag{2.9}$$

allowing $Z_{h,v}$ for rain to be calculated as

$$Z_{h,v} = \int_0^\infty D^6 N(D) dD \tag{2.10}$$

and, more generally for any hydrometeor species x,

$$Z_{h,v} = \frac{1}{|K_w|^2}\int_0^\infty |K_x|^2 D^6 N(D) dD. \tag{2.11}$$

Because the range of $Z_{h,v}$ values can span many orders of magnitude, it is typically expressed as

$$Z_{H,V} = 10\log_{10} Z_{h,v} \tag{2.12}$$

in units of dBZ. As seen from Eq. (2.11), for spherical particles in the Rayleigh scattering regime, $Z_{h,v}$ is proportional to the sixth moment of the PSD and thus is a strong function of the largest particles within the volume.

2.1.2 Differential Reflectivity ($Z_{\mathbf{DR}}$)

The differential reflectivity (Z_{DR}; Seliga and Bringi 1976) is the logarithmic ratio of the Z at horizontal and vertical polarizations, given by

$$Z_{\mathrm{DR}} = 10\log_{10}\left(\frac{Z_{\mathrm{h}}}{Z_{\mathrm{v}}}\right) = Z_{\mathrm{H}} - Z_{\mathrm{V}}. \tag{2.13}$$

Spherical particles have an intrinsic Z_{DR} of zero whereas oblate particles within the Rayleigh scattering regime have positive values of Z_{DR}. For some hydrometeors, such as rain, the aspect ratio is a known and constrained function of size, with drops becoming more oblate with size (e.g., Brandes et al. 2002, 2005; Thurai et al. 2009), and the Z_{DR} changes accordingly, making it a useful tool for the estimation of the median drop size within a volume. For other hydrometeor species, such as snow and hail, the aspect ratio as a function of size is less well defined. Z_{DR} is sensitive to the dielectric constant, causing hydrometeors with smaller dielectric constants to have smaller Z_{DR} than particles of the same shape with larger dielectric constants. Particle orientation also affects the Z_{DR}, with a decrease in Z_{DR} as particles become less preferentially aligned in the horizontal (i.e., as the width of the canting angle distribution increases). Unlike Z, the Z_{DR} is independent of concentration, but can be prone to calibration errors.

2.1.3 Co-polar Correlation Coefficient ($\rho_{\mathbf{hv}}$)

The co-polar correlation coefficient (ρ_{hv}), commonly referred to as the correlation coefficient, is the correlation between the backscattered signals at h and v polarizations at lag-zero and is given by

$$\rho_{\mathrm{hv}} = |\rho_{\mathrm{hv}}(0)| = \frac{\langle f_{vv} f_{hh}^{*} \rangle}{\sqrt{\langle |f_{hh}|^2 \rangle \langle |f_{vv}|^2 \rangle}} \tag{2.14}$$

where f_{hh} and f_{vv} are the complex scattering functions for scattered and incident wave polarizations of h and v, respectively, asterisks denote the complex conjugate, and angled brackets denote an average over the ensemble of hydrometeors. The ρ_{hv} provides a measure of scatterer diversity within a volume and is sensitive to particle sizes, shapes, dielectric constants, and orientations. It is thus a good measure for discriminating non-meteorological echoes (which tend to have low values of ρ_{hv}) from meteorological ones (which tend to have ρ_{hv} closer to unity). The ρ_{hv} is also prominently used in melting layer detection algorithms, as the diversity of hydrometeor composition, shape, and orientations within the melting layer typically lowers the ρ_{hv} appreciably.

2.1.4 Specific Differential Phase Shift (K_{DP})

When electromagnetic waves propagate through media, they slow down. For oblate particles, more medium is encountered by h polarized waves than v polarized waves, and a phase difference develops between them, with the h polarized wave lagging relative to the v polarized wave. The measured phase difference is known as the differential phase shift (Φ_{DP}) and consists of the aforementioned difference owing to forward scattering as waves propagate to and from the radar, as well as a differential phase shift imparted upon backscatter (δ). The former component is often expressed as the two-way range derivative of this accumulation in phase shift and is known as the specific differential phase (K_{DP}), given by

$$K_{\text{DP}} = \frac{1}{2}\frac{d\phi_{\text{DP}}}{dr} = \frac{180\lambda}{\pi}\int_0^\infty \Re\left[f_a^{(0)} - f_b^{(0)}\right] N(D)dD \tag{2.15}$$

and expressed in units of $^\circ$ km^{-1}. Because the slowing of the wave is related to the amount of medium encountered by the wave, along with its insensitivty to radar miscalibration and other nonmeteorological artifacts, K_{DP} offers advantages for quantitative precipitation estimation (QPE) applications over Z (e.g., Zrnić and Ryzhkov 1996). It is also unaffected by isotropic scatterers, and thus has been explored for mitigating hail contamination in QPE (e.g., Balakrishnan and Zrnić 1990; Aydin et al. 1995).

2.1.5 Specific Attenuation (A_{H})

As electromagnetic waves propagate, they weaken due to both scattering and absorption by atmospheric particles. The rate at which this occurs, per unit distance, is known as the specific attenuation (in this case at h polarization; A_{H}) and, neglecting the minimal losses due to air, is given by

$$A_{\mathrm{H}} = 10\log_{10}\left(\frac{I_0}{I}\right) = 8.686\lambda\Im\langle f_{hh}^{(0)}\rangle \tag{2.16}$$

where I_0 is the initial intensity of the wave entering a unit distance, I is the intensity at the end of the unit distance, and $\Im\langle f_{hh}^{(0)}\rangle$ is the imaginary component of the complex scattering function in the forward direction at the h polarization averaged over the ensemble of hydrometeors in a volume. Attenuation of radar waves has historically been considered problematic, with many methods developed to correct the other radar variables, such as Z (e.g., Hitschfeld and Bordan 1954; Testud et al. 2000; Bringi et al. 2001; Snyder et al. 2010). However, research at X- and $\mathrm{K_a}$-band wavelengths has shown that A_{H} is relatively insensitive to drop size distribution variability and nearly linearly related to rain rate (Atlas and Ulbrich 1977; Matrosov 2005). This approach has also been extended to S-band radars (Ryzhkov et al. 2014). Specific attenuation also has additional the benefit of being immune to radar miscalibration and partial beam blockage (Ryzhkov et al. 2014).

Although not utilized in this study, other polarimetric variables do exist, such as the linear depolarization ratio (L_{DR}), circular depolarization ratio (C_{DR}), and the co-cross-polar correlation coefficients.

For the purpose of organizing the literature, the remainder of this chapter is divided into what has been done to retrieve both microphysical and thermodynamic information from radar data and to assimilate radar data into NWP models. However, these are not necessarily separate goals, and the distinctions in some cases are arbitrary and only for organizational purposes. Rather, they are both part of a spectrum that seeks to define the entire state of a precipitation system in terms of hydrometeors, dynamics, and

thermodynamics. This information, beyond improving our conceptual understanding of meteorological phenomena, has many applications, only one of which is initializing these fields within a NWP model for the purpose of forecasting. Retrieved information can be assimilated into NWP models; conversely, NWP models can themselves be used to retrieve unobserved variables from radar data.

2.2 Retrievals from Radar Data

2.2.1 Microphysical Retrievals

2.2.1.1 Traditional Approaches

The relationship between hydrometeor content in a volume and its measured Z, and the retrieval of the former from the latter, has been examined for decades and is a main research thrust of the radar meteorology community. Due to its widespread coverage, the comparatively limited number of rain gauges, and the economic and societal impacts of the distribution and magnitude of precipitation, radar has been used for QPE, which requires retrieving the rainfall rate (R) or snowfall rate (S) and integrating it over time for a given location. This has traditionally been from Z, with various empirical $R(Z)$ and $S(Z)$ relations being proposed over the years. The sensitivity of Z to the largest particle sizes and the variability of drop size distributions due to differing climate regimes, the relative contributions of cold and warm rain processes, and even cloud condensation nuclei (CCN) concentration (e.g., Khain 2009) results in significant variability in $R(Z)$ relationships. Battan (1973) famously presented 69 different $R(Z)$ relations reported in the literature, highlighting the uncertainty in finding an optimal relation. For $S(Z)$ relations, these issues are exacerbated by additional uncertainties in particle density, habit, and fallspeed. In the same vein as Battan (1973), Bukovčić (2017) compared 13 $S(Z)$ relations presented in the literature or used by the WSR-88D network in different regions, finding estimates of S that span up to an order of magnitude for a given Z.

The retrieval of precipitation content within a volume, in the form of liquid water content (LWC) or ice water content (IWC), in g m^{-3}, from Z is also common. For the purpose of radar data assimilation, hydrometeor mixing ratios (q; kg kg^{-1}), which differ from LWC and IWC by a factor of air density (ρ_a), are often retrieved instead as hydrometeor mixing ratios are typically NWP model state variables and form a link between observations of Z and the model. Assimilating q retrieved from Z can help alleviate the time needed for hydrometeors and convective-scale circulations to develop in NWP models, known as the "spin-up" time, which is an important factor for rapidly-developing convective-scale weather or real-time applications that require minimal latency. In addition, both the amount of hydrometeor mass and its distribution across the PSD dictate the impact of microphysical processes, which can subsequently drive non-linear responses and the evolution of the forecast in a NWP model. As such, relating observed Z to hydrometeor mixing ratios for use in NWP models is common. Many empirical relations exist for retrieving the bulk LWC (e.g., Marshall and Palmer 1948; Atlas 1954; Sauvageot and Omar 1987; Baedi et al. 2000; Khain et al. 2008) and IWC (e.g., Sekhon and Srivastava 1970; Heymsfield 1977; Sassen 1987; Liu and Illingworth 2000; Heymsfield et al. 2016) from Z based on disdrometer data, *in situ* aircraft data, and scattering calculations of simulated PSDs.

2.2.1.2 Polarimetric Approaches

Improving retrievals of R and q over those from Z alone is a comparatively mature application of dual-polarization radar, and has been one of its primary benefits. As with Z, much of the work has focused on the retrieval of R. Seliga and Bringi (1976) introduced Z_{DR} as a second radar measurement to constrain the parameters of an assumed inverse exponential size distribution (Eq. 4.2) alleviating the need to hold one of them constant. The method was found to be successful in reducing errors in the estimates of R by a factor of two when compared to rain gauges over the use of Z alone (Seliga

et al. 1981). This degree of improvement was corroborated with disdrometer measurements by Ulbrich and Atlas (1984) for distributions assumed to be inverse exponential in form, although a bias was introduced by this assumption compared to the full gamma distribution (Eq. 4.1). These studies also neglected any canting of raindrops away from having their minor axis aligned in the vertical, as well as the effect of drop oscillations on aspect ratio.

As a consensus formed that dual-polarization measurements could significantly improve the accuracy of microphysical retrievals, other polarimetric variables began being investigated. Sachidananda and Zrnić (1987) obtained measurements of $K_{\rm DP}$ and compared $R(K_{\rm DP})$ with $R(Z)$ and $R(Z, Z_{\rm DR})$ for simulated size distributions, finding better performance of $R(K_{\rm DP})$ than $R(Z, Z_{\rm DR})$ for larger rain rates but with both exceeding $R(Z)$. $R(K_{\rm DP})$ also offers improved performance in rain/hail mixtures, where Z and $Z_{\rm DR}$ may be skewed high and low, respectively, hurting the accuracy of $R(Z, Z_{\rm DR})$ retrievals (Aydin et al. 1995). Improvements when looking at areal averages of polarimetric R estimates may be even more pronounced than validation at one point in space and time, with Ryzhkov et al. (2005a) finding a reduction in errors by up to a factor of 3.7 compared to $R(Z)$.

While they all offer improvements over Z, retrievals employing the polarimetric variables have their own difficulties. Sachidananda and Zrnić (1987) found that, unlike $R(K_{\rm DP})$, $R(Z, Z_{\rm DR})$ was quite sensitive to the assumed aspect ratio-size relation. Additionally, $K_{\rm DP}$ can be noisy at low rain rates and hard to measure accurately, requiring more range averaging than other variables which limits the resolution at which R can be retrieved. Recognizing these limitations, as well as the necessary assumption of an inverse exponential size distribution when using $(Z, Z_{\rm DR})$, Zhang et al. (2001) proposed a method to estimate all three parameters of the gamma distribution, rather than just bulk R values, by deriving a constraining $\mu - \Lambda$ relation. This allows for more accuracy

and flexibility in the range of size distributions that are able to be represented. Another three-parameter estimation method employing Z, Z_{DR} and K_{DP} was developed by Gorgucci et al. (2002). Most recently, Ryzhkov et al. (2014) proposed using $R(A_H)$ for rainfall estimation. Although it has long been known that A_H is nearly linearly related to rainfall rate (e.g., Atlas and Ulbrich 1974; Matrosov 2005), it has been difficult to estimate from single-polarization radar and use in practice. Ryzhkov et al. (2014) proposed using Φ_{DP} in conjunction with Z to estimate A_H. The results indicate robust retrievals of R, particularly at S band, although the method fails in the presence of hail. There are many other studies that have been and continue to be done in the realm of polarimetric QPE (e.g., Giangrande and Ryzhkov 2008; Cifelli et al. 2011). However, as noted by Ryzhkov et al. (2005a), despite the variability in the details of the results, there is an overall strong consensus that estimates of R are improved by using dual-polarization radar due to its decreased sensitivity to variability of drop size distributions and, for variables such as K_{DP} and A_H, immunity to miscalibration errors.

Although comparatively fewer studies have sought to derive explicit relations for polarimetric estimates of q_r, similar improvements over Z to those seen for R have been found. Ulbrich and Atlas (1984) first introduced a polarimetric estimate for LWC based on Z and Z_{DR} for rain size distributions assumed to be inverse exponential in form. Additional relations were found by Seliga et al. (1986) from linear regressions performed on observed drop size distributions (DSDs), which performed favorably versus Z even at distances far from the radar (Aydin et al. 1987). Yet another set of relations for $q_r(Z_H, Z_{DR})$, $q_r(K_{DP})$, and $q_r(K_{DP}, Z_{DR})$ at C-band was presented in Bringi and Chandrasekar (2001) from linear regressions of radar variables calculated from simulated gamma DSDs whose parameters spanned the typical range of observed values. These equations have been used in the few studies that have assimilated polarimetric estimates of q_r (e.g., Li and Mecikalski 2010, 2012).

Polarimetric retrievals of ice phases remain less explored. A handful of studies have examined the retrieval of IWC in snow. Vivekanandan et al. (1994), noting the inherent uncertainty of retrieving IWC from Z, offered a relation for retrieving IWC from K_{DP} as a function of the mean aspect ratio and density of ice particles in a volume. However, these factors are rarely known in practice *a priori*. Aydin and Tang (1995), assuming the density of particles in the volume was equal to that of solid ice, derived a relation for IWC from K_{DP} and Z_{DR}. Ryzhkov et al. (1998) expanded on these modeling approaches by allowing the particle densities and shapes to vary as a function of size based on observational data for different crystal habits, and found moderately good agreement of IWC retrieved from K_{DP} and Z_{DR} with *in situ* aircraft data. However, the method will suffer when ice crystals become heavily aggregated as the particles become more spherical and less dense. Recently, Bukovčić et al. (2018) capitalized on the inverse relationship between Z and K_{DP} in aggregating snow and developed a novel approach of estimating IWC from Z and K_{DP} using a 2D video disdrometer dataset. This method proved to be quite insensitive to the different geographic regions in which it was validated, although assumptions were still required about the mean particle aspect ratio, canting angle distribution, and degree of riming.

Although dual-polarization radar has contributed to significant advancements in the detection (e.g., Heinselman and Ryzhkov 2006) and, more recently, the size discrimination (Ortega et al. 2016) of hail, and has been used indirectly to partition the contribution of rain and hail to Z (e.g., Balakrishnan and Zrnić 1990), the author is unaware of any quantitative polarimetric retrievals of ice water content in hail and graupel. This is perhaps unsurprising, as hail is often assumed to be spherical or nearly-spherical as it tumbles and falls, limiting anisotropic scattering and thus the usefulness of polarimetric measurements. Indeed, it is this quality that has enabled the reliable detection of hail from other species. However, the limitations of using Z for retrievals of other species

apply equally to hail and graupel, with the added complexity of non-Rayleigh scattering possible for large hail, even at S band.

2.2.2 Wind Retrievals

The derivation of the full three-dimensional wind field has been a primary application of Doppler radar and is widely used today. Historically, this has necessitated the use of multiple Doppler radars, which together can be used to derive the horizontal wind field and, when integrated using a mass continuity equation, the vertical wind field (Armijo 1969; Lhermitte 1970). The derivation of the three-dimensional wind field from multiple Doppler radars has been widely adopted and used to study the wind field in, among other phenomena, snow (e.g., Frisch et al. 1974), mesocyclones (e.g., Ray et al. 1975; Ray 1976; Brandes 1978), tornadic circulations (e.g., Dowell and Bluestein 2002; Wurman et al. 2007), bow-echoes (e.g., Jorgensen and Smull 1993), and downbursts (e.g., Lee et al. 1992). This technique has been expanded upon to utilize variational analysis (see section 2.3.2.3) when deriving the three-dimensional wind field (e.g., Ziegler 1978; Gao et al. 1999; Shapiro et al. 2009), and much effort has been undertaken in addressing some of the sources of uncertainty in multiple-Doppler wind analyses, including the specification of boundary conditions, differences in observation time, measurement errors, and interpolation errors.

Owing to the wide spacing between WSR-88D sites and the general lack of multi-Doppler radar data for operational use, many studies have sought to retrieve the wind field from single-Doppler data. Early studies attempting to use single-Doppler data employed adjoint model techniques to retrieve all unobserved variables from simulated (e.g., Sun et al. 1991) and real (e.g., Sun and Crook 1994, 1997, 1998) data cases. However, due to the computational expense of using adjoint techniques, nonuniqueness, and the potential for issues related to model error, single-Doppler velocity retrievals were pursued. Qiu and Xu (1992) developed a method for retrieving the horizontal

wind field using time-averaged single-Doppler radar data and conservation equations for either Z or radial velocity. This method was expanded to all three dimensions by Gao et al. (2001). Another method for retrieving the full three-dimensional wind from single-Doppler data based on Z conservation, incompressibility, and a temporal constraint on the velocity field was put forth by Shapiro et al. (1995). Regardless of how it is derived, knowledge of the three-dimensional wind field derived from radar data has proven to be an invaluable source of information for a wide array of applications.

2.2.3 Thermodynamic Retrievals

The structure and impacts of the latent heating budget of precipitation systems has been an active area of research for decades. Much of the research has focused on mesoscale convective systems (MCSs) due to their outsized contribution to the large-scale heating budget, particularly in the tropics (e.g., Riehl and Malkus 1958). The archetypal heating structure of MCSs features distinctive heating regimes between the convective and stratiform portions (e.g., Houze Jr. 1982, 1989; Johnson 1984). The convective region features strong heating through most of the depth of the atmosphere, primarily due to condensation within the updraft and with smaller contributions from freezing. Cooling at the lowest levels of the atmosphere in the convective zone can occur due to the melting of graupel (Trapp et al. 2018) and the evaporation of rain. In contrast, stratiform regions feature warming above the environmental 0°C level due to depositional growth of snow and graupel, cooling within the melting layer due to the melting of snow and graupel, and cooling due to evaporation of rain beneath that. Although the magnitude of heating and cooling is greater in the convective region, the cooling within the melting layer in the stratiform region can be spatially extensive and is confined to a relatively thin layer.

Condensational heating within updrafts is the primary energy source for thunderstorms (Braham Jr. 1952). The consequences of this latent heat release can be felt across

all scales, however. Latent heat release due to condensation has been shown to impact extratropical cyclone intensity and structure (e.g., Aubert 1957), the internal flow field of MCSs (e.g., Pandya and Durran 1996), and serves as the primary source of energy for tropical cyclones (e.g., Gray 1968) and the driver of large-scale circulations, including the Walker circulation (e.g., Hartmann et al. 1984) and the Madden-Julian Oscillation (MJO; e.g., Schumacher et al. 2004; Barnes et al. 2015). Although condensation is the primary source of heating within the updraft, with the latent heat of vaporization nearly an order of magnitude larger than the latent heat of fusion, freezing within the updraft can be consequential. Numerous studies examining the impact of aerosols on convection have reported invigorated convection with enhanced updrafts as the concentration of CCN that delay warm processes and enhance ice processes above the 0°C level is increased (e.g., van den Heever et al. 2006; Khain 2009; Morrison and Grabowski 2013).

Cooling due to the evaporation and melting of precipitation in both convective and stratiform precipitation can also have important dynamical consequences. These processes are responsible for the formation of cold pools, which can have dominant impacts on storm longevity and structure and subsequent storm formation (e.g., Rotunno et al. 1988; Dawson et al. 2010; Schumacher and Peters 2017). In more intense cases, strong downdrafts can result from cooling-induced negative buoyancy (e.g., Srivastava 1985, 1987). Evaporation is also hypothesized to play a role in tornadogenesis (e.g., Markowski et al. 2002, 2003; Snook and Xue 2008), with less evaporation allowing for more buoyant rear flank downdrafts believed to be needed for tornadogenesis. Indeed, both Kumjian (2011) and French et al. (2015) have found larger Z_{DR} in non-tornadic rear flank downdrafts than tornadic ones. Evaporation may increase Z_{DR} due to a depletion of smaller raindrops that results in larger median drop sizes and enhanced cooling (although Xie et al. (2016) present evidence that, depending on the PSD, evaporation can also decrease Z_{DR}). This evidence, while circumstantial and without direct observation, lends credence to the idea that evaporation (and the cooling it produces) may

play a significant role in tornadogenesis potential. The concentration of CCN can also affect low-level drop size distributions depending on whether the rain stems from warm or cold processes.

Cooling within the melting layer in stratiform precipitation can also have noteworthy impacts. As the isothermal layer deepens, it can lead to sudden precipitation type transitions at the surface (e.g., Wexler 1955; Bozart and Sanders 1991; Kain et al. 2000). This cooling can also have dynamical consequences, including downdraft and gravity wave generation (e.g., Szeto et al. 1988), turbulence and convection within the melting layer due to instability created below the deepening isothermal layer (e.g., Findeisen 1940; Stewart et al. 1984), mesoscale wind perturbations (e.g., Atlas et al. 1969; Heymsfield 1979), and impacts on cyclogenesis (e.g., Stewart and Macpherson 1989).

2.2.3.1 Traditional Approaches

Direct observations of latent heating and cooling are typically unavailable. However, the significant impacts latent heating and cooling can have across all scales make it highly desirable to estimate in both time and space. Radar data is a natural source to exploit for this purpose, as the hydrometeors it measures are at least indirectly related to the phase changes responsible for the heating and cooling. The following discussion highlights many methods that have been developed over the past few decades to retrieve diabatic heating and cooling rates from radar.

Dynamic Retrieval Methods Doppler wind radar data is utilized prominently in many approaches for thermodynamic retrievals, as the three-dimensional wind field is intimately tied to thermodynamic fields through physical constraints. Seminal papers were published concurrently by Gal-Chen (1978) and Hane and Scott (1978) describing a new methodology for retrieving thermodynamic information from radar data, differing in their mathematical approach. In this method, the wind field derived from multi-Doppler radar analysis (see section 2.2.2) is used to calculate the pressure perturbation

field and, subsequently, diagnose the local buoyancy using the equations of motions. The technique was first applied to real radar data in Roux et al. (1984), and expanded to include the thermodynamic equation in Roux (1985) to predict the full temperature field instead of only its perturbations. Since then, numerous refinements to the technique have been proposed (e.g., Roux and Ju 1990; Roux et al. 1993; Guimond et al. 2011) and the method has successfully been used to study the dynamic and thermodynamic characteristics of various meteorological phenomena, including tornadic thunderstorms (e.g., Brandes 1984; Hane and Ray 1985), tropical cyclones (e.g., Guimond et al. 2011), and narrow cold-frontal rainbands (e.g., Parsons et al. 1987; Roux et al. 1993). Dynamic thermodynamic retrieval methods have also been applied to winds derived from single-Doppler radar data (e.g., Weygandt et al. 2002a,b). The results of these retrievals can be used to initialize NWP models suitable for forecasts provided that the moisture field can be assumed or otherwise specified (e.g., Lin et al. 1993; Bielli and Roux 1999; Weygandt et al. 2002b; Guimond and Reisner 2012).

Microphysical Retrieval Methods Another approach that utilizes radar velocity data is a class of complementary thermodynamic retrieval techniques known as microphysical retrieval methods. In contrast to the dynamical retrievals discussed in the preceding section that employ the equations of motions, a microphysical retrieval method that employs the continuity equations for water and heat was developed by Rutledge and Hobbs (1984) and extended to three dimensions by Ziegler (1985). In this method, the continuity equations for heat and moisture are integrated until a steady-state solution is found that matches the wind field specified from a multi-Doppler anlaysis. Ziegler (1988) additionally showed the retrieved thermal fields to be relatively insensitive to the details of the microphysical parameterization. A unified framework for the microphysical and dynamic retrieval methods was presented in Hauser et al. (1988), who compared the methods and found they were mutually consistent, with good agreement with the limited observations available to compare with. This framework was used successfully in

Marécel et al. (1993) to study a narrow cold-frontal rainband, with the rain and graupel mixing ratios retrieved from Z. Although this method has the benefit of being able to include complex microphysical processes, it does not use the momentum equation directly and thus balance between the derived thermodynamic field with the wind field is not guaranteed (Hauser et al. 1988). Recently, Ziegler (2013a,b) developed a "diabatic Lagrangian analysis" that uses radar-derived wind fields and hydrometeor distributions to diagnose the temperature, buoyancy, and water vapor field by calculating backward trajectories and integrating them forward using a prediction model, combining advantages of both the microphysical and dynamic retrievals methods. Both methods are advantageous in that they are based on physical constraints, but they require an analysis of the full three-dimensional wind field to be available, which is often not the case. In addition, as with all radar-based velocity approaches, the methods require ways to deal with data-void regions and radar echo boundaries.

Budgeting Methods Other methods of estimating latent heating and cooling rates rely on solely Z. One of the earliest methods for estimating latent heat release within observed thunderstorms was by relating the water budget to that for energy. Sikdar and Anderson (1974) first applied this to an Oklahoma supercell by retrieving the change in storm total LWC and rainfall rate from Z and parameterizing the evaporation rate, from which the condensation rate, and therefore overall heating rate, was able to be determined. Though simple, the calculated heating rate was comparable to that for a modeled thunderstorm. A conservation approach was also utilized by Leary and House Jr. (1979) for estimating cooling within the melting layer of stratiform precipitation. By assuming no sources or sinks of moisture within the melting layer, retrieving LWC (IWC) below (above) the radar brightband from Z, and provided a depth of the melting layer and the terminal velocities of particles, they were able to calculate cooling rates of several degrees per hour within the melting layer. A similar approach using the difference in

retrieved LWC between 2.5 - 0.5 km was used to find the cooling rate due to evaporation below the melting layer. However, neither approach allowed for the determination of the vertical distribution of cooling within each layer, instead assuming a constant rate through the depth.

Look-up Table Methods More recently, the use of look-up tables for retrieving latent heating and cooling profiles has become prevalent. The launch of the Tropical Rainfall Measurement Mission (TRMM; e.g., Simpson et al. 1996) satellite in 1997, the goal of which was to observe precipitation across the tropics globally, lead to the development of a suite of methods for latent heating retrievals (for a comprehensive review see Tao et al. 2006). Central to most of these methods is the Precipitation Radar, a vertically-pointing K_u-band radar with up to 250 m vertical resolution at nadir. Due to its emphasis on global tropical coverage and precipitation impacts, much of the focus for the TRMM's latent heating retrievals has focused on MCSs, which for the purpose of employing look-up tables need to be divided into convective and stratiform portions due to their differences in archetypal latent heating structure. The lack of corresponding three-dimensional wind observations prevents the use of any dynamic or microphysical retrievals. However, the increasing utility of CAMs in recent years, when coupled to a radar operator, has allowed for the compilation of many CAM runs into look-up tables of vertical profiles of latent heating and cooling indexed by parameters of various radar observables. Two of the most commonly-used algorithms are the Convective-Stratiform Heating (CSH; Tao et al. 1993, 2010) algorithm and the Spectral Latent Heating (SLH; Shige et al. 2004, 2007, 2009) algorithm, which both employ look-up tables generated from multiple runs of the Goddard Cumulus Ensemble model (Tao and Simpson 1993). The former generates vertical profiles of heating by weighting the relative area of convective and stratiform regions, using the normalized heating profiles for each region, and scaling the resultant profile by the surface rain rate. In contrast, the SLH uses look-up tables indexed by precipitation top height for convective and shallow stratiform

regions, which are scaled by the surface precipitation rate. For deep stratiform regions, the look-up tables are indexed by melting-layer precipitation rate, with profiles scaled by the precipitation rate above the melting level and by the difference in precipitation rate between the melting layer and the surface below the melting layer to account for losses due to evaporation. These algorithms have been shown to be successful for large-scale applications, although Shige et al. (2007) notes the sensitivity of the profiles to the model runs used, the case-dependency of the applicability of the derived profiles, and that "instantaneous matching between a certain rainfall profile and a heating profile is an ill-conceived concept", perhaps limiting its use at high-resolutions on the convective scale. Indeed, Park and Elsberry (2013) compared results of a dynamic retrieval of latent heating to those of the SLH and showed deficiencies in applying the SLH at small scales, with the use of averaged profiles precluding the retrieval of cooling downdrafts aloft. Nelson et al. (2016) attempted to alleviate some of the deficiencies of using the SLH deterministically by using Bayesian Monte Carlo methods to generate probability distributions of heating profiles based on the observed Z, finding that a limited number of parameters could retrieve the surface rain rate and height of maximum heating very well. However, the authors note that random errors can be large due to the inability of Z alone to constrain the drop size distributions responsible for diabatic heating and cooling, which suggests the potential for dual-polarization radar measurements to improve these retrievals.

2.2.3.2 Polarimetric Approaches

Most of the work done tying dual-polarization radar observations to diabatic heating and cooling is qualitative and relates distinct polarimetric signatures to microphysical processes, including the freezing of raindrops into graupel or hail in convective updrafts (e.g., Kumjian et al. 2012), the evaporation of raindrops (e.g., Kumjian and Ryzhkov 2010), riming (e.g., Vogel et al. 2015; Ryzhkov et al. 2016), depositional growth (e.g.,

Kennedy and Rutledge 2011; Andrić et al. 2013; Kumjian and Lombardo 2017), and the refreezing of hydrometeors in winter precipitation (e.g., Kumjian et al. 2013; Bukovčić et al. 2017). Some of these signatures, such as that of evaporation, are typically very subtle and can easily be masked by other non-diabatic processes such as size sorting. Others, such as the freezing or refreezing of raindrops, have not been studied quantitatively but can at least serve as a marker that a diabatic process is occurring. Despite the widespread examination of the radar brightband through observations and modeling studies, no work exists using the polarimetric brightband observations to study the diabatic cooling within the melting layer to the author's knowledge.

In addition to looking at the polarimetric signatures of specific microphysical processes, a number of signatures have been identified that are due to dynamical features within precipitation (which themselves are intimately related to diabatic processes). A well-studied example is Z_{DR} columns, vertical protrusions of positive Z_{DR} above the environmental 0°C level that are indicative of wet ice particles and oblate, supercooled raindrops in the process of freezing being lofted by the updraft. Because Z_{DR} columns are associated with convective storm updrafts, they can theoretically be used as identifiers for regions of positive temperature perturbations from latent heat release due to condensation and/or freezing. Although not directly retrieving the diabatic heating rate due to condensation and freezing within the updraft, recent work has begun to investigate the relationship between Z_{DR} columns and updraft intensity (Picca et al. 2010; Kumjian et al. 2014; French and Snyder 2016; Snyder et al. 2017b). In contrast, downbursts are formed by negatively buoyant air that has been cooled by the evaporation and melting of hydrometeors within the downdraft region of a thunderstorm (Srivastava 1987). A polarimetric signature associated with downbursts consisting of a trough in Z_{DR} and an enhancement of K_{DP} within the Z core has been identified in numerous studies (e.g., Wakimoto and Bringi 1988; Scharfenberg 2003) due to the presence of melting hail below the environmental 0°C level. In addition to identifying downbursts for the

threats they pose to public safety, this signature could be used as an identifier for areas of ongoing strong diabatic cooling.

There remains a dearth of studies using polarimetric radar data in a quantitative way to estimate diabatic heating and cooling. Tong et al. (1998) investigated the latent heating rate due to condensation within a thunderstorm. They used the difference reflectivity (Z_{DP}; Golestani et al. 1989), defined as the logarithmic difference between Z_h and Z_v, to partition the contributions of rain and hail to Z based on the premise that hail scatters isotropically. A budgeting approach analogous to Sikdar and Anderson (1974) and Leary and House Jr. (1979) was then employed that included ice microphysics. LWC and IWC were retrieved from Z, and the surface rainfall rate was estimated using Z and Z_{DR}. With the sink of LWC due to rainfall and the temporal change in LWC and IWC (assumed to be equal to the net gain/loss from freezing and melting) known, the heating rate (the residual of condensation and evaporation) could be estimated. Results from this approach were in modest agreement with those retrieved from a multi-Doppler analysis, but only yielded the total estimated latent heating rate within the storm over time, not its spatial distribution. Penide et al. (2013) utilized polarimetric data to classify precipitation as stratiform versus convective using a DSD approach and compared it to the traditional method of using Z texture, as the resultant retrieved latent heating profiles have been shown to be quite sensitive to the determined partitioning of convective and stratiform regions (Lang et al. 2003). Although not directly related to retrieving the diabatic heating and cooling profiles, the study demonstrates the improvement in classification that results from using polarimetric data, which could be applied to the many retrieval techniques that rely on partitioning precipitation into convective or stratiform portions. More recently, Xie et al. (2016) studied X-band polarimetric observations of evaporation, which compared favorably with those simulated from the evaporation model of Kumjian and Ryzhkov (2010). The model was used to show that, for the same

environmental conditions, the cooling rate profile varied (both in magnitude and distribution) based on the median drop diameter of the distribution, a measure related to Z_{DR}. The observed Z and Z_{DR} just below the melting layer were used to retrieve the drop size distributions to initialize the model and, when combined with environmental data from a NWP model, the local cooling rate due to evaporation in time and space was able to be simulated. The limitations of neglecting size sorting, coalescence, and drop breakup in the model were noted, as these can appreciably change the polarimetric characteristics of the precipitation being compared to. Still, the demonstrated potential for quickly retrieving the spatial and temporal distribution of cooling due to evaporation for a real event using a simple model is encouraging and warrants further investigation.

2.2.4 Moisture Retrievals

In addition to microphysical and thermodynamic retrievals, some studies have examined deriving information about the moisture field from radar data, primarily for the purpose of storm-scale data assimilation. As discussed in sections 2.3.2.2 and 3.1.4.2, cloud analyis techniques, which are in widespread use, take a simple approach and typically assume saturated conditions anywhere a prescribed Z threshold is exceeded. A more complex approach was developed by Caumont et al. (2010) and Wattrelot et al. (2014) in which one-dimensional profiles of relative humidity are derived from a model background based on the agreement between observed and simulated profiles of Z. Positive impacts of assimilating these retrievals have been found (see section 2.3.2.3), but difficulties exist with retrieving the moisture profile in cases where observed precipitation fails to exist in the model. In addition, while the moisture field can be very important to retrieve in order to specify accurately in storm-scale models (e.g., Weygandt et al. 2002a,b; Ducrocq et al. 2002), it is only indirectly related to the hydrometeors that comprise the observed Z and thus will continue to require indirect retrieval methods.

2.3 Assimilation of Radar Data into NWP Models

2.3.1 General Considerations

The aforementioned thermodynamic and hydrometeor information content available from radar data motivates its assimilation into NWP models. Regardless of the method chosen, there are a number of considerations for using radar data that must be addressed preceding assimilation. Sun (2005a) provides a thorough review of such factors. Data quality is a primary concern, with a number of undesirable artifacts frequently present in Z and radial velocity including ground clutter and biological echoes, anomalous propagation, velocity folding, range folding, three-body scatter spikes, and sidelobe contamination. All of these must be removed before the data can be assimilated, and a variety of methods exist for combating these such as thresholding and the use of texture fields. In order for the assimilation process to proceed, the model data and radar data must be compared at the same point in space. Radar data can be interpolated onto the model grid using a number of different methods, although the poor vertical resolution of traditional conical volume scans can make interpolation to model grids with dense vertical spacing difficult. The data may also need to be thinned near the radar site due to the increasing resolution at shorter ranges. As an alternative, the model data can be cast onto conical volumetric surfaces to emulate the radar scans, which can involve beam weighting in azimuth and elevation, calculating the refracting of the simulated radar beam, and matching the beamwidth and scanning angles of the radar being compared to (e.g., Lei et al. 2007). Radar operators, and more specifically the polarimetric radar operator employed in this study, will be further explored in section 3.2.

2.3.2 Existing Methods for the Assimilation of Radar Data

A review of various existing methods of assimilating radar data focusing primarily on assimilating Z (rather than radial velocity) is presented below. Although separated into

sections for organiational purposes, it is important to reitereate that many methods do not fit neatly into such categories and instead employ variations on, or combinations of, the different methods below.

2.3.2.1 Nudging Methods

One of the most straightforward, efficient, and easy to implement methods of radar data assimilation is "nudging". Based on Newtonian relaxation, nudging methods operate by taking the difference between a model forecast and an observation and gradually adding increments of this difference to "nudge" the model toward the observation. This method was popularized for radar data assimilation by Jones and Macpherson (1997) and Macpherson (2001), who developed the so-called Latent Heat Nudging (LHN) technique that is based on the idea of a connection between latent heating in a model column and the subsequent precipitation in the corresponding surface grid box. In this approach, model precipitation forecasts are compared with radar-derived rainfall, with the latent heating profile of the model gradually scaled by the difference between the two. This method was found to be successful with improvements that lasted 6-9 hours, and was particularly beneficial for frontal precipitation. Leuenberger and Rossa (2007) investigated the sensitivity of the method to assimilation frequency and biases in the environmental wind and found that the method may struggle in areas of fast-moving precipitation, which speaks to the method's assumption that the precipitation at a grid point is due to the latent heating directly above it, which may not necessarily hold true, particularly as a model's horizontal grid spacing decreases. Stephan et al. (2008) proposed a number of modifications to the original LHN scheme to make it better suited for higher resolution models. Despite the successes, the authors note that the efficacy of the method may be hindered by the accuracy of the background environment and whether it supports the nudged increments. Outstanding questions also remain about how to best

assign a latent heating profile for observed precipitation where the model has none. Although not technically a nudging method, Rogers et al. (2000) sought to alleviate this concern by simply activating the model's convective parameterization scheme wherever Z was observed. In addition, precipitation is the end result of a pathway that begins with latent heating due to condensation, so LHN methods based on radar-inferred rainfall at the surface will necessarily always be delayed in their ability to drive convection, particularly for rapidly-developing situations.

Nudging methods also exist for quantities other than the latent heating rate. Davolio and Buzzi (2004) used radar-estimated precipitation to nudge the model specific humidity toward or away from saturation, with different vertical application curves for whether the model column is considered to be convective or stratiform precipitation. A slightly modified procedure was studied by Korsholm et al. (2015), who applied drying to low-level and in-cloud moisture for the case of overpredicted precipitation but enhanced the horizontal velocity divergence term for the case of underpredicted precipitation to induce further vertical motion. Very positive benefits were found using this method, with little to no spin-up time or imbalances introduced into the model. A combination of LHN and "cloud nudging" of relative humidtiy inferred from Z and satellite data, as in cloud analysis methods, was implemented into the Met Office Unified Model with positive results (Dixon et al. 2009). Similarly, a comparison of nudging water vapor and LHN was performed by Sokol and Rezacova (2009), who found positive results using both methods and improved performance using water vapor over latent heating in certain cases. All of these approaches fall under the umbrella of "diabatic initialization" (Krishnamurti et al. 1991) and are somewhat analogous in that moisture, latent heat release, and divergence are all coupled for deep moist convection. Additionally, all rely on either model-generated (in the case of LHN) or subjectively-determined vertical profiles (in the case of specific humidity or divergence) of the variables being nudged, and all are sensitive to the accuracy of the Z-derived rainfall, which may be prone to large

errors. Despite these potential limitations, nudging methods have the benefit of being straightforward, computationally inexpensive, and are not tied to any one microphysics scheme or model, making them easy to transfer and implement.

2.3.2.2 Cloud Analysis Method

Another approach for radar data assimilation based on the principle of diabatic initialization is the cloud analysis technique. Unlike nudging methods for single model variables, cloud analysis techniques make adjustments to the model temperature, moisture, and hydrometeor q fields through direct insertion based on Z. The basis of modern cloud analysis techniques is the Local Analysis Prediction System (LAPS; Albers et al. 1996), which was designed to synthesize information from a background model, volumetric radar, satellite, and surface observations into a single analysis for forecasters. This approach was extended to serve as a part of the data assimilation routine to initialize the ARPS model (see section 3.1.4) by Zhang et al. (1998) and Zhang (1999), the details of which are described in section 3.1.4.2. Cloud analysis techniques are in widespread use and are conceptually straightforward, computationally efficient, and are useful for reducing the spin-up time of observed storms and improving short-term convective forecasts (e.g., Ducrocq et al. 2000, 2002; Xue et al. 2003, 2014; Souto et al. 2003; Dawson and Xue 2006; Hu et al. 2006a; Zhao and Xue 2009; Schenkman et al. 2011a; Dawson et al. 2015; Zhuang et al. 2016). The cloud analysis is typically run after radial velocity (along with other observations) has been assimilated (e.g., by a variational assimilation routine), as the positive impacts of the cloud analysis are enhanced when used in conjunction with radial velocity (e.g., Hu et al. 2006b). However, variations in the implementation of cloud analysis results are possible. For example, Weygandt et al. (2008) describes the Rapid Update Cycle (RUC) model's Diabatic Digital Filter Initialization (DDFI), which integrates the RUC backwards without physics, inserts the latent heating rate derived from Z in the cloud analysis into the microphysics scheme

and re-integrates the model forward. This has the additional advantage of evolving the wind field in balance with the adjusted latent heating rate.

Modifications to the original cloud analysis have been made since its inception. For example, Brewster (2002) improved the interpolation of Z onto the model grid, the diagnosis of cloud water and ice mixing ratios, and the temperature increments due to latent heating, while Hu et al. (2006a) further improved the retrieval of hydrometeor mixing ratios from Z and incorporated entrainment effects on cloud water and ice and the thermal adjustment. In order to update so many model state variables from Z alone, however, cloud analysis techniques rely on a number of semi-empirical quantiative relations (e.g., retrieving hydrometeor mixing ratios from Z as in section 2.2.1.1) and general rules (e.g., saturating regions within a given Z threshold) that require simplifying assumptions and may introduce errors.

2.3.2.3 Three-Dimensional Variational Assimilation (3D-Var) Method

Variational assimilation methods are a very commonly used class of assimilation methods in NWP at all scales. Variational methods seek to minimize a cost function of the differences between the optimal analysis state and the model background and observations, weighted by their respective error covariances. Through these covariances, analysis increments in an observed variable can update other unobserved variables both at the observation point and nearby. This is the basis for the three-dimensional variational assimilation (3D-Var) method, which operates on all three spatial dimensions at a single point in time. For use with radar data, techniques were initially developed for the assimilation of radial velocity (Gao et al. 1999, 2004; Xiao et al. 2005; Hu et al. 2006b). Xiao et al. (2007) modified the Weather Research and Forecasting (WRF; Skamarock et al. 2005) 3D-Var system for assimilating Z in a tropical cyclone. In this approach, the total water content was used as the control variable and the increment was divided between water vapor, cloud water, and q_r using a linearized warm-rain partitioning scheme.

This spread the influence of the increment spread to the thermodynamic and dynamic variables as well. The impacts were positive, with an improvement over a comparison run without assimilation. Sugimoto et al. (2009) supplemented this methodology with a cloud analysis to condition the background in areas with large departures from the observations (e.g., stable air with no precipitation where the radar indicates there is precipitation) to investigate the ability for the 3D-Var system to retrieved unobserved variables. It was found that the 3D-Var system could partly retrieved unobserved variables, but struggled with retrieving the moisture field and, in the case of assimilating only a single radar, the unobserved cross-radial wind component. In comparison to single-case studies, Sun et al. (2012) tested the WRF 3D-Var system for a six-day period to mimic an operational environment and found generally positive impacts from assimilating both radial velocity and Z, although improvements were case-dependent and found to only exist for daytime, surface-based convection. Recently, Gao and Stensrud (2012) took a different approach and incorporated a hydrometeor classification based on model background temperature into the assimilation routine. A simple temperature thresholding system was used to address the underdetermined problem of retrieving mixing ratios for rain, snow, and hail from a single Z observation by determining which hydrometeor species were present at an observation point, and unlike previous studies allowed for the hydrometeors to be updated in the analysis vector. Results showed that the analysis converged more quickly and accurately when using this hydrometeor classification.

3D-Var routines are desirable for their computational efficiency, which is an important consideration for any operational system. However, many challenges remain for using 3D-Var effectively at the convective scale. In general, the balances and background error statistics that help constrain 3D-Var solutions at large scales cannot be used at the convective scale. In addition, there remain uncertainties in how to effectively update unobserved variables from increments in the hydrometeor fields derived from Z. Because of this, many studies have sought to use 3D-Var for winds in conjunction with

a diabatic initialization technique (either nudging or a cloud analysis) for Z, and have found success in doing so (Hu and Xue 2007; Kain et al. 2010; Rennie et al. 2011). Others have combined these methods. For example, Wang et al. (2013) assimilated retrieved q_r from Z rather than assimilating Z directly, which avoids errors stemming from the use of a linearized radar operator, and assimilated psuedo-observations of relative humidity found by inferring saturation in areas above a Z threshold. Improvements lasting up to 7 hours after assimilation were found. Based on the premise that relative humidity is more important to adjust than hydrometeors, another novel method is presented in Caumont et al. (2010) and Wattrelot et al. (2014). This method uses a 3D-Var approach to assimilate retrieved one-dimensional profiles of relative humidity (called the "1D+3DVAR" approach; see section 2.2.4). The method was found to have positive impacts and has been implemented operationally at Météo-France and is now being investigated for operational use at the Japan Meteorological Agency (Iguchi et al. 2014) and for multinational radar data assimilation (Ridal and Dahlbom 2017).

2.3.2.4 Four-Dimensional Variational Assimilation (4D-Var) Method

In contrast with 3D-Var, which assimilates observations at a single time, four-dimensional variational (4D-Var) assimilation techniques assimilate observations within a time window, with the model itself being integrated through the period. In this way, the entire model framework serves as a dynamical constraint within the cost function and allows the technique to incorporate flow dependencies into its minimization. Because of the short timescales in which convective weather can develop, incorporating observations as they occur over time offers advantages over 3D-Var. The seminal work for assimilating radar data using 4D-Var is Sun and Crook (1997, 1998), who assimilated radial velocity and retrieved q_r as part of a warm-rain microphysics scheme (for reasons similar to those stated in Wang et al. 2013). The system was able to retrieve the temperature, wind, and

hydrometeor fields that compared mostly favorably with observations. The impact of assimilating radar observations at the time they occur rather than grouping them at a single time was noteworthy, with vertical velocities that were up to 50% stronger in the former rather than the latter case. This system was applied to a supercell case and compared favorably against observations for a 2-h forecast period (Sun 2005b), and was successfully extended to include data from multiple radars (Sun and Zhang 2008). A comparison of this 4D-Var approach with an analogous 3D-Var approach and the 3D-Var approach of Wang et al. (2013) for a squall line case indicated quicker spin-up of precipitation, improved quantative precipitation forecast verification scores, and improved analyses of the wind field as well as the low-level convergence and cold pool structure when using the 4D-Var routine (Sun and Wang 2013).

Despite the known advantages of incorporating the time dependency of observations during assimilation, challenges with using 4D-Var for radar data assimilation remain. The formulation and maintenance of the adjoint, particularly for nonlinear processes at the convective-scale, is one of the primary difficulties in a 4D-Var system. Microphysical processes can be very nonlinear, so the formation of the adjoint often requires modification of the microphysics scheme to enable proper convergence of the cost function. 4D-Var is also computationally expensive, making it challenging to use in an operational setting. Finally, 4D-Var has generally been limited to only warm-rain microphysics, although recent work by Chang et al. (2016) has extended the method to include simple ice microphysics. They found that the inclusion of ice phases improved the forecast of convection and significantly affected the retrieved vertical velocity, temperature perturbation, and hydrometeor fields.

2.3.2.5 Ensemble Kalman Filter (EnKF) Method

Recently, the ensemble Kalman filter method (EnKF; Evensen 1994) has become an increasingly popular choice for convective-scale radar data assimilation. The EnKF

method employs an ensemble of model forecasts to estimate the background error covariance, which allows for flow-dependency (unlike 3D-Var) and avoids having to code and maintain an adjoint (unlike 4D-Var). EnKF was first applied at the convective-scale by Snyder and Zhang (2003) for assimilating simulated radial velocity observations, with the system able to retrieve the unobserved variables accurately within seven assimilation cycles. A comparison of 4D-Var and EnKF by Caya et al. (2005) found that, while the 4D-Var method was superior at first, the EnKF method performed better at retrieving the unobserved variables once the storm was established in the model. Dowell et al. (2004) also incorporated observations of Z and successfully assimilated data from an observed supercell storm using a warm-rain microphysics scheme, with Tong and Xue (2005) adding ice microphysics. Due to these early promising results, there has been significant work done to improve the use of EnKF at the convective scale since (e.g., Xue et al. 2006; Aksoy et al. 2009; Yussouf and Stensrud 2010; Snook et al. 2011, 2012; Yussouf et al. 2013; Wheatley et al. 2014, 2015). However, due to the ensemble sizes needed, EnKF methods remain computationally expensive and generally limited to the research realm. In addition, there are still uncertainties in how best to combat issues related to rank deficiency (e.g., filter divergence due to sampling errors; Gao et al. 2014) and nonlinear error growth in the forecast model, which can contaminate the derived covariances and lead the analysis away from reality. Despite these outstanding issues, the EnKF method offers a lot of potential for convective-scale radar data assimilation.

2.3.2.6 Hybrid Methods

Hybrid methods are a relatively new data assimilation method that seek to combine the relative strengths of variational and ensemble methods. To do this, hybrid methods derive flow-dependent covariances from the ensemble and use those, in full or in part, as the covariances in the variational routine. This allows for the capitalization of the variational schemes' computational efficiency along with the efficacy of ensemble

methods to derive rigorous background covariances. Although hybrid methods have been investigated at larger scales (e.g., Wang et al. 2008a,b), the methodology was implemented at the convective-scale by Gao et al. (2013). In a follow-up study, Gao and Stensrud (2014) found the hybrid technique to outperform both the 3D-Var and EnKF techniques, with the optimal weighting of the background covariance between the static variational covariance and the ensemble-derived covariance to increase toward the latter with increasing ensemble size. A slightly different hybrid approach was recently developed by Gao et al. (2016) that derives the background covariance from an ensemble of perturbed 3D-Var analyses rather than using an EnKF. This method performed similarly to that of Gao and Stensrud (2014) using simulated observations but was more computationally efficient. However, the method proved quite sensitive to the choice of microphysics scheme. Pan et al. (2017) used this method to assimilate satellite-derived cloud liquid water path and precipitable water observations alongside radial velocity and Z. Although much work remains to be done, hybrid assimilation methods offer promising results while still being potentially well-suited for operational implementation.

2.3.3 Assimilation of Polarimetric Radar Data

Despite the connection between dual-polarization radar and the microphysical and thermodynamic characteristics of deep moist convection, leveraging polarimetric data for NWP is a relatively new area of research. Much of the work thus far has focused on comparing the polarimetric characteristics of convection in models to those of observations, predicated on the idea that a physically-accurate microphysics scheme should be able to reproduce realistic polarimetric signatures. Relating model state variables to observed polarimetric variables requires the use of a polarimetric radar forward operator (e.g., Jung et al. 2008a, 2010a; Pfeifer et al. 2008; Ryzhkov et al. 2011), which combine the model's forecast hydrometeor size distributions with assumptions about their canting angles, aspect ratios, and dielectric constants to produce simulated polarimetric

variables. Many recent studies have used these operators to compare the performance of and identify deficiencies in model microphysics schemes (e.g., Jung et al. 2008a, 2010a, 2012; Ryzhkov et al. 2011, 2013a; Kumjian and Ryzhkov 2012; Dawson II et al. 2013, 2014; Kumjian et al. 2014; Putnam et al. 2014; Johnson et al. 2016; Snyder et al. 2017a,b). Alternatively, if a model faithfully reproduces polarimetric signatures as they are observed in nature, the model can be used to investigate what physical processes are responsible for a given signature. Other studies have attempted to use polarimetric data to inform the model analysis state. Sun and Crook (1998) used Z_{DR} in conjunction with Z to retrieve q_r and found that, when assimilated into their 4D-Var system, the resultant fields of rainwater and cloud water were closer to the aircraft observations than when using Z alone. Wu et al. (2000) attempted to use Z_{DR} to differentiate between liquid and ice phases for hydrometeor mass retrievals using a 4D-Var scheme but found little success attributed to inadequecies in the model physics. Using an EnKF framework, simulated polarimetric radar data were assimilated to estimate state variables (Jung et al. 2008a,b) and microphysical parameters (Jung et al. 2010b), with positive impacts found in both cases. Few studies have sought to assimilate real dual-polarization radar observations. Li and Mecikalski (2010, 2012) compared the impacts of using both Z and the polarimetric variables to update q_r in a mesoscale convective system using a 3D-Var system and warm rain microphysics and found positive impacts with forecasts that better matched the observations. Yokota et al. (2016) also assimilated estimates of rainwater mixing ratio retrieved from Z and K_{DP} in an EnKF system. However, in all of these studies, ice phases were neglected and, despite these encouraging results, assimilating observed polarimetric data remains difficult due to data quality concerns and remaining uncertainties in polarimetric operators. Posselt et al. (2015) examined the information content of the polarimetric variables in a modeled convective storm using a Markov chain Monte Carlo method and found that, whereas rain mass is generally well constrained by the polarimetic variables, ice phases are much more difficult to retrieve, particularly when

the intercept parameters and densities are allowed to vary. In addition to the data quality issues already discussed for Z (see section 2.3.1), polarimetric data may exhibit other artifacts, including nonuniform beam filling, differential attenuation and general biases in Z_{DR} due to radar miscalibration, and depolarization streaks (Kumjian 2013c), with certain variables prone to significant noisiness (e.g., Z_{DR}, K_{DP}). Despite these considerations and early successes, more work remains to be done to fully capitalize on the additional information content that polarimetry offers for storm-scale assimilation.

Chapter 3

Description of Tools Used

3.1 Models

Throughout this work, a number of models are used, and are briefly described below.

3.1.1 One-Dimensional Melting Hail Model (1D-MH)

The 1D-MH is a one-dimensional Lagrangian spectral bin model that contains prescribed hail and graupel size distributions at the top of the model domain, coincident with the 0°C level, and follows them as they fall and melt. Melting, shedding of meltwater, differential sedimentation, and drop breakup are included in the model, but processes involving interactions between hailstones or size bins (e.g., collisions) are not included. Mass water fraction is allowed to vary across the size distribution and meltwater and ice cores are treated separately, with the mass water fraction counted as LWC and the remaining ice core counted as IWC. Both spongy and solid hail are permitted. The treatment of melting hailstones follows Rasmussen and Heymsfield (1987a,b). Drops begin to be shed once there is no air volume remaining in the hailstone. Shed drops assume a gamma size distribution with $\mu = 2.0$ (Milbrandt and Yau 2005a), $\Lambda = 2.0$ mm^{-1}, and N_0 as a function of the mass of shed water. Drops larger than 8 mm begin to spontaneously break up and assume an inverse exponential distribution following Kamra et al. (1991). For more about the 1D-MH, see Ryzhkov et al. (2013a).

3.1.2 One-Dimensional Melting Snow Model (1D-MS)

The 1D-MS is a one-dimensional Lagrangian spectral bin model for melting snow. In addition to melting, the model was expanded from its previous version to include evaporation and the sublimation of snow. Feedbacks of temperature and moisture with the environment were also added, allowing the evolution of the melting layer and associated brightband to be modeled rather than only looking at one point in time. Because the time evolution of the environment is now allowed, the prescribed snow distribution at the top of the domain can also vary in time. The initial density of snowflakes is assumed to be inversely proportional to their diameter following Brandes et al. (2007). The degree of riming, f_{rim}, is allowed to vary from 1 (no riming) to 5 (heavy riming). The terminal velocity of melting particles is given as a function of that of a fully-melted particle of equivalent mass and the meltwater fraction following Szyrmer and Zawadzki (1999). The aspect ratio of melting snowflakes are treated in an analogous way, linearly weighted between that of dry snow and the equivalent melted raindrop based on meltwater fraction. Ventilation and shape effects are included in the microphysical equations, but processes that occur between different bins (e.g., aggregation) are neglected. By doing this, the number concentration flux can be conserved at all heights, emulating steady-state precipitation at a given time. In this study, the vertical grid spacing is 10 m, with the model integration is performed downward toward the surface. A full description of the model is included in section 5.2.2.

3.1.3 Hebrew University Cloud Model (HUCM)

The HUCM is a state-of-the-art non-hydrostatic Eulerian spectral bin model (Khain et al. 2004, 2011; Ilotoviz et al. 2016). It contains 43 mass-doubling bins for cloud water/rain, snow, three categories of ice (dendrites, plates, and columns), graupel, hail, and freezing drops, with the smallest size bin corresponding to a particle with the mass of a 2-μm liquid drop. Both dry and wet hail growth with liquid water above the 0°C level

is included (Phillips et al. 2015, 2014). A size distribution of aerosols is also included, with their activation treated explicitly. The concentration of CCN is set to be constant in the lowest 2 km and decreases exponentially with height above that. More information about the details of the HUCM microphysics scheme is available in Ilotoviz et al. (2016). The simulation employed in this study was two-dimensional in the $x-z$ plane and simulated a hailstorm that struck Villingen-Schwenningen, Germany on 28 June 2006 and caused significant damage (Noppel et al. 2010). By default and unless otherwise specified, the CCN was set to 3000 cm^{-3} following Khain et al. (2011) to represent polluted conditions. The initial horizontally-homogenous conditions were initialized by the observed 12:00 UTC sounding at Stuttgart, Germany modified for additional diurnal heating (Khain et al. 2011). Storms are initiated by negative temperature tendencies inserted in the low-levels meant to simulate a cold pool. The computational area of the HUCM simulations used is 120 km $\times$ 19 km, with a horizontal grid spacing of 300 m and a vertical grid spacing of 100 m. The model is run for 120 minutes, with output written every 1 min. Radar variables were calculated at S band.

3.1.4 Advanced Regional Prediction System (ARPS)

The Advanced Regional Prediction System (ARPS; Xue et al. 2000, 2001, 2003), developed by the Center for Analysis and Prediction of Storms (CAPS) at the University of Oklahoma, is a nonhydrostatic, compressible NWP model designed to function at multiple scales with an emphasis on the assimilation of data and the explicit prediction of convective-scale phenomena. The ARPS Data Assimilation System (ADAS) contains two primary steps: a 3D-Var routine for radial velocity and traditional surface and upper air observations, and a cloud analysis package for assimilating radar and satellite data.

3.1.4.1 ADAS 3D-Var Routine

The ADAS 3D-Var routine seeks to minimize a cost function, $J(x)$, defined as

$$J(\mathbf{x}) = \frac{1}{2}(\mathbf{x}-\mathbf{x}_b)^{\mathrm{T}}\mathbf{B}^{-1}(\mathbf{x}-\mathbf{x}_b) + \frac{1}{2}(H(\mathbf{x})-\mathbf{y}_o)^{\mathrm{T}}\mathbf{R}^{-1}(H(\mathbf{x})-\mathbf{y}_o) + J_c(\mathbf{x}) \tag{3.1}$$

where $\mathbf{x}_b$ is the background vector, $\mathbf{B}^{-1}$ is the inverse of the background error covariance matrix, H is the observation operator that converts model space to observation space, $\mathbf{y}_o$ is the observation vector, $\mathbf{R}^{-1}$ is the inverse of the observation error covariance matrix, $J_c(\mathbf{x})$ is a constraint (or penalty) term, and $\mathbf{x}$ is the analysis field (Gao et al. 2004; Hu et al. 2006b). The optimal analysis, $\mathbf{x}_a$, is obtained by finding $\mathbf{x}$ that minimizes $J(\mathbf{x})$ (i.e., $\nabla J(\mathbf{x}) = 0$). The analysis vector $\mathbf{x}$ in ARPS contains the three-dimensional wind components (u, v, and w), potential temperature (θ), pressure (p), and water vapor mixing ratio (q_v). As it was designed for use at the storm-scale, the routine includes multiple analysis passes with varying scales of spatial influence to help resolve flows at different scales. The observation error covariance matrix $\mathbf{R}$ is assumed to be diagonal (i.e., the observation errors are uncorrelated), and the model error covariance matrix $\mathbf{B}$ does not include covariances between model variables. The spatial covariances for a given variable in $\mathbf{B}$ are modeled by a recursive filter (Hu et al. 2006b). The constraint term, J_c, is a weak mass divergence constraint given by

$$J_c = \frac{1}{2}\lambda_c^2\left[\alpha\left(\frac{\partial\bar{\rho}u}{\partial x}+\frac{\partial\bar{\rho}v}{\partial y}\right)+\beta\frac{\partial\bar{\rho}w}{\partial z}\right] \tag{3.2}$$

where λ_c is a weighting factor for the constraint term and the bracketed term is a divergence term where $\bar{\rho}$ is the mean air density at each level and α and β represent weighting factors for the horizontal and vertical divergence terms, respectively (Hu et al. 2006b). This constraint term is designed to aid in the accurate retrieval of the full three-dimensional wind field from only radial velocity. Observations that are being assimilated are often not the same variables that are in the model. To assimilate these observations, the model variables must be converted to the observation space through H

so that a comparison can be made. For assimilating radial velocity (V_r), the observation operator H for calculating V_r from the model is given by

$$V_r = \frac{(x-x_0)u + (y-y_0)v + (z-z_0)w}{r} \tag{3.3}$$

where (x, y, z) is the model grid point, (x_0, y_0, z_0) is the location of the radar, (u, v, w) are the wind compoments at the model grid point, and r is the distance from the radar location to the model grid point (Hu et al. 2006b). This is then compared against the observed V_r, which is interpolated to the model grid and quality-controlled before the assimilation cycle. Once all data is assimilated and the optimal analysis state is found, this posterior analysis typically serves as the background for the cloud analysis routine.

3.1.4.2 ADAS Cloud Analysis

The ADAS cloud analysis (Zhang et al. 1998; Zhang 1999; Brewster 2002; Hu et al. 2006a) is based on the Local Area Prediction System (Albers et al. 1996) and is designed to reduce the spin-up time of precipitation in the model.

Quality Control The radar data are first quality controlled and interpolated to the model grid. Radar data between 3 km and 230 km from the radar site are used to avoid near field noise. Ground clutter is detected and removed using gradient and texture fields of Z and areas of low V_r, with additional filtering using a user-defined ρ_{hv} threshold (default of 0.85 for S-band). K_{DP}, is calculated from Φ_{DP} from a local least squares fit on smoothed data using a Z-dependent averaging window. A 9-point median filter is also applied to all fields. The radar data is then interpolated to the model grid using a least squares fit to a local polynomial function, which thins the data near the radar and interpolates it at distances far from the radar (Brewster et al. 2005). For the latest changes to the cloud analysis, see Brewster and Stratman (2015).

Assimilation Once the radar data are on the model grid, a number of empirical relations are applied to modify the model state variables. An initial cloud fraction field is

diagnosed from the background relative humidity field following a similar approach to Koch et al. (1997), with additional options to incorporate satellite data and Automated Surface Observing System (ASOS) sky observations. Subsequently, clouds are directly inserted by setting the cloud fraction to 100% above the surface-based lifted condensation level anywhere Z exceeds a threshold, set to 15 dBZ above 2 km by default. Cloud water and ice content can be determined either adiabatically or using the Smith-Feddes model (Haines et al. 1989) with a reduction for entrainment following Hu et al. (2006a), which is used in this study. Next, the dominant hydrometeor species in each grid box is determined using temperature and Z thresholds. Snow/rain are considered when the temperature is below/above 0°C, respectively, and where hail is considered when the Z exceeds 45 dBZ (Albers et al. 1996; Pan et al. 2016). When run in a cycling mode, the species can also be determined by the existing species in the model background. The mixing ratios of each hydrometeor species are then typically retrieved using the single-moment retrieval equations for rain, snow, and hail discussed in section 2.2.1 and summarized in Dowell et al. (2011) and Pan et al. (2016). However, recent work has initialized intercept parameters (and, if needed, shape parameters) for multi-moment schemes using iterative techniques (Brewster and Stratman 2015), whereas other studies have found positive impacts from using single-moment microphysics schemes with intercept parameters diagnosed from hydrometeor mixing ratios (e.g., Wainwright et al. 2014; Pan et al. 2016), as developed in Zhang et al. (2008).

After the hydrometeors have been inserted, a temperature adjustment is made to account for latent heat release within the updraft. This can be done by simply adding the latent heating associated with the added cloud water and ice content (Zhang et al. 1998) or by assuming a moist-adiabatic temperature profile from cloud base with entrainment effects included (Brewster 2002; Hu et al. 2006a). In this study, the latter method is applied to regions with vertical velocity $w >$ -0.2 m s^{-1} (determined from the 3D-Var analysis) with a linear ramp from no heating to full heating between $w =$ -0.2 and 0.0 m

s^{-1}. Final moisture adjustments are made by re-establishing saturation anywhere the Z threshold for clouds is exceeded (incorporating the previously-made temperature adjustment) or to 95% anywhere the analyzed hydrometeor mass is less than the background hydrometeor mass to help avoid over-moistening. Further details of the cloud analysis and its latest updates can be found in Brewster and Stratman (2015) and Tong (2015).

3.2 Polarimetric Radar Operator

As mentioned in sections 2.3.1 and 2.3.3, radar operators are necessary to convert model state variables into radar variables. For radial velocity this task is trivial, with the largest uncertainty being how to characterize the terminal velocity of the hydrometeors. The calculation of Z, and in particular the polarimetric variables, is more complicated due to the number of factors that influence these radar variables that are not typically predicted by models' microphysics schemes. In this study, the polarimetric radar operator of Ryzhkov et al. (2011) is used in conjunction with the 1D-MH, 1D-MS, and HUCM models, and is the subject of the following discussion, whereas the polarimetric radar operator of Jung et al. (2010a) is used to compute Z from the ARPS model. Some modifications and changes to the default polarimetric radar operator discussed below are examined and discussed for the 1D-MS in section 5.2.3. In the operator of Ryzhkov et al. (2011), particles are treated as either oblate or prolate spheroids. Scattering amplitudes can be computed using the Rayleigh scattering approximation or using a full T-Matrix calculation (Mishchenko 2000).

The dielectric constants of water and ice are given by Ray (1972), whereas the dielectric constants of mixed-phase media are found using Maxwell-Garnett mixing formulas (Maxwell Garnett 1904). For the case of two-layer spheroids within the Rayleigh regime, such as melting hail that can be understood as solid ice with a water shell, the scattering amplitudes are found by using the formulation of Bohren and Huffman

(1983). The operator allows for the volume mass water fraction to vary across the size spectrum.

The aspect ratio of hydrometeors are not typically predicted by microphysics schemes and thus must also be specified. The aspect ratio of a spheroid is defined as the ratio of the length along its axis of symmetry to its tranverse axis. For rain, the aspect ratio as a function of size is relatively well-constrained and given by Brandes et al. (2002, 2005). The aspect ratios of ice crystals of different habits are specified from the parameters given in Matrosov et al. (1996). Snow aggregates are, by default, assumed to have an aspect ratio of 0.8 following Straka et al. (2000). Graupel is assumed to have an aspect ratio that varies linearly from 1.0 to 0.8 for particles whose diameter is smaller than 10 mm and is then capped at 0.8 for particles with diameters exceeding 10 mm. The aspect ratios of melting particles are harder to define. For melting snow, it is assumed to vary linearly with mass water fraction between that of snow and that of the raindrop the snow melts into. For melting graupel and hail, the parameterization given by Rasmussen et al. (1984) is used.

Another factor that can affect the polarimetric characteristics of hydrometeors is their orientation. The operator assumes that all hydrometeors have Gaussian canting angle distributions with a mean canting angle of 0°. By default, it is assumed that the width of the canting angle distribution is 10° for rain and oblate crystals and 40° for dry snowflakes, graupel, and hail. As with aspect ratio, the width of the canting angle distribution for melting particles is assumed to vary linearly with mass water fraction.

These factors, along with the radar wavelength, can then be used to calculate the polarimetric variables by summing along the model-provided size distributions. This study will focus on the use of Z, Z_{DR}, K_{DP}, and A_{H}. Although the operator has been shown to qualitatively reproduce the observed features of ρ_{hv}, the magnitudes are biased high. This is hypothesized to be due to the exclusion of δ (when the Rayleigh assumption is being used) as well as the simplified treatment of hydrometeors as spheroids instead

of the complex and jagged shapes that hydrometeors such as hail and melting snow aggregates may attain in reality (Ryzhkov et al. 2011, 2013b).

Chapter 4

Hydrometeor Mass Retrievals

The work presented in this chapter is taken from: Carlin, J. T., A. V. Ryzhkov, J. C. Snyder, and A. Khain, 2016: Hydrometeor Mixing Ratio Retrievals for Storm-Scale Radar Data Assimilation: Utility of Current Relations and Potential Benefits of Polarimetry. *Mon. Wea. Rev.*, **144**, 2981-3001, doi:10.1175/MWR-D-15-0423.1 and evolved from the author's Master's thesis.

Hydrometeor size distributions are most generally assumed to follow a gamma distribution, given by (e.g., Ulbrich 1983)

$$N_x(D) = N_{0,\mathrm{x}} D^{\mu_x} e^{-\Lambda_x D} \tag{4.1}$$

where $N_{0,x}$ is the intercept parameter, μ_x is the shape parameter, and Λ_x is the slope parameter of hydrometeor species x. However, simplifying assumptions about the size distribution are often made. By assuming $\mu_x = 0$, as is commonly done, Eq. (4.1) reduces to the inverse exponential distribution,

$$N_x(D) = N_{0,\mathrm{x}} e^{-\Lambda_x D}, \tag{4.2}$$

becoming a two-parameter distribution used by so-called "double-moment" microphysics schemes.

The mixing ratio of hydrometeor species x (q_x) is proportional to the third moment of the PSD and is given by

$$q_x = \frac{\rho_x}{\rho} \frac{\pi}{6} \int_0^\infty D^3 N_x(D) dD \tag{4.3}$$

where ρ is the air density, ρ_x is the hydrometeor density, D is the particle equivolume diameter, and $N_x(D)$ is the PSD of x. If an inverse exponential size distribution and the Rayleigh scattering assumption are used, Z_x (Eq. 2.11) can be expressed as

$$Z_x = N_{0,x} \frac{|K_x|^2}{|K_w|^2} \frac{\Gamma(7)}{\Lambda^7} \tag{4.4}$$

where

$$\Lambda_x = \left(\frac{\rho_x \pi N_{0,x}}{\rho q_x} \right)^{0.25}. \tag{4.5}$$

Substituting Eq. (4.5) into Eq. (4.4), the $Z - q$ relation for inverse exponential size distributions within the Rayleigh scattering regime can be expressed most generally as

$$Z_x = \frac{7.2 \times 10^{20} \frac{|K_x^2|}{|K_w^2|} (\rho q_x)^{1.75}}{\pi^{1.75} N_{0x}^{0.75} \rho_x^{1.75}}. \tag{4.6}$$

Equation (4.6) is the general form of the forward operator equations used in many studies to calculate simulated Z from NWP model forecasts (e.g., Tong and Xue 2005; Dowell et al. 2011). It also serves as the root for retrieving hydrometeor q from Z. However, assuming the composition (affecting both ρ_x and K_x) of a hydrometeor species is known, the relation is a function of two parameters of the size distribution, $N_{0,\mathrm{x}}$ and Λ_x. The retrieval of both parameters of the size distribution requires at least two independent radar variables (Atlas and Ulbrich 1974). In the absence of utilizing dual-polarization or dual-wavelength data, there are a few different approaches for determining the size distribution parameters. A $N_{0,x} - q_x$ relation (e.g., Zhang et al. 2008) can be used to constrain the problem to a single parameter. This approach is used in Wainwright et al. (2014) and Pan et al. (2016), who derive $N_{0,x} - q_x$ relations from a NWP model employing double-moment microphysics and use it with a single-moment microphysics scheme to allow for a variable N_0. If the retrieved q_x is being assimilated into an NWP model in a cycling mode, such as through a cloud analysis (see section 2.3.2.2), the background $N_{0,x}$ can be used. However, the most common approach by far is to fix the $N_{0,x}$ at a constant value typical of a species, allowing Λ_x to be determined from Z_x and q_x to be

retrieved. Although retrieving q from Z has many different applications, the following discussion is in the context of retrieving q for assimilation into an NWP model.

For rain (r), $N_{0,r}$ is typically fixed at 8×10^6 m^{-4} (the well-known "Marshall-Palmer distribution"; Marshall and Palmer 1948). Using the density and dielectric constant for water, Eq. (4.6) for rain becomes

$$Z_r = 3.63 \times 10^9 (\rho q_r)^{1.75}. \tag{4.7}$$

For snow (s), $N_{0,s}$ is usually assumed to be 3×10^6 m^{-4} (Gunn and Marshall 1958). The dielectric constant for snow, K_s, depends on whether the snow is wet or dry. For dry snow, K_s can be defined in terms of the dielectric constant for ice, K_i, and the density of snow, ρ_s, according to (Smith 1984)

$$|K_s|^2 = |K_i|^2 \left(\frac{\rho_s^2}{\rho_i^2} \right), \tag{4.8}$$

where $|K_i|^2 \approx 0.17$ and ρ_i = 917 kg m^{-3}. A second formulation exists that uses the equivolume diameter of fully-melted snowflakes in which ρ_i is replaced with ρ_w (e.g., Dowell et al. 2011; Gao and Stensrud 2012). In this instance, $|K_i|^2$ must be adjusted to account for this decrease in diameter and instead takes the value 0.21. If ρ_s is assumed to be constant at 100 kg m^{-3}, as if often done (e.g., Lin et al. 1983), the $Z-q$ relation for dry snow (ds) becomes

$$Z_{ds} = 9.80 \times 10^8 (\rho q_{ds})^{1.75}. \tag{4.9}$$

If the snow is assumed to be wet (often done if $T > 0$°C), K_s is assumed to be equal to K_w, and the $Z-q$ relation for wet snow (ws) becomes

$$Z_{ws} = 4.26 \times 10^{11} (\rho q_{ws})^{1.75}. \tag{4.10}$$

Finally, for hail (h), it is commonly assumed that $N_{0h} = 4 \times 10^4$ m^{-4} (Federer and Waldvogel 1975), $\rho_h = 900$ kg m^{-3}, and with $|K_h|^2$ adjusted in an analogous manner to Eq. (4.8). This results in the retrieval equation for (dry) hail of

$$Z_h = 4.33 \times 10^{10} (\rho q_h)^{1.75}. \tag{4.11}$$

This set of simplified retrieval equations exhibit limitations ranging in validity due to the assumptions made in deriving them. The most restrictive assumption is fixing the $N_{0,x}$ of all species to be constant. Kessler (1969) described the assumption of a fixed $N_{0,r}$ as one that "does some violence to the physics of the evaporation process", and Sun (2005a) noted that it is "not trivial to quantify" the error in the retrieved q induced by such an assumption. The assumption of constant density may be a poor one for ice hydrometeors, particularly for ρ_s, which generally varies nearly inversely with diameter with a mass-diameter relation for snow having a diameter exponent closer to 2 than 3 (e.g., Brandes et al. 2007), resulting in an approximate D^4 dependence for Z from snow rather than a D^6 dependence. The density of hail and graupel may also vary from that of pure ice as they may be spongy and contain air cavities, and may be either wet or dry below the melting layer depending on whether meltwater seeps inside to fill the voids (Dowell et al. 2011). Additionally, by invoking the Rayleigh approximation, resonance scattering from large hydrometeors is neglected and subsequently any dependence on radar wavelength or nonsphericity is excluded. However, efforts have been made in some studies (e.g., Dowell et al. 2011) to account for the effects of non-Rayleigh scattering of large hail by exponentiating a modified retrieval equation for wet hail to 0.95, based on the work of Smith et al. (1975) and given by

$$Z_h = \left(\frac{7.2 \times 10^{20} (\rho q_h)^{1.75}}{\pi^{1.75} N_{0h}^{0.75} \rho_h^{1.75}} \right)^{0.95} = 6.13 \times 10^{10} (\rho q_h)^{1.6625}. \tag{4.12}$$

These simplified $Z - q$ relations also assume *a priori* knowledge of what hydrometeor type to retrieve, and an approach for retrieving multiple hydrometeor species within a volume and partitioning the Z is not immediately clear. Because of this, many systems that retrieve q from Z, such as cloud analysis techniques, rely on empirical criteria (e.g., temperature and Z thresholds) for determining which species to retrieve (see section 3.1.4.2 for details). A demonstrative example of the application of these $Z - q$ relations is shown in Figure 4.1 from the HUCM using the retrieval relations previously described and species determined from the criteria used in the cloud analysis. A number

of differences between the retrieved hydrometeor field and the model hydrometeor field are present. Naturally, as the species in each grid box is determined using temperature and Z thresholds, only one species is allowed to exist and the areas of hail/graupel and snow and hail/graupel and rain are not reproduced. Above the environmental 0°C level (located at approximately z = 3.5 km), there is too much snow retrieved, whereas appreciable amounts of snow only exist in the model hydrometeor field above approximately z = 8 km. Accordingly, the hail/graupel mass is thus underestimated in the mid-levels. Below the environmental 0°C level, the retrieved rain field is much more expansive than the model rain field, and features very large values in excess of 10 g m^{-3} in the main precipitation core, whereas the model rain field peaks at approximately 4 g m^{-3}. This is very likely due to the assumption of rain alone below the environmental 0°C level, whereas the model field makes clear that the Z exceeding 60 dBZ in this region is due to melting hail.

Despite these limitations, assimilating retrieved q into storm-scale NWP models using these relations has proven to be beneficial, including reducing the spin-up time and forecast error (e.g., Souto et al. 2003; Dawson and Xue 2006; Hu et al. 2006a; Zhao and Xue 2009; Schenkman et al. 2011a). Thus, they still remain in widespread use for radar data assimilation applications (e.g., Hu and Xue 2007; Kain et al. 2010; Stensrud and Gao 2010; Schenkman et al. 2011b; Xue et al. 2014; Dawson et al. 2015; Chang et al. 2016).

In this study, the 1D-MH and HUCM models (described in sections 3.1.1 and 3.1.3, respectively) are used to examine the utility of the retrieval equations for q_r and q_h in the context of radar data assimilation and whether dual-polarization radar data can aid in improving the accuracy of these retrievals. More specifically, it is the most limiting versions of these Z-based retrieval relations with the most restrictive assumptions, given by Equations (4.7) and (4.11), that are studied as they have the most potential for significant errors and are still widely used. Hereafter, the phrase "legacy retrieval equations"

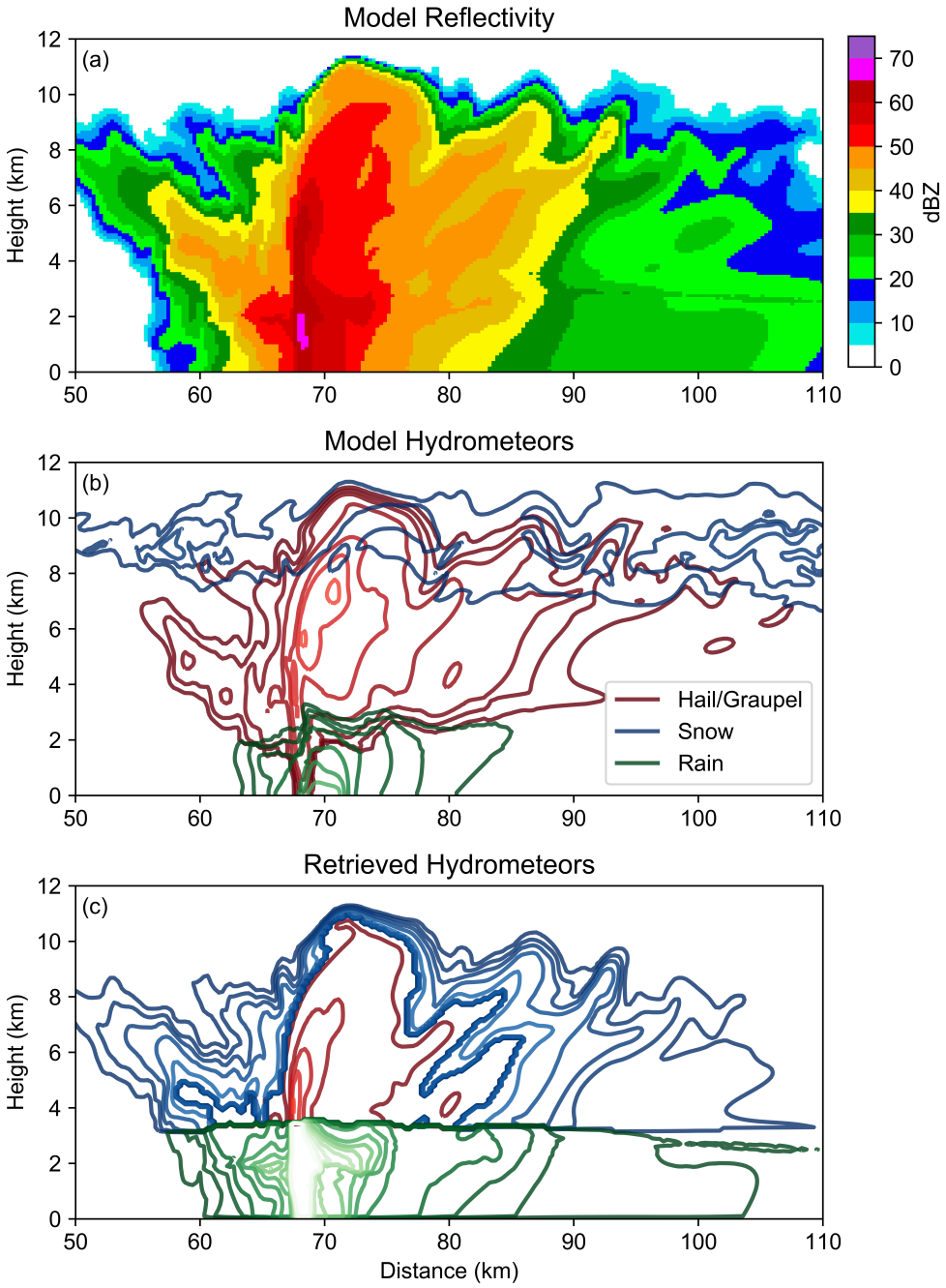

Figure 4.1: An example comparison of (a) model Z from the HUCM at t = 6000 s, (b) the corresponding model q_r (green), q_s (blue), and q_{h+g} (red) fields, and (c) the retrieved hydrometeor q_r, q_s, and q_h from Z using Eqs. (4.7), (4.9), and (4.11) and the temperature thresholds described in section 3.1.4.2. The hydrometeor fields are contoured every 1.0 g m^{-3} up to 10 g m^{-3}, along with 0.1, 0.25, and 0.5 g m^{-3}.

will specifically refer to this set of simplified equations. In addition, LWC and IWC, both in g m^{-3}, are used in place of q_r and q_h (and graupel mixing ratio, q_g, where noted) due to convention, differing by only a factor of ρ. Section 4.1 examines the performance of various relations for retrieving R and LWC using disdrometer observations. The specific setup of the 1D-MH and HUCM used in this study is presented in section 4.2, and the evolution in space and time of the biases of the retrieved LWC field will be shown in section 4.3. Section 4.4 then examines the separate estimation of LWC and IWC in rain/hail mixtures. A summary of the main conclusions is presented in section 4.5.

4.1 Inherent performance of polarimetric retrievals in rain

To investigate the use of dual-polarization data for improving LWC retrievals and to review the utility of polarimetric R relations, data from a large two-dimensional video disdrometer during pure rain (i.e., not mixed with hail, graupel, or snow) were used. The data were collected over a seven year period in Oklahoma and contain 47,144 unique DSDs from both stratiform and convective rain events. Following Ryzhkov et al. (2014), polarimetric radar variables at S band (λ = 11.0 cm) and C band (λ = 5.3 cm) were computed for each DSD at a temperature of 20°C using the canting angle distribution and aspect ratio relation for rain discussed in section 3.2. Full details of the disdrometer dataset can be found in Schuur et al. (2005). The derived retrieval relations were found by performing weighted least squares regressions on the median of each variable within bins of $\log_{10}(R)$ and $\log_{10}$(LWC) ranging from -1.2 to 2.0 and -2.2 to 1.0, respectively, in intervals of 0.1. Each bin was weighted by the center R or LWC within the bin multiplied by the number of points within that bin. Retrievals using Z, Z and Z_{DR}, K_{DP}, A_{H}, and Z and the normalized drop concentration (N_w) are performed. N_w (Testud et al. 2001) is given by

$$N_w = \frac{4^4}{\pi \rho_w} \frac{\mathrm{LWC}}{D_m^4}, \tag{4.13}$$

where D_m is the volume-weighted mean diameter (equal to the ratio of the fourth to the third moment of the DSD). N_w represents the intercept parameter for an exponential size distribution with an equivalent D_m and LWC *regardless of actual DSD shape*. For the case of the Marshall-Palmer DSD (in which $N_w = N_{0r}$), $\log_{10} N_w \approx 3.9$. Tropical rain with DSDs skewed toward smaller drops feature high values of N_w whereas rain from strong continental convection with DSDs skewed toward larger drops features low values of N_w (Bringi et al. 2003). The goal of deriving retrieval relations for R and LWC using the disdrometer data is to investigate the inherent usefulness of various polarimetric variables for rain retrievals, as each derived retrieval equation was found using the same method and dataset. A summary of all of these derived retrieval equations, along with their root mean square errors (RMSE), Pearson correlation coefficients (r), and standard deviations (σ) are shown in Table 4.1.

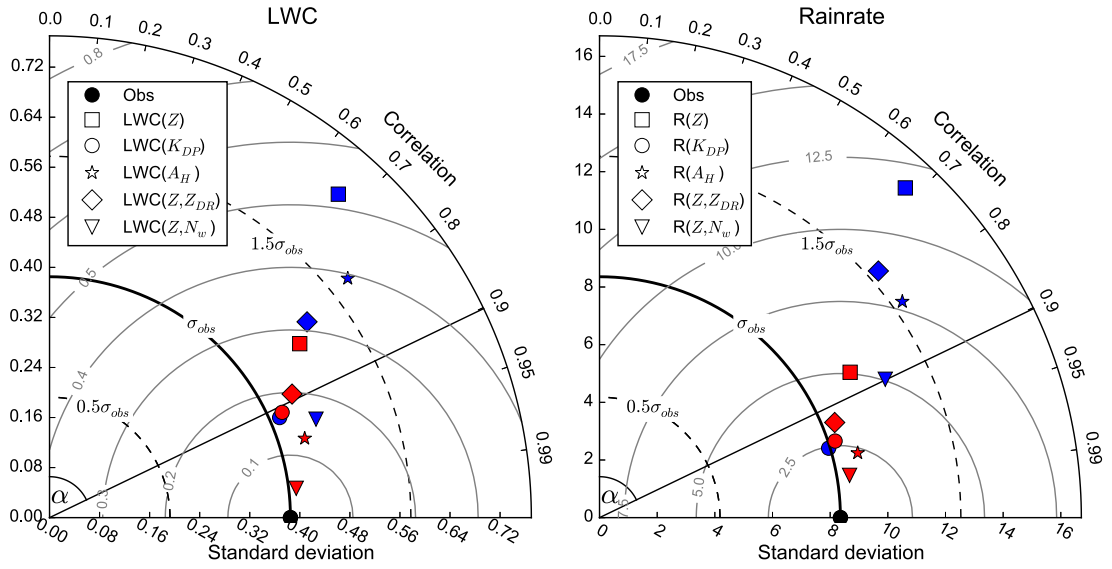

Figure 4.2: Taylor diagram comparing the performance of retrievals at S band (red) and C band (blue) for (left) LWC (g m^{-3}) and (right) R (mm h^{-1}), corresponding to Eqs. (1) - (10) and (11) - (20) in Table 4.1, respectively. The black circle represents the characteristics of the observed disdrometer dataset. A line corresponding to a correlation of 0.9 is shown for readability.

Table 4.1: Retrieval relations for LWC and R at both S- and C-band from disdrometer data, along with the root mean square error (RMSE), Pearson correlation coefficient (r), and standard deviation (σ) of each relation, where LWC is in g m^{-3}, R is in mm hr^{-1}, Z is linear in units of mm^6 m^{-3}, Z_{dr} is linear and unitless, N_w is in m^{-3} mm^{-1}, K_{DP} is in $^\circ$ km^{-1}, and A_H is in dB km^{-1}.

S Band					C Band				
No.	*Relation*	*RMSE*	*r*	σ	*No.*	*Relation*	*RMSE*	*r*	σ
	LWC Observations	—	—	0.39		LWC Observations	—	—	0.39
1	$\mathrm{LWC}(Z) = 1.74\times10^{-3}Z^{0.640}$	0.28	0.82	0.49	6	$\mathrm{LWC}(Z) = 1.59\times10^{-3}Z^{0.657}$	0.53	0.67	0.69
2	$\mathrm{LWC}(K_{DP}) = 2.24K_{DP}^{0.725}$	0.17	0.91	0.41	7	$\mathrm{LWC}(K_{DP}) = 1.27K_{DP}^{0.714}$	0.16	0.92	0.40
3	$\mathrm{LWC}(A_H) = 115A_H^{0.917}$	0.13	0.96	0.43	8	$\mathrm{LWC}(A_H) = 11.0A_H^{0.777}$	0.40	0.78	0.61
4	$\mathrm{LWC}(Z,Z_{dr}) = 1.33\times10^{-3}Z^{0.696}Z_{dr}^{-0.981}$	0.20	0.89	0.44	9	$\mathrm{LWC}(Z,Z_{dr}) = 1.29\times10^{-3}Z^{0.701}Z_{dr}^{-0.790}$	0.32	0.80	0.52
5	$\mathrm{LWC}(Z,N_w) = 1.16\times10^{-4}Z^{0.550}N_w^{0.411}$	0.05	0.99	0.40	10	$\mathrm{LWC}(Z,N_w) = 1.51\times10^{-4}Z^{0.572}N_w^{0.363}$	0.16	0.94	0.45
	R Observations	—	—	8.36		R Observations	—	—	8.36
11	$\mathrm{R}(Z) = 1.94\times10^{-2}Z^{0.692}$	5.07	0.87	10.05	16	$\mathrm{R}(Z) = 1.72\times10^{-2}Z^{0.714}$	11.69	0.68	15.60
12	$\mathrm{R}(K_{DP}) = 46.9K_{DP}^{0.794}$	2.67	0.95	8.59	17	$\mathrm{R}(K_{DP}) = 25.0K_{DP}^{0.777}$	2.46	0.96	8.30
13	$\mathrm{R}(A_H) = 3380A_H^{0.995}$	2.34	0.97	9.23	18	$\mathrm{R}(A_H) = 243A_H^{0.826}$	7.83	0.81	12.90
14	$\mathrm{R}(Z,Z_{dr}) = 1.60\times10^{-2}Z^{0.738}Z_{dr}^{-0.912}$	3.33	0.93	8.80	19	$\mathrm{R}(Z,Z_{dr}) = 1.63\times10^{-3}Z^{0.731}Z_{dr}^{-0.399}$	8.68	0.75	12.91
15	$\mathrm{R}(Z,N_w) = 2.68\times10^{-3}Z^{0.638}N_w^{0.295}$	1.48	0.99	8.80	20	$\mathrm{R}(Z,N_w) = 2.37\times10^{-3}Z^{0.654}N_w^{0.301}$	5.04	0.90	11.01

Fig. 4.2 is a Taylor diagram[1] (Taylor 2001) examining the performance of these derived retrieval relations for both R and LWC at S and C band. For both LWC and R at both wavelengths, retrievals using only Z perform the worst, with the largest RMSE, standard deviations, and lowest correlations with the disdrometer dataset. At S band, the LWC(Z, N_w) and $R(Z, N_w)$ retrievals show the best performance. LWC(Z, N_w) also shows superior performance at C band, whereas the error for R(Z, N_w) at C band is larger for larger values of R.

In practice, however, the use of N_w may not be ideal. Estimates of N_w can be obtained from dual-polarization radar data using the so-called "$Z - Z_{\rm DR}$ method" by assuming a value of μ (Illingworth and Thompson 2005; Tabary et al. 2011), and estimates of median volume diameter D_0, which is quite close to D_m, can be found via $Z_{\rm DR}$ (e.g., Gorgucci et al. 2002; Cao et al. 2008), which can then be used to retrieve the LWC. However, the accurate estimation of N_w requires high-quality, well-calibrated radar measurements of the intrinsic Z and $Z_{\rm DR}$, which can become difficult at shorter wavelengths owing to attenuation. Additionally, to achieve estimates of Z and $Z_{\rm DR}$ with sufficient accuracy, the $Z - Z_{\rm DR}$ method requires the use of multiple consecutive radar gates, resulting in a decreased spatial resolution for N_w. Owing to potential difficulties in using N_w, alternative relations should also be considered.

Second to LWC(Z, N_w), LWC($A_{\rm H}$) exhibits the smallest RMSE at S band whereas LWC($K_{\rm DP}$) exhibits the smallest RMSE at C band (though may also suffer from inferior resolution compared to the other polarimetric retrieval methods due to a similar need

[1]Taylor diagrams are useful for assessing overall performance of models compared to a reference dataset (in this case, disdrometer observations). The thick solid black line represents the standard deviation of the observations (σ_{obs}), with $0.5\sigma_{obs}$ and $1.5\sigma_{obs}$ denoted in dashed lines. Pearson correlation coefficient is shown as a function of angle α. RMSE values are shown in concentric thin gray rings centered at the observation point at the bottom of the plot (black dot) which corresponds to an RMSE of 0.0, a correlation of 1.0 and the standard deviation of the dataset. For example, LWC($A_{\rm H}$) at S-band has a correlation coefficient of 0.96, a σ of 0.43, and an RMSE of 0.13 g m^{-3}, and is shown by a red star above and slightly to the right of the observation point.

for averaging as N_w). For R retrievals, similar conclusions are drawn as for LWC, with $R(A_{\mathrm{H}})$ retrievals featuring the smallest RMSE at S band and $R(K_{\mathrm{DP}})$ having the smallest RMSE at C band. For both LWC and R at both wavelengths, retrievals incorporating Z_{DR} improve upon those using Z alone but perform less well relative to the other polarimetric retrievals presented. The performance of LWC(Z, Z_{DR}) and $R(Z, Z_{\mathrm{dr}})$ retrievals will likely be even poorer in areas dominated by rain derived from melting hail and graupel, which tends to feature large drops with large Z_{DR} that falls even further outside of the typical $Z - Z_{\mathrm{DR}}$ parameter space. Overall, with the exception of K_{DP}, all retrievals perform worse at C band than S band and for increasing RMSE exhibit larger standard deviations and smaller correlations.

The above relations have been derived for the case of pure rain. In the case of a mixture of rain and hail, different relations should be used to estimate LWC and IWC separately.

4.2 Model setup

To investigate the performance of the legacy retrieval relations for the estimation of LWC and IWC within rain and rain/hail mixtures, the 1D-MH and HUCM models coupled to the polarimetric operator (described in sections 3.1.1, 3.1.3, and 3.2, respectively) are used. The use of these two models for this purpose is intended to be complementary: the HUCM can explicitly calculate the development of hydrometeor PSDs from the modeled storm's inception, with no restrictions on PSD form, whereas the 1D-MH must have hydrometeor size distributions prescribed but can be initialized with the user's choice of PSD parameters, allowing for the selection of PSDs that encompass the entire range of possible values observed in nature.

The HUCM run used is the default run described in section 3.1.3. For the 1D-MH, the top of the model domain, and the coincident 0°C level, was set at 4 km with a constant relative humidity of 100% and lapse rate of 6.5 °C km^{-1}. All ice was assumed

to be solid ($\rho = 917$ kg m^{-3}). Meltwater was allowed to accumulate on the surface of ice particles and began to be shed once a critical threshold was reached. Radar calculations were performed for both S band (λ = 11.0 cm, hereafter denoted in red) and C band (λ = 5.45 cm, hereafter denoted in blue). To get a comprehensive and representative sample, the 1D-MH was run with varying parameters across the reported parameter space for hail PSDs. Based on previous findings of bi-exponential distributions within hailstorms (Smith et al. 1976), initial ice distributions were given by

$$N(D) = N_{0g}\exp(-\Lambda_g D) + N_{0h}\exp(-\Lambda_h D) \tag{4.14}$$

where $N_{0g} = 8000$ m^{-3} mm^{-1} and Λ_g = 1.6 mm^{-1} for all distributions. This graupel distribution was chosen to replicate a Marshall and Palmer (1948) raindrop distribution at the surface. Three size categories for the hail portion of the distributions were used: "small" ($10 < D_{max} \leq 25$ mm), "large" ($30 < D_{max} \leq 50$ mm), and "giant" ($55 < D_{max} \leq 75$ mm), with D_{max} varying in 5 mm increments. The slope parameter Λ_h varied in increments of 0.05 mm^{-1} such that the product $D_{max}\Lambda_h$ fell between approximately 5 and 11, following the findings of Ulbrich and Atlas (1982) and Cheng et al. (1985). The intercept parameter was computed according to $N_{0h} = A\Lambda_h^{4.11}$ following Cheng et al. (1985) and Federer and Waldvogel (1975) with A varying from 50 to 800 in increments of 50. Once the parameters of the graupel and hail distributions were specified, they were combined and treated as one encompassing ice distribution. A total of 1,952 unique ice distributions were modeled. The parameters of these distributions are summarized in Table 4.2.

4.3 Variability of retrieval biases in time and space for rain

Although it is known that the assumptions made in deriving the legacy retrieval relation for rain (Eq. 4.7) may introduce errors in the retrieved LWC, it is worth investigating these biases as they evolve in time and space within the storm. Figure 4.3 shows the

Table 4.2: Summary of the range of parameters used in determining the modeled hail distributions in the 1D-MH.

Size	Λ_h (mm^{-1})	$\Delta\Lambda_h$ (mm^{-1})	D_{max} (mm)	ΔD_{max} (mm)	A	ΔA
Small	0.25 - 1.10	0.05	10 - 25	5	50 - 800	50
Large	0.10 - 0.30	0.05	30 - 50	5	50 - 800	50
Giant	0.05 - 0.25	0.05	55 - 75	5	50 - 800	50

predicted LWC and Z of rain at various points of the simulated storm's life cycle from the HUCM, colored according to $\log_{10} N_w$. It is immediately evident that the relation between LWC and Z in rain is highly variable and changes significantly over time.

At t = 2460 s (Fig. 4.3a,e), raindrops have begun to form atop and fall alongside of the burgeoning updraft (as discussed in Khain et al. 2013), with LWC approaching 1 g m^{-3}. Rapid size sorting due to differential sedimentation occurs with this initial rain, with most of the updraft featuring DSDs skewed toward smaller drops with relatively low Z for the given LWC. This is seen prominently in the N_w field with very high values throughout the updraft indicative of a categorical underestimation of LWC by the legacy retrieval equation, which could negatively impact efforts to achieve an accurate analysis of the q_r in developing convection. A very sharp transition to low values of N_w is seen on the bottom fringe of the rain field, representing the size sorted large drops that have fallen out almost instantly upon formation.

By t = 2880 s (Fig. 4.3b,f), rain DSDs have matured and are reasonably close to that predicted by the legacy retrieval relation, though distinct signatures for both the updraft (z = 5-8 km) and size sorted drops (z = 0-2 km) still exist, resulting in a range of over 40 dBZ for LWCs under 1 g m^{-3}.

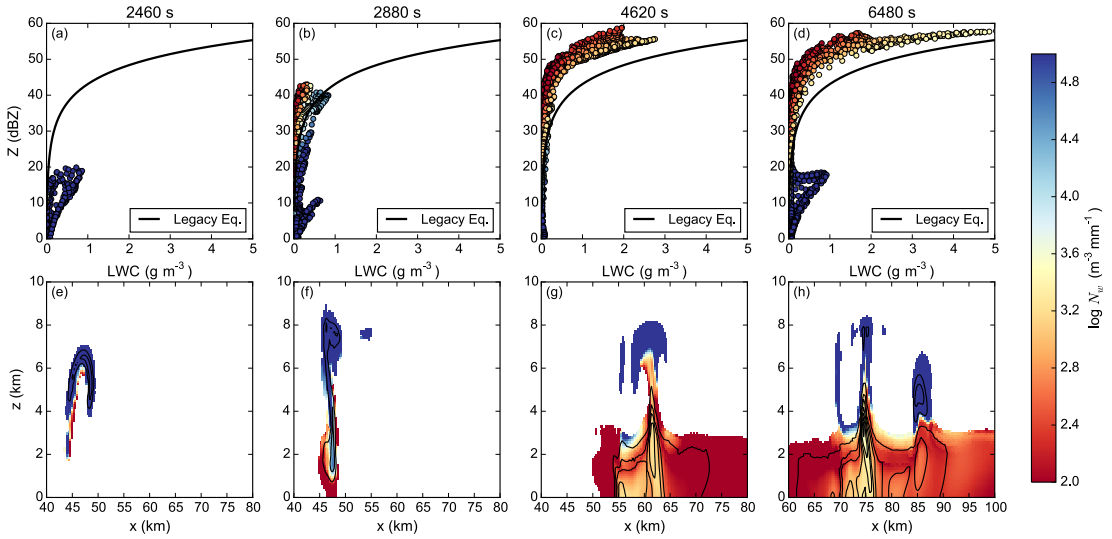

Figure 4.3: Comparison of the legacy LWC-Z retrieval relation (Eq. 4.7) to LWC and Z (due to rain only) from the HUCM at (a,e) t = 2460 s, (b,f) t = 2880 s, (c,g) t = 4620 s, and (d,h) t = 6480 s. The top row shows the parameter space of the LWC vs. Z relationship colored according to $\log_{10} N_w$ in comparison to the legacy retrieval relation. The bottom row shows the vertical cross section of $\log_{10} N_w$ (shown only for LWC $>$ 0.01 g m^{-3}) at each time with LWC contoured at 0.1, 0.5, 1.0, 2.0, 3.0, and 4.0 g m^{-3}.

Nearly 30 minutes later at t = 4620 s (Fig. 4.3c,g), the LWC-Z relationship has changed significantly, with the most of the rain found below the melting level and dominated by the melting of hail and graupel. Relatively low values of N_w are present in the entire region indicative of large drops and a categorical overestimation of LWC from the legacy retrieval equation by up to 500%. This is in agreement with previous studies (e.g., Ryzhkov et al. 2009) that found that melting graupel and hail is associated with high Z_{DR} values. The predominance of rain generated from ice microphysical processes persists throughout the storm's lifecycle once it has matured. The microphysical characteristics of the updraft have changed as well. By this time, a well-formed Z_{DR} column (e.g., Illingworth et al. 1987; Kumjian et al. 2014) is seen within the updraft as large raindrops are recycled into the updraft and undergo time-dependent freezing. In this

region, the LWC-Z relationship is similar to that beneath the melting level. Outside of and above the Z_{DR} column, where raindrops have frozen and converted to hail or the "freezing drops" category, N_w rises sharply as the DSDs are once again skewed toward smaller drops.

Finally, at t = 6480 s (Fig. 4.3d,h), a new updraft centered around x = 86 km and z = 5 km begins to develop, with high values and a very sharp gradient of N_w and an LWC-Z relationship similar to that seen at t = 2460 s. This occurs alongside the former updraft with a Z_{DR} column and widespread rain generated from ice, highlighting the spatial variability in the LWC-Z relationship that may exist at any given time in addition to the temporal variability.

Based on these results, it is clear that the variability in space and time of the LWC-Z relationship must be taken into account to achieve accurate retrievals of LWC. In all of these cases, the stratification of the LWC-Z relationship with respect to N_w is pronounced, with N_w providing a clear indication of the bias of the legacy retrieval relation regardless of area or stage of development.

4.4 Retrievals in rain/hail mixtures

4.4.1 Estimation of LWC

In practice, it is not known *a priori* what the relative contributions of rain and hail are to the measured radar variables, where each measurement is a function of all hydrometeors contained in the volume. However, determining the complete hydrometeor fields for assimilation necessitates the separate estimation of LWC and IWC within the volume. The difficulties in accurately retrieving rain LWC(Z) are exacerbated if hail is contained in the volume. Any information about LWC from Z is completely lost if even a small amount of hail is contained in the volume as the signal from hail can completely dominate Z and result in a severe overestimation of LWC if the volume is assumed to be

entirely rain. Unfortunately, the calculation of A_{H} proposed by Ryzhkov et al. (2014) is corrupted in the presence of hail, so other methods must be sought.

The use of K_{DP} for retrieving R and LWC in the presence of hail has been widely proposed (e.g., Seliga and Bringi 1978; Doviak and Zrnić 1993; Ryzhkov and Zrnić 1995; Zrnić and Ryzhkov 1996). Beyond its reduced sensitivity to the rain PSD compared to Z, the premise of using K_{DP} to effectively estimate LWC in rain/hail mixtures is based on the assumption that K_{DP} is immune to hail due to random tumbling that results in isotropic scattering. This assumption requires better justification for wet, melting hail which may contain a torus of water on its surface (see Figure 1 of Rasmussen and Heymsfield 1987a), causing it to stabilize and reduce the degree of tumbling.

Vertical profiles of IWC, LWC and K_{DP} for each hail size category at both S and C band from the 1D-MH are shown in Figure 4.4. Within the 1D-MH, there are three sources of hydrometeor mass: solid ice cores, the meltwater that collects on the surface of each ice core, and shed drops. Because bulk schemes do not typically allow for mixed-phase particles, in the absence of information about the PSDs modelers are most concerned with accurately representing the bulk values of LWC and IWC with a volume. Here, LWC was considered to be the sum of the surface meltwater and shedwater, whereas the ice cores were considered the IWC. The K_{DP} and LWC profiles shown in Figure 4.4 are those associated with the initial species and phase of the particles within a given bin in order to conserve the source (i.e., the vertical profile of graupel K_{DP} is that due to graupel particles as they melt and after they are completely melted). Shedding only begins to take place below 2 km whereas breakup primarily takes place in the lowest 1 km. In general and as expected, K_{DP} is positively correlated with the total LWC. For all of the modeled distributions, the almost all of the graupel melts in the first 1.0-1.5 km below the 0°C level and contributes almost all of the LWC and K_{DP} in the first km below the 0°C level, particularly for the distributions with larger hail (Fig. 4.4b,c,e,f). For the small hail distributions, the smaller hailstones also completely melt, resulting in

a preponderance of large raindrops (see Fig. 5 in Ryzhkov et al. 2013a). This causes a slight enhancement of K_{DP} at S band (Fig. 4.4a) but a much larger enhancement at C band (Fig. 4.4d), where median K_{DP} values are 5.5 ° km^{-1} and reach as high as 9.1 ° km^{-1} as resonance effects become pronounced.

The impact of melting hail on K_{DP} can be seen between 2 and 3 km for large and giant hail (e.g., Fig. 4.4b,c,e,f). The total LWC in this layer grows by a few tenths of g m^{-3} above that due to graupel, which is almost entirely melted at heights of 2-2.5 km. Shedding of meltwater has not yet begun at these heights, so the increase of total LWC above that of graupel is due to melting hail. There is a corresponding increase in total K_{DP} above the K_{DP} due to just graupel up to or exceeding 1.0 ° km^{-1} at S band in some cases (Fig. 4.4b between 2 and 2.5 km). This effect is more pronounced at S band than C band, as also found for $R(K_{DP})$ retrievals in Ryzhkov et al. (2013b). These results are somewhat in contrast to the ideas discussed in Hubbert et al. (1998) which assumed that observed areas of enhanced K_{DP} aloft necessitated the presence of shed drops and are more in line with the results of Loney et al. (2002) and Snyder et al. (2017b), whose present evidence of a notable K_{DP} contribution from wet ice particles aloft. As such, it is determined that wet hailstones can contribute to K_{DP}, although for the estimation of bulk LWC K_{DP} is still quite insensitive to IWC within the hailstone and thus represents the potential for a marked improvement for retrieving LWC over the use of Z.

4.4.2 Estimation of IWC

The estimation of IWC within rain/hail mixtures is challenging. Results from the previous section agree with the wider literature and indicate that K_{DP} can be used reliably to isolate the contribution from LWC in a rain/hail mixture. One proposed method to separate the contributions from rain and hail (Balakrishnan and Zrnić 1990; Doviak and Zrnić 1993) is to assume that IWC in the mixture contributes negligibly to K_{DP}, estimate

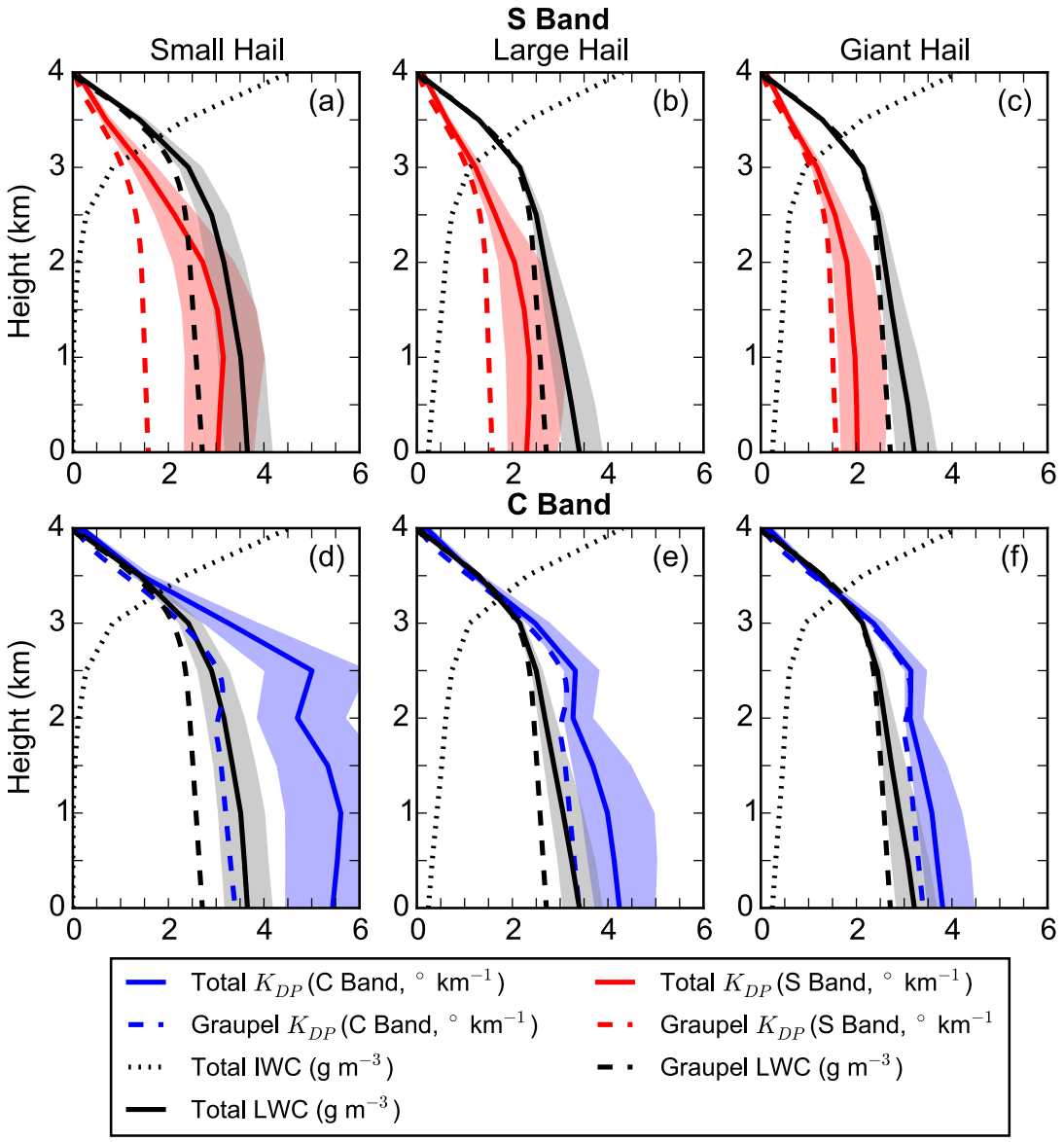

Figure 4.4: Vertical profiles of median IWC (g m^{-3}, dotted black line), LWC (g m^{-3}, solid black line), and K_{DP} (° km^{-1}) at (a-c) S-band (solid red line) and (d-f) C-band (solid blue line) for small, large, and giant hail from the 1D-MH. The LWC and K_{DP} due to graupel alone at each wavelength are also shown in dashed lines, respectively. The shaded regions for total LWC and total K_{DP} depict the interquartile range of the distributions.

Z due to rain (Z_{LWC}) from K_{DP}, and then estimate IWC from the remaining Z which is assumed to be due to hail (Z_{IWC}) according to

$$Z_{\mathrm{IWC}} = Z - Z_{\mathrm{LWC}} \tag{4.15}$$

where Z, Z_{IWC}, and Z_{LWC} are in linear units of mm^{-6} m^{-3}. $Z_{\mathrm{LWC}} - K_{\mathrm{DP}}$ relations were derived from the disdrometer dataset following a procedure analogous to that described in section 4.1 and are as follows:

$$Z_{\mathrm{LWC}} = 8.406 \times 10^4 (K_{\mathrm{DP}})^{1.168}, (\lambda = 11.0\ \mathrm{cm}) \tag{4.16}$$

$$Z_{\mathrm{LWC}} = 2.790 \times 10^4 (K_{\mathrm{DP}})^{1.097}, (\lambda = 5.33\ \mathrm{cm}). \tag{4.17}$$

These relations are in relatively good agreement with relations that can be derived from parameters reported in Doviak and Zrnić (1993) and Ryzhkov et al. (2013b) that implicitly assumed the standard $Z_{\mathrm{LWC}} - R$ relation Z_{LWC}=$200R^{1.6}$ (Marshall and Palmer 1948), although the exponents shown here are a bit smaller. The Doviak and Zrnić (1993) and Ryzhkov et al. (2013b) sets of relations were also tested using the following procedure and achieved very similar results to Eqs. (4.16) and (4.17) (not shown).

Figure 4.5 shows median and interquartile values from this method (calculating Z_{LWC} from K_{DP} using Eqs. (4.16) and (4.17), finding Z_{IWC} from Eq. (4.15), and retrieving IWC from Z_{IWC} using the legacy retrieval equation (Eq. 4.11)) applied at both S band (a-e) and C band (f-j) for all size distributions from the 1D-MH. Despite the good correlation between LWC and K_{DP}, there is seemingly no functional relation between the retrieved Z_{IWC} and the actual IWC (Fig. 4.5e,j, in black), along with a much larger spread in retrieved IWC than exists in the 1D-MH model results. Consequently, the retrieved IWC using the legacy retrieval equation for hail (Fig. 4.5e,j, in color) exhibits very large errors (RMSEs of 2.93 g m^{-3} at S band and 1.64 g m^{-3} at C band) with almost no skill (Pearson correlations of -0.27 and -0.02 at S and C band, respectively).

The possible sources of error in this technique include the assumption that K_{DP} has only a negligible contribution from hail, the derived $Z_{\mathrm{LWC}} - K_{\mathrm{DP}}$ relation, and the legacy

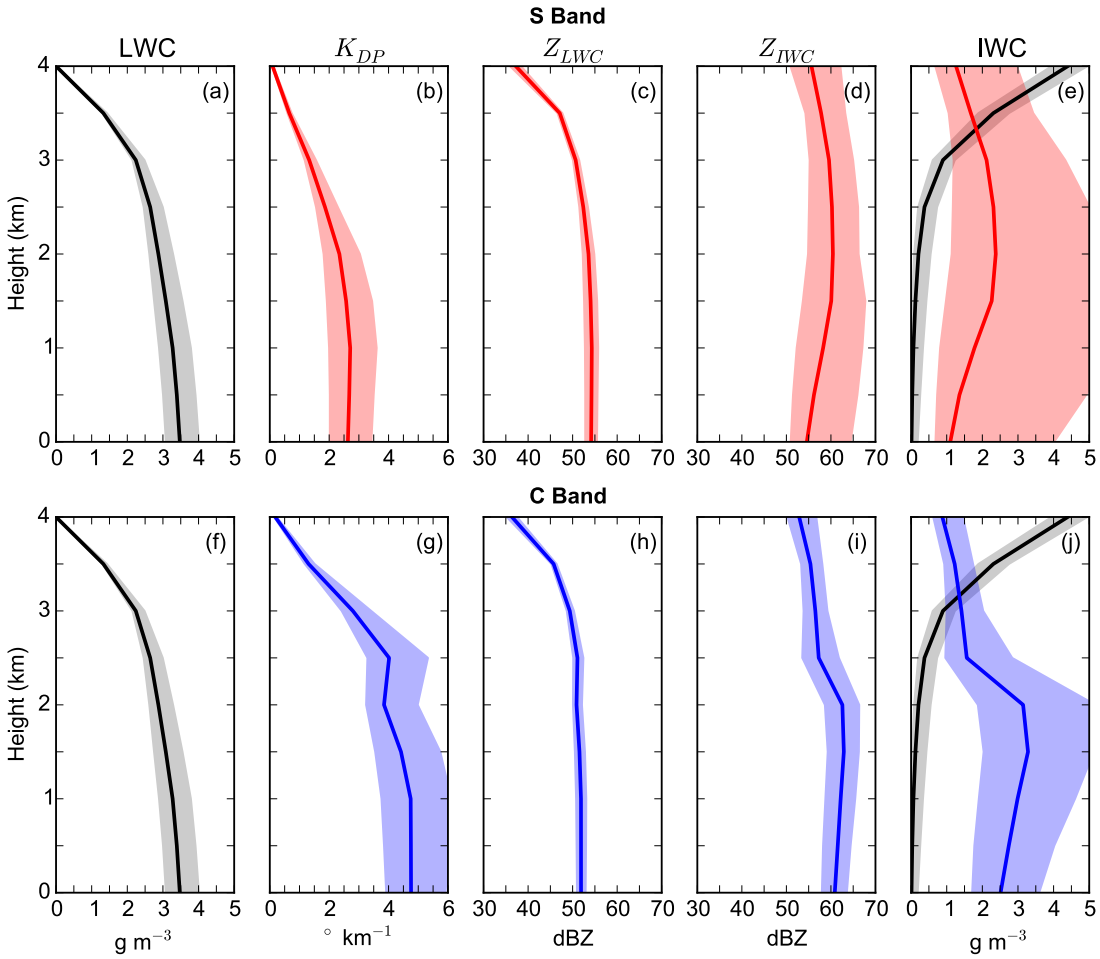

Figure 4.5: Vertical profiles of median (a,f) LWC (g m^{-3}), (b,g) K_{DP} (° km^{-1}), (c,h) retrieved Z_{LWC} (dBZ) using Eqs. (4.16) and (4.17), (d,i) retrieved Z_{IWC} (dBZ) using Eq. (4.15), and (e,j) IWC (black, g m^{-3}) and retrieved IWC (color, g m^{-3}) using Eq. (4.11) from the 1D-MH. S band calculations are shown in red and C band calculations are shown in blue. The shaded regions depict the interquartile range of the distributions.

retrieval relation for IWC(Z). The relationship between LWC and K_{DP} is in general quite immune to hail and robust (see previous section) although not perfect. Beyond the possible aforementioned slight impacts of accumulated meltwater at larger hail sizes at S band and possibly resonant effects from the melting of small hail at C band, the small but nonzero K_{DP} at 4 km above ground level ($\approx$ 0.08 deg km^{-1}), where only ice exists, results in an estimated Z_{LWC} of approximately 35 dBZ. This is quite small in an absolute sense in relation to the total Z, however, and should not introduce significant error into the retrieved Z_{IWC}. The $Z_{LWC} - K_{DP}$ relations, Eqs. 4.16 and 4.17, are robust and quite constrained, with RMSEs of 1.34 dBZ and 1.09 dBZ at S band and C band, respectively, for all values of Z. This RMSE increases to 3.07 dBZ at C band for Z_{LWC} greater than 40 dBZ due to the aforementioned resonance effects though the relationship is still a strong one. Because the contributions to Z are due to only the LWC of rain and the IWC of hail and graupel, the estimates of Z_{IWC} seem plausible. Thus, the significant errors in retrieved IWC are very likely due to the legacy retrieval relation for hail.

This conclusion was examined further in Figure 4.6, in which the IWC from the 1D-MH is plotted against the retrieved Z_{IWC} (using the previously described approach) for all distributions and compared to the legacy hail retrieval relation. In addition to radar wavelength and maximum hail size within the volume (where resonance effects may begin to affect Z measurements at larger sizes, even at S band), the strongest dependency is seen with respect to height below the melting level. For a decrease in IWC of two orders of magnitude, Z_{IWC} can remain nearly constant (e.g., Z_{IWC} = 60 dBZ corresponding to 5.5 g m^{-3} of IWC near the melting level to nearly no IWC near the surface). At both wavelengths, the use of the legacy retrieval equation results in a consistent negative bias at and above the 0°C level and a positive bias below the 0°C level, qualitatively similar to the findings for rain in section 4.3.

Figure 4.7 is a conceptual model showing the relative contributions to IWC and Z_{IWC} at both S and C band from mixed-phase particles of different sizes. Proportional to the

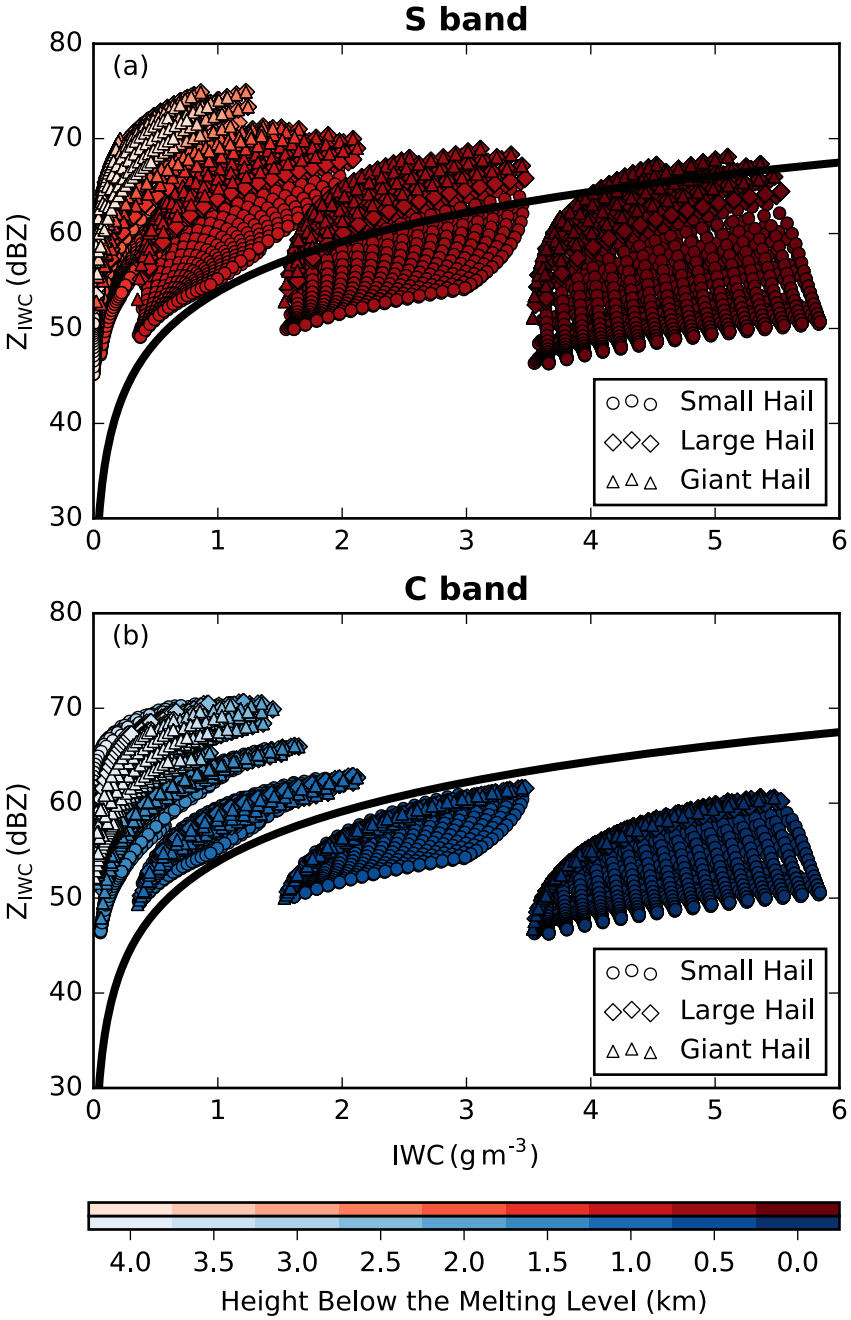

Figure 4.6: IWC vs. retrieved Z_{IWC} (via Eqs. 4.16 and 4.17) for both (a) S band and (b) C band (blue), partitioned by maximum hail size, from the 1D-MH. The legacy relation (Eq. (4.11)) is shown in black.

third moment of the ice size distribution, the majority of the IWC is concentrated in the smaller sizes, which is particularly the case when significant amounts of graupel are present, as is necessarily the case for our results given the bi-exponential distributions modeled using the 1D-MH. In contrast, Z_{IWC} is equal to the sixth moment of the distribution (assuming Rayleigh scattering) and has a much broader maximum contribution at larger sizes. By the time the ice reaches the surface, all graupel and hail below a certain size (represented by the shaded regions) have completely melted, representing a loss of the majority of the IWC. However, their contribution to Z_{IWC} was relatively low, and the larger hailstones that are the dominant contributors to Z_{IWC} do not contribute very much to the IWC. This also demonstrates the impact of the maximum hail size in the volume, which results in a decrease in Z_{IWC} while only minimally affecting IWC. Additionally, the contribution to Z_{IWC} at C band is larger than at S band for small hail sizes and smaller than at S band for large hail sizes due to resonance effects playing a role at smaller hail sizes at C band (see Fig. 10 in Ryzhkov et al. 2013a). All of these factors result in a very indirect relationship between IWC and Z_{IWC}.

Based on these results, it is clear that radar wavelength, maximum hail size, and particularly the height below the 0°C level of the radar resolution volume in question must be taken into account to retrieve accurate estimates of IWC. To demonstrate how the IWC(Z) relation changes with wavelength, height, and maximum hail size, power-law regressions of the form $Z_{\mathrm{IWC}} = a(\mathrm{IWC})^b$ were found at 500 m intervals below the 0°C level from the 1D-MH results and are shown in Fig. 4.8. Distance below the melting level plays the dominant role over radar wavelength and maximum hail size, with the largest changes occurring in the first 2.0 km below the melting level before leveling off and becoming quite steady. These coefficients are only valid for the atmospheric conditions prescribed in the 1D-MH, though it is reasonable to expect that similar conclusions would hold for most atmospheric profiles beneath the 0°C level representative of environmental conditions conducive to convection and hail production. These results are

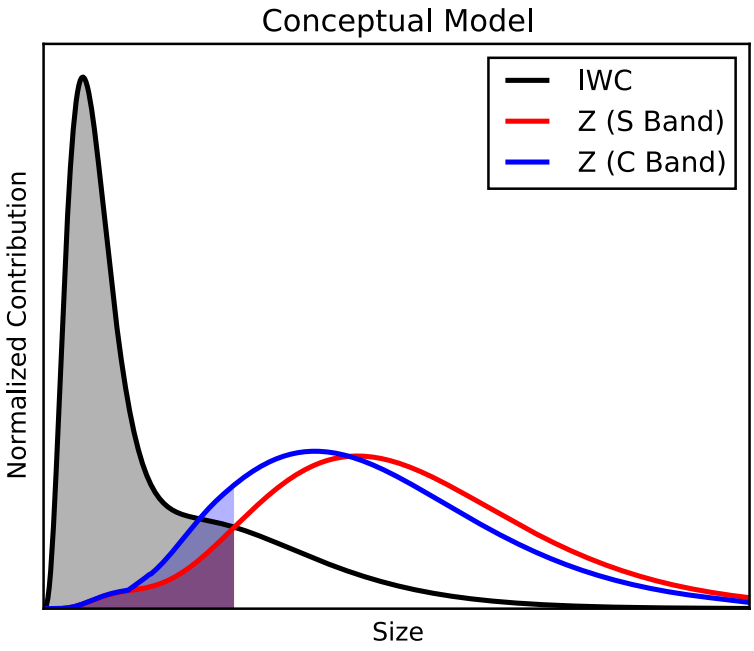

Figure 4.7: Conceptual model of the normalized IWC (black) and Z (red - S Band, blue - C Band) as a function of size. The shading represents the contributions that may be removed due to total melting.

reflected in the proposed Hail Size Discrimination Algorithm (HSDA; Ryzhkov et al. 2013b), which seeks to identify the maximum hail size within a radar resolution volume by using the polarimetric variables in an analogous manner to the operational hydrometeor classification algorithm. In agreement with the results shown here, the membership functions are constant below 3 km below the 0°C level. Thus, the radar wavelength, maximum hail size in the volume estimated from the HSDA, and the height of the volume with respect to the 0°C level can all be used to select more appropriate retrieval relations and improve the estimates of IWC from Z.

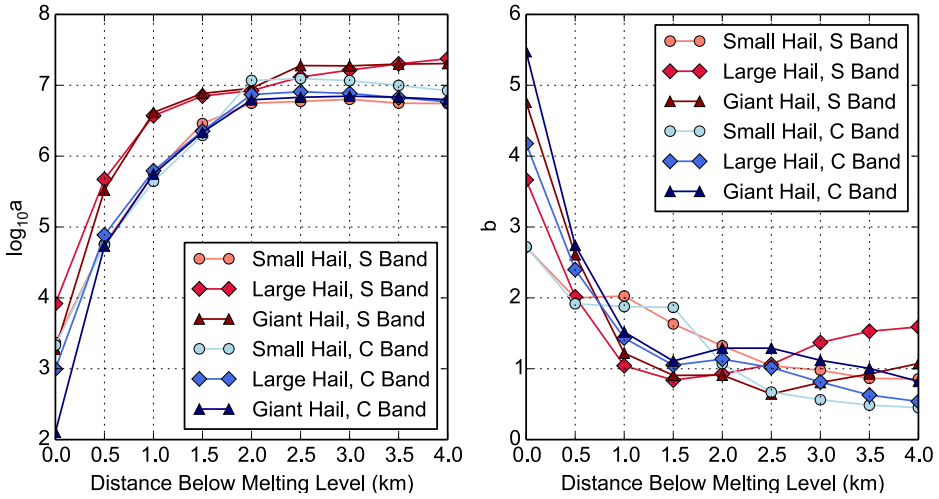

Figure 4.8: Regression coefficients from the 1D-MH of the form $Z_{\mathrm{IWC}} = a(\mathrm{IWC})^b$, where Z_{IWC} is in linear units of mm^6 m^{-3} and IWC is in g m^{-3} for small, large, and giant hail at 500 m intervals below the melting level for S and C band.

To further strengthen the justification for the estimation of Z_{IWC} using this approach, the relationship between IWC and Z_{IWC} partitioned by height from the HUCM is shown in Fig. 4.9. Model output was accumulated over a 30 min period starting from when hail first reached the surface to capture the variability of IWC-Z relations throughout the developing and mature stages of the storm at each height interval. Here, as before, IWC represents hail and graupel together due to the often abrupt conversion between the two categories in some cases in the HUCM microphysics (due to graupel reaching a size or

density threshold; see Ilotoviz et al. 2016 for more details) as well as the fact that many microphysics schemes do not explicitly treat graupel and hail separately. This sudden transition is easily seen in Figure 4.10a at z = 4-6 km.

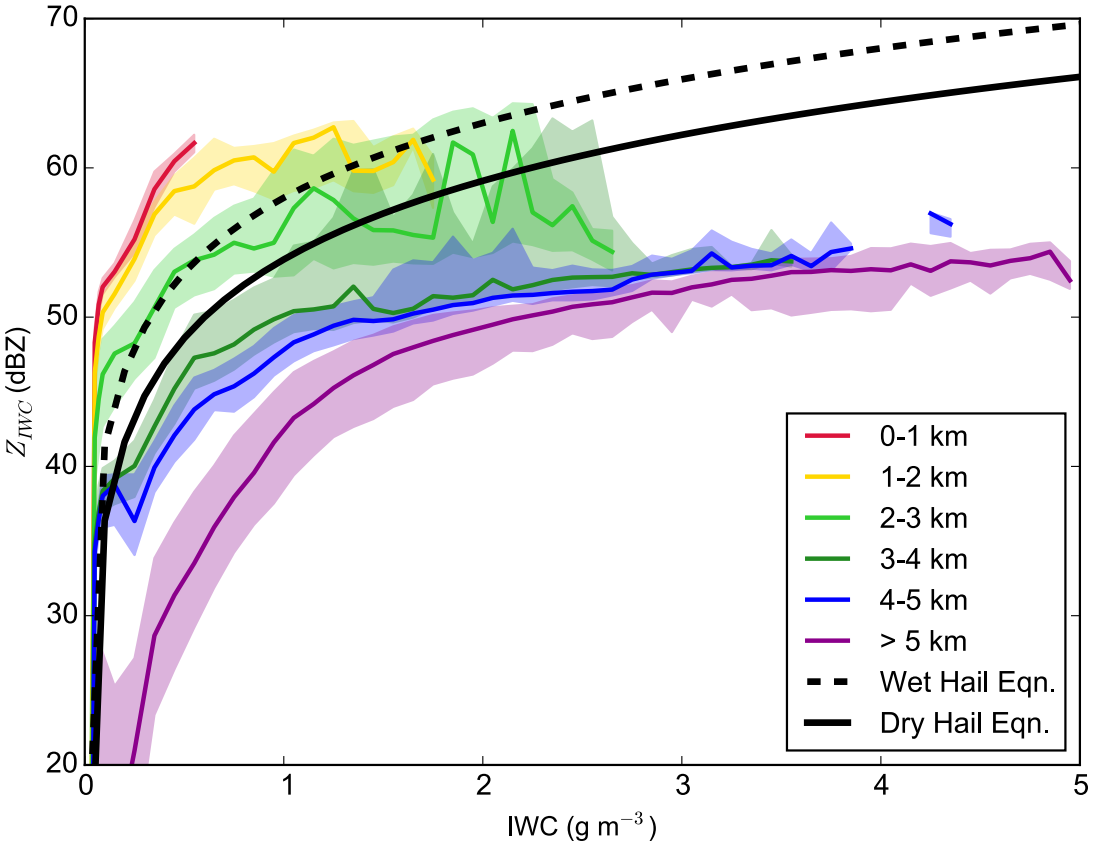

Figure 4.9: Median Z_{IWC} for binned IWC from the HUCM partitioned by height for bins with 10 or more points. IWC was binned at every 0.02 g m^{-3} between 0.0 and 0.1 g m^{-3} and at every 0.1 g m^{-3} between 0.1 and 5.0 g m^{-3}. The shaded regions depict the interquartile range of the distributions. The legacy retrieval relations for dry (solid black; Eq. 4.11) and wet hail (dashed black; Eq. 4.12) are shown. The melting level is at approximately z = 3.5 km.

The results seen in Figure 4.9, for which Z_{IWC} is calculated explicitly and rigorously for each hydrometeor class, agree quite well with the retrieved Z_{IWC} from the 1D-MH in Figure 4.6. The legacy IWC(Z) relationship generally performs poorly above z = 4 km,

where graupel dominates from the riming of snowflakes aloft before quickly melting below the 0°C level or converting to hail (Fig. 4.10a). For a given value of Z, graupel exhibits a much larger IWC than is predicted by the legacy hail retrieval relation due to its lower density and smaller size. The use of the legacy retrieval relations for hail will thus result in a severe underestimation of IWC aloft of up to 3 g m^{-3} through a large depth of the storm (Fig. 4.10g). A separate graupel retrieval relation should instead be considered.

At and below the 0°C level, the same biases found from the 1D-MH are seen from the HUCM data. The use of the wet hail retrieval relation (Eq. 4.12) does a better job than the dry hail retrieval relation (Eq. 4.11) although there is still a positive bias in retrieved IWC (Fig. 4.10g) and the full variability of the IWC(Z) relation is not well represented. As the Z calculated for hail in the HUCM consists of both the ice core and surface meltwater, there is an increase in Z owing to the increase in the dielectric constant of hail as meltwater accumulates on the surface. However, the primary source of error in using a static hail retrieval relation comes from the precipitous loss of IWC as hail and graupel fall and melt. This is easily seen in Figure 4.10(b-e), where graupel and small hailstones melt very quickly into rain below the 0°C level while the largest hail, which dominates the Z_{IWC}, does not lose much mass. The hail mass distributions tend to become relatively stable about 2 km below the melting level (Fig. 4.10e,f) in good agreement with the 1D-MH. Although this example is from a Eulerian frame of reference at a given time and therefore is not following the same volume of precipitation as it falls in a Lagrangian sense, the results are broadly consistent with the 1D-MH as well as conceptual expectations of the impact of melting hail on Z.

4.5 Summary and Future Work

Radar data are the only source of hydrometeor information available for assimilation on the scale of convection-resolving models, which have seen a surge in development in

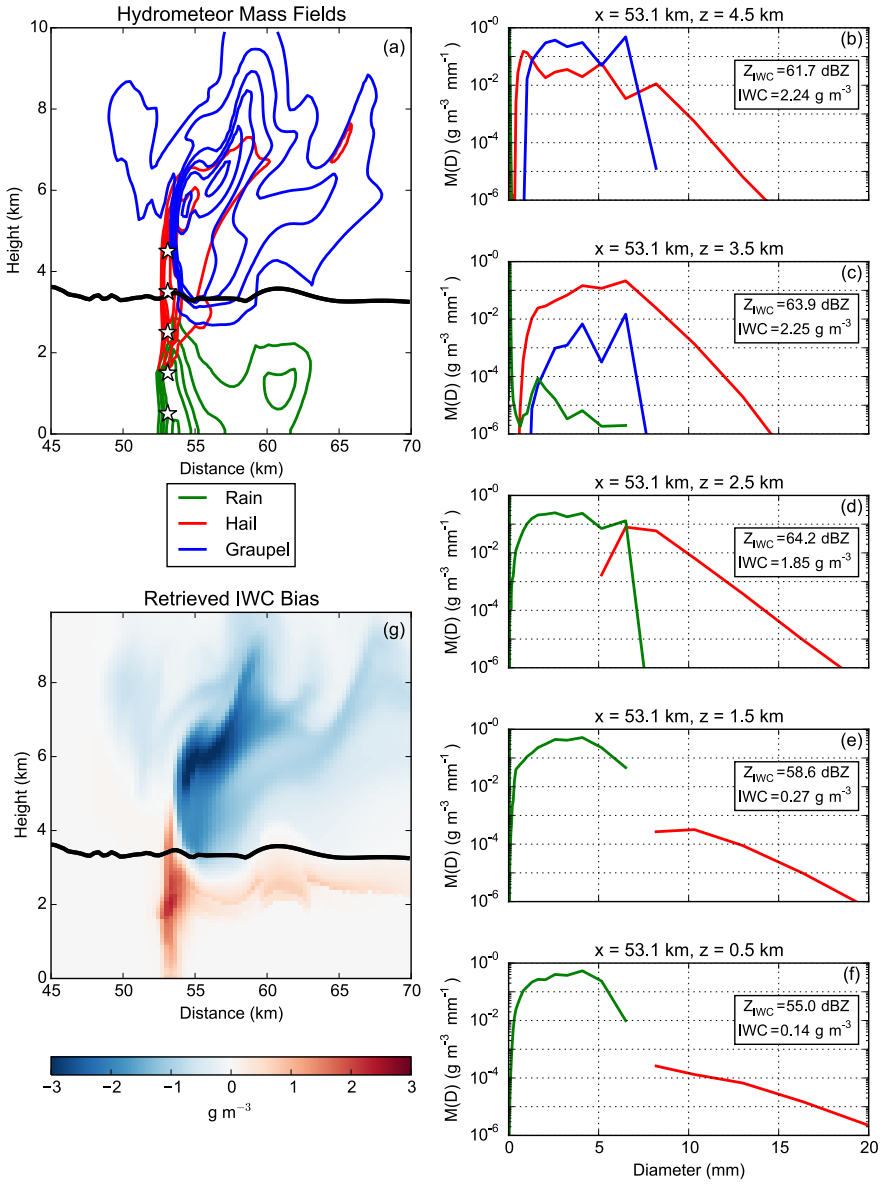

Figure 4.10: HUCM output for $t = 4260$ s showing (a) contours of rain (green), hail (red), and graupel (blue) mass every 0.5 g m^{-3} beginning at 0.5 g m^{-3}, (b-f) mass distributions of rain (green), hail (red) and graupel (blue) at 1-km intervals in the vertical at $x = 53.1$ km and with the IWC and Z_{IWC} of the distributions shown, and (g) the bias in retrieved IWC (g m^{-3}) when using the legacy retrieval equation (Eq. (4.11)). The 0°C isotherm is shown in black in (a) and (g) whereas the stars in (a) denote the locations of the sampled mass distributions.

the past two decades and will play an increasingly large role in the warning decision process of forecasters in the future. Both forward operators and retrieval equations can be used to accomplish this but often require many limiting assumptions.

The goal of this study was to investigate the utility of the most simplified versions of commonly-used retrieval equations for LWC in pure rain and LWC and IWC within rain/hail mixtures and the consequences of making such assumptions. These simplified retrieval equations for rain, hail, and snow are derived in detail, and their assumptions and limitations are discussed. Two spectral bin models are used in the study: the 1D-MH model (see section 3.1.1) and the HUCM (see section 3.1.3). The 1D-MH model is used to simulate the polarimetric radar characteristics of 1,952 different melting hail size distributions for both S and C band. The HUCM is used to simulate a hailstorm from its inception and to get a qualitative look at how the biases of these retrieval relations behave in space and time. The general conclusions are that:

1. The relation between LWC and Z for rain varies significantly and is not constant in space or time, corroborating the results of many previous studies (e.g., Atlas and Chemla 1957; Battan 1973; Austin 1987). The use of the legacy retrieval equation for rain results in a systematic underestimation of LWC in developing updrafts and a systematic overestimation of LWC in rain derived from melting hail and graupel, the dominant source of rain below the melting level in mid-latitude convection. Size sorting processes will also limit the accuracy of the legacy retrieval equation as PSDs deviate from the Marshall-Palmer distribution implicit in the rain retrieval relation. The use of N_w, which can be estimated from Z and Z_{DR}, offers reliable insight into where and how severely the retrievals of LWC from the legacy retrieval relation will be biased.

2. In pure rain at both wavelengths, LWC(Z) exhibits the largest errors whereas incorporating N_w results in the best retrievals. Estimates of R are also superior when

using N_w at S band. However, accurate estimates of N_w require reduced resolution when compared to other radar variables and may be more difficult to estimate accurately at C band due to possible attenuation affects. With that in mind, the next best retrievals of R and LWC at S band are from A_{H}, which can be obtained with knowledge of the radar wavelength and a background temperature field from a model, whereas at C band the best retrievals of R and LWC are from K_{DP}. Both A_{H} and K_{DP} have the additional advantage over Z of being immune to radar miscalibration and partial beam blockage.

3. Within rain/hail mixtures, the LWC and IWC must be estimated separately. All information content about LWC in Z using the legacy retrieval relation for rain can be lost if even a small amount of hail is present in the volume. The calculation of A_{H} also fails in the presence of hail, so the use of K_{DP} to estimate the LWC in the presence of hail is recommended for both S and C band.

4. Once the LWC within a rain/hail mixture is known, the Z_{IWC} can be estimated. However, the legacy retrieval relation for hail may result in large errors, where neither the dry or wet forms of the legacy hail retrieval equation capture the full variability of the parameter space. A categorical underestimation of IWC exists above the 0°C level where lower-density graupel dominates the IWC, whereas a consistent overestimation of IWC below the 0°C level exists as Z is dominated by the largest hailstones and the bulk of the IWC comes from the smallest hailstones and graupel, which quickly melt. The radar wavelength, maximum hail size, and particularly the height below the melting level must be taken into account when attempting to retrieve the IWC.

Although more accurate estimates of LWC and IWC are desirable for model analyses, they still represent only one moment of the hydrometeor PSDs and once assimilated will suffer from the same limitations encountered when using single-moment microphysics more generally. In addition to the rain and rain/hail mixtures investigated here,

more work needs to be done on the utility of retrieval relations for other hydrometeor types (e.g., snow) as well as the impacts of the performance. Other possibilities exist for employing dual-polarization radar data for microphysical retrievals. For example, results from the polarimetric hydrometeor classification algorithm could be used to determine the dominant hydrometeor species in a volume and subsequently which retrieval relation to use instead of relying on empirical rules based on model background temperature. In addition to identifying regions containing hail (a crucial responsibility if one is to achieve useful estimates of LWC using Z), the "big drops" category in the operational hydrometeor classification algorithm (Park et al. 2009) can be used to identify regions with rain PSDs skewed toward larger drops due to size sorting. The impact of determining q from the hydrometeor classification algorithm was examined by Tong (2015) for the ARPS cloud analysis (see section 3.1.4.2). It was found that q determined from a polarimetric hydrometeor classifiation algorithm produced more realistic hydrometeor fields in the analysis (such as rain within updrafts above the environmental 0°C level) and allowed for multiple species to be retrieved within a volume. However, 1-h forecasts showed little impact of the modified q fields, with the choice of microphysics scheme instead exerting the dominant control on forecast outcomes. For the purpose of improving short-term forecasts, model analyses may be better served by utilizing dual-polarization radar data to improve other model state variables beyond q. As such, the remaining two chapters of this dissertation focus on using dual-polarization data for retrieving and assimilating thermodynamic and moisture fields to improve short-term forecasts.

Chapter 5

Polarimetric Thermodynamic Retrievals

5.1 Diabatic heating in updrafts

5.1.1 Connection between Z_{DR} columns and heating rate

Numerous distinct polarimetric "signatures" have been identified and tied to dynamical and microphysical processes within storms. One of the most ubiquitous polarimetric signatures observed in deep moist convection is the so-called "Z_{DR} column". Z_{DR} columns are vertical protrusions of positive Z_{DR} above the environmental 0°C level and are indicative of wet ice particles and large, oblate raindrops in the process of freezing lofted by the updraft. Values of Z_{DR} within these columns can exceed 4 dB at S band and can reach beyond 3 km above the 0°C level in extreme cases (Kumjian et al. 2014; Snyder et al. 2015). Because Z_{DR} columns are associated with convective storm updrafts, they can theoretically be used as identifiers for regions of positive temperature perturbations from latent heat release due to condensation and/or freezing, a primary driver of vertical motion in convection. Although the connection between Z_{DR} columns and updraft *location* has been long known (e.g., Hall et al. 1984; Illingworth et al. 1987; Tuttle et al. 1989; Ryzhkov et al. 1994), recent work has begun to investigate the relationship between Z_{DR} columns and updraft *intensity*. Simulations in Kumjian et al. (2014) showed a relationship between Z_{DR} column depth (that is, the distance above the 0°C level that enhanced values of Z_{DR} extend within the column) and updraft strength. These simulation results have been bolstered by observational evidence. Both Picca et al. (2010) and Kumjian et al. (2014) showed a correlation between Z_{DR} column height and hail mass at the surface at appreciable lag times, which has the potential to provide increased lead time for forecasting hail at the surface as compared to traditional metrics such as 20-dBZ

echo top height. Associations between the environmental instability (i.e., CAPE), storm relative helicity, and lifted condensation level temperature and the depth of Z_{DR} columns have also been uncovered (van den Broeke 2016), along with some evidence of larger aerial extent of Z_{DR} columns for stronger tornadoes compared to weaker ones (van den Broeke 2017). However, evidence of systematic differences between Z_{DR} columns in non-tornadic versus tornadic storms remains elusive and warrants further study (Picca et al. 2015; van den Broeke 2017). For a more complete review of Z_{DR} columns, see Kumjian et al. (2014) and Snyder et al. (2015).

Both the conceptual understanding of Z_{DR} columns as well as the aforementioned results from both observational and modeling studies support the notion of Z_{DR} column characteristics (e.g., depth, aerial extent) being positively associated with updraft strength. However, the connection between the latent heating rate and Z_{DR} column characteristics has not been thoroughly investigated. Although one would expect there to be a correlation given latent heat release due to condensation being a major driver of convective updrafts, this has yet to be shown definitively. To serve as motivation for the assimilation work presented in Chapter 6, a brief examination is presented here.

Observing Z_{DR} column depth with precision can be difficult owing to the coarse vertical resolution of the WSR-88D network at distances far from the radar (e.g., van den Broeke 2016, 2017). In addition, direct observations of the latent heating rate within updrafts are not readily available. The HUCM is used to simulate Z_{DR} columns and compare them to the modeled net latent heating rate. The case used is the same as described in section 4.2. However, simulations are performed for five CCN_{sfc} concentrations to increase the sample size and incorporate the effects of CCN concentration: 100 cm^{-3}, 500 cm^{-3}, 1000 cm^{-3}, 1500 cm^{-3}, and 3000 cm^{-3}. All other aspects of the model configuration are held constant.

Predicated on the widespread use of look-up tables for deriving vertical profiles of convective heating, such as those utilized in the SLH algorithm (see section 2.2.3.1), a

similar approach is used to show the connection between Z_{DR} columns and the latent heating profile. Using the maximum height of the 0.5-dB surface as an index, the mean vertical profile of maximum heating is found for each index in increments of 0.1 dB using data from the entire duration of each run. The results combining all five CCN concentrations are shown in Figure 5.1. Due to the relatively small sample size, a 3 x 3 mean filter is applied to the chart to remove some noise. Overall, there is a very pronounced and monotonic relationship between the height of the 0.5-dB surface and the latent heating rate in the column above it. For the tallest columns – those extending up to 3.0 km above the environmental 0°C level — the maximum heating rate exceeds 300 K h^{-1}. The height at which the maximum heating rate occurs also rises, from $\approx$ 4.0 km when the 0.5-dB surface is 0.4 km above the environmental 0°C level to $\approx$ 7.0 km when the 0.5-dB surface reaches 3.0 km above the environmental 0°C level. This result is particularly encouraging because the profile of latent heating shown is occurring simultaneously with the measured height of the Z_{DR} column with no latency. Although not shown, there was no change evident in the relationship between Z_{DR} column depth and the vertical profile of latent heating with a change with CCN. The standard deviation of the heating rate typically increases with height and peaks between $\approx$ 7.0 and 8.0 km before dropping precipitously above that (along with the heating rate itself). As individual plumes rise, the height of the maximum heating rate ascends and its magnitude increases, and the Z_{DR} column grows underneath it in tandem. At a certain point, however, the plume becomes disconnected from the surface and begins to weaken, causing the Z_{DR} column to rapidly descend. As a consequence, the standard deviation of the heating rates comprising the mean values shown in Figure 5.1 is maximized for Z_{DR} column heights of $\approx$1.0-1.5 km, as the 0.5-dB surface exists at this height both during the initial growth phase of the plume (where the heating is concentrated at relatively low levels with minimal heating aloft) and the collapsing phase of the plume and Z_{DR} column, where the heating is maximized aloft. However, overall the standard deviation

is relatively low when compared to the mean heating rate, with some of the smallest standard deviations ($\approx$ 50 K h^{-1}) for the largest heating rates, indicative of a constrained dispersion and high confidence of strong heating in this region. Although not shown due to the possible presence of negative heating rates (which could slightly skew the mean), the coefficient of variation, defined as the standard deviation normalized by the mean, shows this well, with the smallest values in the regions of maximum heating that reaches a minimum for the tallest columns. Other Z_{DR} column thresholds (e.g., 1.0-dB, 1.5-dB) were examined with similar conclusions.

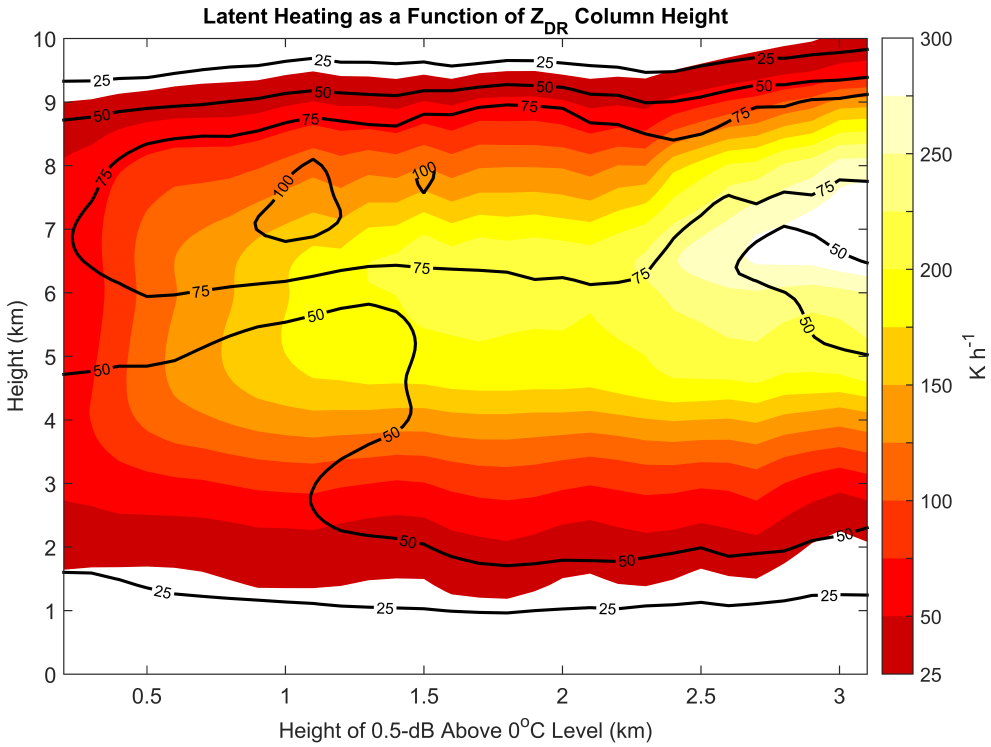

Figure 5.1: Mean vertical profile of latent heating (K h^{-1}, shading) and its standard deviation (K h^{-1}, contours) as a function of the 0.5-dB height above the environmental 0°C level composited from the HUCM for runs with CCN_{sfc} = 100 cm^{-3}, 500 cm^{-3}, 1000 cm^{-3}, 1500 cm^{-3}, and 3000 cm^{-3}.

As a point of comparison, a similar approach based on the SLH algorithm was taken using the maximum height of the 10-dBZ surface in 0.1 km increments and smoothed

in the same way as Fig. 5.1. Although the authors of the SLH algorithm note that it is not meant to be used at such high resolutions in its current form, it is still instructive to evaluate its performance compared to using Z_{DR} columns. Figure 5.2 shows the mean vertical profile of latent heating as a function of the 10-dBZ echo top height. In order to guarantee the results apply only to regions of convection, only model columns with surface $Z \geq 50$ dBZ are used. Overall, there is still a monotonic relationship between the 10-dBZ height and the magnitude of the latent heating. However, there is more variability in the heating profiles, which manifests as smaller values of mean heating rate and larger standard deviations for a given magnitude of heating. For 10-dBZ heights of less than ≈ 9.5 km, for which the mean maximum heating rate is less than 25 K h^{-1}, standard deviations exceed 50 K h^{-1} due to the presence of latent cooling in downdrafts. The coefficient of variation (not shown) also indicated more dispersion than when using Z_{DR} columns for the highest 10-dBZ echo top heights. Although the highest heating rates are, overall, in the region of the highest 10-dBZ heights, more modest 10-dBZ echo top heights offer little predictive value, with cooling downdrafts occurring alongside warming updrafts for the same 10-dBZ heights and standard deviations that exceed the magnitude of the maximum heating rate. The performance of the 10-dBZ height was even poorer when using lower thresholds of surface Z (not shown).

As noted previously, it is often difficult to observe both the height of Z_{DR} columns and the 10-dBZ echo top height with great precision in practice due to poor vertical resolution of most operational radars. However, it is evident from these results that Z_{DR} columns have the advantage of more precisely pinpointing the location of the strongest heating plumes, with changes in the maximum heating rate scaling more linearly and over a large range of values compared to the 10-dBZ echo top height.

Despite combining the results from runs with different CCN concentrations, the sample size is still quite limited. Only a case of very strong convection was examined in the HUCM, which neglects the importance of accurately determining the vertical profile

of heating in weaker convection. Additionally, although only one thermodynamic and kinematic environment was examined, such variability may impact the quantitative nature of the relationship between Z_{DR} column height and the latent heating rate. Future work will study the relationship between Z_{DR} column height and updraft strength by using vertically-pointing radars to measure vertical velocity in tandem with co-located Z_{DR} columns observed from nearby polarimetric radars.

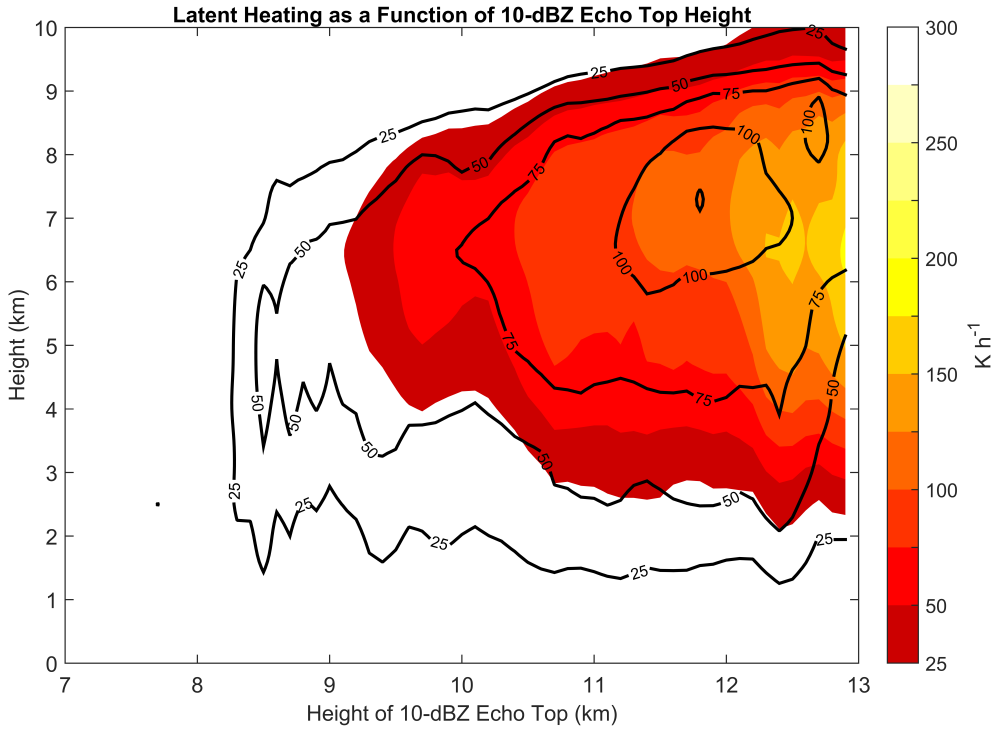

Figure 5.2: As in Fig. 5.1, but as a function of the maximum 10-dBZ height.

5.1.2 Early Z_{DR} signature of developing convection

In addition to the aforementioned Z_{DR} columns associated with mature updrafts in deep moist convection, enhanced Z_{DR} coincident with low values of Z has been observed aloft in the nascent stages of both developing tropical (Caylor and Illingworth 1987; Illingworth 1988; Knight et al. 2002) and continential (Knight 2006) convection. These

Z_{DR} values may be quite anomalous, with Z_{DR} values approaching 3 dB reported for Z of only ≈5 dBZ (Knight 2006). This was initially hypothesized to be due to the presence of ultragiant nuclei, which can grow rapidly by deposition in the lowest portions of clouds, but no conclusive evidence yet exists to explain the formation of such large drops so quickly. Details remain elusive in part because of the difficulty of observing such phenomena; planes will struggle collect *in situ* data due to the latency in getting the plane into developing convection during its earliest stages, and the plane may undersample such sparse large drops (Knight 2006), whereas range-height indicator (RHI) radar scans need to be pre-emptively pointed in the correct direction of developing convection, which is not always known.

An example of this signature observed from an operational radar is shown in Figure 5.3. Radar data from each scan were binned by height in 1-km increments (except above 10 km, where a 2-km increment is used) for a developing thunderstorm. It is seen that for the first scan in which the Z reaches 10 dBZ (21:47:09 UTC), the mean Z_{DR} at this level (between 5 and 6 km) exceeds 0.5 dB. Less than 5 minutes later, at 21:54:45 UTC, the Z field has deepened appreciably and extends up to 10 km, and the anomalous Z_{DR} signature is less distinct, instead resembling a more typical size sorting signature for Z values of reaching approximately 30 dBZ.

Figure 5.4 shows a time-height series of the maximum Z and Z_{DR} from the aforementioned run of the HUCM with CCN_{sfc} = 3000 cm^{-3} compared to the same plots for radar observations of convection in Knight (2006). The HUCM is able to reproduce this anomalously high Z_{DR} during the earliest stages of development, with Z_{DR} values exceeding 1.0 dB between ≈ 3.5 and 5.0 km for Z values less than 10 dBZ. The time-height series from the HUCM is also in qualitative agreement with the overall evolution in the observations (Fig. 5.4, bottom).

Notably, although the HUCM run in this example is highly polluted, no giant or ultragiant nuclei were included. The evolution of this feature is examined further in

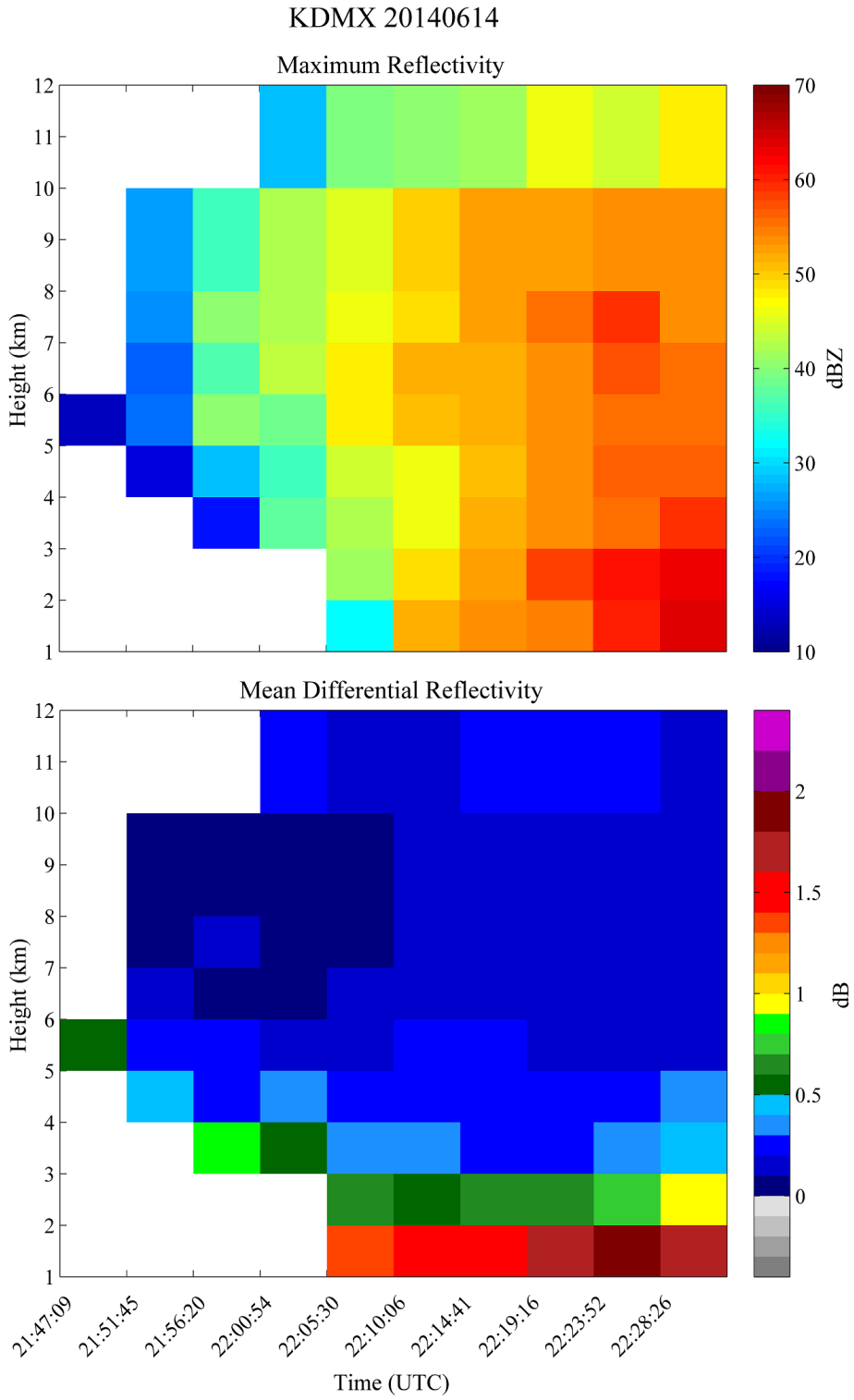

Figure 5.3: Time-height series of (top) maximum Z and (bottom) mean Z_{DR} of a developing thunderstorm from the Des Moines, IA (KDMX) WSR-88D on 14 June 2014.

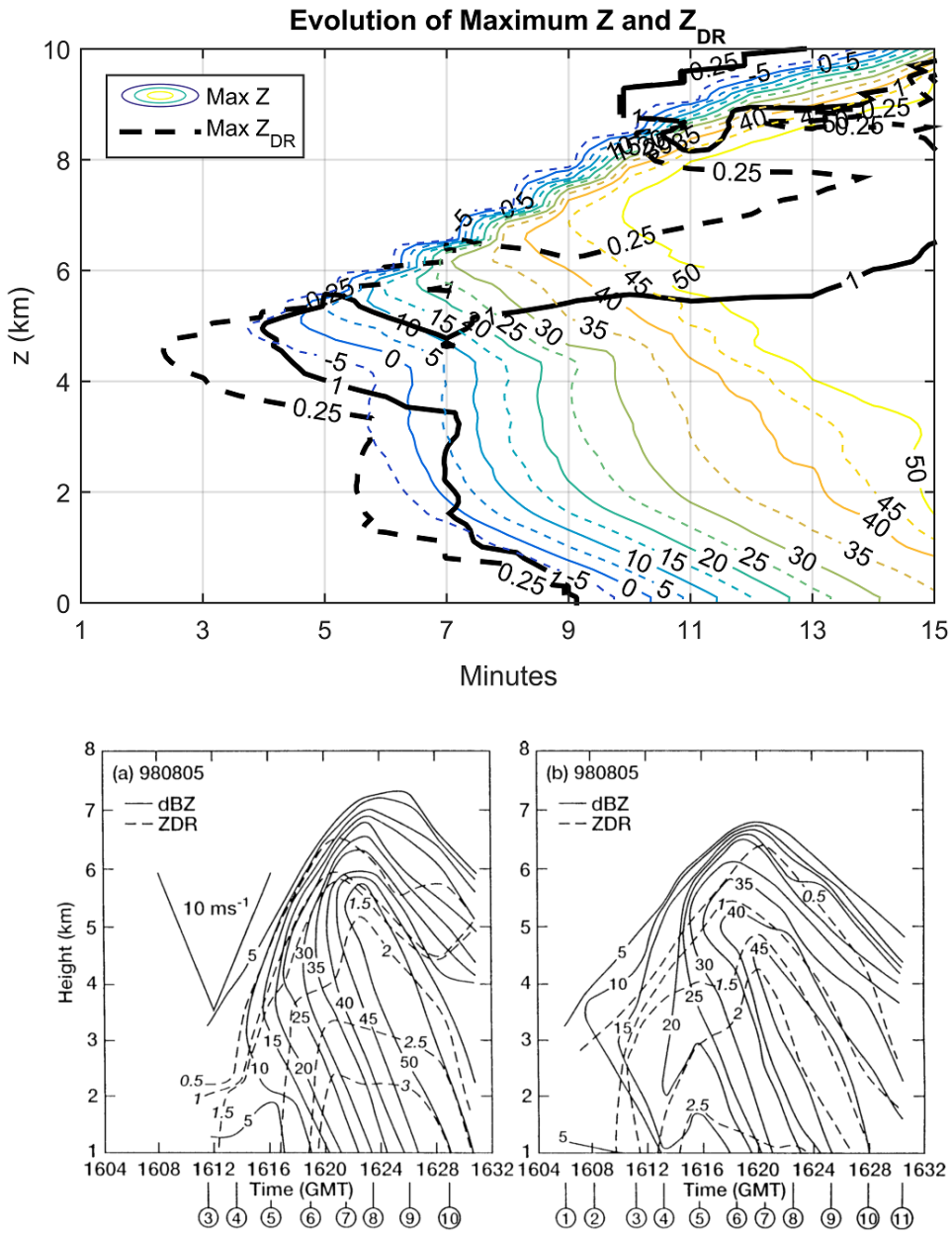

Figure 5.4: (Top) Time-height series of maximum Z (color) and Z_{DR} (black) from the HUCM for a storm in a highly polluted environment (CCN_{sfc} = 3000 cm^{-3}). (Bottom) Analogous plots from radar observations for strong convective cases (Fig. 6 of Knight et al. 2002).

Figure 5.5, which shows vertical cross sections of Z, Z_{DR}, and the rain PSDs in the area of enhanced Z_{DR}. The traditional "first echo" forms atop the burgeoning updraft before beginning to fall down the sides of the updraft. A separate stem of Z forms on the upwind (in the case of Fig. 5.5, on the left) side of the updraft. The anomalously high Z_{DR} forms at the base of this stem, exceeding 1.0 dB for Z of -3.6 dBZ and exceeding 2.0 dB for a Z of 6.4 dBZ (Figure 5.5, bottom). This is remarkably consistent with Knight's description of his observations, in which he stated that "positive Z_{DR} is found within and to the upwind side of the updraft, separate from the conventional first precipitation echoes, which appear first at higher altitude, generally downwind of the updraft core, and have no significantly positive Z_{DR}" (Knight 2006). The rain PSDs (Figure 5.5, bottom) through this time suggest very rapid growth through coalescence, as the distribution flattens out appreciably in the span of 5 minutes.

The impact of the initial CCN concentration on the radar variables during the early stages of convection is examined in Figure 5.6 using the aforementioned five simulations. The burst of anomalously high Z_{DR} during the initial stages of development (t = 13-17 min) is absent for the lowest CCN concentrations, and becomes increasingly robust as CCN concentration increases. This seems to be consistent with the conceptual model for the impact of CCN concentration on precipitation development. For low CCN cases, the available moisture is spread among relatively few CCN, eventually inducing collision-coalescence processes and a gradual increase in Z_{DR}. For the highest CCN cases, warm rain production is generally suppressed as the drop spectrum is narrowed and ice phases play an increasing role in precipitation production. However, there are many small drops available to be collected, such that any single drop that stochastically begins to grow (or ice particle falling from above in the traditional "first echo" region, as hypothesized in Knight 2006) can grow large very quickly.

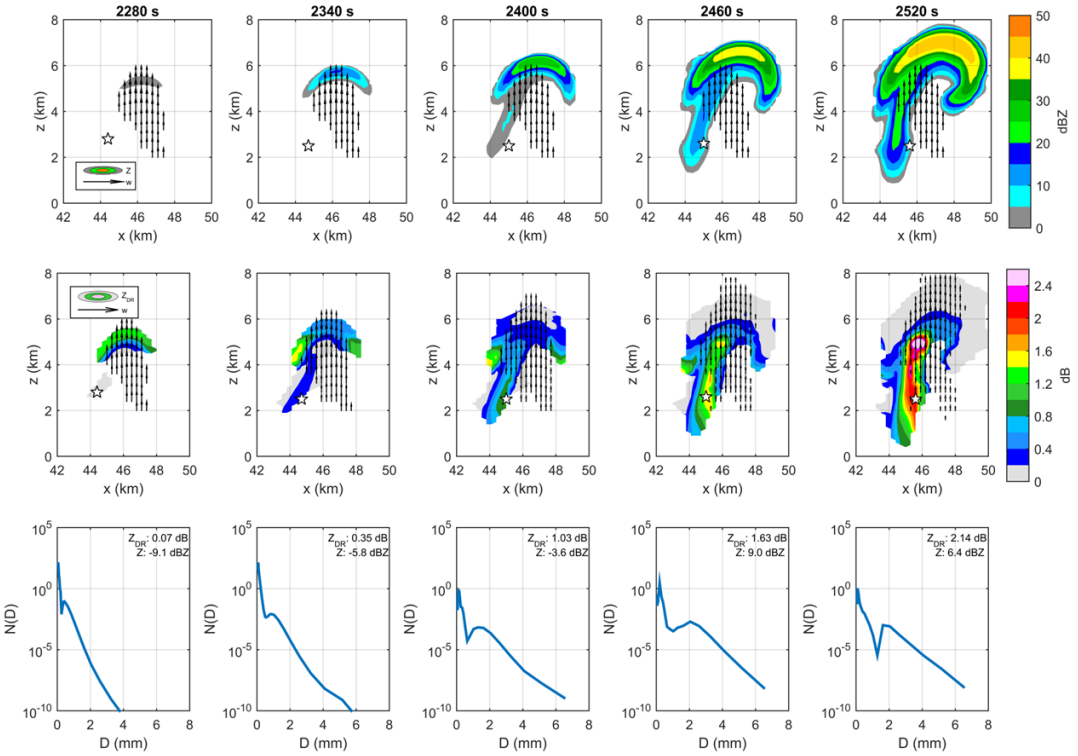

Figure 5.5: Vertical cross sections of (top) Z, (middle) Z_{DR}, and (bottom) rain PSDs at 1-min intervals in the developing stages of a storm in a highly polluted environment (CCN_{sfc} = 3000 cm^{-3}) from the HUCM. Vertical velocities in excess of 5 m s^{-1} are shown by vectors. The rain PSDs are for locations denoted by stars in the top and middle rows.

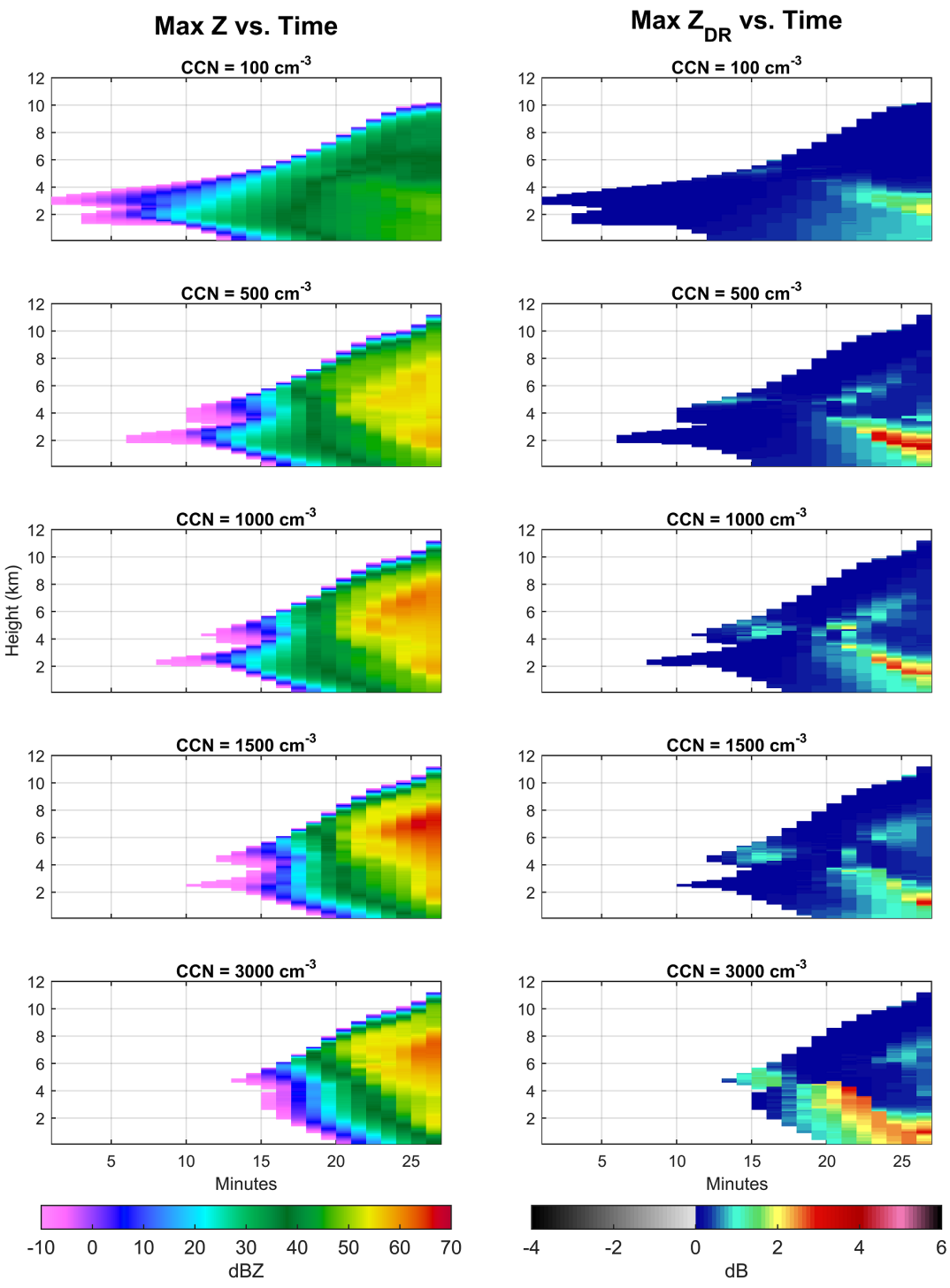

Figure 5.6: Time-height series of (left) maximum Z and (right) Z_{DR} at the location of the maximum Z for CCN_{sfc} = 100 cm^{-3}, 500 cm^{-3}, 1000 cm^{-3}, 1500 cm^{-3}, and 3000 cm^{-3} from the HUCM.

If the magnitude of this early anomalous Z_{DR} signature may be tied to the initial CCN concentration, how should this inform any application for storm-scale NWP models? The rate of development of convection as a function of CCN is shown in Figure 5.7. A number of changes are evident. First, as expected from previously described theory, the time of the first -10 dBZ echo is delayed for larger CCN concentrations as warm rain processes are increasingly suppressed. Perhaps more importantly, the rate of the increase in the maximum Z with time is positively correlated with CCN concentration, as is the height of the maximum Z and the magnitude of the maximum Z. This suggests that, if the early Z_{DR} signature is indeed tied to the available CCN or ongoing microphysical processes in the earliest stages of developing convection, information could theoretically be garnered about the expected rate and characteristics of the pending convective development.

The investigation of this early Z_{DR} signature was only cursory, and is limited by a small sample size from the HUCM and a continued lack of high spatial and temporal resolution observations. Other proposed mechanisms for the formation of this signature cannot be ruled out, and there is no guarantee that only one pathway is available to produce this signature (e.g., both ultragiant nuclei with any CCN concentration, or areas free of ultragiant nuclei with otherwise high CCN concentrations could result in the production of anomalously high Z_{DR}). Still, it seems noteworthy that the HUCM was able to reproduce this signature as described for observations in the literature in the absence of giant and ultragiant nuclei and with a clear impact of CCN concentration. Knight (2006) note that this curious feature may not have significant dynamical consequences because it is transient and likely due to only a very small number of drops, but rather may be important for what it may signify indirectly (i.e., the presence of a considerable amount of small drops in the early stages of developing convection). Regardless of the exact mechanisms responsible or the connection with resultant storm development and intensity, the presence of a size sorting signature consisting of anomalously high Z_{DR}

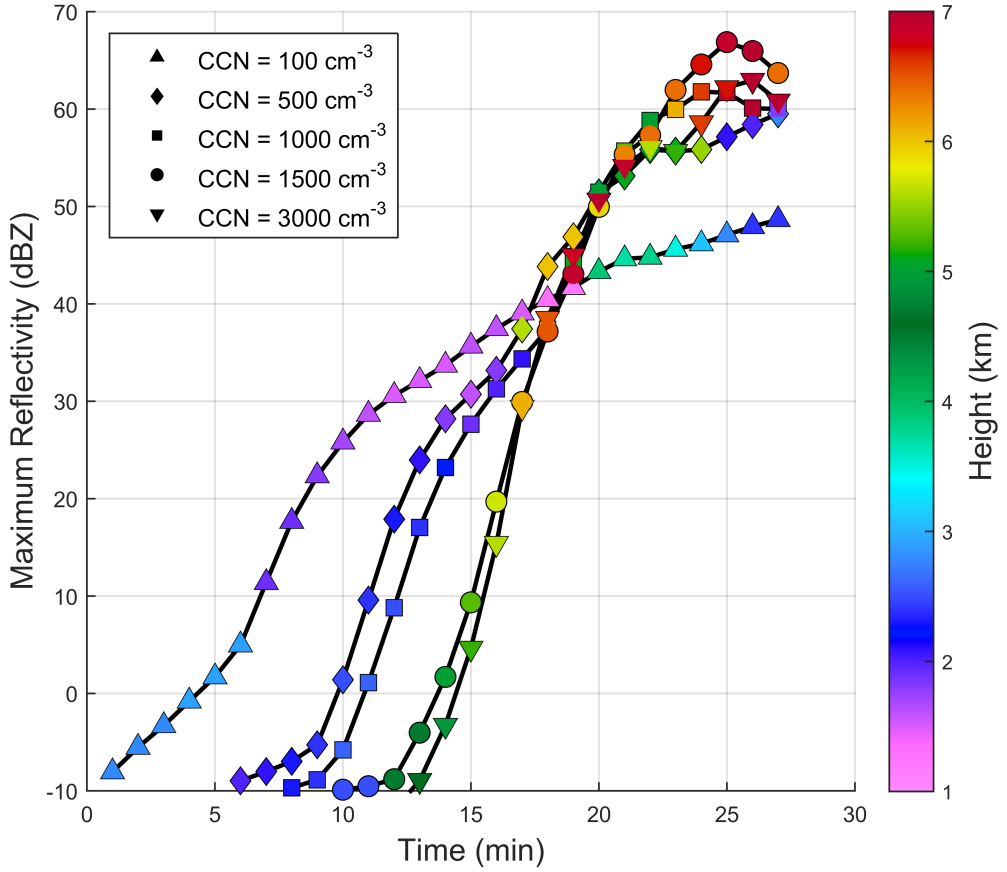

Figure 5.7: Time-series of the maximum Z for CCN_{sfc} = 100 cm^{-3}, 500 cm^{-3}, 1000 cm^{-3}, 1500 cm^{-3}, and 3000 cm^{-3} from the HUCM starting at the first appearence of -10 dBZ. Markers are colored according to the height at which the maximum Z occurs.

colocated with low Z at the earliest stages of developing convection can at the very least be used to locate burgeoning updrafts and remains potentially relevant to storm-scale NWP. The ubiquity of this signature in developing convection is the motivation behind the ongoing development of a size-sorting detection algorithm for use in aviation to detect developing convection effectively (Picca et al. 2017).

5.2 Diabatic cooling in the melting layer

5.2.1 Background

Nearly concurrent with the adoption of radar for weather surveillance was the discovery of the so-called radar "bright-line" (now known as the "brightband"; e.g., Byers and Coons 1947), which was quickly and correctly understood to be associated with the melting layer (e.g., Cunningham 1947; Austin and Bemis 1950). The brightband signature was first identified by a layer of enhanced Z, which to a first order is due to the sharp increase in the dielectric constant of snowflakes as they begin to melt before collapsing into smaller raindrops and decreasing their number concentration due to increased fallspeeds. However, a number of secondary processes can occur within the melting layer, including aggregation and breakup of snowflakes, although there is no consensus about the significance of such processes (e.g., Fabry and Zawadzki 1995, see section 5.2.3.5). The unique polarimetric characteristics of the brightband were also observed relatively early on. Pronounced enhancements in the linear depolarization ratio (L_{DR}; Browne and Robinson 1952; Humphries 1974; Anderson 1974) and circular depolarization ratio (C_{DR}; Humphries and Barge 1979) below the height of the Z maximum were observed soon after the discovery of the brightband. Similar observations were subsequently made in Z_{DR} by Bringi et al. (1981). Zrnić et al. (1993) presented a detailed analysis of polarimetric melting layer signatures coupled with *in situ* aircraft measurements, noting a pronounced reduction in ρ_{hv} (e.g., Illingworth and Caylor 1989) attributed to appreciable δ caused by large wet aggregates exceeding 1 cm in diameter,

rather than simply having a wide range of hydrometeor types, shapes, and sizes within the layer. This change in δ as particles grew due to aggregation also resulted in an oscillatory K_{DP} profile through the melting layer, which was otherwise positive with a maximum near the height of the Z maximum. The maximum Z_{DR} occurs at a lower height than the maximum Z. The distance between the Z and Z_{DR} maxima can vary widely, with depths of 700 m (e.g., Zrnić et al. 1993) to 200 m or less (e.g., Humphries and Barge 1979) reported.

More recently, quasi-vertical profiles (QVPs; Ryzhkov et al. 2016) have emerged as a convenient way to study the evolution of the polarimetric signatures of microphysical processes in time. QVPs display a timeseries of azimuthally-averaged radar data from a high elevation scan in a time-height format. The large increase in the number of samples due to the averaging procedure results in significantly reduced errors and enhanced data quality compared to typical plan-position indicator scans, allowing for the detection of more subtle polarimetric signatures that may have otherwise been obscured by noise (e.g., Griffin et al. 2018). However, the averaging procedure will obscure any heterogeneities within the averaging domain and so works best in uniform precipitation, such as stratiform rain or snow. The time-height format of QVPs makes them ideal for comparing against the output of the 1D-MS.

A demonstrative example of a typical polarimetric brightband signature is shown in Figure 5.8. These vertical profiles were derived from averaging QVP data from an MCS in northern Oklahoma on 20 May 2011 from Vance Air Force Base WSR-88D (KVNX) between 10:14:51 UTC and 11:15:33 UTC during a pronounced and fairly intense bright band signature. The K_{DP} is calculated using the methodology of Griffin et al. (2018) that removes the contribution of δ to Φ_{DP} by removing noisy Φ_{DP} and replacing it with a linear interpolation from above and melting the melting layer when calculating K_{DP} along a given radial. The melting layer is approximately 1300 m deep (based on the depth of the layer with reduced ρ_{hv}) and features an increase in Z of

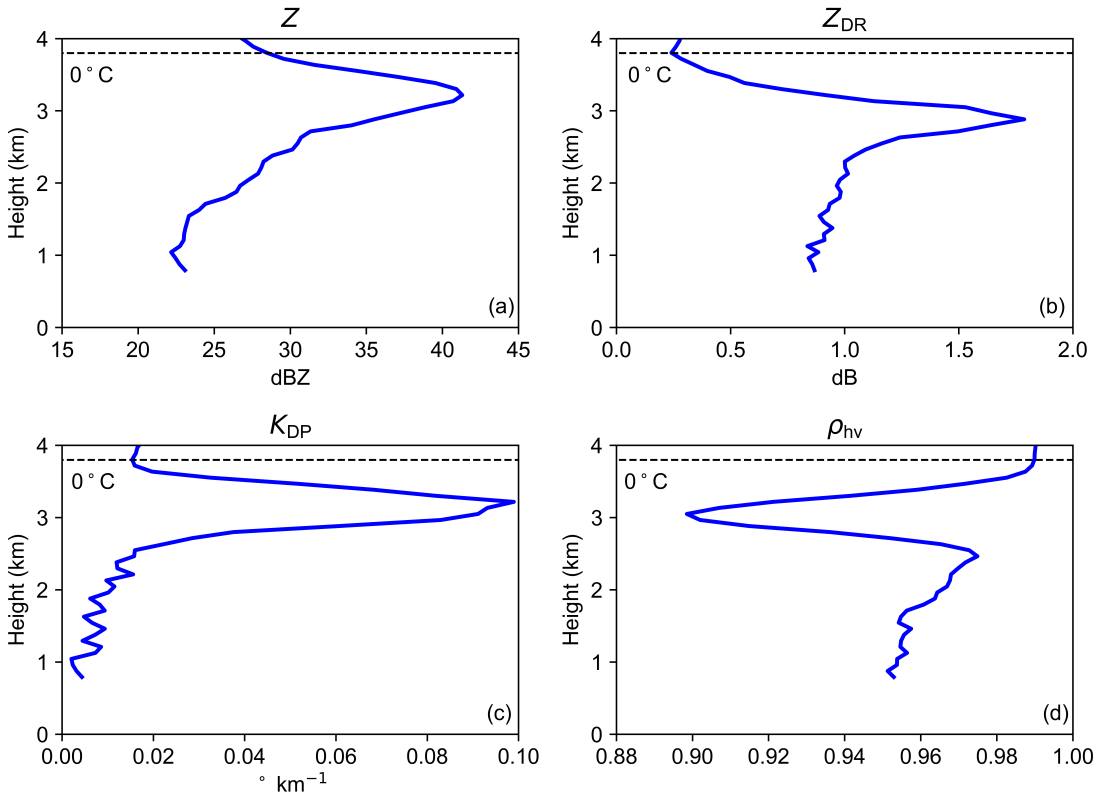

Figure 5.8: Vertical profiles of (a) Z, (b) Z_{DR}, (c) K_{DP}, and (d) ρ_{hv} derived from a QVP from the Vance Air Force Base WSR-88D (KVNX) radar averaged between 10:14:51 UTC and 11:15:33 UTC on 20 May 2011. The approximate height of the 0°C level is shown by the dashed line.

approximately 13 dBZ, a Z_{DR} maxima of 1.8 dB located 400 m below the height of the Z maxima, an increase in K_{DP} to nearly 0.1 $^{\circ}$ km^{-1}, and a reduction in ρ_{hv} to below 0.9. This depth is larger than that of a typical melting layer and is due to the averaging of the QVP over a range of times in which the height of the brightband varied. Although the average profiles in Figure 5.8 do not show the large degree of variability of brightband characteristics for this event, they provide a general sense of the polarimetric features characteristic of a melting layer within stratiform precipitation.

Because of its ubiquity and importance, many studies have sought to model the brightband and its effects to gain insight into the microphysical characteristics of the

melting layer. Despite their widespread use, models with bulk microphysical parameterization schemes generally fail to accurately represent the bright band (e.g., Li et al. 2008; Gallus and Preifer 2008) due to the lack of mixed-phase hydrometeor species and rigorous melting procedures, which strongly impact the particle scattering characteristics (Iguchi et al. 2014). Phillips et al. (2007) found that the assumption of instantaneous melting will underestimate the cooling due to melting, which results in insufficient feedback processes that may drive convection. Because of the insuffiencies of bulk microphysical models to properly simulate the complexity of the melting layer, many studies employ spectral bin models with a more explicit treatment of the melting process.

The earliest studies in modeling the melting layer focused primarily on the representation of the physical processes of a melting snowflake (e.g., Matsuo and Sasyo 1981; Mitra et al. 1990). However, due to the connection between the melting layer and its observed radar signature, many subsequent studies have included electromagnetic scattering components of differing complexity to compare the observed Z in brightbands with the modeled Z in one-dimensional (e.g., Yokoyama and Tanaka 1984; Klaasen 1988; Hardaker et al. 1995; Fabry and Szyrmer 1999; Gray et al. 2001; Olson et al. 2001; Zawadzki et al. 2005) and three-dimensional (e.g., Phillips et al. 2007; Planche et al. 2014; Iguchi et al. 2014) models. A lesser number of studies have made efforts to reproduce observed polarimetric signatures in the bright band (e.g., Russchenberg and Ligthart 1996; D'Amico et al. 1998; Giangrande 2007; Trömel et al. 2014). The objective of these studies has generally been to better understand the physical processes within the melting layer that lead to brightband signatures and to evaluate the performance of microphysics schemes in their ability to reproduce these signatures.

As discussed in section **??**, cooling due to the melting and evaporation of precipitation within the melting layer can have significant impacts not only for observed weather conditions at the surface but for the dynamics and subsequent downstream development

of precipitation systems. Given the potential for polarimetric measurements to provide increased insight into ongoing microphysical processes, it is worth investigating whether these measurements can be utilized for improved thermodynamic retrievals by better quantifying microphysical processes within the melting layer. In this study, the 1D-MS model described in section 3.1.2 (with full details of the model available in the Appendix) is used to relate the polarimetric characteristics of modeled brightbands to the diabatic cooling rate within them. Sensitivity tests for a number of model parameters will be shown in section 5.2.3, along with a brief validation of the model against observations in QVP format for the stratiform region of a severe MCS. Section 5.2.4 will investigate the impact of the environment on the resultant polarimetric brightband, and the efficacy of utilizing polarimetric brightband signatures for thermodynamic retrievals. Finally, a brief examination of the "sagging" brightband signature using the 1D-MS will be undertaken in section 5.2.5.

5.2.2 Model description

The 1D-MS is a one-dimensional Lagrangian spectral bin model that resembles those used in other studies of melting snow (e.g., Szyrmer and Zawadzki 1999; Zawadzki et al. 2005; Giangrande 2007; Grim et al. 2009; Trömel et al. 2014) with a number of improvements. As part of this effort, the model was translated from the Interactive Data Language (IDL) language it was originally written in to Python in an effort to increase its portability and shareability. A full list of variables and their units (and values, if applicable) is presented in Table 5.1.

PSDs consist of 80 size bins, and particles are tracked downward from the top of the model as they melt and/or evaporate/sublimate. Interactions between particle bin sizes (e.g., aggregation, breakup, and shedding of meltwater) are not currently included, allowing for one snowflake aloft to correspond to one raindrop at the surface

and the size of each particle bin to change with height (i.e., in the absence of evaporation/sublimation, the bins are mass-conserving).

To calculate the initial bin sizes of snow aloft, the density of snow (ρ_s) is assumed to be a function of the particle diameter (D) and f_{rim} according to

$$\rho_s = 0.178 f_{\text{rim}} D^{-0.922} \tag{5.1}$$

Brandes et al. (2007), and is capped at a maximum allowable snow density ($\rho_{s,max}$) of 0.5 g cm^{-3} (Zawadzki et al. 2005). The f_{rim} is allowed to vary from 1 (unrimed snow) to 5 (heavily rimed snow). It can be shown that, using Eq. (5.1) and the assumptions of snowflake-raindrop correspondence, the initial diameter of a snowflake corresponding to a given raindrop of an equivalent mass (with diameter D_r) can be found according to

$$D = 2.29 f_{\text{rim}}^{-0.48} D_r^{1.443}. \tag{5.2}$$

Example bin sizes as a function of height for typical raindrop diameters are shown in Figure 5.9 using Eq. (5.2).

Two options exist for defining the PSD at each height. In the original model formulation, the PSD for rain is defined at the surface ($N(D_r, z_0)$; referred to here as the "bottom-up" approach). Various PSD options have been implemented in the model, including monodispersed size distributions, inverse exponential distributions, and size distributions derived from mean rain size distributions measured at the surface by a disdrometer in Oklahoma (Schuur et al. 2005) and partitioned by surface Z. These rain DSDs are defined using 0.1-mm-wide bins ranging from 0.05 to 7.95 mm. The concentration of particles at each height z, $N(D,z)$, is found by conserving concentration flux (Szyrmer and Zawadzki 1999):

$$u(D,z)N(D,z)dD = u_r(D_r,z_0)N(D_r,z_0)dD_r \tag{5.3}$$

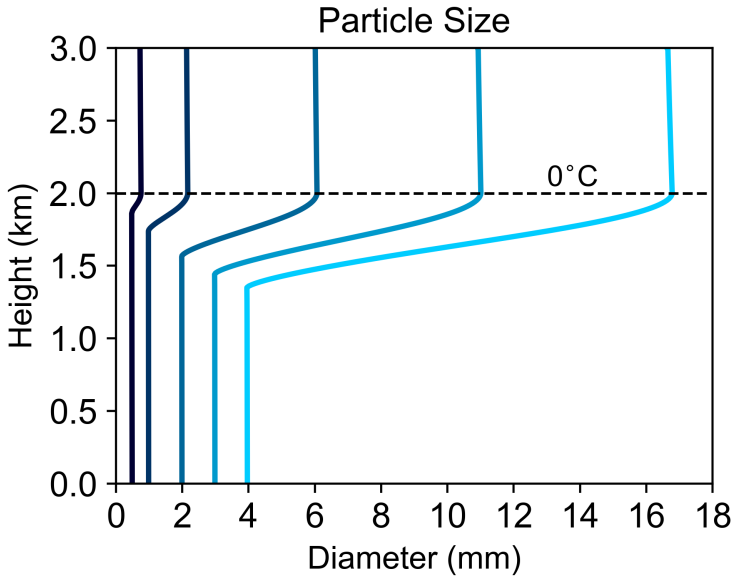

Figure 5.9: Particle size for unrimed snow as a function of height for raindrop diameters of 0.5, 1.0, 2.0, 3.0, and 4.0 mm found according to Eq. (5.2).

where $u(D,z)$ is the terminal velocity of particles of diameter D at height z and any stage of melting and $u_r(D_r,z_0)$ is the terminal velocity of rain at the surface. The terminal velocity of rain is given by Brandes et al. (2005),

$$u_r(D_r,z) = \left(\frac{\rho_{a,0}}{\rho_a(z)}\right)^{0.4}\Big(-0.1021+0.4932D_r- 0.9551D_r^2+0.07934D_r^3-0.002363D_r^4\Big) \tag{5.4}$$

where $(\rho_{a,0}/\rho_a(z))^{0.4}$ is a correction factor for the local air density (Foote and du Toit 1969). The terminal velocity of a particle at any stage of melting is found as a function of the meltwater mass fraction (f), defined by

$$f = \frac{m_w}{m_i+m_w} \tag{5.5}$$

where m_w and m_i are the mass of water and ice in the particle, respectively, and the terminal velocity of a raindrop of equivalent mass, following Szyrmer and Zawadzki (1999):

$$u(D,z) = \frac{u_r(D_r,z)}{g(f)}, \tag{5.6}$$

where

$$g(f) = a - bf(1+f), \tag{5.7}$$

$a = 1.26\rho_s^{-1/3}$ and $b = 0.5(a-1)$. Equation (5.6) becomes equivalent to (5.4) when the particle is fully melted ($f = 1.0$).

The "bottom-up" approach was used in previous studies employing the prior iterations of this model (e.g., Kumjian et al. 2016). However, inherent in the assumption of extrapolating upward from a surface rain distribution to get an initial PSD is mass conservation, which was appropriate in the older version of this model where only particle melting was considered. In addition, when using a PSD of rain at the surface (e.g., the average observed PSDs of Schuur et al. 2005), it does not account for any modifications that may have modified the rain PSD below the melting layer (e.g., breakup). In this updated version of the model, evaporation and sublimation are incorporated, and mass losses from the bin are possible. Therefore, a second option has been added to define the snow distribution aloft (referred to as the "top-down" approach) that defines the size distribution at each height in reference to the top distribution according to

$$u(D,z)N(D,z)dD = u_s(D_s, z_{\text{top}})N(D_s, z_{\text{top}})dD_s. \tag{5.8}$$

where D_s is the equivolume diameter of the initial unmelted snow particles. The concentration flux is conserved in a similar manner, with the initial bin sizes (Eq. 5.2) determined by assuming 0.1-mm bin sizes for rain as before and calculating u_r using the D of fully-melted particles of equivalent mass.

Once the initial particle sizes and densities have been established, each particle size bin is tracked as it falls and evolves. The transfer of heat by radiation and the collection of cloud droplets by the particle are neglected as they are small in comparison to the primary microphysical processes (e.g., Szyrmer and Zawadzki 1999). Curvature and solute effects are also neglected. In addition, when considering the heat balance of the particle, it is assumed that the particle's temperature is homogenous, and that no sensible heat is stored in the particle (i.e., all input heat goes toward the ongoing phase

change). The relevant microphysical process acting on a particle is determined by the local environmental conditions as well as the particle composition and temperature.

When ice particles are located in air that is subsaturated with respect to ice, sublimation occurs, which decreases the particle's temperature. Following Pruppacher and Klett (1997) and by assuming $f_v \approx f_h$, the equilibrium temperature of the particle (T_p) undergoing sublimation can be found according to

$$T_p = T - \frac{L_s D_v}{\kappa_a R_v}\left(\frac{e_{s,i}(T_p)}{T_p} - \frac{e(T)}{T}\right), \tag{5.9}$$

which results from solving for the equilibrium condition between the sensible heat and latent heat transfer to the particle. This equation is solved iteratively for each particle at each height to within a 0.01 °C threshold. Because the terminal velocity of dry snow is relatively slow, the residence time within a grid box of Δh = 10 m, the vertical grid spacing used in this study, is long enough to permit the assumption of equilibrium with the environment.

The rate of mass diffusion for a particle due to sublimation, following Rogers and Yau (1989), can be expressed as

$$\frac{dm_{i,subl}}{dt} = 2\pi D D_v f_v \Delta\rho_v \tag{5.10}$$

where $\Delta\rho_v$ is the difference in vapor density (with respect to ice) between the environment and the surface of the particle. Recognizing that for a falling particle

$$\frac{dm}{dt} = \frac{dm}{dz}\frac{dz}{dt} \approx \frac{\Delta m}{\Delta h}\frac{\Delta h}{\Delta t} = \Delta m \frac{(u-w)}{\Delta h}, \tag{5.11}$$

where w is the local vertical velocity, the change in mass of a single particle in a given grid box due to sublimation ($\Delta m_{i,subl}$) assuming steady-state conditions can be found according to

$$\Delta m_{i,subl} = \frac{4\pi c f_v D_v}{R_v}\frac{\Delta h}{(u-w)}\left(\frac{e}{T} - \frac{e_{s,i}(T_p)}{T_p}\right) \tag{5.12}$$

where the variables are as listed in Table 5.1 and described below.

If the air is subsaturated above the 0°C level, the particle temperature can be subzero when it crosses the 0°C level, and must warm up to 0°C before melting can occur. This can delay the onset of melting by up to a few hundred meters below the 0°C level (Matsuo and Sasyo 1981, see section 5.18). Melting commences once the particle temperature reaches 0°C. During the entire melting process, it is assumed that the particle temperature remains at 0°C.

The ice loss due to melting for a particle within a grid box is a balance between the sensible heat flux to melt the ice and the cooling due to evaporation of meltwater and can be found according to

$$\Delta m_{i,melt} = \frac{-4\pi c}{L_f}\frac{\Delta h}{(u-w)}\left[f_h \kappa_a (T - T_p) + f_v \frac{D_v L_v}{R_v}\left(\frac{e}{T} - \frac{e_{s,w}(T_p)}{T_p}\right)\right]. \tag{5.13}$$

If the bracketed term on the right hand side of Eq. (5.13) is < 0, evaporative cooling exceeds the sensible heat flux used to melt ice, and sublimation is instead considered. When it is > 0, melting occurs, and the loss of ice mass is converted into melt water (i.e., $\Delta m_{i,melt} = -\Delta m_{w,melt}$). With $f > 0.0$, loss of water due to evaporation (discussed below) is also calculated in accordance with the evaporative cooling component in Eq. (5.13). Currently, refreezing (which would occur if $f > 0.0$ and $T_p \leq T_0$) is not included.

Finally, evaporation (by itself) occurs when $f = 1.0$ and $T_p \geq T_0$ (which necessitates that the particle is entirely melted). Similar to sublimation, the rate of mass loss of a single particle due to evaporation is described by

$$\frac{dm_{w,evap}}{dt} = 2\pi D D_v f_v \Delta\rho_v \tag{5.14}$$

where $\Delta\rho_v$ is the difference in vapor density (with respect to water) between the environment and the surface of the particle. However, due to the relatively high terminal velocity of raindrops compared to Δh and the thermal relaxation time for raindrops (on the order of a few seconds; e.g., Tardif and Rasmussen 2010), it cannot be assumed that raindrops are in equilibrium with the environment within a given grid box in the presence of changing environmental conditions (Caplan 1966) as was done for dry snow

and as is frequently done in other studies (e.g., Srivastava 1985). The rate of change of T_p can be found by the balance of the sensible heat transfer due to conduction and the cooling due to evaporation (Tardif and Rasmussen 2010):

$$m_w c_w \frac{dT_p}{dt} = L_v \frac{dm_w}{dt} + \frac{dh}{dt}. \tag{5.15}$$

When the sensible and latent heat terms are expanded, the change of T_p within a grid box can be found according to

$$\Delta T_p = \frac{\Delta h}{(u-w)m_w c_w} \left[4\pi c f_v \frac{L_v D_v}{R_v} \left(\frac{e_{s,w}(T_p)}{T_p} - \frac{e}{T} \right) - 4\pi c f_h \kappa_a (T_p - T) \right] \tag{5.16}$$

where the T_p used on the right side of Eq. (5.16) comes from the grid point above. This process begins as soon as melting is complete, when T_p = 0°C, and the maximum temperature attainable by a raindrop is capped at the equilibrium T_p, found using Eq. (5.9) except replacing L_s and $e_{s,i}$ with L_v and $e_{s,w}$. An example comparison of particle temperatures for a variety of raindrop sizes and their equilibrium temperatures as well as the environmental temperature is shown in Figure 5.10. The environmental 0°C level is at 2.0 km, the lapse rate is constant at 6°C km^{-1}, and the relative humidity is constant at 90%. Melting is delayed by 130 m due to sublimation as the particles need to warm to 0°C. Once melting begins, the different sized particles take different distances to completely melt, ranging from 190 m for a particle with D_{sfc} = 0.58 mm to 780 m for a particle with D_{sfc} = 5.97 mm. Because of this, along with their different masses, the particles warm at different rates once fully melted; smaller raindrops reach their equilibrium temperature quickly, whereas the largest drops never quite reach their equilibrium temperature. If the environment is dry, raindrops may remain appreciably colder than the environment (e.g., for a constant relative humidity of 50%, raindrops are up to 5.5°C colder than the environment (not shown)).

Once the T_p of the raindrops is known, the mass loss due to evaporation can be found with an analogous equation to Eq. (5.12):

$$\Delta m_{w,evap} = \frac{4\pi c f_v D_v}{R_v} \frac{\Delta h}{(u-w)} \left[\frac{e}{T} - \frac{e_{s,w}(T_p)}{T_p} \right] \tag{5.17}$$

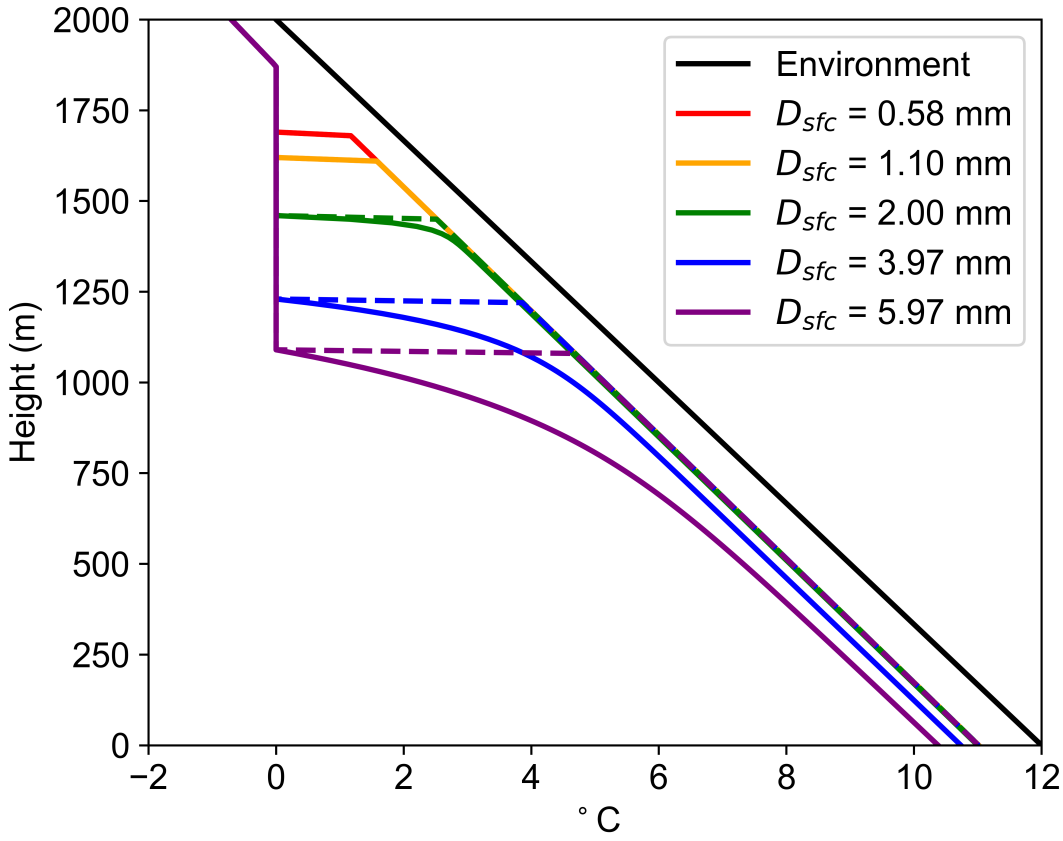

Figure 5.10: Example comparison of particle temperatures (solid lines) and their equilibrium temperatures (dashed lines) for raindrops with surface diameters of 0.58 mm (red), 1.10 mm (orange), 2.00 mm (green), 3.97 mm (blue), and 5.97 mm (purple) for a lapse rate of 6°C km^{-1} and a constant relative humidity of 90%. The environmental temperature is shown in black, with the 0°C level at 2000 m.

The capacitance (c) in Eqs. (5.12), (5.13), and (5.17) reflects the impact of the particle's shape on its rate of mass transfer. Particles are assumed to be oblate spheroids representing low-density snow aggregates. Although much more detailed models of melting aggregates are beginning to be explored (e.g., Leinonen et al. 2017), oblate spheroids greatly simplify the treatment of the microphysical processes and have been shown to be a good approximation (e.g., Matrosov et al. 1996; Hogan et al. 2012) and reproduce observed polarimetric signatures fairly well (e.g., Ryzhkov et al. 2011). For spherical particles, c is equal to the particle's radius. For oblate spheroids, c is equal to (McDonald 1963):

$$c = 0.5 D r_m^{-1/3} \frac{x}{\sin^{-1} x} (0.8 + 0.2 f) \tag{5.18}$$

where r_m is the aspect ratio of the particle at any stage of melting and is given as a linear function of f between that of dry snow, r_s, and that of a completely melted particle of the same mass, r_r:

$$r_m = r_s + f(r_r - r_s). \tag{5.19}$$

and the ellipticity of the spheroid, x, is equal to $\sqrt{1 - r_m^2}$. The aspect ratio for raindrops is well established and given by (Brandes et al. 2002, 2005):

$$\begin{aligned} r_r = 0.9951 + 0.0251 D_r - 0.03644 D_r^2 + \\ 0.005303 D_r^3 - 0.0002492 D_r^4 \end{aligned} \tag{5.20}$$

There is more uncertainty with regard to the aspect ratio for dry snow aggregates, which can be set to a constant value (e.g., Vivekanandan et al. 1994; Ryzhkov et al. 2011; Thompson et al. 2014) or vary slightly across the size spectrum (e.g., Brandes et al. 2007) or as a function of riming (Garrett et al. 2015, see section 5.2.3.2).

The venatilation coefficients for heat (f_h) and vapor (f_v) in Eqs. (5.12), (5.17), and (5.13) account for the removal of heat and vapor away from the falling particle due to air motion. Two options exist for calculating f_h and f_v. The first (and default

option) employs the empirical formulas of Hall and Pruppacher (1976), which defines the ventilation coefficient for vapor as

$$f_v = \begin{cases} 1 + 0.14\chi^2, & \text{for } \chi < 1 \\ 0.86 + 0.28\chi, & \text{for } \chi \geq 1 \end{cases} \tag{5.21}$$

where $\chi = N_{\text{Sc}}^{1/3} N_{\text{Re}}^{1/2}$, N_{Sc} is the Schmidt number given by

$$N_{\text{Sc}} = \frac{\nu_a}{D_v} \tag{5.22}$$

and N_{Re} is the Reynolds number given by

$$N_{\text{Re}} = \frac{L^* U}{\nu_a} \tag{5.23}$$

where ν_a is the kinematic viscosity of air, and L^* is the particle characteristic length, which for an oblate spheroid can be expressed as (Pruppacher and Klett 1997):

$$L^* = \frac{D}{4 r_m^{\frac{1}{3}}} \left[2 + r_m^2 \frac{1}{x} \ln \left(\frac{1+x}{1-x} \right) \right]. \tag{5.24}$$

The diffusivity of water vapor (D_v) is found by Hall and Pruppacher (1976)

$$D_v = 2.11 \times 10^{-5} \left(\frac{T}{T_0} \right)^{1.94} \left(\frac{p_0}{p} \right) \tag{5.25}$$

whereas the kinamatic viscosity of air, ν_a, is given by

$$\nu_a = \frac{\eta_a}{\rho_a} \tag{5.26}$$

where the dynamic viscosity of air, η_a, is given by

$$\eta_a = (0.379565 + 0.0049T) \times 10^{-5}. \tag{5.27}$$

The ventilation coefficient for heat (f_h) follows a similar form as Eq. (5.21), except uses the Prandtl number (N_{Pr}) instead of the Schmidt number (i.e., $\chi = N_{\text{Pr}}^{1/3} N_{\text{Re}}^{1/2}$), where N_{Pr} is given by

$$N_{\text{Pr}} = \frac{\nu_a}{k_a} \tag{5.28}$$

where the thermal diffusivity of air, k_a, is defined as

$$k_a = \frac{\kappa_a}{c_p \rho_a} \tag{5.29}$$

and the thermal conductivity of air, κ_a, is given by

$$\kappa_a = (0.441635 + 0.0049T) \times 10^{-2}. \tag{5.30}$$

An additional option of using the ventilation coefficients put forth in Szyrmer and Zawadzki (1999) is included. In this instance, the ventilation coefficients for heat and vapor are assumed equal and given by

$$f_h = f_v = 33.0 \frac{D_r^{1.7}}{D} \tag{5.31}$$

where D and D_r are given in cm.

Once dm_i or dm_w have been calculated, the mass and volume of each constituent (i.e., water, ice, and air) is updated. During the melting process, it is assumed that the density of the snow core increases, up to $\rho_{s,max}$. By modifying Eq. (5.1) for volume instead of diameter, the volume of snow (v_s) can be found according to

$$v_s = 343 \left(\frac{P}{f_{rim}} \right)^{1.443} \tag{5.32}$$

where P is defined as

$$P = (\rho_i - \rho_a) v_i + \rho_a v_s \tag{5.33}$$

and where v_s in P comes from the grid box above. From this, the new snow density is found according to

$$\rho_s = 1.75 \times 10^{-2} f_{rim} v_s^{-0.307}, \tag{5.34}$$

which is simply Eq. (5.1) expressed in terms of volume. Once ρ_s reaches $\rho_{s,max}$, it is kept constant regardless of v_s.

The option to include temperature and moisture feedbacks with the environment has been added to the model. The change of the environmental temperature at each height is found according to

$$\Delta T(z) = \frac{\Delta t}{c_p \rho_a(z)} \Bigg[L_s \sum \Delta m_{i,subl}(D,z) N(D,z) dD + L_v \sum \Delta m_{w,evap}(D,z) N(D,z) dD + L_f \sum \Delta m_{i,melt}(D,z) N(D,z) dD \Bigg] \tag{5.35}$$

where steady-state conditions are assumed to exist for 1 min (i.e., Δt = 60 s) by default. Similarly, the change in the environmental water vapor mixing ratio, q_v, is found according to

$$\Delta q_v(z) = -\frac{\Delta t}{\rho_{a,d}(z) \Delta h} \sum (u(D,z) - w(z)) \left[\Delta m_{i,subl}(D,z) + \Delta m_{w,evap}(D,z) \right] N(D,z) dD. \tag{5.36}$$

where $\rho_{a,d}(z)$ is the density of dry air at height z. For both temperature and moisture, the summation is applied across all 80 particle size bins at each height, and all other variables (e.g., e_s, ρ_a, ε_w, etc.) are subsequently updated.

At each height, Z, Z_{DR}, and K_{DP} are calculated using the Ryzhkov et al. (2011) polarimetric operator discussed in section 3.2 with the modifications discussed below in section 5.2.3. The scattering amplitudes can be calculated using Rayleigh scattering equations or the PyTMatrix package (Leinonen 2014), an open-source Python package containing an implemention of the Mishchenko (2000) T-Matrix formulation. The dielectric constants for ice and air, ε_i and ε_a, are considered constants whose values are given in Table 5.1. The dielectric constant of water, ε_w, varies with temperature and is found according to the equations put forth in Ray (1972).

Table 5.1: Summary of the variables and constants used in the 1D-MS.

Symbol	*Variable*	*Value*	*Units*
c	Capacitance of particle		mm
c_p	Specific heat of air at constant pressure	1005	J kg^{-1} K^{-1}

Table 5.1: Summary of the variables and constants used in the 1D-MS.

Symbol	*Variable*	*Value*	*Units*
c_w	Specific heat of water at constant pressure	4181	J kg^{-1} K^{-1}
D	Equivolume particle diameter		mm
D^*	Diameter of particle in terms of largest dimension		mm
$D_{\max}$	Diameter of largest particle in the PSD		mm
D_r	Equivolume diameter of a completely melted particle		mm
D_v	Diffusivity of water vapor in air		m^2 s^{-1}
e	Vapor pressure		Pa
$e_{s,w}$	Saturation vapor pressure w.r.t. water		Pa
$e_{s,i}$	Saturation vapor pressure w.r.t. ice		Pa
$e_{s,0}$	Saturation vapor pressure at 0°C	611.2	Pa
f	Mass water fraction		
f_{rim}	Riming factor		
f_h	Ventilation coefficient for heat		
f_v	Ventilation coefficient for vapor		
Δh	Vertical grid spacing	10	m
k_a	Thermal diffusivity of air		m^2 s^{-1}
L_f	Latent heat of fusion at 0°C	3.35×10^5	J kg^{-1}
L_s	Latent heat of sublimation at 0°C	2.85×10^6	J kg^{-1}
L_v	Latent heat of vaporization		J kg^{-1}
$L*$	Characteristic length of particle		mm
m	Total mass of particle		g

Table 5.1: Summary of the variables and constants used in the 1D-MS.

Symbol	*Variable*	*Value*	*Units*
m_i	Total mass of ice in particle		g
m_s	Total mass of "snow" (ice + air) in particle		g
m_w	Total mass of water in particle		g
$N_{0,s}$	Intercept parameter for snow PSD		$\mathrm{m}^{-3}\ \mathrm{mm}^{-(1+\mu_s)}$
N_{Pr}	Prandtl number		
N_{Re}	Reynolds number		
N_{Sc}	Schmidt number		
$N(D)$	Number of particles of size D		$\mathrm{m}^{-3}\ \mathrm{mm}^{-1}$
p	Atmospheric pressure		Pa
p_0	Reference atmospheric pressure	101325	Pa
q_v	Water vapor mixing ratio		$\mathrm{kg\ kg}^{-1}$
$q_{v,s}$	Saturation vapor mixing ratio		$\mathrm{kg\ kg}^{-1}$
r_m	Aspect ratio of melting particle		
r_r	Aspect ratio of raindrop		
r_s	Aspect ratio of snowflake		
R_d	Gas constant for dry air	287.0	$\mathrm{J\ kg}^{-1}\ \mathrm{K}^{-1}$
R_v	Gas constant for water vapor	461.5	$\mathrm{J\ kg}^{-1}\ \mathrm{K}^{-1}$
RH	Environmental relative humidity		%
T	Air temperature		K
T_p	Particle temperature		K
T_0	Triple point temperature of water	273.15	K
u	Terminal velocity of particle		$\mathrm{m\ s}^{-1}$
u_r	Terminal velocity of raindrop		$\mathrm{m\ s}^{-1}$
u_s	Terminal velocity of snowflake		$\mathrm{m\ s}^{-1}$

Table 5.1: Summary of the variables and constants used in the 1D-MS.

Symbol	*Variable*	*Value*	*Units*
v	Total volume of particle		g cm^{-3}
v_a	Volume of air in particle		g cm^{-3}
v_i	Volume of ice in particle		g cm^{-3}
v_s	Volume of "snow" (ice + air) in particle		g cm^{-3}
v_w	Volume of water in particle		g cm^{-3}
w	Vertical velocity of air		m s^{-1}
z_0	Reference surface level		
Γ	Environmental lapse rate		$^\circ$ km^{-1}
ε_a	Dielectric constant of air	(1.0, 5×10^{-7})	
ε_i	Dielectric constant of ice at 0°C	(3.18, 8.54×10^{-3})	
ε_w	Dielectric constant of water		
η	Dynamic viscosity of air		kg m^{-1} s^{-1}
κ_a	Thermal conductivity of air		J m^{-1} s^{-1} K^{-1}
λ	Radar wavelength		cm
Λ_s	Slope parameter for snow PSD		mm^{-1}
μ_s	Shape parameter for snow PSD		
ν	Kinematic viscosity of air		m^2 s^{-1}
ρ_a	Air density		g cm^{-3}
$\rho_{a,d}$	Dry air density		g cm^{-3}
$\rho_{a,0}$	Reference air density	1.292	g cm^{-3}
ρ_i	Density of solid ice	0.917	g cm^{-3}
ρ_s	Density of snow		g cm^{-3}

Table 5.1: Summary of the variables and constants used in the 1D-MS.

Symbol	*Variable*	*Value*	*Units*
$\rho_{s,max}$	Maximum allowable density of snow	0.5	g cm^{-3}
ρ_w	Density of water	1.0	g cm^{-3}
σ_r	Canting angle width of rain	10°	
σ_s	Canting angle width of snow		

5.2.3 Model sensitivity tests and validation

There are a number of parameters in the 1D-MS pertaining to particle characteristics that require selection and can significantly alter the results, but the nature of which remain highly uncertain. Although the 1D-MS is in itself a valuable tool for studying the impact of these various uncertainties and assumptions, the remainder of this work necessitates a reduction in the degrees of freedom in the model. The following sections describe these uncertainties, the model sensitivity to the range of possible values, and provide justifications for parameter choices going forward. Although the impact of changing one parameter is often sensitive to the value of others, efforts have been made to isolate the impact of each parameter to the furthest extent possible.

The same model settings were used for all of the following sensitivity tests, with only the relevant parameter being investigated varying from its otherwise specified value. The settings used are shown below in Table 5.2. In this case, the primary concern is how non-environmental parameters affect the resultant profile of radar variables. The model was run in its "top-down" mode with a constant lapse rate of 6 °C km^{-1} and a RH of 100% with the 0°C level at 2.0 km. The selection of a representative PSD was more difficult, as there is a large degree of variability in observed snow PSD parameters. For simplicity, an inverse exponential distribution (μ_s = 0.0) was used to initialize the model. From the

in situ observations in and above the melting layer reported in Heymsfield et al. (2002) and Heymsfield et al. (2015) from a number of field experiments, the $N_{0,s}$ was selected to be 1×10^4 m^{-3} mm^{-1}, Λ_s was 1.15 mm^{-1}, and the maximum particle diameter was 1.0 cm, representing a typical PSD observed in stratiform precipitation. Despite the large degree of variability among observed snow PSDs and the resultant radar variables, the qualitative conclusions were insensitive to the choice of initial PSD; although not shown for brevity, the same sensitivity tests were performed using various $N_{0,s}$ and Λ_s combinations as well as the "bottom-up" approach assuming a Marshall-Palmer rain size distribution at the surface with R = 5 mm h^{-1} that resulted in the same conclusions. All calculations were done at S band (λ = 11.0 cm) using T-matrix scattering calculations unless otherwise specified.

Table 5.2: Summary of the default criteria used to evaluate the sensitivity of the 1D-MS.

Variable	*Default*
Approach	"Top-down"
PSD	Inverse exponential
$N_{0,s}$	1×10^4 m^{-3} mm^{-1}
Λ_s	1.15 mm^{-1}
ε_e	MG: (I | W) | A
r_s	0.6
f_{rim}	1.0
λ	11.0 cm
σ_s	30°
Γ	6.0 °C km^{-1}
RH	100%

5.2.3.1 Dielectric constant

One of the largest uncertainties in the modeling of the bright band is how to appropriately calculate the dielectric constant of a melting snowflake. A common choice for calculating the effective dielectric constant of a mixed-phase particle (ε_e) is the Maxwell-Garnett mixing formula (Maxwell Garnett 1904). In this approach, one medium is considered the matrix whereas the other is considered to be randomly-distributed inclusions within the matrix. Following Zhang (2016),

$$\varepsilon_e = \varepsilon_{mat} \frac{1+2fy}{1-fy} \tag{5.37}$$

where ε_{mat} is the dielectric constant of the matrix material, f is the fractional volume of the inclusions, and y is given by

$$y = \frac{\varepsilon_{inc} - \varepsilon_{mat}}{\varepsilon_{inc} + 2\varepsilon_{mat}} \tag{5.38}$$

where ε_{inc} is the dielectric constant of the inclusions. For particles with three phases (i.e., ice, water, and air, as is the case for a melting snowflake), this formula should be applied twice: first to a combination of media, and then again using the first calculation as either the matrix or the inclusions with the third media. However, it is not immediately clear which combination of ice, water, and air is most appropriate for melting snow, as the formula results in different dielectric constants depending on which media is chosen as the matrix and the inclusions.

To address this, the Polder-van Santen mixing formula (Polder and van Santen 1946) can be applied, which is given by

$$f_1 \frac{\varepsilon_1 - \varepsilon_e}{\varepsilon_1 + 2\varepsilon_e} + f_2 \frac{\varepsilon_2 - \varepsilon_e}{\varepsilon_2 + 2\varepsilon_e} = 0 \tag{5.39}$$

where f_1 and ε_1 (f_2 and ε_2) are the fractional volume and dielectric constant of the first (second) materal in the mixture. The Polder-van Santen mixing formula does not require an assumption of which media acts as the matrix and gives a result that is between the Maxwell-Garnett mixing formula results with either combination of media as the matrix

and inclusions. In addition, like the Maxwell-Garnett formula, it can be applied twice sequentially to calculate ε_e for a three-phase particle. For both the Maxwell-Garnett and Polder-van Santen approaches using the Rayleigh approximation, the calculated ε_e is used in Eq. (2.5) to calculate the scattering amplitudes.

A third approach is that of Bohren and Huffman (1983), which computes an effective dielectric constant for a particle assuming spheroids of two separate layers. In this instance, the factor ξ in Eq. (2.4) is instead given by

$$\xi = \frac{(\varepsilon_{\text{out}} - 1)(\varepsilon_{\text{out}} + (\varepsilon_{\text{inn}} - \varepsilon_{\text{out}})L_{a,b}(1-\zeta)) + \zeta\varepsilon_{\text{out}}(\varepsilon_{\text{inn}} - \varepsilon_{\text{out}})}{\varepsilon_{\text{out}} + (\varepsilon_{\text{inn}} - \varepsilon_{\text{out}})L_{a,b}(1-\zeta)(1 + (\varepsilon_{\text{out}} - 1)L_{a,b}) + \zeta L_{a,b}\varepsilon_{\text{out}}(\varepsilon_{\text{inn}} - \varepsilon_{\text{out}})} \quad (5.40)$$

where ε_{inn} is the dielectric constant of the inner spheroid, ε_{out} is the dielectric constant of the outer spheroid, and ζ is the volumetric fraction of the inner spheroid. Here, the inner layer is considered to be snow (for which ε is found using the Maxwell-Garnett mixing formula with an air matrix and ice inclusions) and the outer layer is water. This approach is frequently used for melting hail and graupel for which meltwater accumulates on the surface. Other, more complex methods (e.g., those that use a weighted-average of the ε_e computed from various combinations of Maxwell-Garnett formulas; Meneghini and Liao 1996) also exist.

Previous modeling studies have employed a wide variety of approaches for calculating the ε_e of melting snow, and there is no well agreed-upon approach. Both Yokoyama and Tanaka (1984) and Hardaker et al. (1995) assumed a two-layer concentric sphere model consisting of an inner core of ice and air and an outer shell of water. Klaasen (1988) used the Maxwell-Garnett formula with air inclusions inside of a wet snow matrix consisting of ice inclusions in a water matrix, whereas D'Amico et al. (1998) assumed a water matrix and inclusions of ice and air. Russchenberg and Ligthart (1996) used the average ε_e from the previous two methods. Other studies have expressly studied the applicability of various mixing formulations. Fabry and Szyrmer (1999) found a

strong impact of the choice of which media is the matrix in the Maxwell-Garnett mixing formula, with a complex two-layer spheroid with each layer consisting of a three-component Maxwell-Garnett approach performing the best. Subsequently, Battaglia et al. (2003) found that the Maxwell-Garnett mixing formula using an air matrix and inclusions composed of a water matrix and ice inclusions performed best when compared to brightband observations.

All three aforementioned approaches for calculating the ε_e are included in the model, which can serve as an insightful tool for investigating the impacts of different mixing formulas. However, given its dominant effect in the resultant radar calculations, an appropriate choice for the calculation of the dielectric constant must be made for the remainder of this study. Figure 5.11 shows the resultant vertical profiles of Z using sixteen different mixing formulas. The Maxwell-Garnett mixing formulas (MG) are labeled in the form "Matrix | Inclusion" for both applications (i.e., "W | (I | A)" refers to a water matrix with inclusions composed of an ice matrix with air inclusions). The Polder-van Santern (PS) mixing formulas are labeled similarly, showing the two media that are combined first before being combined with the third. An f_{rim} of 1.0 was used as the differences due to the choice of ε_e are most dramatic for unrimed snow. For the sake of completeness, all twelve MG combinations are shown, although they are not all equally physically valid. For example, Mitra et al. (1990) showed that water melts at the tips of ice crystals and is then drawn into the inner core of the particle, making formulas that assume a dominant outer media of water less physically plausible.

It is immediately evident that the choice of ε_e can have a profound effect on both the shape and magnitude of the brightband signature in Z. As found in previous studies (e.g., Fabry and Szyrmer 1999), the formulations that consider water to be the matrix (or the outer shell, in the case of the two-layer spheroid) have a brightband that is much too strong, with a $\Delta Z = Z_{\text{max}} - Z_{\text{rain}}$ over 15 dBZ (and up to 20 dBZ for sensitivity tests with alternative PSDs). Using 600 h of vertically-pointing X-band radar data in stratiform

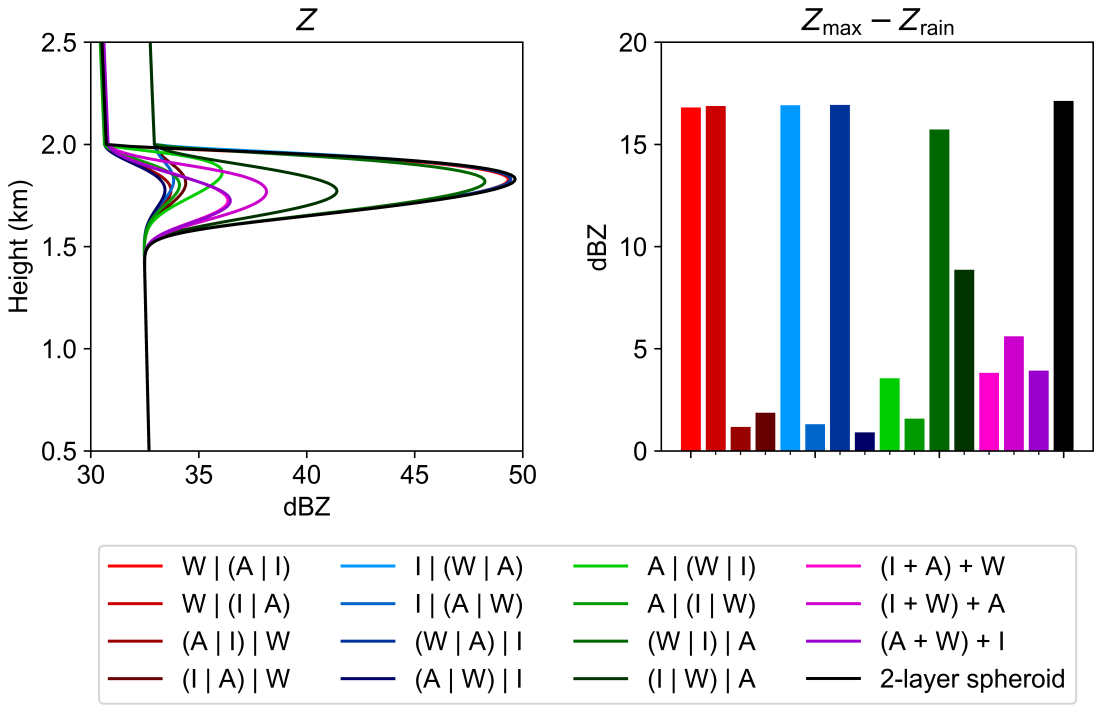

Figure 5.11: Comparison of (left) simulated vertical profiles of Z at S band and (right) the maximum brightband enhancement of Z using different mixing formulas for the dielectric constant of melting snow. 'MG' refers to the Maxwell-Garnett mixing formula (where the matrix and inclusions are specified in the form Matrix — Inclusion for both mixing calculations as explained in-text), 'PS' refers to the Polder-van Santen mixing formula, and '2-layer spheroid' refers to the two-layer spheroid calculation of Bohren and Huffman (1983). The environmental 0°C level is at 2 km.

precipitation, Fabry and Zawadzki (1995) found a mean ΔZ in the brightband that ranged from 8-10 dBZ for light to moderate precipitation. More recently, Trömel et al. (2017) found similar results using QVPs, reporting an average ΔZ of 7.7 dB. Many other mixing formula combinations, particularly those that use air as a matrix, have a ΔZ that is too small ($\approx$ 1-2 dBZ). In addition to the ΔZ within the brightband, Fabry and Zawadzki (1995) report that the maximum Z remains near the middle of the brightband at all precipitation intensities, which certain mixing formula combinations fail to reproduce

(e.g., A | (W | I)). All of the mixing formulas shown here make simplifying assumptions about the nature of scattering in a melting snowflake, and it is likely none of them perfectly represent the actual scattering of a melting particle. However, based on the above analysis of Z the Maxwell-Garnett mixing ratio using a combination of ice and water that is mixed with air ("MG: (I | W) | A") seems to perform the best, with the analogous Polder-van Santen mixing formula ("PS: (I + W) + A") performing second best with a weaker brightband than is typically observed. Although the magnitude of the Z (both in the brightband and outside it) is dependent on the chosen input PSD, the relative comparisons and conclusions of the various options for ε_e remain the same.

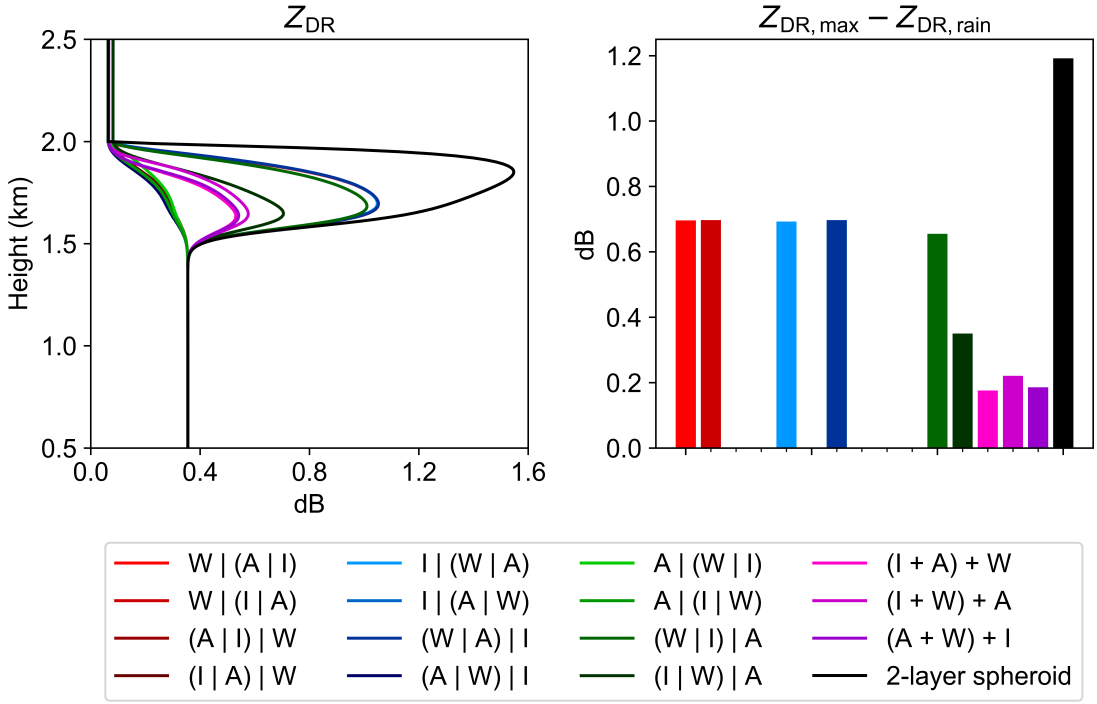

Figure 5.12: As in Figure 5.11, but for Z_{DR}.

In addition to Z and unlike previous studies, the impact of ε_e on the polarimetric variables can be examined to aid in the determination of an optimal ε_e. The vertical profiles of Z_{DR} using the various mixing formulas for ε_e are shown in Figure 5.12. There is typically (for snow that is not heavily rimed) a "bump"' in the Z_{DR} profile (e.g., Figure

5.8b) with a maximum near the bottom of the melting layer (e.g., Wolfensberger et al. (2016) show the maxima in Z_{DR} to be 200-300 m above the bottom of the melting layer on average) as large wet snowflakes collapse into raindrops. In contrast to this idea, many of the mixing formulas (primarily the ones that posit air as the matrix) instead show a monotonic increase in Z_{DR} and fail to reproduce this feature. As before, the two-layer spheroid mixing formula produces an increase in Z_{DR} that is larger than typically observed (more than 1.0 dB over that of rain). In addition, sensitivity tests of other distributions often produced a bimodal Z_{DR} field within the melting layer (not shown). All three Polder-van Santen mixing formulas produce almost equivalent results. There is some difficulty in using observations of Z_{DR} within the melting layer to validate the choice of mixing formula here due to the exclusion of aggregation, which should act to increase the magnitude of the Z_{DR} maxima. However, the optimal choices for calculating ε_e based on Z (i.e., "MG: (I | W) | A)" and "PS: (I + W) + A"') seem to also hold for Z_{DR}.

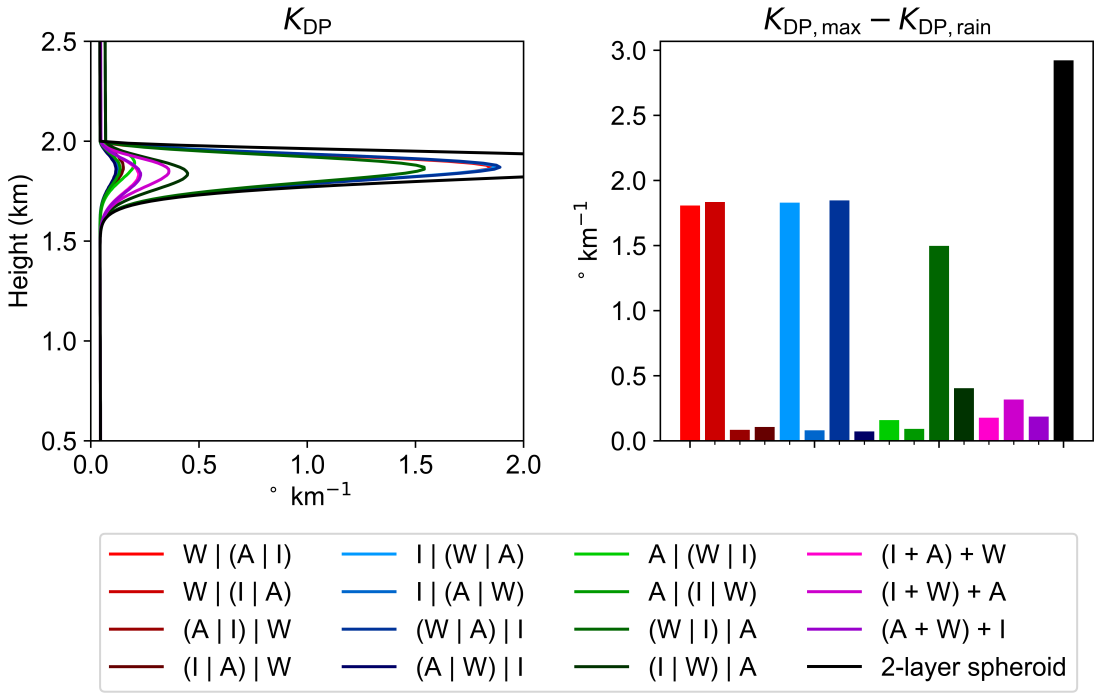

Figure 5.13: As in Figure 5.11, but for K_{DP}.

The validation of K_{DP} within the melting layer is a bit more challenging due to limited observations and the difficulty of estimating K_{DP} in the presence of possible δ within the melting layer. In addition, the range of sensitivity tests performed indicate that K_{DP} in the brightband is highly sensitive to the input PSD, which can vary widely between and within precipitation systems and in time. Wolfensberger et al. (2016) report a mean (standard deviation) peak K_{DP} of 0.11 (0.21) $^{\circ}$ km^{-1} associated with a mean (standard deviation) peak Z of 29.04 (7.97) dBZ using RHIs, with a wide range mean K_{DP} across the four sites examined. In contrast, Trömel et al. (2017) report a mean (standard deviation) peak K_{DP} of 0.60 (0.37) $^{\circ}$ km^{-1} associated with a mean (standard deviation) Z of 31.2 (5.7) dBZ using QVPs and the K_{DP} estimation methodology of Griffin et al. (2018). Both of these studies used X-band radars (λ = 3.2 cm). As K_{DP} is inversely proportional to λ in the Rayleigh regime, this translates to a range of equivalent K_{DP} at S-band of roughly 0.03 - 0.18 $^{\circ}$ km^{-1}. Considering the robustness of the K_{DP} estimation presented in Trömel et al. (2017), it is reasonable to expect K_{DP} values on the order of 0.05 - 0.2 $^{\circ}$ km^{-1} in moderate precipitation at S band. Indeed, the K_{DP} in Figure 5.8c peaks at 0.10 $^{\circ}$ km^{-1}. The variability in the vertical profiles of K_{DP} as a function of ε_e is shown in Figure 5.13. The increase in K_{DP} within the melting layer is large and spans two orders of magnitude. As with Z and Z_{DR}, the K_{DP} associated with mixing formulas that assume a water shell or water as the matrix are biased very high (even keeping in mind that the Z profiles suggest a more intense brightband being modeled here than in the previously cited studies). Many other mixing formulas have only very weak increases in K_{DP}. The preferred mixing formula ("MG: (I | W) | A)" has a peak K_{DP} of just over 0.4 $^{\circ}$ km^{-1}. Although this is larger than the *median* observations presented in the literature, it falls within the realm of reported melting layer K_{DP} and seems to be an appropriate value for the corresponding Z of this distribution. At X band, the peak Z and K_{DP} values for this modeled distribution are 40.7 dBZ and 1.47 $^{\circ}$

km^{-1}, which fall squarely in the right tail of both the Z and K_{DP} distributions reported in Trömel et al. (2017).

Based on all three of the aforementioned variables, the remainder of this work will employ the "MG: (I | W) | A" mixing formula unless otherwise noted.

5.2.3.2 Aspect ratio of snow

In contrast to rain, for which the aspect ratio is relatively well known, there is some uncertainty when it comes to characterizing the aspect ratio of snow and snow aggregates. Pristine ice particles can have large aspect ratios that result in high Z_{DR}. For example, aspect ratios of 0.1-0.3 are often assumed for pristine dendrites (e.g., Matrosov 2006), which can result in Z_{DR} values for dendrites up to 6 dB (Straka et al. 2000). Snow aggregates, on the other hand, tend to be closer to spherical. Many studies assume a constant aspect ratio across the size spectrum. Ryzhkov et al. (2011) suggest using 0.8, whereas other studies have begun to form a consensus of a mean aspect ratio for aggregates of approximately 0.6 (Korolev and Isaac 2003; Matrosov et al. 2005; Hogan et al. 2012; Garrett et al. 2015). The results of Garrett et al. (2015) also suggest a dependence on riming, with rimed snow (graupel) having a median aspect ratio of 0.70 (0.85). This notion is supported by Straka et al. (2000) and Ryzhkov et al. (2011), who assume an aspect ratio for graupel that linearly decreases from 1.0 to 0.8 for particles smaller than 10 mm and stays constant at 0.8 for larger particles. To approximate this relationship, an additional option for the aspect ratio of snow (r_s) as a function of f_{rim} has been included in the 1D-MS and is given by

$$r_s = 0.60 + 0.25 \left(\frac{f_{\mathrm{rim}} - 1}{4} \right). \tag{5.41}$$

Finally, the results of Brandes et al. (2007) suggest more spherical particles that become less oblate with size according to the (statistically insignificant) relation of

$$r_s = 0.8467 + 0.01714D, \tag{5.42}$$

where D is in mm, which has also been included as an option in the 1D-MS.

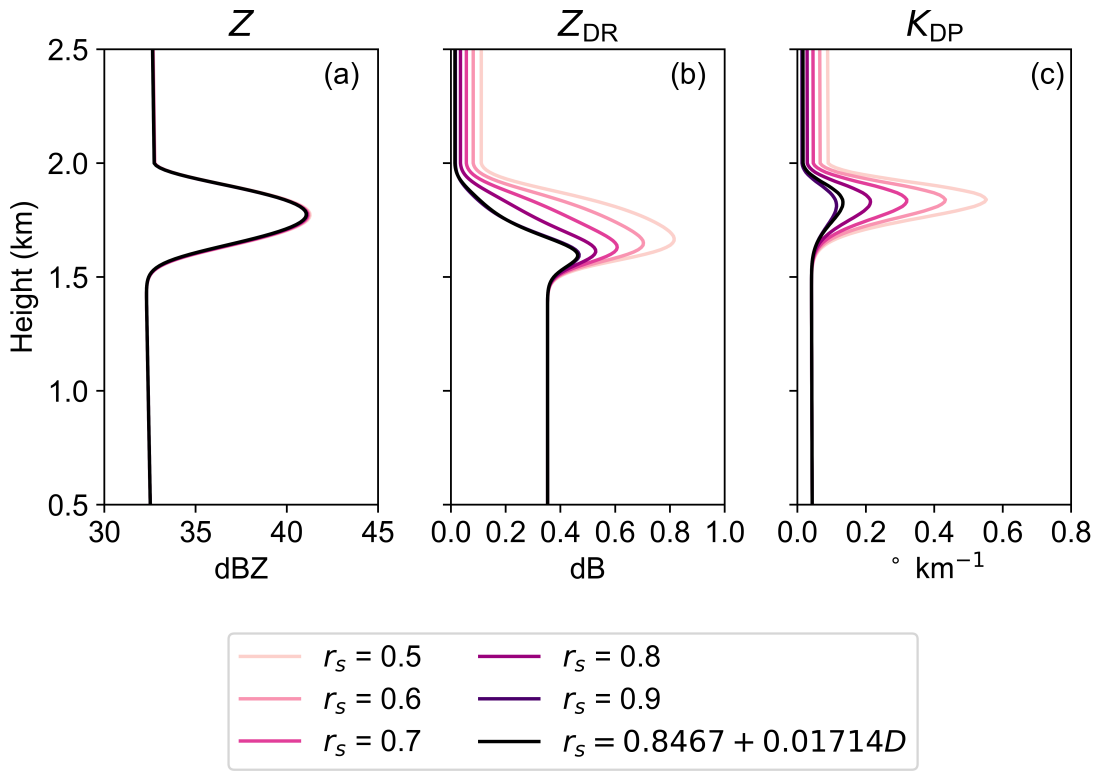

Figure 5.14: Comparison of vertical profiles of (a) Z, (b) Z_{DR}, and (c) K_{DP} for r_s values of 0.5, 0.6, 0.7, 0.8, 0.9 and as a function of size (Eq. 5.42).

Figure 5.14 shows the impact of varying r_s on the resultant profiles of Z, Z_{DR}, and K_{DP}. In this case, the f_{rim}-dependant r_s is not shown separately as unrimed snow is being modeled, resulting in an r_s of 0.6. There is essentially no impact on the resultant Z profile both above and within the melting layer (Fig. 5.14a). However, r_s can have noticeable impacts on the polarimetric variables, especially within the melting layer. With a decreasing aspect ratio, both Z_{DR} and K_{DP} increase both above and particularly within the melting layer (Fig. 5.14b,c). These impacts are particularly pronounced for K_{DP}, for which the maximum value increases by a factor of four for r_s of 0.9 to 0.5 (Fig. 5.14c). Because of the increasing consensus that r_s = 0.6 is a good approximation for the r_s of snow aggregates (Korolev and Isaac 2003; Matrosov et al. 2005; Hogan et al.

2012; Garrett et al. 2015), the reasonable vertical profiles of polarimetric radar variables it produces, and the conceptual understanding that the riming of particles should cause them to become more spherical, Eq. (5.41) will be used to calculate r_s in the remainder of this work unless otherwise indicated.

5.2.3.3 Riming factor

The degree of riming can have a large impact on the characteristics of the melting layer signature and the resultant profiles of radar variables. Riming results in smaller, denser particles that have faster terminal velocities than unrimed snow particles of equivalent mass. Because they fall faster, rimed particles take longer to melt and act to increase the depth of the brightband. Previous studies have found that riming should result in a weaker brightband signature (e.g., Fabry and Szyrmer 1999; Zawadzki et al. 2005; Vogel et al. 2015) and a decrease of Z aloft (Vogel et al. 2015). Vogel et al. (2015) also found based on observations that riming should also act to reduce the $Z_{\rm DR}$ of snow aloft and within the melting layer for cases of riming that do not result in the production of small ice crystals due to splintering during the riming process, with the opposite found for riming that results in splintering (e.g., Hallett and Mossop 1974).

Figure 5.15 shows the impact of riming on the polarimetric variables for both variable and constant r_s (the latter being shown to isolate the impacts of riming alone). In accordance with observations, increasing $f_{\rm rim}$ acts to deepen the melting layer and brightband in the 1D-MS, as well as decrease Z above the melting layer (Fig. 5.15a,b; e.g., Fabry and Szyrmer 1999; Zawadzki et al. 2005; Vogel et al. 2015). For Z and $K_{\rm DP}$, increasing $f_{\rm rim}$ results in a decreased brightband magnitude (Fig. 5.15a,b,e,f). Meanwhile, for $Z_{\rm DR}$, increasing $f_{\rm rim}$ with a constant $r_s = 0.6$ results in an increase in the magnitude of the brightband, in contrast with observations. (Fig. 5.15d). It is only when r_s varies with $f_{\rm rim}$ that a decrease in the brightband magnitude for $Z_{\rm DR}$ is seen

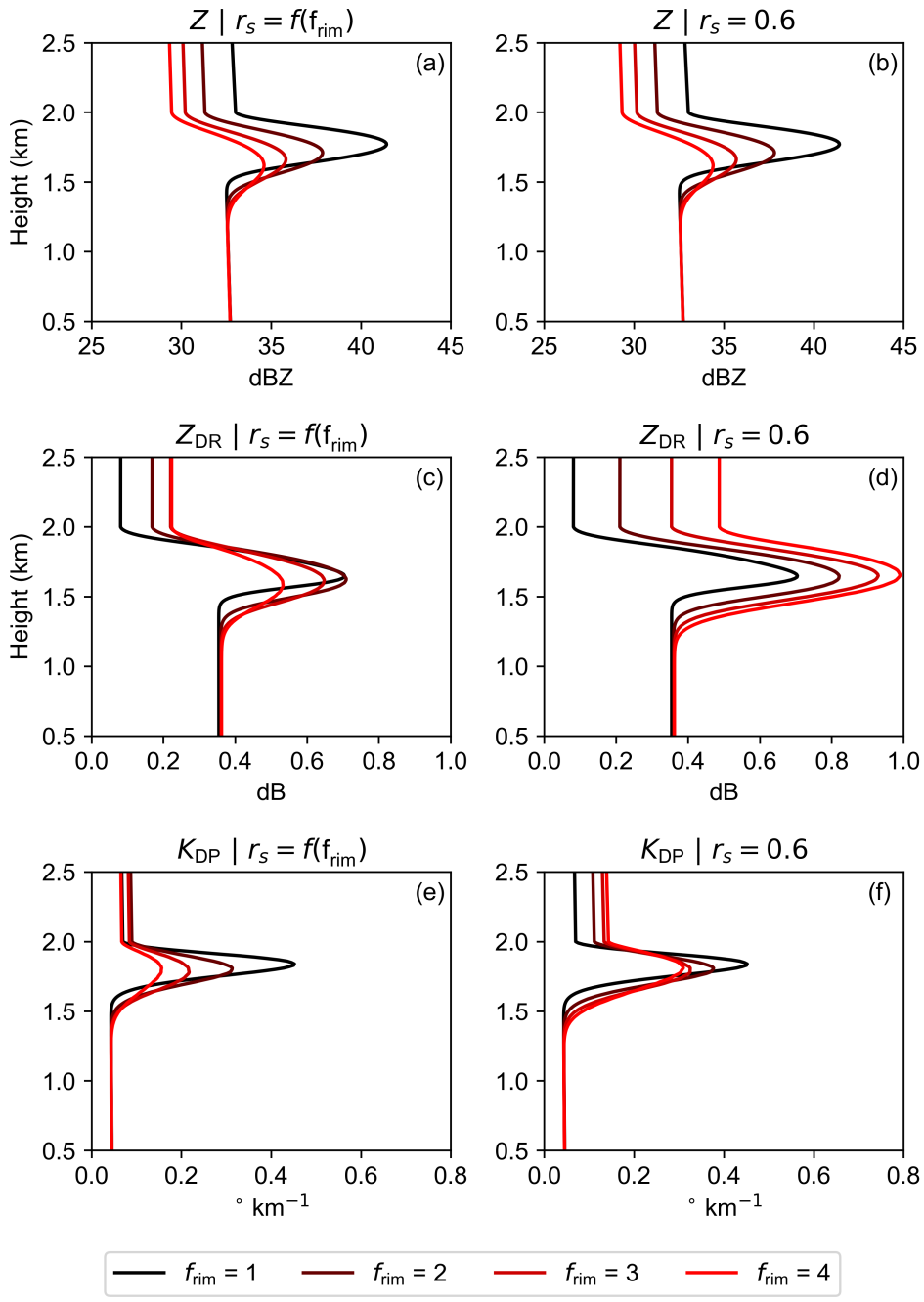

Figure 5.15: Comparison of vertical profiles of (a,b) Z, (c,d) Z_{DR}, and (e,f) K_{DP} using (a,c,e) r_s that varies according to Eq. (5.41) and (b,d,f) a constant r_s of 0.6 for f_{rim} ranging from 1 (unrimed snow) to 4 (heavily rimed snow).

(Fig. 5.15c). In addition, the variable r_s acts to accentuate the differences due to riming for K_{DP} in the melting layer (Fig. 5.15e).

Changes are also seen above the melting layer. With a constant r_s of 0.6, Z_{DR} and K_{DP} are enhanced aloft due to the increase in density, contrary to what is expected from observations (Fig. 5.15d,r). When r_s is allowed to vary with f_{rim}, the increase in K_{DP} above the melting layer is minimized (Fig. 5.15e), and the increase in Z_{DR} is reduced, although not completely negated (Fig. 5.15c). This provides further evidence that r_s should be allowed to vary with f_{rim}. The minute increase in Z, Z_{DR}, and K_{DP} below the melting layer with increasing f_{rim} is due to enhanced condensation onto melting ice particles, as the rimed particles fall further before completely melting and thus have a larger vapor density flux from the warm, saturated environment. This effect is more prominent for distributions with larger raindrops which remain colder than the environment for longer. Although not shown, the differences in Z, Z_{DR}, and K_{DP} due to ε_e shown in Figs. 5.11, 5.12, and 5.13 is reduced as f_{rim} increases.

In the absence of other information, f_{rim} will be assumed to be 1 (no riming) as a default unless otherwise indicated.

5.2.3.4 Canting angle distribution of snow

There is much uncertainty about the distribution of canting angles for snow. Generally, and in the polarimetric radar operator employed here (see section 3.2), hydrometeors are assumed to have a Gaussian canting angle distribution with a mean of 0° (i.e., no preferred canting angle) and a specified canting angle width, σ. Ryzhkov et al. (2011) assumed the canting angle width of snow, σ_s, to be 40°. However, recent particle imager observations by Garrett et al. (2015) indicate a much broader spectrum of canting angles, with a median canting angle of 39°. The authors suggest the canting angle distribution is a function of turbulence, with increasing median and mode canting angles for more

turbulent conditions. Interestingly, neither particle size nor degree of riming were found to have a strong impact on the canting angle distribution.

The impact of σ_s on the vertical profiles of radar variables is shown in Figure 5.16. The impact on Z is negligible (Fig. 5.16a), with small impacts on Z_{DR}, mostly affecting dry snow above the melting layer. The effects on K_{DP} are more prominent, both for dry snow and within the melting layer (Fig. 5.16c). However, the difference in brightband K_{DP} between σ_s of 20° and 50° is only 0.17 ° km^{-1}. Given the large degree of variability and uncertainty of σ_s and its comparatively small impact on the resultant radar variables, 30° seems like a reasonable approximation and will be used for the remainder of this work.

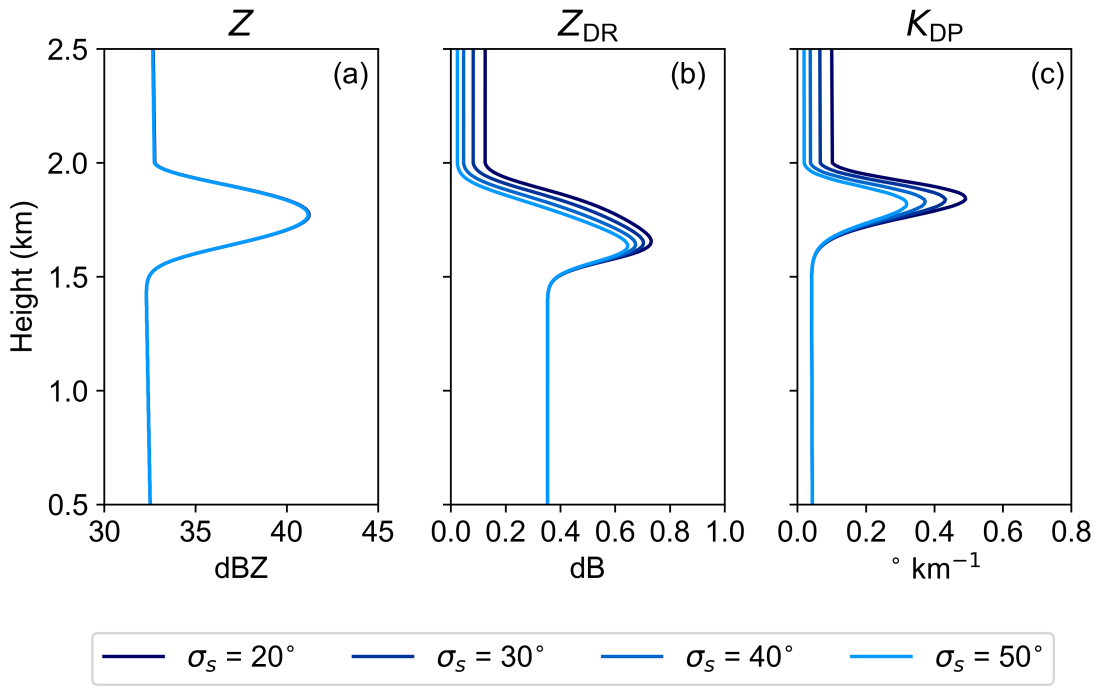

Figure 5.16: Comparison of vertical profiles of (a) Z, (b) Z_{DR}, and (c) K_{DP} for σ_s values of 20°, 30°, 40°, and 50°.

5.2.3.5 Impact of neglecting aggregation and breakup

There is lingering uncertainty about the nature of and frequency of aggregation and breakup processes within the melting layer. A number of studies have found that the size distributions of snow and rain indicate a correspondance of one snowflake above the melting layer to one raindrop below the melting layer (e.g., Ohtake 1969; Barthazy et al. 1998). Ohtake (1969) suggested this to be proof of the absence of breakup processes within the melting layer. Additionally, the wind tunnel observations presented in Mitra et al. (1990) did not typically show spontaneous breakup of melting particles. Szyrmer and Zawadzki (1999) argue in favor of this conclusion and state that, for the typical brightband, aggregation and breakup likely due not play appreciable roles (or are balanced by each other, which they deem unlikely) in causing the observed brightband. However, it is also well known that aggregation and breakup play important roles in determining the snow size distribution above the melting layer (Lo and Passarelli Jr. 1982). In contast to the studies that discount the role of aggregation and breakup within the melting layer, Barthazy et al. (1998) suggested aggregation occurs in the top of the melting layer with counteracting breakup in the bottom due to the largest aggregates being found in the middle of the brightband near its peak, as opposed to at the top of the melting layer as would be the case in the absence of aggregation. More directly, numerous studies have observed aggregation within the top portion of the melting layer with *in situ* PSD data (Stewart et al. 1984; Willis and Heymsfield 1989; Heymsfield et al. 2002; McFarquhar et al. 2007; Heymsfield et al. 2015), with Willis and Heymsfield (1989) attributing the depth of the brightband to the survival of a few very large aggregates well below the 0°C level. These observations make sense intuitively given the wetness of snowflakes and the range of terminal velocities and particle sizes present in the upper region of the melting level, all of which are understood to be favorable for effective snowflake aggregation.

Aggregation and breakup are excluded from the 1D-MS as it is nontrivial to model these stochastic processes. The collision efficiency of melting particles is not known with certainty, and it is unclear how to reconcile whether aggregation or breakup occurs upon particle collisions. In addition, it is not clear that aggregation processes are consistent across cases and environments. Past studies have often relied on simple parameterizations to qualitatively model the effects of aggregation. For example, Willis and Heymsfield (1989) applied a linearized growth term to approximate particle growth due to aggregation while neglecting breakup and the loss of smaller particles; Trömel et al. (2014) included a parameterization for the accretion of small, completely melted raindrops by larger snowflakes to study the impacts on δ of redistributing water from small particles to large, wet aggregates. Unfortunately, although the bulk of latent heating in the melting layer is due to the melting of small particles, Z and Z_{DR} within the brightband may be sensitive to the presence of large aggregates, which can fall outside the Rayleigh scattering regime, even at S band. Fabry and Zawadzki (1995) estimate the impact of aggregation on Z to be less than 2 dB, but to the author's knowledge no systematic study exists examining the impact of neglecting aggregation on Z_{DR} and K_{DP}. In addition, the depth of the melting layer can be extended due to the presence of large aggregates falling further distances before melting completely. Although the 1D-MS is able to reliably reproduce the general characteristics of the melting layer, it should be kept in mind that the quantitative results shown are potentially subject to some unknown error due to these exclusions and thus should be understood qualitatively. Future work should address the inclusion of aggregation and breakup into the 1D-MS.

5.2.3.6 Comparison against observations

Now that the model sensitivity to non-environmental parameters has been explored, it is worth comparing the model results to observations to evaluate its performance. There is a fairly large degree of subjectivity in doing so, as the model results are quite sensitive to

the environmental profile of temperature and humidity as well as the input PSD, which is typically unknown. As a case study, the model is evaluated against the mean QVP shown in Figure 5.8, which was taken in the stratiform portion of a mature mesoscale convective system and covers the period of a particularly intense brightband. A more detailed discussion of the range of observed PSD parameters at and above the melting layer and environmental conditions within the stratiform portion of MCSs is provided in section 5.2.4.2. In agreement with the PSD and environmental observations presented in McFarquhar et al. (2007), a gamma distribution was employed with $N_{0,s}$ = 800 m^{-3} mm$^{-(1+\mu_s)}$, Λ_s = 0.40 mm^{-1}, and μ_s = -1.6, with a $D_{\max}$ of 1.0 cm. The Γ was set to 6.0 °C km^{-1} with a RH lapse rate of 3% °C^{-1}. Radar variables were calculated using the T-matrix scattering calculations at S band. The 0°C level was assumed to be at 3.7 km based on the mean observed QVP profile and the 1200 UTC 20 May 2011 soundings from Norman, Oklahoma and Dodge City, Kansas.

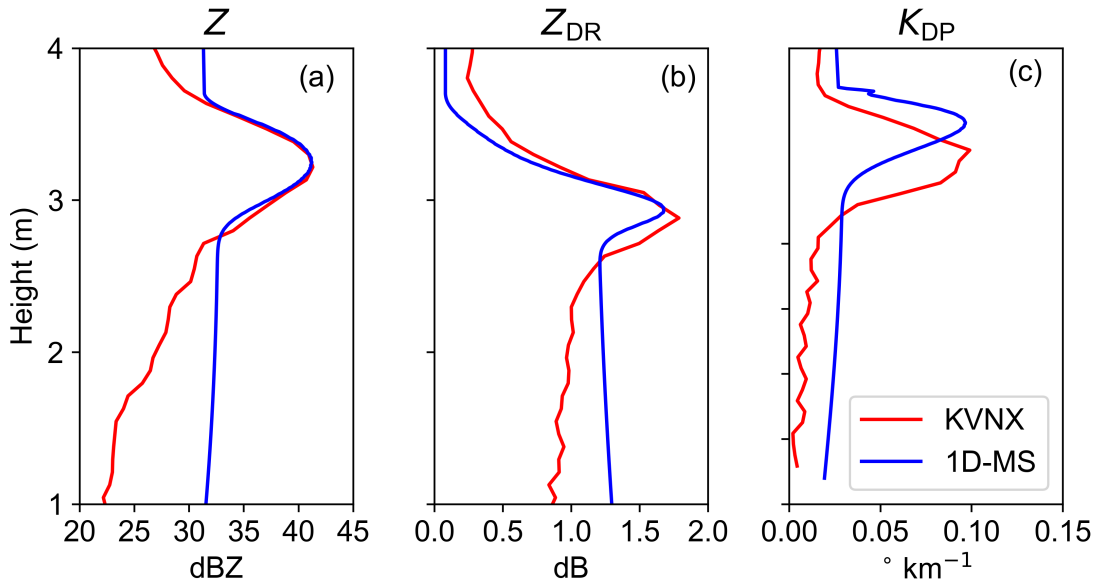

Figure 5.17: Comparison of vertical profiles of (a) Z, (b) Z_{DR}, and (c) K_{DP} from the 1D-MS (blue) and the QVP from the Vance Air Force Base WSR-88D (KVNX) radar averaged between 10:14:51 UTC and 11:15:33 UTC on 20 May 2011 (red).

The results of the comparison are shown in Figure 5.17. Overall, there is good agreement between the 1D-MS and the observations given the number of unknowns. The Z brightband matches the observed quite well (Fig. 5.17a). The Z_{DR} brightband maximum is slightly underpredicted and at a slightly higher altitude than the observed maximum (Fig. 5.17b), and the K_{DP} brightband correctly matches the magnitude although the maximym is displaced $\approx$ 300 m above the actual maximym (Fig. 5.17c). Sensitivity tests (not shown) showed the height of the K_{DP} maxima to be sensitive to μ_s. The depth of the brightband is slightly underpredicted, which along with the Z_{DR} maxima could be a consequence of the exclusion of aggregation or the unknown degree of riming. The difference in Z above the 0°C level (Fig. 5.17a) is due to ongoing aggregation in the observations, whereas the prescribed PSD in the 1D-MS is representative of the 0°C level after said aggregation has taken place. The most prominent differences are below the melting layer, where all three variables are biased high compared to the observations. These differences are consistent with the exclusion of breakup in the 1D-MS, which should act to decrease Z and Z_{DR} and, to a lesser extent, K_{DP}. The results shown here provide confidence that the 1D-MS is able to realistically model the melting layer.

5.2.4 Polarimetric thermodynamic retrievals

5.2.4.1 Impacts of the thermodynamic environment

Before investigating the retrieval of latent heating rates from within the melting layer, it is worthwhile to examine how the *environment* can influence the resultant brightband characteristics. To do this, the 1D-MS was used in its "top-down" mode with the same PSD described in section 5.2.3 applied to a wide variety of environments. The RH was assumed to be constant through the model depth and ranged from 50% to 100% in increments of 2%, and Γ ranged from 3° km^{-1} to 9.8° km^{-1} in increments of 0.2 °C km^{-1} for a total of 910 runs. These runs were performed both for f_{rim} = 1.0 and f_{rim} = 4.0 to get a sense of how these environmental impacts vary due to riming. The 0°C level

was located at 3.0 km. All other parameters remained the same as described in Table 5.2. Although the Γ and the RH profile may not necessarily be independent in nature, they are considered independent here as a theoretical investigation of the full parameter space. As in previous sections, the qualitative conclusions remained the same for other examined input PSDs (not shown).

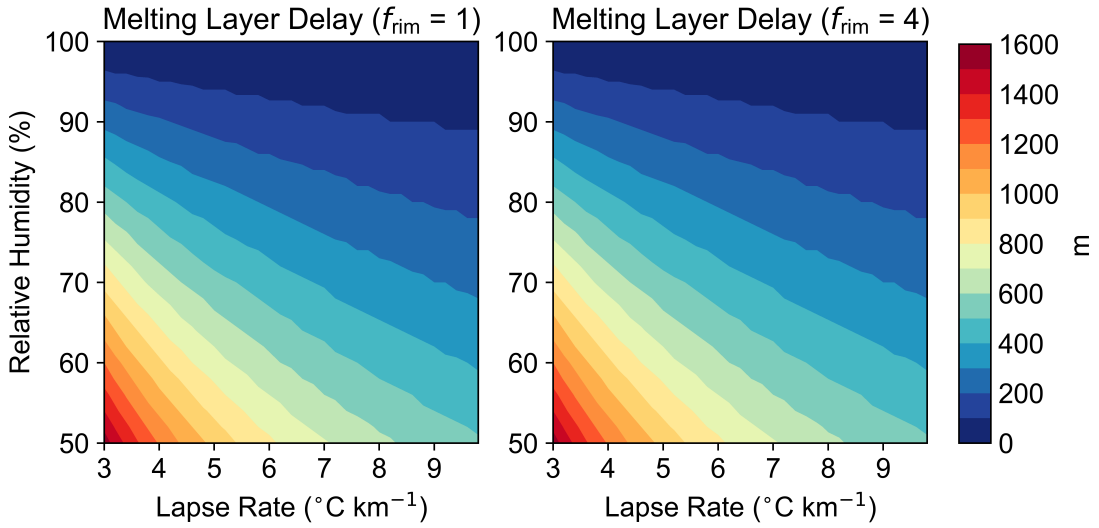

Figure 5.18: Comparison of the height below the 0°C level at which melting begins (m) for lapse rates ranging from 3 ° km^{-1} to 9.8 ° km^{-1} and relative humidities ranging from 50% to 100% for (left) f_{rim} = 1 and (right) f_{rim} = 4.

Figure 5.18 shows the height below the 0°C level at which melting begins. This distance is the same for both $f_{rim} = 1.0$ and $f_{rim} = 4.0$ because the height at which melting begins depends solely on when T_p reaches 0°C, which was assumed to be in equilibrium with the environment for snow and thus only a function of the environmental T and RH. However, that the assumption of a particle's temperature remaining in equilibrium with the environment is less likely to be valid as its fall velocities increases, as occurs with riming. As expected, melting is delayed for drier environments and environments with small lapse rates, with the impact of RH enhanced for environments with smaller lapse rates. For near saturated environments (e.g., RH $\geq$ 95%), melting occurs within

the first 100 m below the environmental 0°C level. With an RH of only 70%, however, melting can be delayed by ≈ 300 m for lapse rates near the dry adiabatic lapse rate to over 800 m for lapse rates of 3°C km^{-1}. This delay in melting reaches almost 1500 m for a lapse of 3°C km^{-1} and an RH of just 50%. Thus, consistent with theory and past observations and modeling studies (e.g., Matsuo and Sasyo 1981; Rasmussen and Pruppacher 1982; Heymsfield et al. 2015), subsaturated environments can substantially displace the location of the brightband with respect to the 0°C level, the degree to which depends upon the environmental lapse rate.

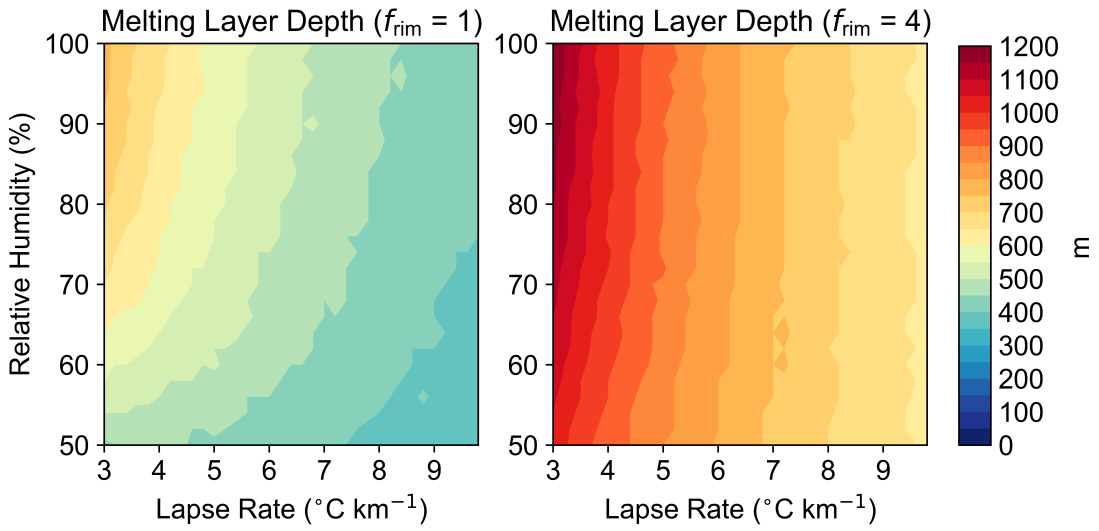

Figure 5.19: As in Figure 5.18, but for melting layer depth (m).

The depth of the melting layer as a function of the environmental Γ and RH is shown in Figure 5.19. The melting layer is defined here to be the layer where melting has begun but ice is still present. For both f_{rim} = 1.0 and f_{rim} = 4.0, the depth of the melting layer increases as lapse rates decrease due to decreased sensible heat flux and slower melting. For a given thermodynamic environment, the depth of the melting layer is also larger by nearly a factor of two for f_{rim} = 4.0 than f_{rim} = 1.0 due to faster particle fallspeeds. Because of this, the brightband can be ≈ 1.2 km deep for very small lapse rates and heavily rimed particles. Counterintuitively, the environmental RH has little effect on

the melting layer depth except for very dry environments and smaller values of Γ, with effects lessened for more heavily rimed particles. This is due to two reasons: drier environments suppress the height at which melting begins, which results in melting occurring in a layer of warmer temperatures that offsets the impact of the decreased RH, and drier environments result in sublimation above the melting layer which acts to decrease the amount of ice and thus the time needed for complete melting. Heavier rimed particles fall more quickly than unrimed particles and thus are less affected by local RH at any one height. Note that the RH was assumed to be constant through the model depth to emphasize the impact of the environmental conditions, when in actuality the environment is often saturated at the 0°C level with an RH profile that decreases toward the ground (e.g., McFarquhar et al. 2007). In cases of a strong decrease in RH toward the ground, the latter type of environment could result in minimal suppression of the height at which melting begins but a more pronounced impact on the melting rate within the melting layer than demonstrated here.

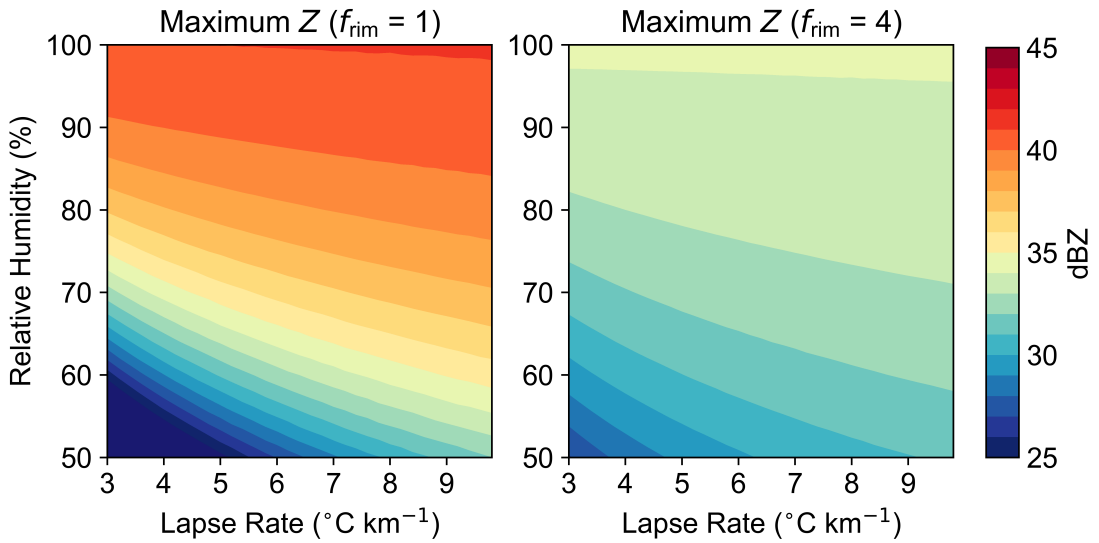

Figure 5.20: As in Figure 5.18, but for the maximum Z (dBZ) within the brightband.

The environment can also strongly impact the radar observables within the brightband. Figure 5.20 shows the maximum Z within the brightband. As with the depth at

which melting begins below the 0°C level, the maximum Z is also strongly affected by the environmental RH but less so by the lapse rate. The strong influence of the environmental RH on the maximum Z is due to the sublimation of ice above the melting occurs that occurs in dry environments and results in smaller and fewer particles within the melting layer. Conversely, the lesser impact of Γ on the maximum Z in the brightband stems from Z being dominated by the largest particles in the volume, whose ε_e increases appreciably as soon as they are wet regardless of Γ. As in Figure 5.15a,b, the maximum Z in the brightband is larger for unrimed particles than heavily rimed ones due to their slower terminal velocity and larger size. This enhanced terminal velocity for rimed particles also limits the amount of sublimation that occurs in dry environments above the melting layer and thus results in a decreased sensitivity to environmental RH for heavily rimed particles compared to unrimed ones.

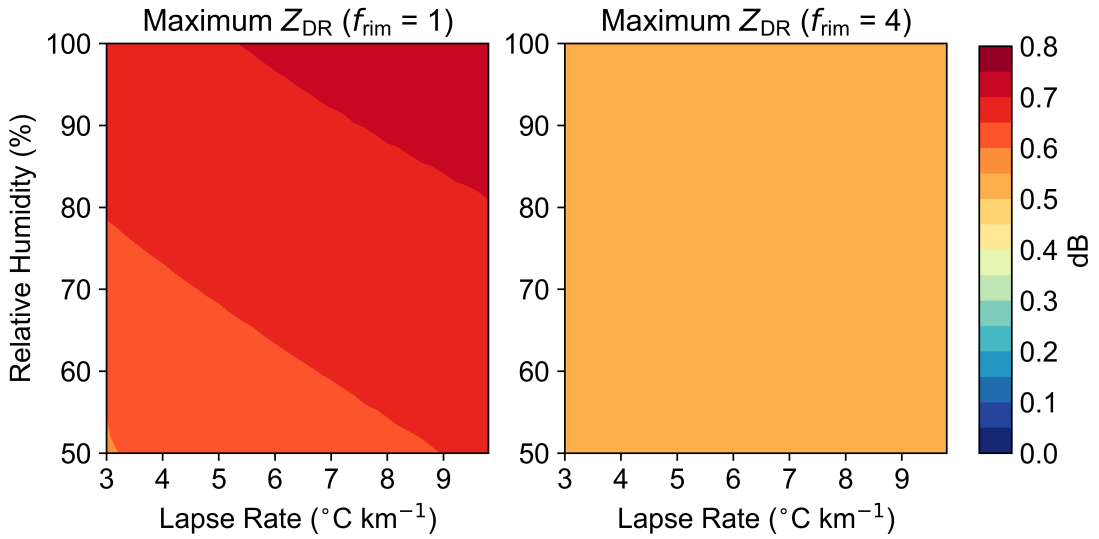

Figure 5.21: As in Figure 5.18, but for the maximum Z_{DR} (dB) within the brightband.

In contrast with Z, the maximum Z_{DR} within the brightband (Fig. 5.21) is mostly insensitive to the environment. This is partly a consequence of the assumption within the model of a constant r_s across the size spectrum and not changing r_s in the presence of sublimation, as well as fixing D_{max} at a constant value. As also shown in Figure 5.15c,d,

the maximum Z_{DR} is smaller for heavily rimed particles than unrimed ones. There is a slight decrease in the maximum Z_{DR} for unrimed particles in drier environments and smaller Γ due to the sublimation of smaller, denser particles, which leaves less dense particles with slightly smaller inherent Z_{DR}. Overall, however, subject to the above model assumptions, the decrease in maximum Z_{DR} across the range of environments shown only amounts to ≈ 0.1 dB.

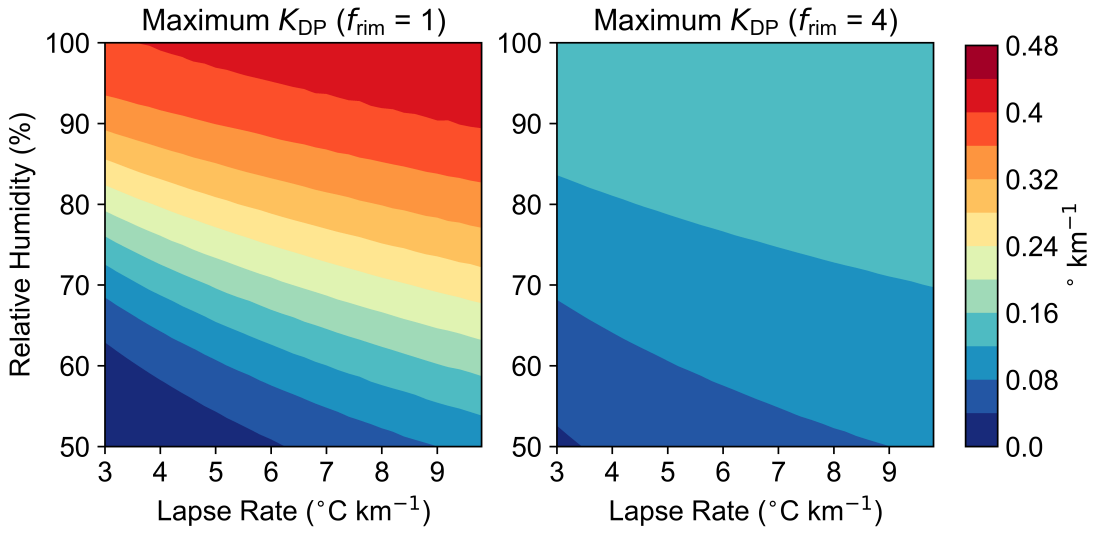

Figure 5.22: As in Figure 5.18, but for the maximum K_{DP} (° km^{-1}) within the brightband.

Figure 5.22 shows the maximum K_{DP} within the brightband. The sensitivity is reminiscent of that of the maximum Z, with less sensitivity for heavier rimed particles and decreasing values of K_{DP} for drier environments with smaller lapse rates due to enhanced sublimation above the melting layer and increased evaporation within it, which decreases the amount of liquid water and thus significantly impacts the K_{DP} maximum.

Finally, Figure 5.23 shows the sensitivity of the maximum cooling rate (where the "maximum cooling rate" refers to the minimum $\partial T/\partial t$) within the melting layer. As with the polarimetric radar variables, both the magnitude and the sensitivity of the environment of the maximum cooling is decreased with increasing f_{rim} due to faster terminal

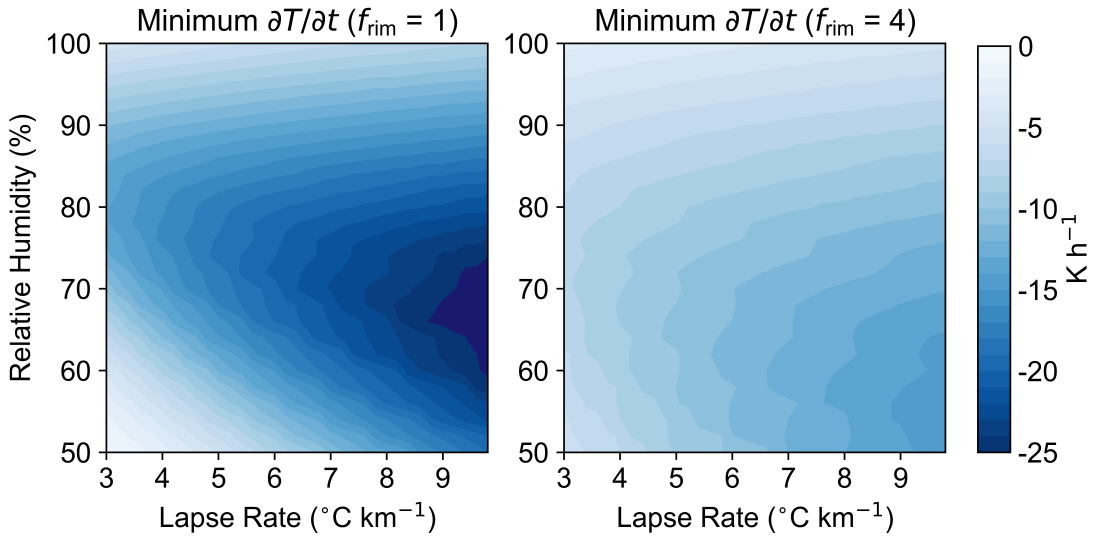

Figure 5.23: As in Figure 5.18, but for the maximum cooling rate (K h^{-1}) within the brightband.

velocities and a larger depth over which the melting is distributed (e.g., Fig. 5.19), peaking at -26.4 K h^{-1} for f_{rim} = 1.0 and only -14.9 K h^{-1} for f_{rim} = 4.0. However, unlike the maximum Z and K_{DP}, which decrease with decreasing RH and, to a lesser extent, increase with increasing Γ, the maximum cooling rate increases for both decreasing RH and increasing Γ. For a given RH with a larger Γ, the environment is warmer at a given depth below the melting layer and has a larger sensible heat flux, which results in more melting in a given layer and thus more cooling. However, as the RH decreases, the cooling due to evaporation increases significantly, which acts to decrease K_{DP} and Z but contributes significantly to the cooling rate within the melting layer. As with the other radar variables, the maximum cooling rate begins to decrease for very dry environments with smaller lapse rates due to sublimation above the brightband, which decreases the mass of particles undergoing melting within the melting layer and instead leads to significant cooling above it, which is not reflected in Figure 5.23 which focuses only on the melting layer. The axis of maximum cooling exists from an RH of 78% for Γ = 3.0 C°

km^{-1} to an RH of 64% for Γ = 9.8 C$^{\circ}$ km^{-1} for f_{rim} = 1.0, and from an RH of 70% for Γ = 3.0 C$^{\circ}$ km^{-1} to an RH of 52% for Γ = 9.8 C$^{\circ}$ km^{-1} for f_{rim} = 4.0.

5.2.4.2 Relation between the polarimetric brightband and the cooling rate

To investigate the connection between the polarimetric radar variables and the latent heating rate, an approach analogous to that used in section 4.2 was used to sample a full, realistic parameter space for the input PSDs. Studies have employed both inverse-exponential distributions (e.g., Lo and Passarelli Jr. 1982; Woods et al. 2008) and gamma distributions (e.g., Heymsfield et al. 2002; McFarquhar et al. 2007; Neumann 2016) to model observed snow PSDs. For this study, gamma distributions are used to describe the snow PSD in the 1D-MS in its "top-down" mode due to the increased variability in the PSD it allows for and the volume and fidelity of the datasets used in the aforementioned studies that suggest gamma distributions are appropriate.

In an effort to use realistic distributions, studies with *in situ* observations of snow PSDs near the melting layer were consulted as parameters of ice PSDs can vary appreciably by climate regime and the height and position within the cloud. A large number of relations between PSD parameters have been proposed and are summarized in Patade et al. (2015). Special consideration was given to the observations from the Midlatitude Continential Convective Clouds Experiment (MC3E; Neumann 2016) and the Bow Echo and Mesoscale Convective Vortex Experiment (BAMEX; McFarquhar et al. 2007), which used gamma distributions and focused on the PSDs above the melting layer in the stratiform portion of MCSs.

The parameter that is most agreed upon across observation datasets is the slope parameter, Λ_s, which tends to increase toward the melting layer due to aggregation. There is relatively good agreement about the range of Λ_s near the melting layer, which ranged from $\approx$ 0.2 mm^{-1} to 0.8 mm^{-1} in the MC3E observations and from $\approx$ 0.2 mm^{-1} to 1.5 mm^{-1} in the BAMEX observations. Numerous other studies from a wide variety of field

campaigns support Λ_s falling in the range of 0.2 mm^{-1} to 1.5 mm^{-1} in this region (e.g., Heymsfield et al. 2002, 2013, 2015; Patade et al. 2015; Neumann 2016; Matrosov and Heymsfield 2017). Thus, in this study, Λ_s is varied from 0.2 mm^{-1} to 1.5 mm^{-1} in increments of 0.05 mm^{-1}. However, one consideration that must be taken into account is how the particle diameter is defined when calculating these values of Λ_s. The particle bin sizes in the 1D-MS are given in equivolume diameter (D), whereas many of these studies (e.g., Heymsfield et al. 2002; McFarquhar et al. 2007; Heymsfield et al. 2013; Patade et al. 2015) use the maximum particle diameter (D^*), which will always be larger than equivolume diameter for oblate particles. Thus, the values of Λ_s used when defining the PSD in the 1D-MS need to be adjusted to take this fact into consideration. Without this adjustment, the concentration of particles will be overestimated across the PSD. Because r_s is assumed to be constant at 0.6 across the PSD, each size bin is decreased by a constant factor, given by

$$D^*(0.6)^{\frac{1}{3}} = D \tag{5.43}$$

to conserve mass between particle size definitions. As such, it can be shown that the equivalent Λ_s for use with bins of equivolume diameter in the 1D-MS is equal to $(0.6)^{-\frac{1}{3}}\Lambda_s$ and ranges from $\approx$ 0.25 mm^{-1} to 1.8 mm^{-1}.

Defining the intercept parameter $N_{0,s}$ and the shape parameter, μ_s, is less clear, particularly so for $N_{0,s}$ given its range of many orders of magnitude in the observations. There is also a large degree of variability between cases and campaigns, with the $N_{0,s}$ values reported for MC3E being typically 1-2 orders of magnitude smaller than those observed during BAMEX. However, the intercept parameter, $N_{0,s}$ and the shape parameter, μ_s, are not necessarily independent of Λ_s, which can aid in constraining the parameter space (e.g., Heymsfield et al. 2002; McFarquhar et al. 2007; Heymsfield et al. 2013; Patade et al. 2015). McFarquhar et al. (2007) provides derived relations between these parameters, given by

$$\mu_s = 0.93\Lambda_s^{0.314} - 3.05 \tag{5.44}$$

and

$$\log_{10} N_{0,s} = -4.14 \exp\left(-0.082 \Lambda_s\right) \tag{5.45}$$

where Λ_s is in cm^{-1} and $N_{0,s}$ is in cm$^{-(4+\mu_s)}$. Rather than varying μ_s and $N_{0,s}$ linearly and independently of each other and Λ_s, Eqs. (5.44) and (5.45) are used here to draw a sample of $N_{0,s}$ and μ_s values dependent on Λ_s. In this way, both the constraining relations between the parameters presented by McFarquhar et al. (2007) are preserved while still allowing for a large degree of internal variability and the generation of outliers. For each value of Λ_s, a "mean" μ_s is found using Eq. (5.44). Then, 10 samples are randomly selected assuming a Gaussian distribution centered on the mean μ_s with a σ_μ of 0.2. This σ_μ was roughly determined from the data presented in Fig. 19 of McFarquhar et al. (2007) (reproduced in Fig. 5.25 for reference). Similarly, a mean $N_{0,s}$ was determined from Eq. (5.45), with 10 samples randomly selected from an assumed Gaussian distribution (in logarithmic-space) assuming a $\sigma_{N_{0,s}}$ of 0.2, similarly determined from the data presented in Fig. 18 of McFarquhar et al. (2007) (reproduced in Fig. 5.26 for reference). However, the conversion from units of cm$^{-(4+\mu_s)}$ in Eq. (5.45) to units of m^{-3} mm$^{-(1+\mu_s)}$ compatible with the units used in the 1D-MS is μ_s-dependant. In this way, every $N_{0,s}$ drawn from the distribution is converted to units of m^{-3} mm$^{-(1+\mu_s)}$ using all ten sampled μ_s values. This results in a total of 2700 distributions being sampled across the range of parameters shown here.

Histograms of the resultant Λ_s, μ_s, and $N_{0,s}$ distributions for one realization are shown in Figure 5.24. The distribution of Λ_s (using the original values associated with D_{max} and used to retrieve $N_{0,s}$ and μ_s, not those used in the 1D-MS) is flat between 0.2 and 1.5 mm^{-1} as the values increase linearly in increments of 0.05 mm^{-1}. The μ_s distribution forms a Gaussian distribution with a mean (median) of -1.27 (-1.26) and ranges from -2.0 to -0.5, in agreement with the ranges shown in both the MC3E and BAMEX observations. The distribution of $\log_{10} N_{0,s}$ is a somewhat-skewed Gaussian distribution, with a mean (median) of 4.11 (4.15) and ranges from $\approx$ 2.5 to 5.0, spanning

the range reported for both MC3E ($O(2)$ - $O(3)$ m^{-3} $mm^{-(1+\mu_s)}$) and for BAMEX ($O(3)$-$O(4)$ m^{-3} $mm^{-(1+\mu_s)}$). Thus, the range of PSDs sampled here covers those that have typically observed in the stratiform region of MCSs.

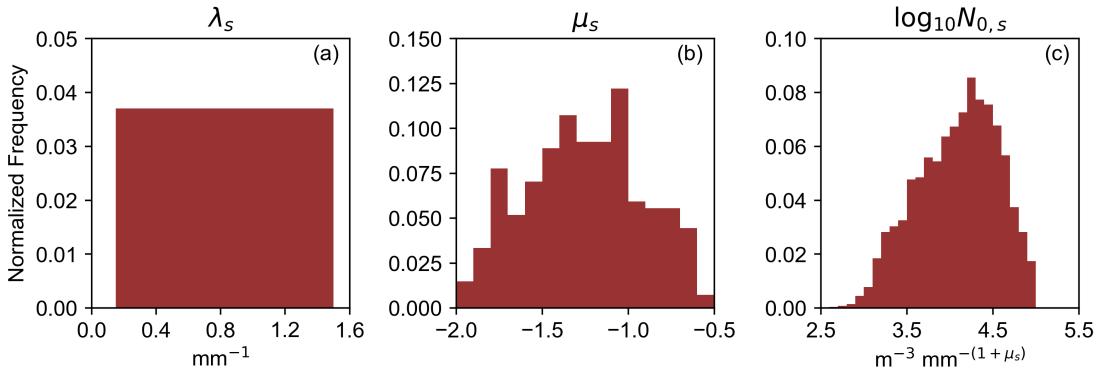

Figure 5.24: Normalized histograms for (a) Λ_s, (b) μ_s, and (c) $\log_{10} N_{0,s}$ for one realization of PSD parameters.

To further validate the range of parameters used and the use of Gaussian sampling around a mean to derive it, Figure 5.25 compares the sampled parameter space of μ_s versus Λ_s from the 1D-MS to the parameter space observed in McFarquhar et al. (2007). There is good agreement between the two, with perhaps a slight underdispersion of the μ_s in the 1D-MS parameters, primarily for larger values of Λ_s. Good agreement is also seen between the sampled $N_{0,s}$ and the values reported in McFarquhar et al. (2007) (Fig. 5.26). Note that the units for the McFarquhar et al. (2007) data shown in Figure 5.26 should be $cm^{-(4+\mu_s)}$ and match those used for the 1D-MS data. These comparisons provide confidence that the sampling routine employed in the 1D-MS is performing well in sampling the observed range of parameters reported from *in situ* observations.

Earlier *in situ* studies of PSDs may have unknowingly been contaminated by particle shattering, which would act to artifically increase the number of small crystals observed (Field et al. 2003; Heymsfield 2007). However, the values of $N_{0,s}$ reported in McFarquhar et al. (2007), which ranged from 10^{-4} to 10^{-1} $cm^{-(4+\mu_s)}$, have been corroborated by more recent studies that have taken explicit measures to combat this possible shattering

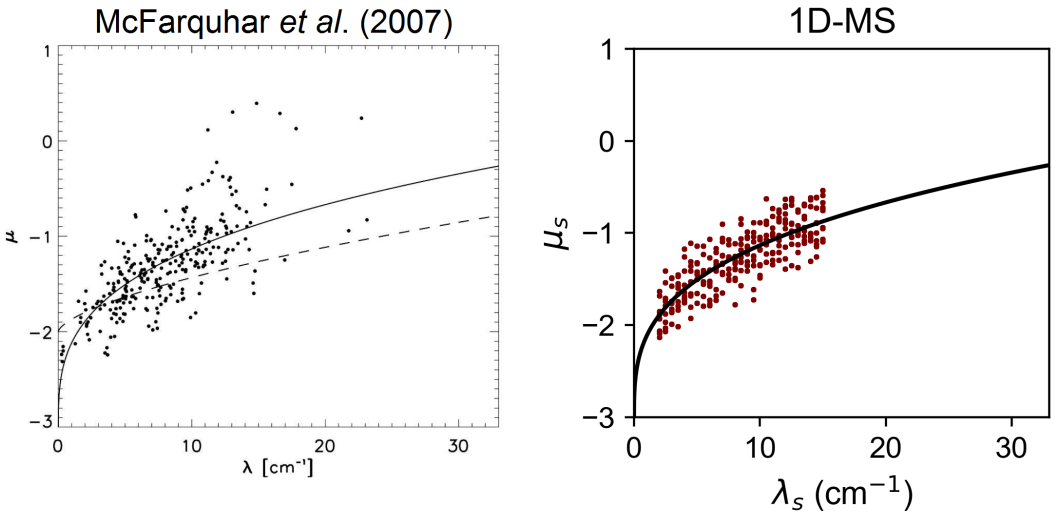

Figure 5.25: Comparison of the $\Lambda_s - \mu_s$ parameter space from (left) the observations reported in McFarquhar et al. (2007) (their Fig. 19) and (right) the Gaussian sampling procedure employed in the 1D-MS. Λ_s from the 1D-MS is shown in units of cm^{-1} for consistency.

effect. For example, Patade et al. (2015) report a range of 10^{-4} to 10^{-1} $cm^{-(4+\mu_s)}$ in the region above the melting layer, and Neumann (2016) report values of 10^{-5} to 10^{-2} $cm^{-(4+\mu_s)}$ for smaller Λ_s values, which is consistent with the data presented in McFarquhar et al. (2007)). The shape parameter μ_s could also be affected by this shattering effect, which could promote superexponential PSDs and thus negative values of μ_s. However, similar to $N_{0,s}$, the negative values of μ_s reported in McFarquhar et al. (2007) have been corroborated by other recent studies, all of which have indicated values of μ_s between $\approx$ -2.0 and 0.0 for larger Z and regions near the melting layer with smaller values of Λ_s (Heymsfield et al. 2013; Patade et al. 2015; Neumann 2016; Matrosov and Heymsfield 2017).

The final parameter that must be defined is the diameter of the largest particle in the PSD, $D_{\max}$. A consensus exists that $D_{\max}$ is inversely related to Λ_s, with larger $D_{\max}$ for smaller values of Λ_s. This is consistent with the effects of aggregation, which broadens

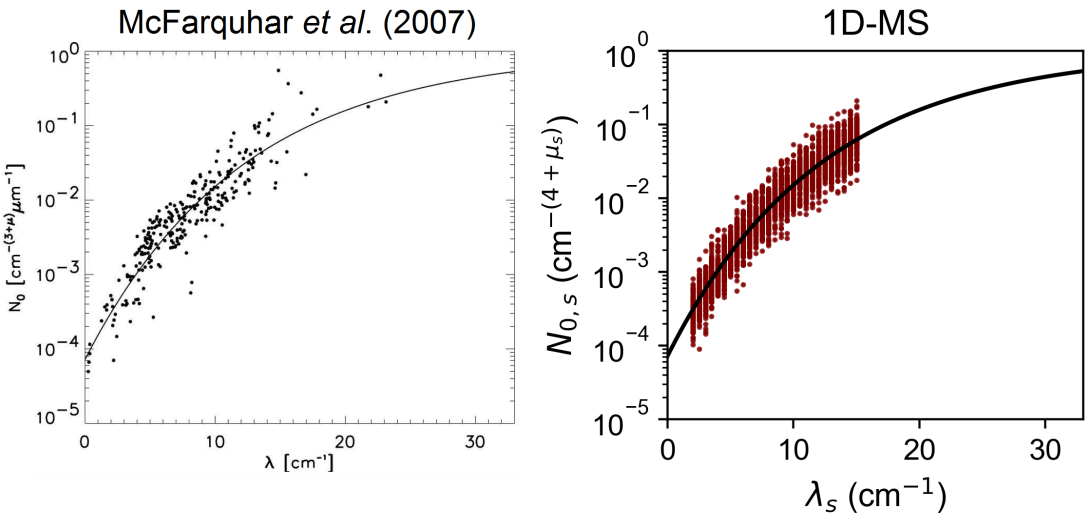

Figure 5.26: As in Figure 5.25, but for the $\Lambda_s - N_{0,s}$ parameter space. Note that the units for the McFarquhar et al. (2007) data shown in Figure 5.26 (their Fig. 18) should be cm$^{-(4+\mu_s)}$ and match those used for the 1D-MS data. Λ_s from the 1D-MS is shown in units of cm^{-1} for consistency.

the size distribution and increases the maximum particle size at the expense of smaller particles, decreasing the Λ_s. In this study, the $D_{\max} - \Lambda_s$ relation from Heymsfield et al. (2013) is used and is given by

$$D_{\max} = (0.6)^{\frac{1}{3}} 4.36 \Lambda_s^{-0.77} \tag{5.46}$$

where $D_{\max}$ and Λ_s are in cm and cm^{-1}, respectively. The factor of $(0.6)^{\frac{1}{3}}$ is again used to convert the resultant $D_{\max}$ to equivolume diameter for the 1D-MS, as the relation was developed for particles using D^*. The modeled distributions were for unrimed snow (f_{rim} = 1.0), and all radar calculations were performed at S band. Unfortunately, due to computational expense, the Rayleigh scattering approximation had to be used. As such, $D_{\max}$ was capped at 10.0 mm (corresponding to Λ_s values below 0.55 mm^{-1}) in an effort to stay within the Rayleigh scattering regime and avoid errors due to resonant scattering of the largest particles. This introduces an error compared to what would occur in nature. For the smallest Λ_s of 0.2 mm^{-1}, Eq. (5.46) indicates a $D_{\max}$ of $\approx$ 2.0 cm (corresponding

to an equivolume D_{max} of $\approx$ 1.7 cm). This is at the upper range of what has been observed (e.g., Heymsfield et al. 2013), with other studies reporting typical D_{max} values of 1.5-1.6 cm. Because only the smallest Λ_s values are impacted by this assumption, the impact of these assumptions is likely to be relatively confined. Sensitivity tests for a few sample distributions (not shown) suggest this impact are comparitively small in the face of the overall uncertainties and range of parameters in the 1D-MS. Still, it is instructive to examine the theoretical worst case scenario of the assumptions of Rayleigh scattering and an equivolume D_{max} capped at 10 mm for Λ_s = 0.2 mm^{-1} with an actual equivolume D_{max} of 17 mm. Other details about the PSD parameters and environment are included in the caption of Figure 5.27.

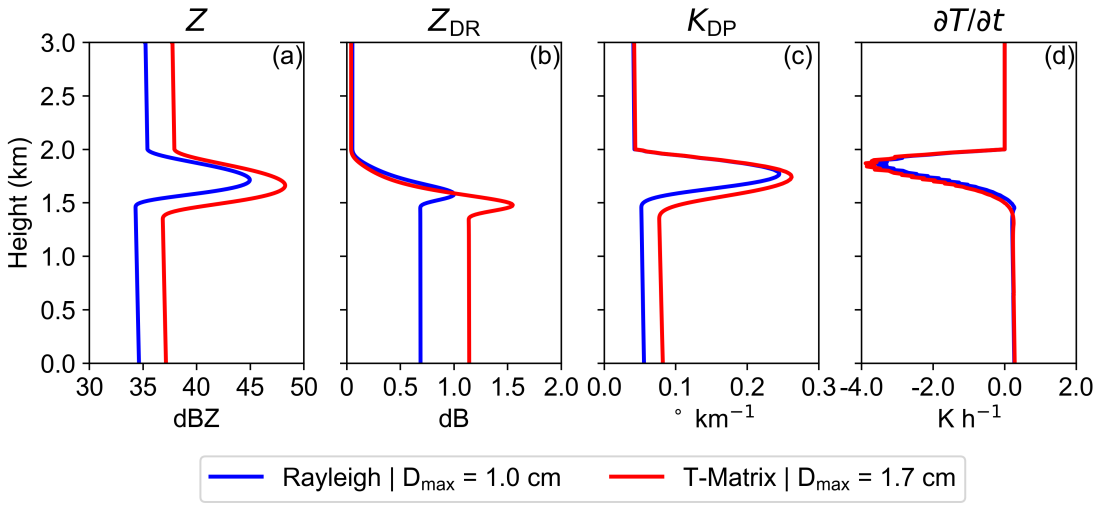

Figure 5.27: Comparison of the vertical profiles of (a) Z, (b) Z_{DR}, (c) K_{DP}, and (d) $\partial T/\partial t$ for an PSD described by $N_{0,s}$ = 2000 m^{-3} mm$^{-(1+\mu_s)}$, μ_s = -1.7, and Λ_s = 0.2 mm^{-1} with (blue) Rayleigh scattering and an assumed equivolume D_{max} of 1.0 cm and (red) T-matrix scattering calculations and an assumed equivolume D_{max} of 1.7 cm. A Γ = 6.0 °C km^{-1} and 100% RH were assumed with the 0°C level at 2.0 km.

Figure 5.27 shows the result of this comparison. The Z is underestimated at all heights by $\approx$ 3 dBZ when using Rayleigh scattering and the smaller D_{max} (Fig. 5.27a). The most severe differences are for Z_{DR}, for which the maximum value in the brightband

is underestimated by 0.54 dB and the resultant values in rain are decreased by 40% (Fig. 5.27b). This is compounded by the existing uncertainty in the calculated Z_{DR} values that results from neglecting aggregation occurring within the melting layer. The profile of K_{DP} is much less affected, with similar maximum values in the brightband and a slight underestimation in rain (Fig. 5.27c) due to being a lower moment of the PSD and concentration-dependent. Finally, the vertical profile of latent heating (Fig. 5.27d) is hardly affected by the assumption of a smaller D_{max}, as most of the cooling in the melting layer is due to smaller particles. The melting layer is also deeper by $\approx$ 100 m due to the largest snowflakes taking longer to melt.

In addition to varying the input PSDs, both the Γ and environmental RH were also varied as the resultant brightband signature can be quite sensitive to the environment (see section 5.2.4.1). As discussed in section 5.2.3.6, McFarquhar et al. (2007) report a mean Γ of $\approx$ 6.0 °C km^{-1} and a mean profile of RH that decreases at a rate of 3% °C^{-1} below the environmental 0°C level (denoted by "∇RH = 3.0" hereafter). However, a range of Γ and RH profiles were reported, with RH lapse rates of up to 4.5% °C^{-1} observed. To incorporate the effects of the environment on the thermodynamic retrieval efficacy, the full range of simulations were performed for Γ values ranging from 3.0 °C km^{-1} to 7.0 °C km^{-1} in increments of 1 °C km^{-1} and for RH lapse rates of 0.0% °C^{-1} to 4.5% °C^{-1} in increments of 1.5% °C^{-1}, resulting in a 54 000 total simulations being considered. The range of PSD parameters, lapse rates, and RH profiles used is summarized in Table 5.3. For the following analysis, the same set of parameters (those shown in Fig. 5.24) were used with each environment to keep the input PSDs consistent. However, a separate set of runs were also performed in which every environment used its own sampling of 2700 distributions, and the conclusions remained the same (not shown), providing confidence that the random sampling procedure is not introducing biases or appreciable sampling error into the analyses.

Table 5.3: Summary of the snow PSD parameters and range of environmental conditions used in the 1D-MS. The units shown here are consistent within the table but differ from those actually used in the 1D-MS and as described in-text. The ε in the values for μ_s and $N_{0,s}$ represent some offset from the mean determined randomly by drawing from a Gaussian distribution centered on the mean value with the specified standard deviation.

Parameter	*Value*	*Units*	*Increment*	*Standard Deviation*
Λ_s	2 - 15	cm^{-1}	0.05	—
μ_s	$0.93\Lambda_s^{0.314}$ - 3.05 + ε		—	0.2
$\log_{10} N_{0,s}$	$-4.14\exp(-0.082\Lambda_s) + \varepsilon$	$cm^{-(4+\mu_s)}$	—	0.2
$D_{\max}$	$\min\left[(0.6)^{\frac{1}{3}} 4.36\Lambda_s^{-0.77}, 1.0\right]$	cm	—	—
Γ	3.0 - 7.0	$°C\ km^{-1}$	1.0	—
RH	0.0 - 4.5	$\%°C^{-1}$	1.5	—

Figure 5.28 shows the normalized distribution of maximum cooling rates in the melting layer from two environments: Γ = 3.0 °C km^{-1} with ∇RH = 0.0 % $°C^{-1}$ and Γ = 7.0 °C km^{-1} with ∇RH = 4.5 % $°C^{-1}$. These represent the environments that should result in the smallest and largest cooling rates, respectively. Both distributions are lognormal distributions with longer right tails and median cooling rates of 4.2 K h^{-1} (interquartile range: 2.8 to 6.5 K h^{-1}) and 9.2 K h^{-1} (interquartile range: 6.0 to 14.3 K h^{-1}), respectively. However, the distribution in the warmer, drier environment is both shifted and notably broader than the distribution in the colder, moister environment, resulting from the variable impacts of drier air across the PSD and the impact of L_v being large for particles in the melting layer that still have relatively slow terminal velocities (i.e., the distribution translates rightward in log-space). Although *in situ* data of cooling rates within the melting layer are somewhat lacking, with most studies focusing primarily on the depth of the isothermal layers caused by latent cooling instead, these values are

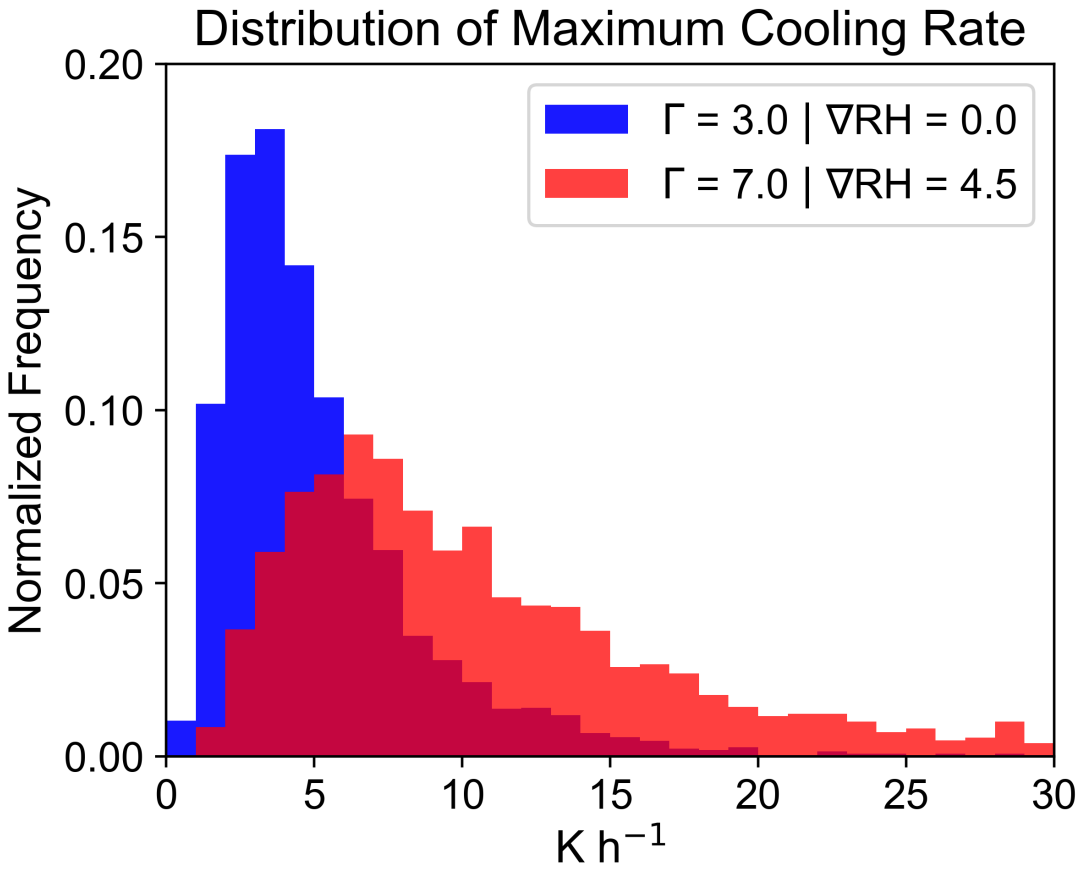

Figure 5.28: Normalized histogram of the maximum cooling rates (K h^{-1}) in the melting layer of the sampled distributions for (blue) Γ = 3.0 °C km^{-1} and ∇RH = 0.0 % $°C^{-1}$ and (red) Γ = 7.0 °C km^{-1} and ∇RH = 4.5 % $°C^{-1}$. The dark red area shows the overlap between the distributions.

within the range of cooling rates reported in the literature (e.g., Willis and Heymsfield 1989; Szyrmer and Zawadzki 1999; Grim et al. 2009; Thériault et al. 2012).

To investigate the relationship between the polarimteric variables in the brightband the cooling rate, the maximum values of each are compared for the array of environments examined using scatterplots. Only Γ = 3.0, 5.0, and 7.0 °C km^{-1} are shown for brevity. The shading is a kernel density estimate intended for visual guidance of the bulk behavior of the data with respect to the environment. Ordinary least squares linear

regressions were performed for each of the environments and variables examined. To combat the pronounced heteroscedasticity of the data (i.e., unequal variance across the range of the data), the linear regressions were performed in logarithmic space for both the radar variables and the cooling rate ($\equiv -\partial T/\partial t$), and are plotted as such. However, the regression equations shown in each subplot have been transformed to linear space for conciseness and to be consistent with linear units of the root mean square error of the retrieved cooling rate. Given the amount of subjectivity in sampling the parameter space for the PSDs, the linear regressions are meant to be used qualitatively.

Figure 5.29 shows the maximum Z versus the maximum cooling rate in the brightband. As shown in previous results, both increasing Γ and particularly increasing ∇RH (defined so that drying occurs downward) results in an increase in cooling rates (seen as a slight overall shift upward in the kernel density shading from Fig. 5.29a to 5.29l). It is evident that the maximum Z is not well-correlated with the maximum cooling rate, with spread of an order of magnitude in the cooling rates for a given value of Z and r^2 values of only ≈ 0.05. In addition, RMSE values are large and range from ≈ 3.5 to 8.5 K h^{-1}, increasing with increasing Γ and ∇RH. In any environment, the bulk of the cooling is due to tiny particles, whereas Z in the Rayleigh regime is a strong function of the largest particles within the volume that do not contribute much to the cooling rate. The actual variability in Z may be even larger than shown due to the decision to cap $D_{\max}$ at 10 mm and the exclusion of aggregation, which could further enhance Z while having little effect on the cooling rate.

Another brightband parameter often considered is the ΔZ, or the difference between the maximum Z in the brightband and the Z at the top of the brightband. The results of comparing ΔZ to the maximum cooling rate are shown in Figure 5.30. In addition to the upward shift in the kernel density field as Γ and ∇RH increase, there is a slight leftward shift with increasing ∇RH as ΔZ decreases due to evaporation. Overall, the maximum cooling rate tends to decrease with increasing ΔZ, though as with $Z_{\max}$ there

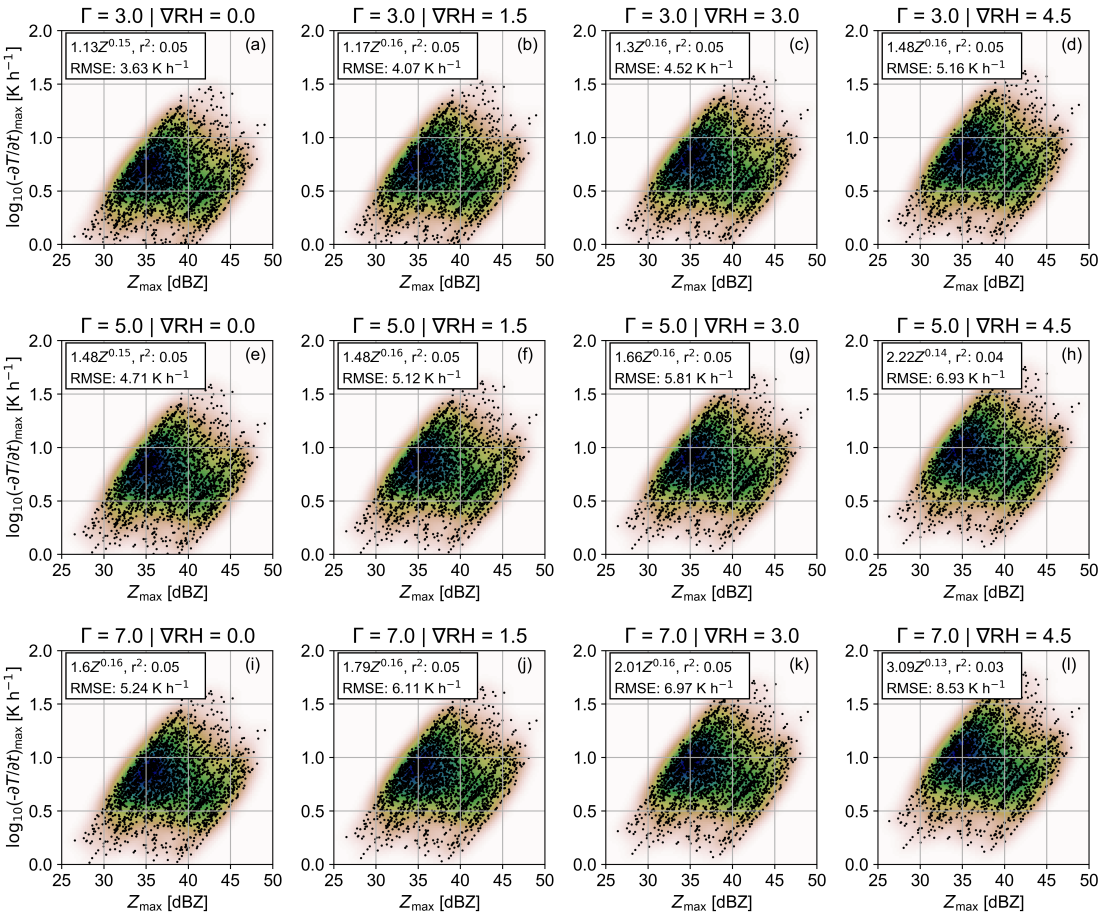

Figure 5.29: Comparison of the maximum Z versus maximum cooling rate in the bright-band for (top row) Γ = 3.0 °C km^{-1}, (middle row) Γ = 5.0 °C km^{-1}, and Γ = 7.0 °C km^{-1} and gradients of RH (∇RH, in units of % °C^{-1} and decreasing downward) ranging from (leftmost column) 0.0 to (rightmost column) 4.5 % °C^{-1} for all 2700 simulations summarized in Table 5.3. The shading indicates a kernel density estimate for visual guidance. The linear regression equation (where Z is in mm^6 m^{-3} and -$\partial T/\partial t$ is in K h^{-1}), r^2, and root mean square error ("RMSE"; in K h^{-1}) are shown for each subplot.

is spread of an order of magnitude in the maximum cooling rate for a given value of ΔZ. Subsequently, RMSE values remain high and similar to those for $Z_{\max}$, and r^2 values are slightly improved but still remain below ≈ 0.25. This counterintuitive result of an inverse relation between ΔZ and the maximum cooling rate likely stems from the fact

that the largest cooling rates result from snow PSDs with many small crystals, which generally have larger values of Λ_s and $N_{0,s}$ and thus smaller $D_{\max}$, which results in smaller values of $Z_{\max}$ and ΔZ. Conversely, distributions that result in large values of ΔZ typically have larger $D_{\max}$ and smaller values of Λ_s and fewer small crystals. Thus, predicted on the general relationships inherent in our selection of PSD parameters from McFarquhar et al. (2007), neither $Z_{\max}$ nor ΔZ may contain much information about the maximum cooling rate within the melting layer.

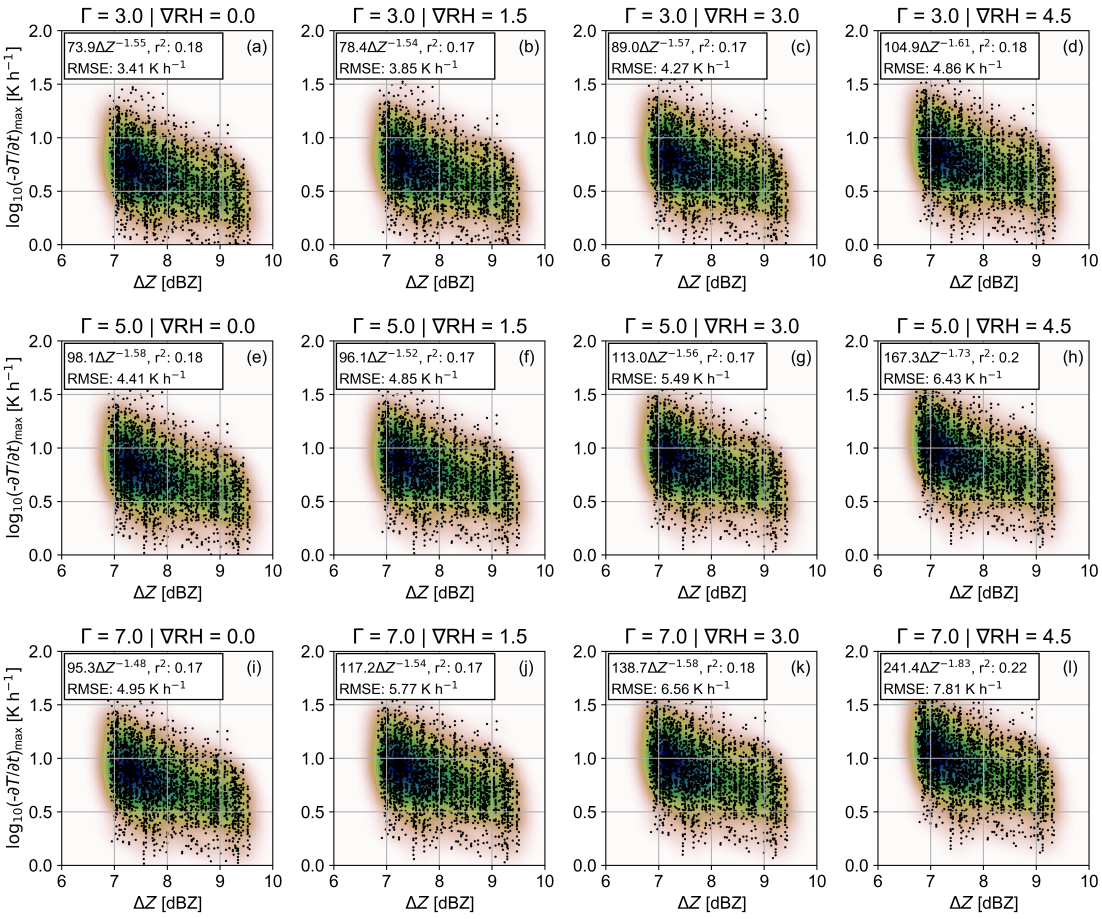

Figure 5.30: As in Fig. 5.29, but for the maximum ΔZ in the brightband (defined as $Z_{\max} - Z_{\text{top}}$).

Figure 5.31 compares the maximum Z_{DR} and cooling rate in the brightband. Almost no functional relationship exists between the two. As noted earlier, the $Z_{\text{DR,max}}$ in nature

may be strongly affected by aggregation, the $D_{\max}$, and non-Rayleigh scattering. However, Z_{DR} is unaffected by concentration and, like Z, is related to the largest particles in the volume that are not responsible for the bulk of the cooling. Thus, as with $Z_{\max}$ and ΔZ, r^2 remains low and RMSE remains high, and it is not expected that $Z_{\mathrm{DR,max}}$ alone can provide appreciable information about the cooling rate within the melting layer. Like the other variables examined, the kernel density shading shifts upward for increasing Γ and ∇RH and slightly to the left for increasing ∇RH.

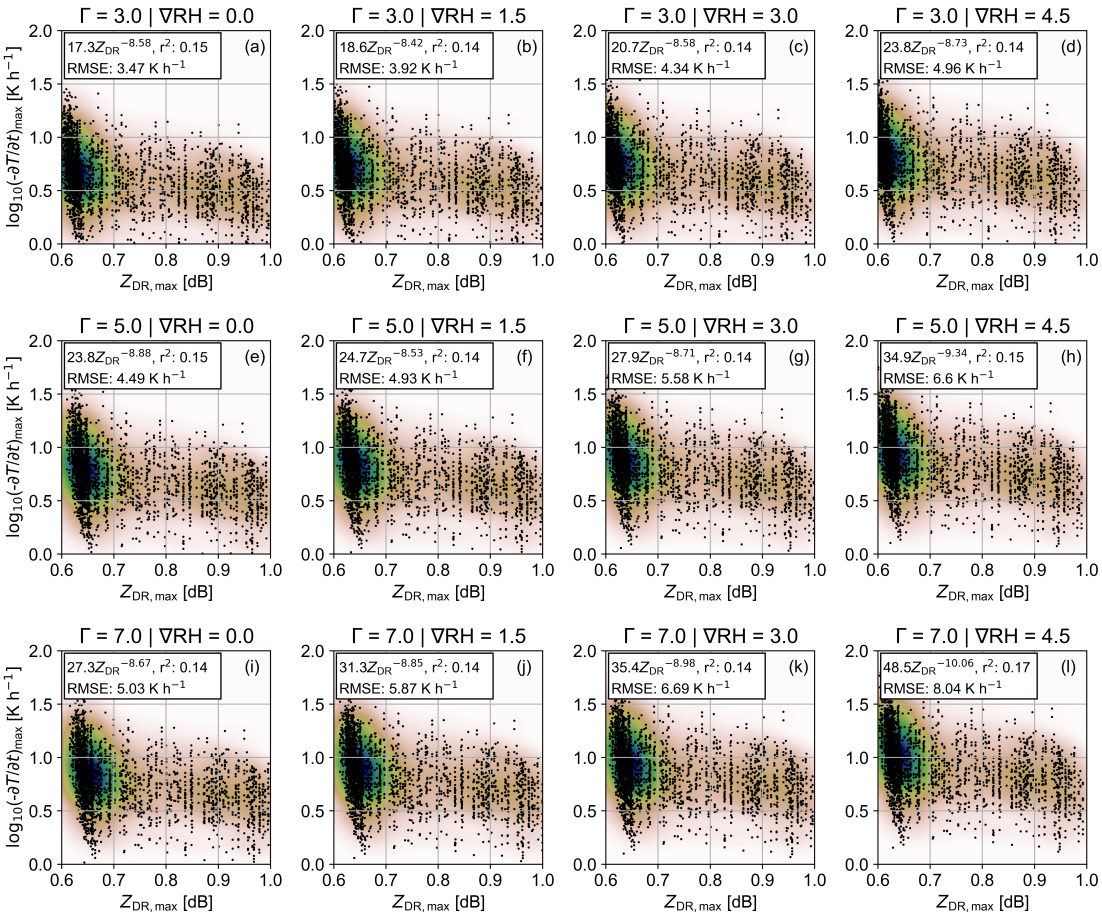

Figure 5.31: As in Fig. 5.29, but for the maximum Z_{DR} in the brightband.

Finally, Figure 5.32 shows the maximum K_{DP} in the brightband versus the maximum cooling rate. In contrast to Z, ΔZ, and Z_{DR}, there is a striking linear relation between $K_{\mathrm{DP,max}}$ and the maximum cooling rate, with r^2 values near 1.0 (note: the r^2 values

equal to 1.0 in Fig. 5.32 are due to rounding). The resultant RMSE values are an order of magnitude smaller than those from Z_{max}, ΔZ, and $Z_{DR,max}$ and remain below ≈ 0.6 K h^{-1}. The impact of the environment on the relation between $K_{DP,max}$ and the maximum cooling rate is also straightforward. For all environments, the exponent in the regression equation remains near 1.0, implying a linear relationship even in linear space. However, the coefficients of the regression relations increase with increasing Γ and ∇RH, as the cooling rate is enhanced for a given value of K_{DP} for warmer and drier air. As with the other variables, it is possible that the PSDs sampled here are underdispersive compared to nature, but it is evident that K_{DP} holds the best potential for estimating the magnitude of the cooling within the melting layer.

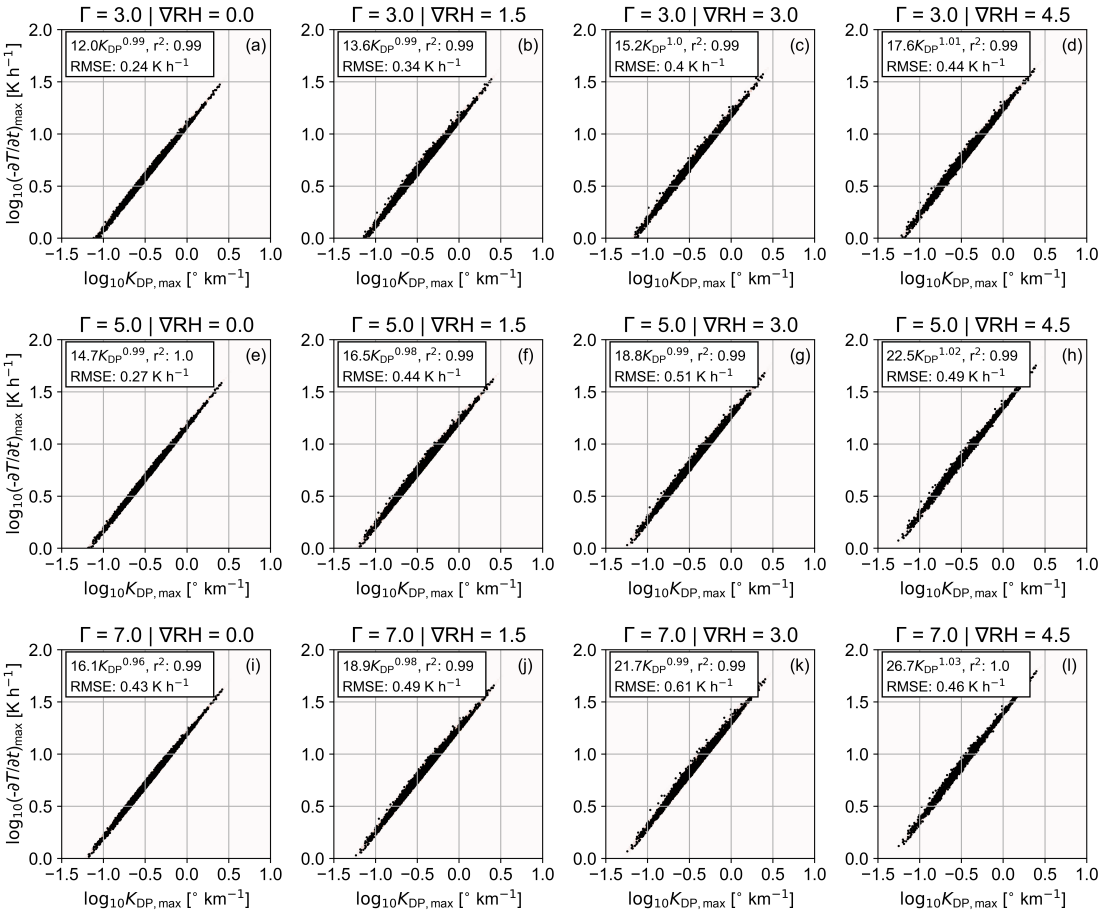

Figure 5.32: As in Fig. 5.29, but for the maximum K_{DP} in the brightband.

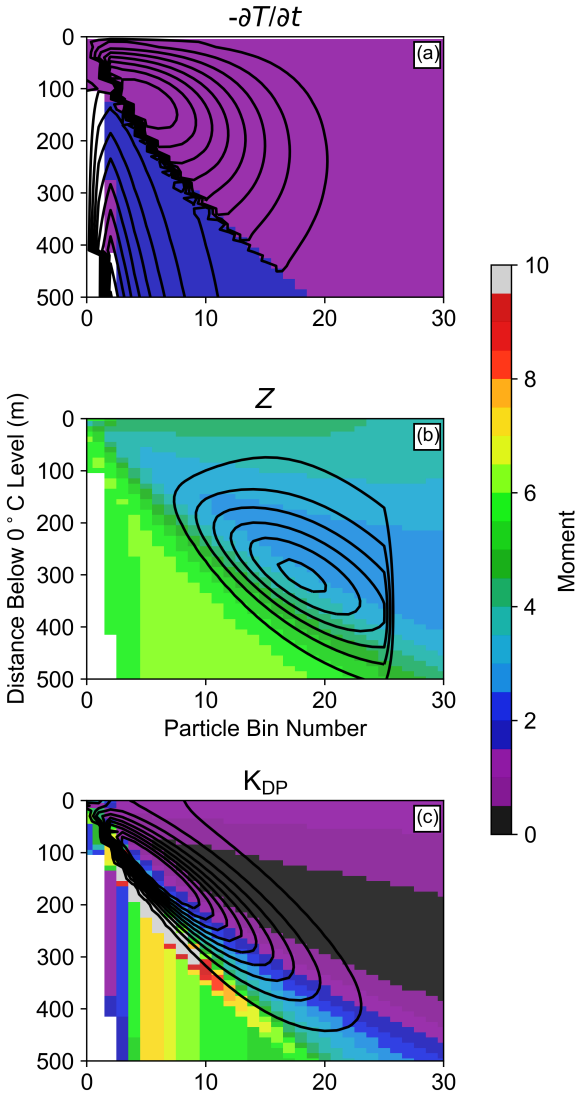

Figure 5.33: Cross sections of particle bin versus height showing the contribution of each bin toward (a) $-\partial T/\partial t$, (b) Z, and (c) K_{DP} (black contours) and the moment-relationship of each variable with particle diameter in each bin (shading) for a sample PSD of $N_{0,s}$ = 938 m^{-3} mm$^{-(1+\mu_s)}$, Λ_s = 0.6 mm^{-1}, μ_s = -1.52, and D_{max} = 9.2 mm and environment of Γ = 6.0 ° km^{-1} and ∇RH = 3.0 % °C^{-1}. Contours are from 0.01 to 0.1 K h^{-1} every 0.01 K h^{-1} for $-\partial T/\partial t$, 0.1×10^{-3} to 1.0×10^{-3} ° km^{-1} every 0.1×10^{-3} ° km^{-1} for K_{DP}, and from 25 to 150 mm^6 m^{-3} every 25 mm^6 m^{-3} for Z.

To examine the cause of this correlation, the contribution of each bin to the cooling rate, Z, and $K_{\rm DP}$ is shown in Figure 5.33 for a sample distribution. The white areas for small bins at heights below 100 m below the 0°C level are bins with completely evaporated particles. The values of both Z (Fig. 5.33b) and $K_{\rm DP}$ (Fig. 5.33c) increase downward as melting progresses, before decreasing markedly due to a rapid decrease in particle concentration (and, in the case of $K_{\rm DP}$, to a collapse of particles into more spherical shapes). It is readily evident that the ellipses of contribution to the cooling rate (Fig. 5.33a) are nearly co-located with the ellipses of contribution to $K_{\rm DP}$ (Fig. 5.33c), with the maxima occuring at similar heights and within the same bins (primarily bins 3 through 9 in this example). The ellipses of contribution to Z are displaced further downward and toward larger particle bin sizes (Fig. 5.33b).

In addition to the differing contributions to each variable, it is instructive to do an analysis of PSD moments across the range of heights and bins. For a given environment, the cooling rate is proportional to the rate of change of meltwater times the concentration,

$$-\frac{\partial T}{\partial t} \propto \frac{\partial m_w}{\partial t} N(D) dD = u \frac{\partial m_w}{\partial z} N(D) dD, \tag{5.47}$$

neglecting the small impact of ρ_a on the cooling rate. The concentration, $N(D)$, is equal to the 0th moment of the PSD. The moment of the rate of change of meltwater can be found using Eq. (5.13). For a given environment and assuming $f_h \approx f_v$, the only terms that are a function of particle size are the capacitance c and the ventilation coefficient f_v,

$$\frac{\partial m_w}{\partial z} u \propto c f_v. \tag{5.48}$$

The capacitance is $\approx 0.5D$ and therefore related to the 1st moment of the PSD. Because the moment M is equal to the slope of the $f_v - D$ relation in logarithmic space, the moment of the PSD of f_v can be found by

$$M = \frac{\nabla(\log_{10} f_v)}{\nabla(\log_{10} D)}. \tag{5.49}$$

For melting particles, M is ≈ 0.3 and rises to ≈ 0.7 for particles with f nearing 1.0. Therefore, the cooling rate is approximately proportional to the 1.3rd-1.5th moment of the PSD, with some slight variability across the size distribution. If evaporation occurs, Eq. (5.17) similarly indicates that Eq. (5.48) applies and the moment of cooling is roughly proportional to the 1.3rd-1.5th moment of the PSD as well. These conclusions are seen graphically in Fig. 5.33a, as all the cooling in the melting layer (shown by the series of ellipses above and to the right of the 1.5th moment line) occurs in bins corresponding to the 1.0-1.5th moment of the PSD. The cooling shown in smaller bins below 100 m below the 0°C level is due to evaporation of small raindrops.

Calculations similar to Eq. (5.49) were performed for the Z and K_{DP} contribution in each bin. The Z (Fig. 5.33b) is initially proportional to the 4th moment of the PSD at the top of the domain for dry snow, as is expected given the inverse relationship between ρ_s and D given in Eq. (5.1) (Brandes et al. 2007). The bulk of the Z occurs in bins proportional to the 3rd to 5th moments of the PSD before melting entirely and becoming proportional to the 6th moment of the PSD, as expected for nearly spherical Rayleigh scatterers. In contrast, while K_{DP} is proportional to the 1st moment for dry snow (Bukovčić et al. 2018) and the 4.24th moment in rain (Sachidananda and Zrnić 1986), the swath of maximum K_{DP} neatly follows the 1.5th moment axis for small to medium size bins (containing the bulk of particles), nearly the same moment that the cooling rate is proportional to. It is not trivial to isolate the factors contributing to the K_{DP}'s moment of the PSD in any given bin when considering the changes in meltwater fraction, terminal velocities (and thus concentration, due to the assumption of flux conservation), and aspect ratios across heights and bin sizes, all of which affect the resultant K_{DP} in a bin. This is further complicated by the linear change of aspect ratio (Eq. (5.19)) but nonlinear change in terminal velocity (Eqs. (5.6)-(5.7)) with meltwater fraction, and the differential changes in concentration across the PSD due to the range of differences

between u_r and u_s across the size spectrum. Suffice it to say that, subject to the preceding model assumptions described in sections 5.2.2 and 5.2.3, these properties that result in K_{DP} being proportional to the $\approx$ 1.5th moment make it an attractive variable for relating to the cooling rate within the melting layer that warrants continuing research.

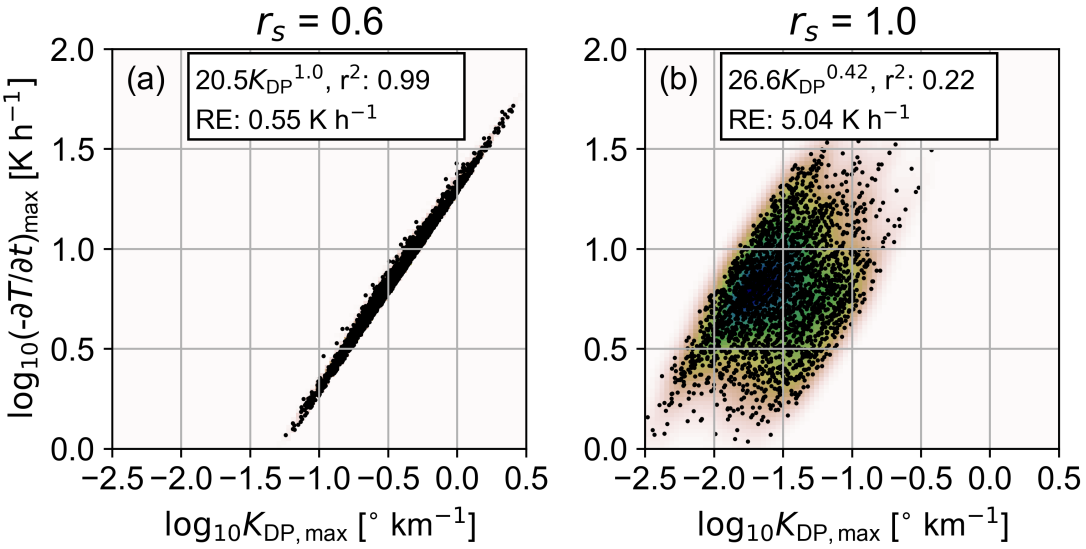

Figure 5.34: As in Fig. 5.32, but assuming (a) $r_s = 0.6$ and (b) $r_s = 1.0$ for an environment characterized by Γ = 6.0 °C km^{-1} and ∇RH = 3.0 % °C^{-1}.

A cursory investigation into the robustness of this result reveals that it is sensitive to the assumed r_s. Figure 5.34 shows the impact of the assumed r_s on the correlation between the maximum K_{DP} and the maximum cooling rate in the melting layer. In comparison to the assumption of r_s = 0.6 (for which the results agree with those from other environments shown in Fig. 5.32), the correlation is strongly degraded for r_s = 1.0, with an r^2 of 0.22 and an increase in RMSE of an order of magnitude over Fig. 5.34a and approaching that of Z (Fig. 5.29). In addition, the values of K_{DP} are smaller by an order of magnitude despite using the same range of PSDs. K_{DP} is a function of both the mass content of a particle and its aspect ratio (i.e., completely spherical particles of any mass will have zero K_{DP}). When $r_s = 0.6$, small particles, which are present in very large concentrations, undergo a large change in r_m while melting, from oblate snow crystals to

nearly spherical raindrops, and contribute appreciably to K_{DP} while they are wet, oblate spheroids. Meanwhile, large particles, which are sparse, do not change their aspect ratio much while melting. This situation is reversed if the snow particles are assumed to be spherical to start. The near-sphericity of small crystals during the melting process when $r_s = 1.0$ severely restricts their contribution to K_{DP}, resulting in much smaller K_{DP} values overall as seen in Fig. 5.34b. However, this also results in larger snow particles exerting the dominant effect on K_{DP} values, which hardly contribute to the maximum cooling rate. This weakened relationship is demonstrated in Figure 5.35. Although the cooling rate (Fig. 5.35a) and the Z (Fig. 5.35b) plots resemble Fig. 5.33a,b, the contribution to K_{DP} is shifted toward lower heights and larger bins and the axis of maximum K_{DP} contribution is now proportional to the $\approx$ third moment of the PSD. Thus, although there is evidence to support the use of $r_s = 0.6$, it should be kept in mind that these results are sensitive to model parameters that influence the distribution of K_{DP} contribution along the PSD. Continuing research into these sensitivities is warranted.

5.2.5 Investigation of the cause of "saggy" brightbands

With the advent of QVPs, one of the most pronounced features to be identified is the so-called "sagging" brightband, a temporary and often sudden downward excursion of the brightband signature (Ryzhkov et al. 2016; Kumjian et al. 2016; Erlingis et al. 2018). This feature was examined in detail by Kumjian et al. (2016) for two cases for which *in situ* thermodynamic and particle imaging data were available: a broad area of stratiform rain above a front, and the trailing stratiform portion of a classical MCS. There were several characteristics common to both cases. During periods of sagging, the Z and Z_{DR} maxima were enhanced and occurred at lower heights. The brightband depth increased. In addition, enhanced Z and decreased Z_{DR} were noted above the brightband at times of sagging, with enhanced values of Z and Z_{DR} present beneath it. The authors hypothesize this to be due to riming, which results in faster falling particles that take longer to acquire

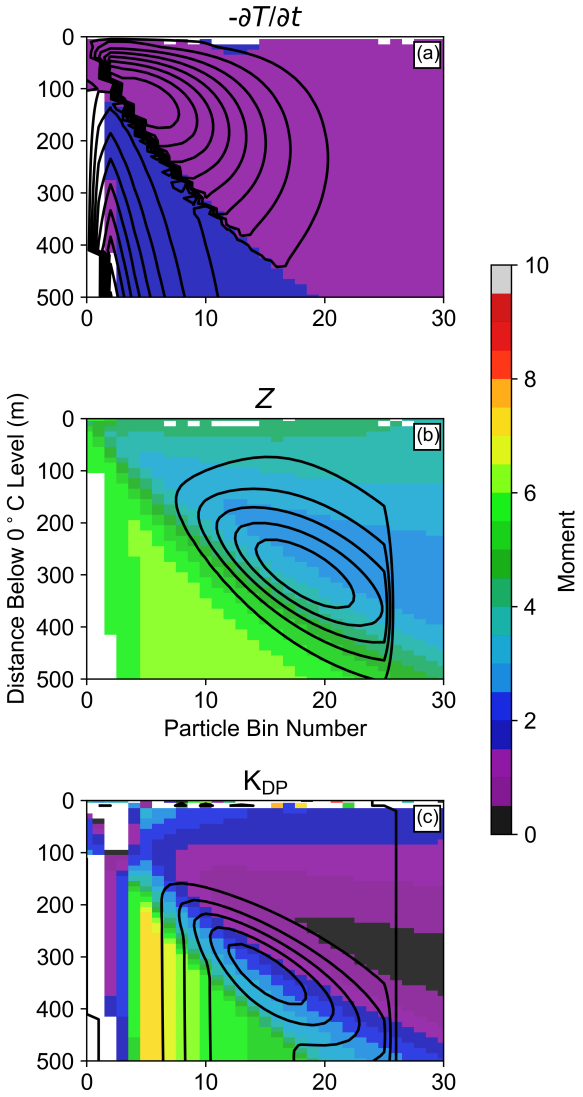

Figure 5.35: As in Fig. 5.33, but for r_s = 1.0.

sufficient meltwater to cause the brightband and thus suppress the brightband height. *In situ* data for one of the cases supports this, with particle imager data showing small, rimed particles and evidence of pristine ice generated from splintering during riming, and vertical profiler data showing enhanced fall speeds aloft. In addition, the region above the melting layer was saturated with respect to liquid water, a necessary condition for riming. Using a simplified version of the 1D-MS, the authors were able to recreate a similar sagging feature by covarying the f_{rim} and precipitation intensity (changing f_{rim}

alone did not reproduce the features), and thus conclude that riming of an existing PSD is likely a cause of sagging brightband features. However, the described profiles of Z and Z_{DR} in regions of sagging are also consistent with ongoing aggregation, and the second case lacks evidence of riming in the *in situ* data. Instead, large aggregates and small isometric crystals are observed, and the air is significantly subsaturated with respect to water, consistent with the presence of a rear inflow jet and suggestive of sublimation above the melting layer and possible downdrafts. The authors propose and discount a number of other reasons brightbands may sag, including the role of cooling-induced isothermal layers, although they note that no thermodynamic feedbacks were included in their version of the model. Thus, it is worth investigating the various potential causes of brightband sagging using the modified 1D-MS with environmental feedbacks.

In addition to the cases shown in Kumjian et al. (2016), Figure 5.36 shows another example of a sagging brightband (between approximately 60 and 90 minutes). The QVP was taken in the trailing stratiform portion of a strong MCS from the KLSX radar and was formatted to correspond with the following figures from the 1D-MS to facilitate an easy comparison. Like those reported in Kumjian et al. (2016), there is an enhancement in Z and Z_{DR} during the period of sagging, as well as a lowering of the height at which the brightband maxima occur by approximately 400 m. The K_{DP} field, which was unavailable from the cases reported in Kumjian et al. (2016), also shows a pronounced enhancement in the sagging region with values up to 0.4 $^{\circ}$ km^{-1}. In contrast, the case here does not show a clear indication of an enhancement in Z and decrease of Z_{DR} above the sagging brightband, although both do remain enhanced below it. This lack of decrease in Z_{DR} values above the brightband is curious, but could be a consequence of competing effects for either riming and aggregation. Riming results in more spherical particles that reduces Z_{DR} but increases their density which increases Z_{DR}; aggregation results in less dense particles which decreases Z_{DR} but could potentially result in more oblate particles, which would serve to increase the Z_{DR}. The ρ_{hv} field shows a clear

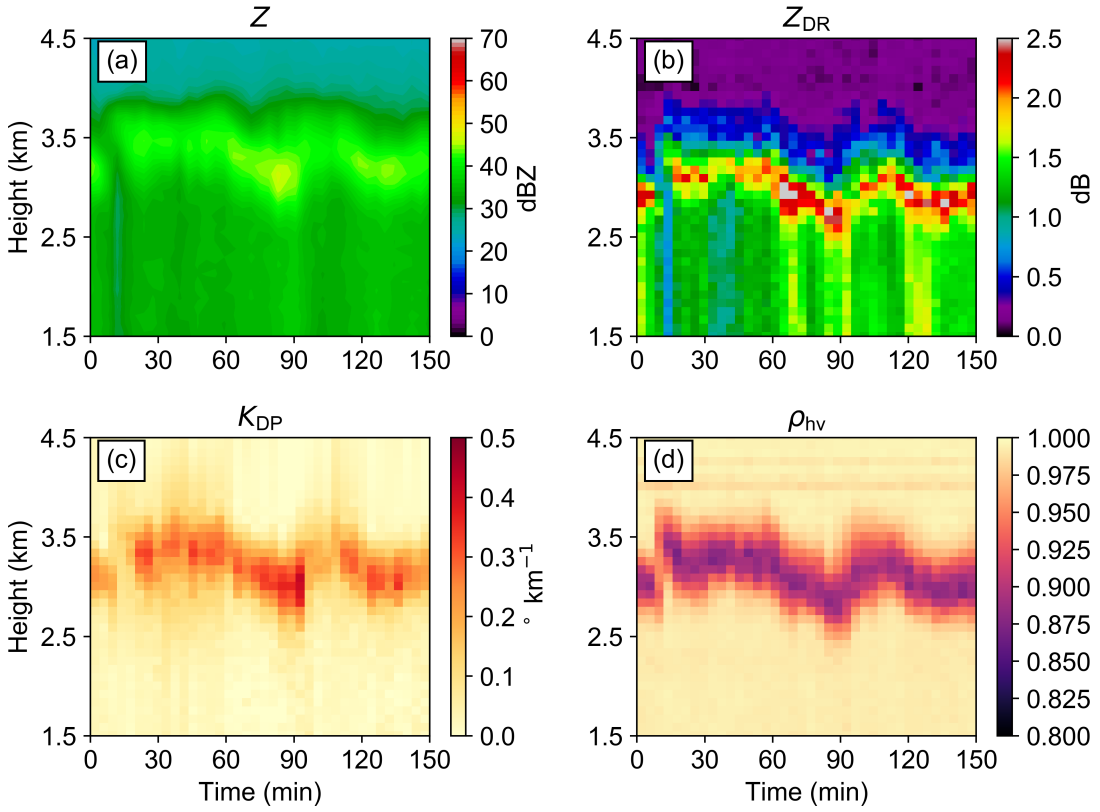

Figure 5.36: QVP data of (a) Z, (b) Z_{DR}, (c) K_{DP}, and (d) ρ_{hv} of a sagging bright band from KLSX on 2017 April 29 between 22:14:52 and 01:45:10 UTC. Data processed and provided by Amanda Murphy.

lowering, suggestive of a delay of melting until lower heights. Given its inclusion of K_{DP}, this case, along with those described in Kumjian et al. (2016), provide a picture of the features of sagging brightbands and will be used to evaluate the performance of the 1D-MS in simulating this phenomenon.

One of the factors contributing to uncertainty regarding sagging brightbands is the different ways in which a brightband can be considered to be sagging. Figure 5.37 shows a conceptual model of a vertical profile of a radar variable (e.g., Z) outside of, and during, periods of sagging. Point A denotes the top of the melting layer, whereas point B denotes the brightband maxima. The various factors that could, in theory, contribute to brightband sagging can all affect the magnitude and/or height of point A and/or point

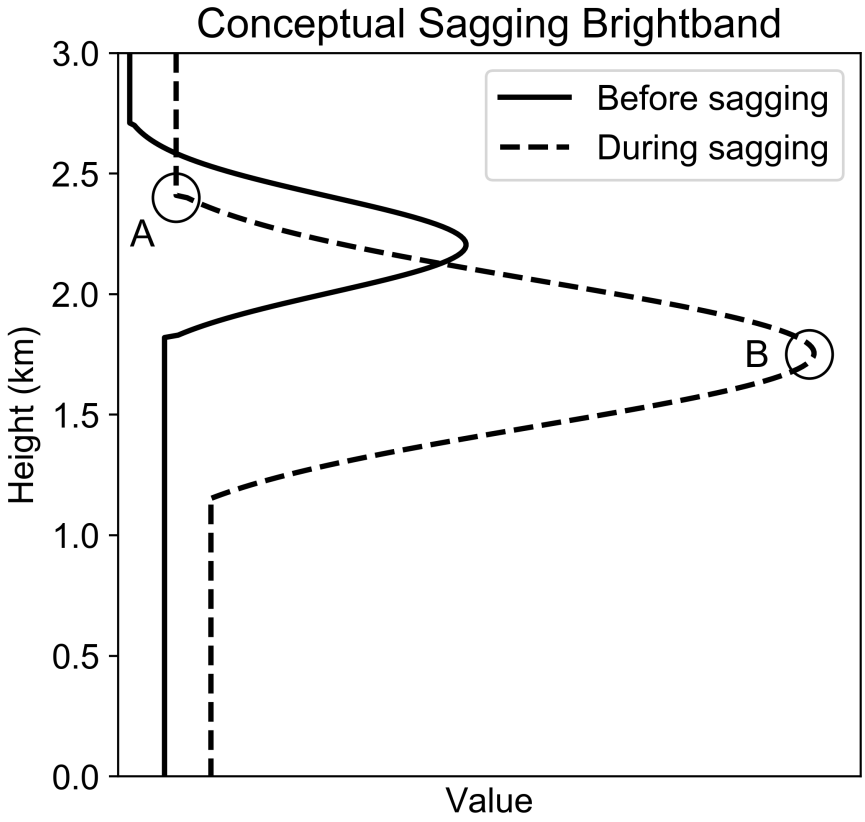

Figure 5.37: Conceptual representation of the vertical profile of a hypothetical radar variable (solid) before sagging and (dashed) during sagging. Point 'A' represents the top of the melting layer, whereas point 'B' represents the peak of the brightband at any given time.

B, and the gradient between them, in different ways. As a framework for the following discussion, changes in the magnitude and height of point A (B) will be referred to as A_{mag} (B_{mag}) and A_{hgt} (B_{hgt}), respectively. Upon visual inspection of time-height cross sections of radar variables, brightbands may appear to sag when B_{hgt} lowers in height. In contrast, or concurrent with this lowering, A_{hgt} may also lower. In addition, B_{max} tends to increase and A_{max} also changes (increases for Z, decreases for Z_{DR}, etc.) during periods of sagging. The depth of the brightband (A_{hgt} - B_{hgt}) is also typically enhanced

during sagging. These differing perspectives on defining sagging brightbands are both investigated below but should be clarified in future literature.

Four possible causes of the changes described above are investigated in isolation to study their individual impacts on the resultant brightband signature: changes in aggregation, precipitation intensity, relative humidity, and vertical velocity. Following the approach of Kumjian et al. (2016), the various parameters of interest were modulated using a Gaussian function with a standard deviation of 15 minutes. A total period of 150 min was examined. For the first 15 minutes, the unperturbed environment is modeled. The left half of the Gaussian distribution is then applied over 45 minutes, with the fully perturbed environment modeled for an additional 30 minutes. Finally, the right half of the Gaussian distribution is modeled before returning to the unperturbed environment for the final 15 minutes. A diagram demonstrating this is shown in Figure 5.38.

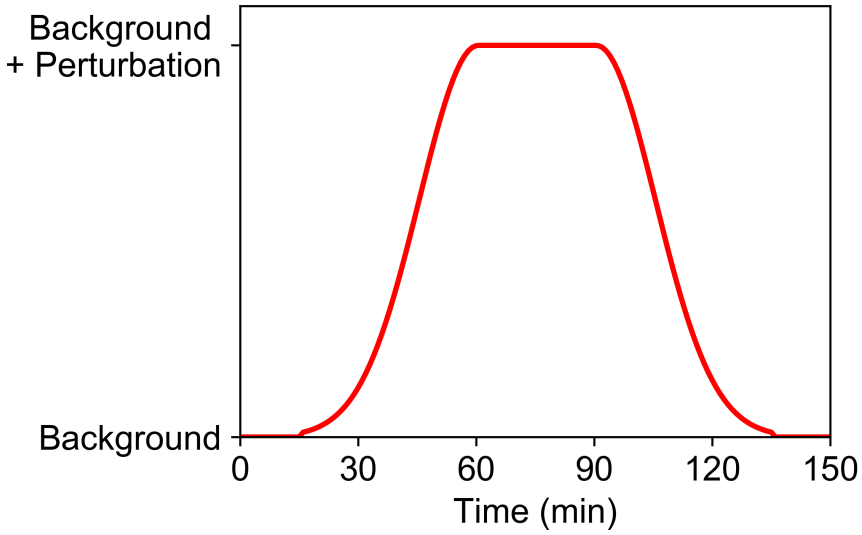

Figure 5.38: Diagram demonstrating the applied condition modulations for the sagging brightband tests.

Unless otherwise specified, the environmental Γ is 6.0 °C km^{-1} and the ∇RH is 3.0.

5.2.5.1 Aggregation

To approximate the effects of aggregation alone, the PSD was varied to decrease Λ_s while conserving the IWC. For a gamma distribution, the IWC can be expressed as (Boudala et al. 2006):

$$\text{IWC} = \frac{\alpha N_{0,s}}{\Lambda_s^{\beta+\mu_s+1}} \Gamma(\beta + \mu_s + 1) \tag{5.50}$$

where α and β are the parameters in the mass-dimension relation for snow (for a relationship of the form $m = \alpha D^{\beta}$). Although not used explicitly, the implicit mass-diameter relation in the 1D-MS features β = 2.08 and α = 9.361×10^{-5} g mm^{-1}, where D is in mm and m is in g. These values fall roughly within the range of values reported in the literature (e.g., Mitchell et al. 1990; Szyrmer and Zawadzki 2010). For demonstrative purposes, the IWC was held constant at 1.0 g m^{-3}, while Λ_s was varied from 1.3 mm^{-1} to 0.3 mm^{-1} to approximate the effects of aggregation. The μ_s was calculated from Eq. (5.44). From this, the $N_{0,s}$ that conserves the IWC was found.

The results of varying aggregation alone are shown in Figure 5.39. For this and each of the following three causes, temperature and moisture feedbacks with the environment are turned off; the latent heating rates shown in panel (d) are instantaneous and due to microphysics alone. The 1D-MS lacks a number of processes that, in reality, act in concert with the latent heating due to microphysics to modify the environmental temperature and moisture field including vertical motion, turbulent mixing, and advection. These processes can act to make the growth of a deep isothermal layer self-limiting, and may even offset the effect of diabatic cooling entirely (e.g., Kain et al. 2000). These contributions are not straightforward to include in the 1D-MS. By turning off the environmental feedback, a quasi-balance between these effects is approximated and allows the instantaneous effect of the modeled changes to be evident.

The resultant brightband shown in Figure 5.39 bears a striking resemble to those reported in the literature (e.g., Fig. 5.36, Figs. 3 and 5 of Kumjian et al. 2016). During the period of enhanced aggregation (between 60 and 90 min), B_{hgt} decreases and B_{max}

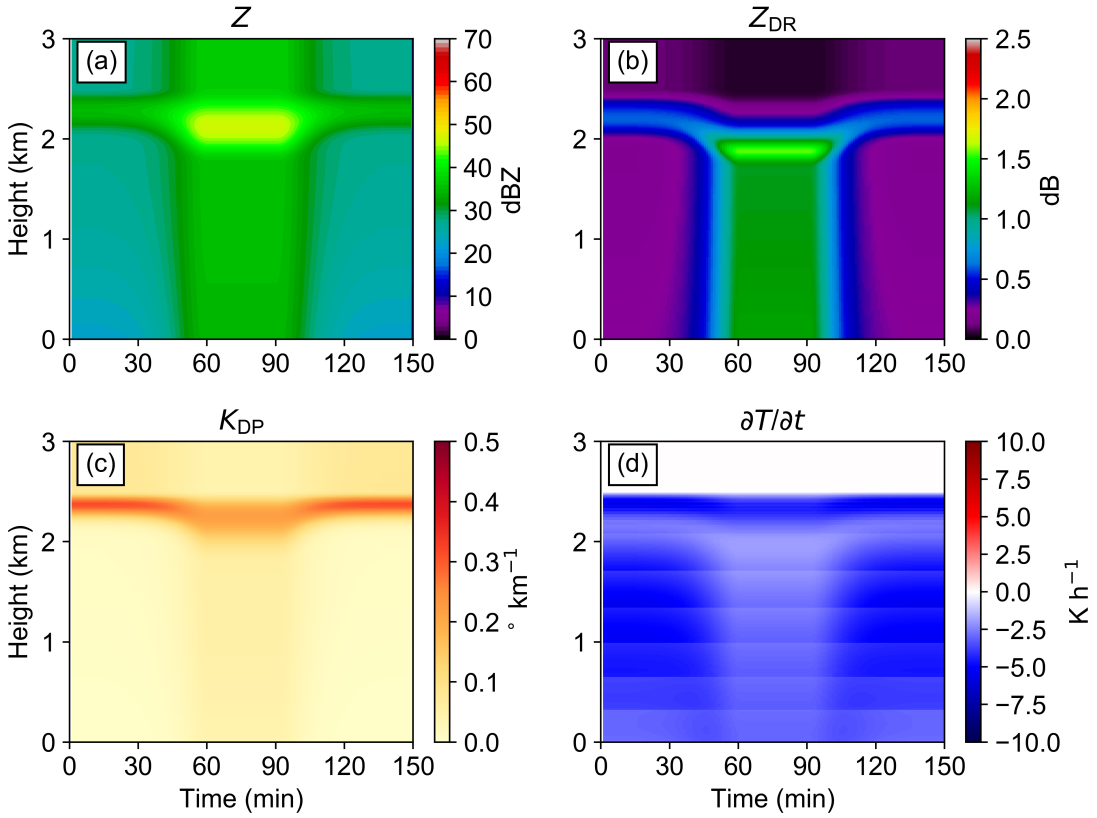

Figure 5.39: Time-height cross sections from the 1D-MS showing the effects of aggregation on (a) Z, (b) Z_{DR}, (c) K_{DP}, and (d) $\partial T/\partial t$ during brightband sagging.

increases for both Z (Fig. 5.39a) and Z_{DR} (Fig. 5.39b). The B_{hgt} for Z and Z_{DR} decrease by 110 m and 330 m, respectively, which agrees nicely with the Z_{DR} sagging of 351 m reported in Kumjian et al. (2016). Thus, there is a very pronounced visual sagging and enhancement of the brightband, particularly in Z_{DR}. The observed increase in the depth of the brightband is also evident in Z during the period of enhanced aggregation. At the top of the brightband, the modeled A_{max} during the period of enhanced aggregation also exhibits the changes seen in the cases examined in Kumjian et al. (2016), with an increase in Z and decrease in Z_{DR}. This decrease in Z_{DR} was attributed to riming in Kumjian et al. (2016), but occurs here (where $f_{rim} = 1.0$ everywhere) despite $r_s = 0.6$ for all particle sizes due to the decrease in density of the median particle size owing to aggregation. The reported enhancemnets of Z and Z_{DR} below the brightband during periods of

sagging are also correctly portrayed here due to the production of larger raindrops during periods of aggregation (as well as less mass loss due to evaporation owing to faster terminal velocities, as evidenced by the decrease in cooling rate below the melting level in Fig. 5.39d). Despite the reproduction of observed sagging brightband characteristics, A_{hgt} is unaffected (i.e., melting begins at the same height regardless of the state of aggregation; Fig. 5.39d). The cooling rate in the melting layer is also slightly lower during the period of enhanced aggregation due to the cooling being spread out through a deeper layer. In addition, the K_{DP} in the brightband is actually decreased during periods of sagging, in contrast with Figure 5.36c. Regardless, it is noteworthy that changing only the slope parameter for a constant IWC (to model the effects of aggregation) can reproduce the most noteworthy and pronounced observed features of sagging brightbands.

5.2.5.2 Precipitation Intensity

The next possible factor contributing to the sagging of brightbands is an increase in precipitation intensity. In contrast to aggregation, where the IWC was held constant and only Λ_s was varied, here Λ_s (and μ_s) are held constant while $N_{0,s}$ is varied. By default, Λ_s = 1.0 mm^{-1} and its corresponding μ_s are used with the value of $N_{0,s}$ corresponding to an IWC of 1.0 g m^{-3} from the previous section. $N_{0,s}$ is then varied up to twice its original value, resulting in a doubling of input IWC with everything else held constant. The results are shown in Figure 5.40.

In contrast to Figure 5.39, B_{hgt} remains unchanged (i.e., there is no visual sagging in the height of the brightband maximum), although the thickness of the brightband does seem to increase (for Z and K_{DP}). B_{max} does increase for Z (Fig. 5.40a) but remains constant for Z_{DR} (Fig. 5.40b), which is not affected by concentration. The B_{max} for K_{DP} (Fig. 5.40c) is also increased due to the increase in concentration. The doubled concentration also results in a doubling of the cooling rate within and above the melting layer (Fig. 5.40d). Based on these results, although a change in precipitation intensity

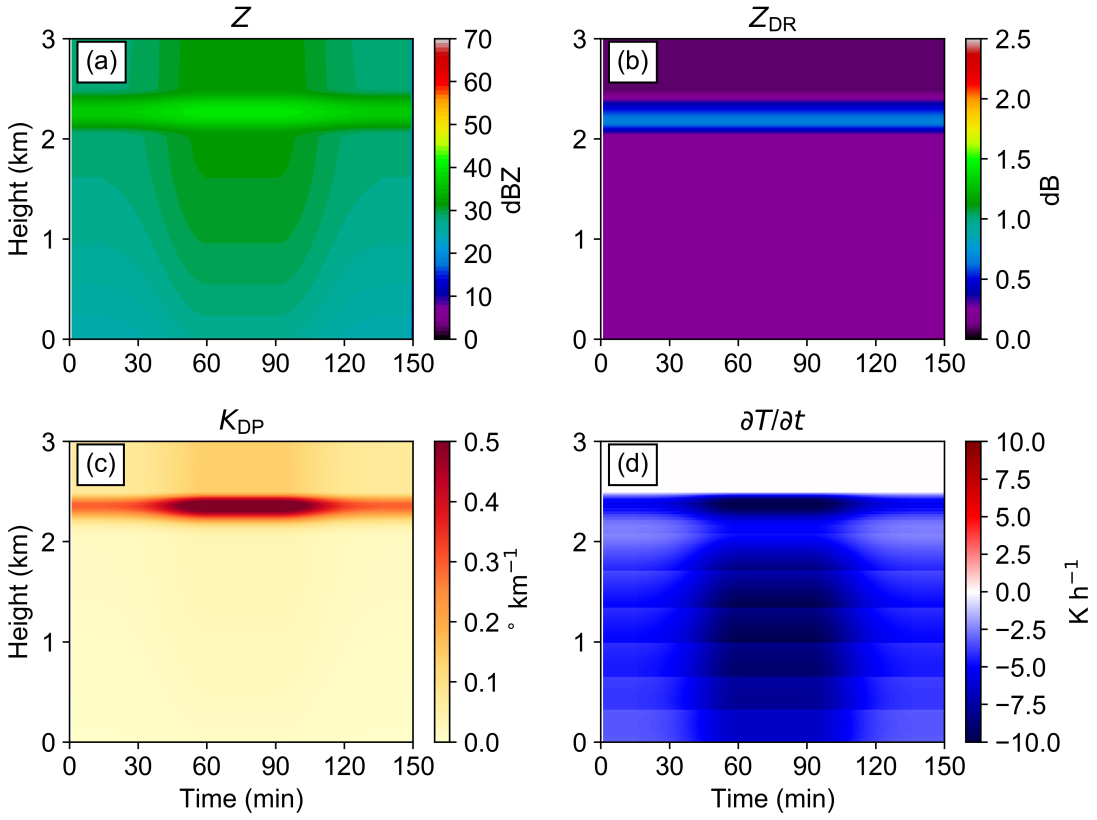

Figure 5.40: As in Figure 5.39, but for variable precipitation intensity.

can result in the enhanced brightband values observed for Z and K_{DP}, it is unable to explain the sagging of the brightband (in terms of either A_{hgt} or B_{hgt}) by itself.

5.2.5.3 Vertical velocity

By default, the vertical velocity in the 1D-MS has been assumed to be zero. However, any nonzero vertical velocity will affect effective hydrometeor fallspeeds and thus their concentration. In organized MCSs, mesoscale downdrafts may occur in the stratiform region as a component of the descending rear-to-front mid-level flow. However, modeling and observational studies indicate that these mesoscale downdrafts typically do not exceed, at most, 1 m s^{-1} in the vicinity of the melting level (e.g., Yang and Houze Jr. 1995a,b; Schuur and Rutledge 2000; Kumjian et al. 2016). To consider the more extreme end of what may be possible, the vertical velocity was varied from 0 m s^{-1} to -1.5

m s^{-1}, with results shown in Figure 5.41. The same PSD for an IWC of 1.0 g m^{-3} from the precipitation intensity experiment is used.

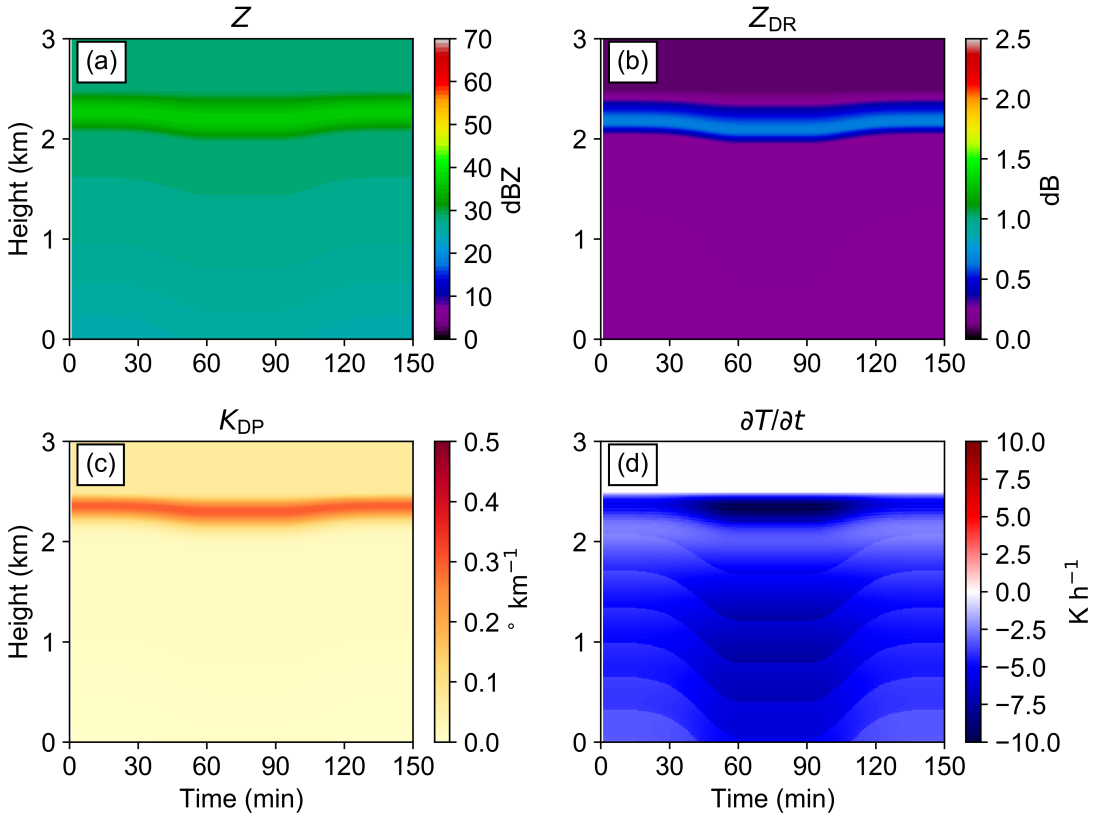

Figure 5.41: As in Figure 5.39, but for variable downdraft intensity.

Even with a downdraft of 1.5 m s^{-1} imposed, the resultant sagging of the brightband is only slight, with B_{hgt} for Z_{DR} only lowering 80 m, less than what is often observed in prominent cases of brightband sagging. There is little to no change in B_{max} for Z, Z_{DR}, and K_{DP}, with only a slight increase in the depth of the melting layer. In addition, because the particle temperature is assumed to be in equilibrium with the environment for snow, particles begin melting at the same point regardless of their slight increase in terminal velocity. Thus, the impact of vertical velocity on particle fallspeeds alone cannot explain sagging brightbands.

5.2.5.4 Relative Humidtiy

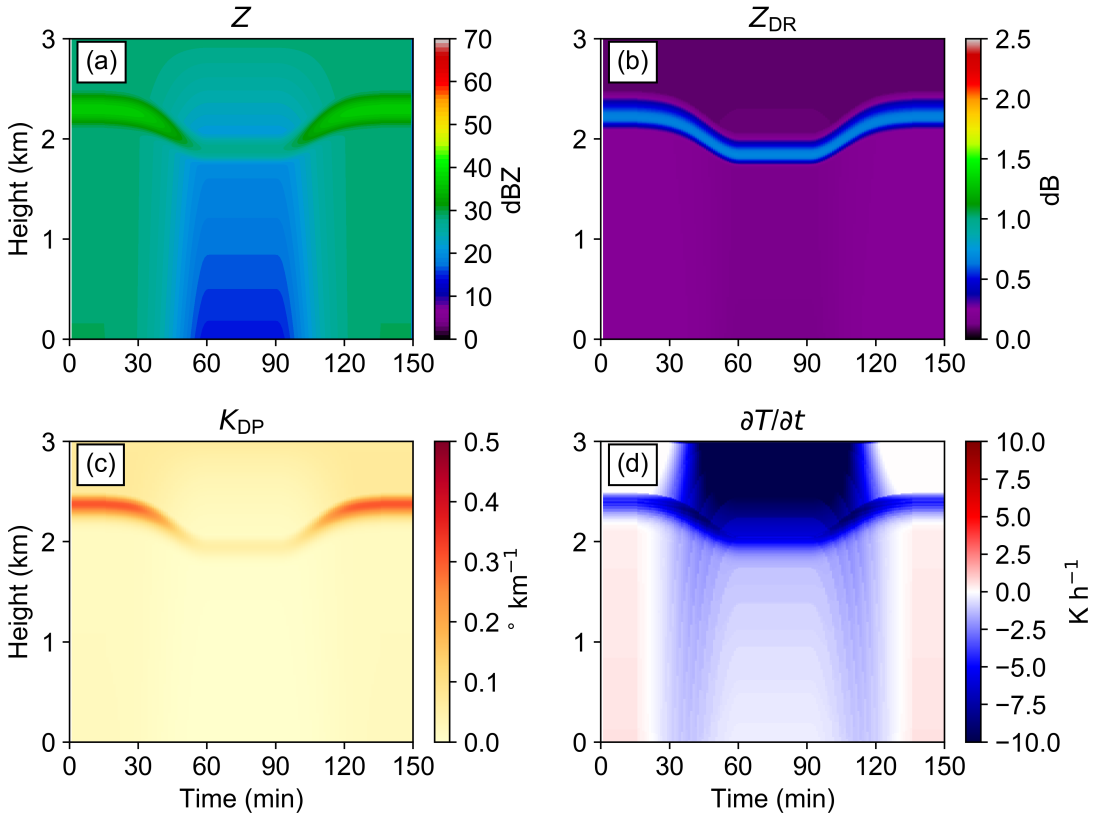

Figure 5.42: As in Figure 5.39, but for variable environmental humidtiy.

Finally, the impact of environmental relative humidity on sagging brightbands is investigated in Figure 5.42 using the same PSD as the previous two sections. Although on average McFarquhar et al. (2007) found the environment to be saturated down to the melting level with a ∇RH of 3.0 % °C^{-1} beneath that, significant variability can exist, with drier air able to be transported into the low and mid-levels via the descending rear-to-front inflow jet (e.g., Houze Jr. 1994). Dry air at and above the environmental 0°C level was seen in the second case reported in Kumjian et al. (2016). Therefore, in contrast to the previous three sections, the environmental RH is assumed to initially be 100% throughout the column and decreases to 70% in order to model a reasonable

"worst-case" scenario for strong impacts from environmental RH on the brightband. The results are shown in Figure 5.42.

As with aggregation, a prominent sagging of the brightband is observed. In this case, B_{hgt} descends by 380 m (for Z_{DR}). However, unlike the three previous experiments, A_{hgt} also descends due to sublimational cooling keeping snowflakes colder than 0°C for an extra 440 m. However this strong sublimation also acts to decrease Z and K_{DP} above and within the melting layer during sagging, in direct contrast to what is observed, along with a slightly thinner brightband. In addition, A_{max} for Z_{DR} is unchanged (as seen in Figure 5.36), although Kumjian et al. (2016) note that snow crystals should preferentially sublimate at the tips and should therefore become more spherical with sublimation, an effect not yet accounted for in the 1D-MS. Therefore, although a surge of dry air results in a sagging of the brightband in terms of A_{hgt} due to sublimation, the same process results in a weaker B_{max} and thinner brightband and thus fails to reproduce the observed features of sagging brightband. However, the degree of drying in this case was significant, and variability in the PSD will affect how much the resultant B_{max} changes in the sagging brightband. For example, a similar experiment using the aggregation PSD results in a much less marked decrease in the B_{max} for Z, Z_{DR}, and K_{DP} than in Figure 5.42 (not shown).

Although the previous analysis shows the benefits and insights to be gained from isolating specific processes, it is likely that much of the variabilities are coupled in reality. For example, it stands to reason that more intense precipitation rates may lead to enhanced aggregation, and thus the impacts of these changes may be additive. Similarly, downdrafts near the melting layer may form and intensify due to cooling from sublimation, melting, and evaporation (e.g., Houze Jr. 1994), and thus the impacts of vertical velocity and relative humidity changes should occur together. Conversely, changes due to aggregation may affect the degree and location of sublimation in any dry layers aloft

and the degree to which the brightband is affected. While no one physical process examined can fully explain every aspect of observed brightband sagging characteristics, the combination of various processes may be able to.

The only remaining factor that has not yet been considered is the impact of environmental cooling and moistening feedbacks. The sublimation, melting, and evaporation of precipitation acts to create 0°C isothermal layers that deepen with time. Of course, as discussed previously, the exclusion of mixing and other processes results in unrealistically deep isothermal layers, which would, in reality, be counteracted by other processes (i.e., the deepening isothermal layer results in an increasingly superadiabatic layer beneath it, which should result in convective mixing and warming of the layer from below).

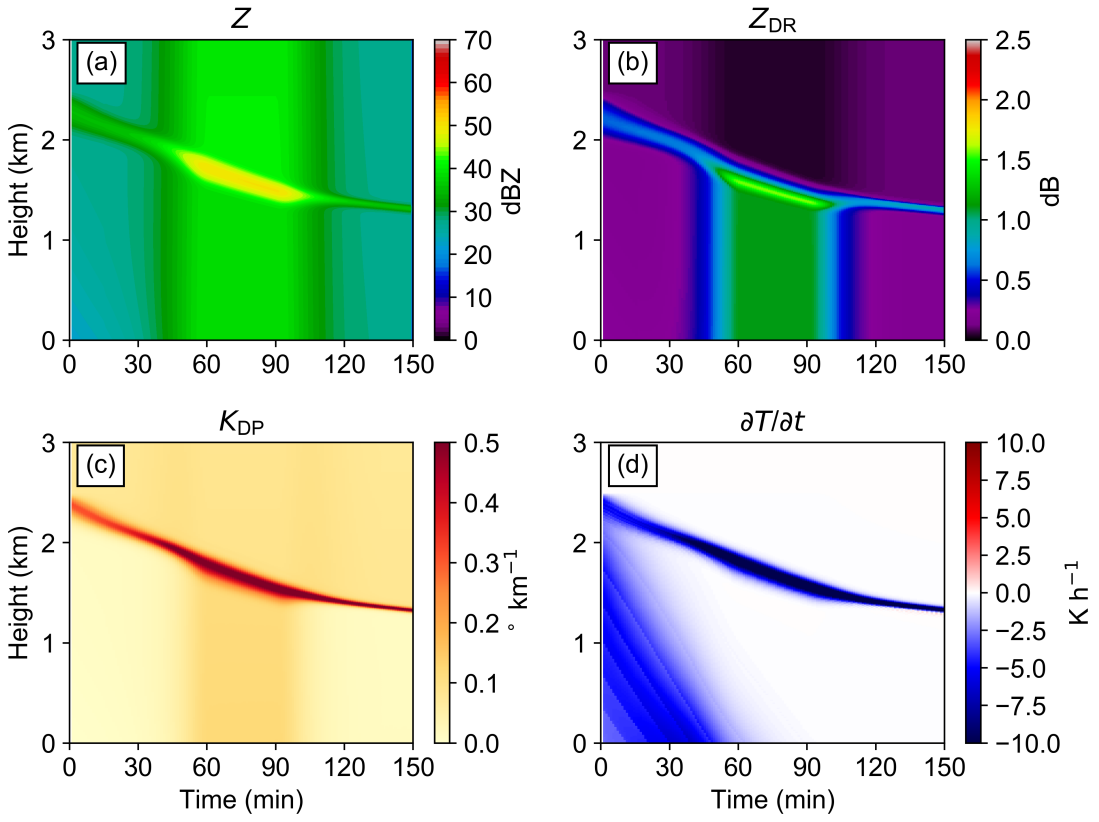

Figure 5.43: As in Figure 5.39, but for variable aggregation and precipitation intensity and including environmental temperature and moisture feedbacks.

A demonstrative example of more realistic variability is shown in Figure 5.43. Here, both aggregation and precipitation intensity are co-varied as described in their respective previous sections so that the IWC is 1.0 g m^{-3} during periods of low aggregation and increases to 2.0 g m^{-3} during intense aggregation. These values are large and result in a brightband that is on the upper end of what is typically observed, but serve as a useful demonstration. With the combination of changes in aggregation and precipitation intensity along with incorporating changes to the environment, all of the observed brightband characteristics during sagging events can be simulated. A_{hgt} descends by 900 m in the span of 150 min due to the formation of an isothermal layer, whereas A_{hgt} increases for Z and decreases for Z_{DR}. This rate of descent is roughly comparable to that seen in Figure 5.36. The thickness of the brightband is enhanced, and B_{max} increases for Z, Z_{DR}, and K_{DP}. Due to the aforemention exclusion of counteracting processes, the "return" of the brightband to its pre-sagging level is not modeled. Although the goal here is not to disprove the theory of riming's contribution to sagging brightbands, for which good evidence has been provided by Kumjian et al. (2016) for at least one case, the results shown here suggest that sagging due to other causes — namely enhanced precipitation/aggregation and the resultant cooling of the atmosphere — cannot be entirely ruled out, and it is possible that there are multiple pathways that result in sagging brightbands. Further research is needed.

5.2.6 Summary and Future Work

In this chapter, a one-dimensional model of melting snow was developed and expanded upon and used to study the sensitivity of the brightband to the environment, the potential for thermodynamic retrievals within the melting layer using polarimetric radar data, and the possible causes of observed brightband sagging. With many customizable inputs and switches, the model itself serves as a valuable research tool for studying the melting layer, and interest has been expressed in using it to improve the representation of melting

snow in bulk microphysical schemes. Notable changes in the brightband are shown to be sensitive to the existing background conditions for equivalent input PSDs. Using a large number of samples that span the range of typically observed PSDs, very promising results have been achieved for using K_{DP} within the brightband to estimate the maximum cooling rate within it, with the potential for significant improvement upon methods that rely on Z. The advent of QVPs provide a robust way to estimate K_{DP} in the melting layer for the first time. In addition, it has been shown that other microphysical processes, such as an increase in precipitation intensity and the resultant cooling, could plausibly be responsible for sagging brightband signatures, in addition to the existing hypothesis of riming. As noted in Kumjian et al. (2016), this could have implications for nowcasting of precipitation type and melting layer height as well as the possible identification of riming conditions dangerous to aviation operations.

Despite the encouraging results, much work remains to be done in studying the melting layer and its associated polarimetric signatures. There are many other ways the 1D-MS can be used in its current form. Preliminary steps have begun to be undertaken to initialize the 1D-MS from QVPs of real data using recently developed retrieval equations for D_m and N_t in snow (Murphy et al. 2018), which, when combined with corresponding environmental conditions (e.g., from a short-term NWP forecast), will facilitate the direct comparison between the 1D-MS and observations for real snow events and potentially permit time-height retrievals of cooling rate for the events. Superexponential gamma distributions were the focus of this study based on reported observations, but it would be worthwhile to investigate the results when using subexponential gamma distributions (e.g. as reported in Brandes et al. 2007) or inverse exponential distributions. The results shown here focused primarily on the maximum cooling rate within the melting layer. While the cooling rate profile is typically parabolic in nature, more work should be done investigating the retrieval of the vertical distribution of cooling and the height at which the maximum occurs. Only S-band wavelengths were studied, and for

the most part employed the Rayleigh scattering assumption; future work should examine other radar wavelengths and employ T-matrix scattering calculations when possible. More sagging brightband cases should be compiled and investigated, preferably with *in situ* particle and thermodynamic data to aid the interpretation of the polarimetric signatures. In particular, as was suggested from in the data from Kumjian et al. (2016), the different characteristics of sagging brightbands in different stratiform precipitation regimes should be clarified.

There are also many ways in which the 1D-MS could be expanded and improved upon. The resultant evolution of the environment and the surface precipitation type is strongly sensitive to the model microphysical parameterizations (Milbrandt et al. 2014). Therefore, a wider variety of $m-D$ and $m-u$ relations for snow should be examined. Aggregation and breakup processes should also be added, as should secondary ice generation processes such as splintering and an explicit representation of the riming process. In addition, given the model sensitivity to its value, the aspect ratio and canting angles of snow should be studied further. Spheroids, although commonly used in modeling studies, are likely an oversimplification of the particle shape and its response to impinging electromagnetic radiation. As our understanding of the complexity of melting particles increases (e.g., Leinonen et al. 2017), this knowledge should be incorporated in future modeling studies. Going forward, the 1D-MS should contain multiple habits of ice crystals, each with their own $m-D$ and aspect ratio relations (e.g., Andrić et al. 2013). From a longer term perspective, the adoption of QVPs and the information they contain begs for a comprehensive 1D model to be developed and used alongside QVPs that expands upon the 1D-MS and includes multiple habits and options for all microphysical processes in the column (e.g., initial ice generation, deposition, breakup, aggregation, secondary ice generation, sublimation, melting, and evaporation).

Chapter 6

Assimilation of Z_{DR} columns via cloud analysis

The work presented in this section is taken from: Carlin, J. T., J. Gao, J. C. Snyder, and A. V. Ryzhkov, 2017: Assimilation of Z_{DR} Columns for Improving the Spin-Up and Forecast of Convective Storms in Storm-Scale Models: Proof-of-Concept Experments. *Mon. Wea. Rev.*, **144**, 5033-5057, doi:10.1175/MWR-D-17-0103.1.

Cloud analysis techniques for assimilating radar data into storm-scale NWP models are in widespread use, and make effective use of radar data to reduce the spin-up time of model precipitation. As described in section 3.1.4.2, cloud analysis techniques rely on a number of empirical relations between Z and model state variables for temperature, moisture, and q in order to analyze the full three-dimensional model state. In addition to deriving q from the legacy retrieval relations discussed in Chapter 4, moisture and temperature fields within areas of precipitation are analyzed by saturating within a Z threshold and heating based on the vertical velocity field after the 3D-Var assimilation of other data sources. Currently, dual-polarization radar data are not utilized in the cloud analysis beyond thresholding within the data quality control routines. However, as the results from section 5.1 indicate, polarimetric signatures, such as Z_{DR} columns, may contain valuable information about areas of heating (and moistening) within convective updrafts that is more targeted and rooted in physical principles than saturating based on a single Z threshold.

The work in this chapter explores the impact of assimilating observed polarimetric data through a modified cloud analysis routine. In addition to its proven success in reducing the spin-up time of modeled precipitation, the cloud analysis technique was

chosen due to ease of implementing modifications into existing code infrastructure. Direct insertion of the retrieved temperature and moisture perturbations is currently more straightforward than assimilating the polarimetric variables using variational techniques, which may require cross covariances between model state variables and the polarimetric variables that are not currently well formulated. Section 6.2 details the modifications made to the existing cloud analysis routine to accomodate Z_{DR} columns, and section 6.3 describes the experimental setup used for the two case studies examined. Results are presented in section 6.4, followed by a summary and discussion in section 6.5.

6.1 Motivation

Studies have shown that both temperature perturbations (e.g., Hu et al. 2006a) and the initial moisture field (e.g., Bielli and Roux 1999; Ducrocq et al. 2002; Weygandt et al. 2002b; Ge et al. 2013) can play primary roles in determining forecast accuracy. The insertion of too much water vapor mass can result in an overestimate of the intensity and areal coverage of convection, leading to a degradation of the forecast (e.g., Schenkman et al. 2011a; Schenkman 2012). This issue was examined in detail in Tong (2015), who found that saturating based on a Z threshold can result in too much moisture being added and large degradations in forecast skill. Forecast skill was greatly improved when a more accurate initial moisture field was provided in an observing system simulation experiment. Due to the lack of a direct relationship between in-cloud moisture and conventionally available observations, Tong (2015) proposed a modification to the cloud analysis in which the relative humidity in downdraft regions, which are generally unsaturated, is reduced. Notable improvements were found for both the analysis and forecast for all state variables examined, further highlighting the importance of improving the initial moisture field for convective storm-scale modeling. Despite these encouraging results, certain issues remain. While unsaturated regions correspond well with downdrafts overall, the specific quantitative relationship between water vapor mixing ratio

(q_v) and w is unknown and poorly constrained. In addition, even with a perfect $q_v - w$ relationship, the success of this method relies on an accurate model analysis of w, which is not always known and/or guaranteed, particularly if limited radars are available for assimilation. As an alternative to using w, a method is proposed here using Z_{DR} columns to provide adjustments to temperature and moisture in the cloud analysis similar to the methodology for assimilating lightning data at the cloud scale put forth by Fierro et al. (2012, 2014, 2015) and Marchand and Fuelberg (2014). Although they are caused by distinct phenomenon, both traditional Z_{DR} columns caused by mature updrafts (section 5.1.1) and those due to early size-sorting in developing convection (section 5.1.2) will be utilized here and collectively referred to as "Z_{DR} columns".

To investigate the validity of the proposed modifications, vertical cross sections of relative humidity, latent heating rate, Z_{DR}, Z, and storm-relative winds for the case described in section 4.2 from the HUCM are shown in Figure 6.1. Throughout the lifetime of the storm, Z_{DR} columns are coincident with updrafts featuring deep plumes of saturation and with the region of latent heating directly above the columns (as discussed in section 5.1.1). Notably, the area contained within the 15-dBZ contour is much more extensive than the areas that are near or at saturation, with large regions exhibiting subsaturation. It is apparent that saturating everywhere within the 15-dBZ threshold — the default Z threshold for saturating within the cloud analysis — would result in too much moisture being added to the system. These results support the conceptual model of Z_{DR} columns and their use as proxies for updrafts and subsequently areas of moistening and heating. It should be noted, however, that the Z threshold used for saturation in the cloud analysis is an adjustable parameter and there is no agreed-upon Z threshold to use. Other studies have addressed overmoistening concerns by instead reducing the frequency of applications of moistening (e.g., Schenkman et al. 2011a).

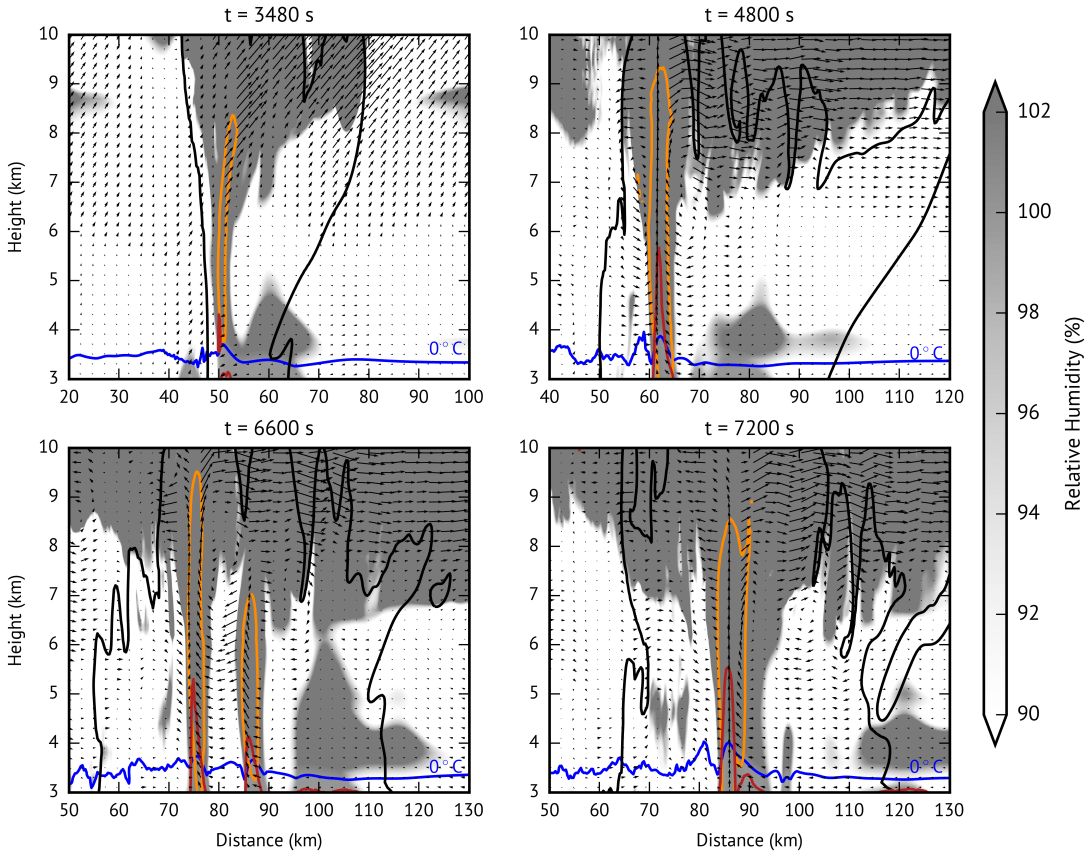

Figure 6.1: Vertical cross sections of simulated deep moist convection from the HUCM showing RH with respect to ice (shaded gray above 90%), the 100 K h^{-1} latent heating rate contour (orange), the 1.0-dB Z_{DR} contour (red), the 15-dBZ Z contour (black), the environmental 0°C level (blue), and storm-relative wind vectors in the x-z plane (vectors).

6.2 Description of modified cloud analysis routine

Polarimetric data are first quality-controlled and mapped to the model grid as described in section 3.1.4.2. Areas of interest for identifying Z_{DR} columns are limited to regions in which $Z \geq 10$ dBZ and $\rho_{hv} \geq 0.85$ to ensure sufficient signal-to-noise ratio and good quality data, and to regions below the environmental -20°C level to mitigate the chance of ice crystals with enhanced Z_{DR} causing false detections. Similar to the criteria used in Snyder et al. (2015) for their Z_{DR} column detection algorithm, a Z_{DR} column is defined here to exist if $Z_{DR} \geq 1.0$ dB for at least two vertically-contiguous grid boxes from the environmental 0°C level upwards. To help ensure that only legitimate Z_{DR} columns are detected and limit the chance of noise in the Z_{DR} field causing false detections, an additional 3 x 3 km horizontal mode filter is applied in which only columns exhibiting $\rho_{hv} \geq 0.85$ and $1.0 \leq Z_{DR} \leq 5.0$ dB in at least five of the nine grid boxes within the filter are counted. A summary of these detection criteria is shown in Table 6.1.

Table 6.1: Summary of the criteria used to detect Z_{DR} columns.

Variable	*Criteria*
T	-20°C $\leq T \leq$ 0°C
Z	$\geq$ 10 dBZ
ρ_{hv}	$\geq$ 0.85
Z_{DR}	$\geq$ 1.0 dB with vertical continuity

As opposed to warming in areas with $w >$ -0.2 m s^{-1} as in the existing cloud analysis, temperature adjustments are instead made anywhere Z_{DR} columns are detected. Adjustments are made both where Z_{DR} columns are located and to one grid box surrounding the Z_{DR} columns to aid in establishing wide-enough updrafts that are not smoothed out before becoming established. Similarly, instead of saturating based on a simple Z

criterion, saturation is only applied to the model columns (within the cloud region as determined by Z) where Z_{DR} columns have been detected. Model columns surrounding detected Z_{DR} columns are also saturated, with the horizontal extent proportional to the detected depth of the columns (in this case, half the number of model levels in the detected Z_{DR} columns) to prevent the added moisture from mixing out and to attempt to add more moisture for "stronger" (i.e., taller) Z_{DR} columns. In addition to moistening and heating at observed Z_{DR} column locations, an additional drying procedure is applied in an attempt to mitigate possible over-moistening by the microphysics scheme. At any locations satisfying $Z \geq 10$ dBZ and relative humidity $\geq 80\%$ but no detected Z_{DR} column, the relative humidity is reduced by half of the excess relative humidity above 80% (e.g., if the relative humidity is 90% with no Z_{DR} column detected, the relative humidity is reduced to 85%). This is, admittedly, an arbitrary process, but remains a succinct way to provide minor drying to areas characterized by precipitation (sufficient to meet the $Z \geq 10$ dBZ criterion) but that are outside of Z_{DR} columns (where, it is hypothesized, deep updrafts are less likely). Future work should examine the sensitivity to the Z_{DR} column detection criteria and the details of the filtering and weighting procedures for moistening and drying.

An example of the differences in potential temperature and water vapor mixing ratio analysis increments between the traditional cloud analysis and the modified cloud analysis is shown in Figure 6.2 for the initial 20:00 UTC assimilation cycle of the 19 May 2013 Oklahoma case (discussed in the following section). Although the magnitudes of the moistening and warming are comparable, the location and extent of the increments vary between the two. The traditional cloud analysis (Fig. 6.2a) shows a large area of moistening with two primary areas of warming west-northwest of Oklahoma City associated with the developing first supercell, and smaller areas of moistening and warming northwest and west-southwest of Oklahoma City. In contrast, the modified cloud analysis employing detected Z_{DR} columns (Fig. 6.2b) shows a smaller area of moistening

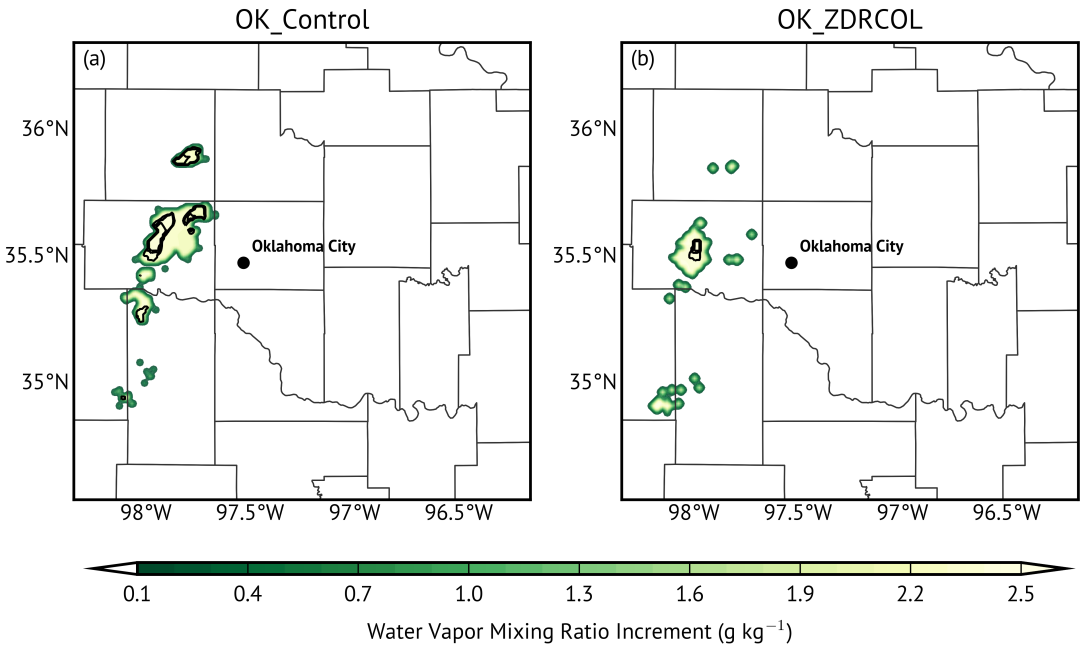

Figure 6.2: 20:00 UTC analysis increments of water vapor mixing ratio (shading, g kg^{-1}) and potential temperature (black contours every 1 K) at approximately 5 km AGL for (a) the traditional cloud analysis and (b) the modified cloud analysis for the 19 May 2013 Oklahoma case.

and warming directly west of Oklahoma City, southwest of the area modified in the traditional cloud analysis, and with little moistening or warming elsewhere. The only exception is far southwest of Oklahoma City, where the modified cloud analysis shows a bit more moistening associated with developing convection than the traditional cloud analysis.

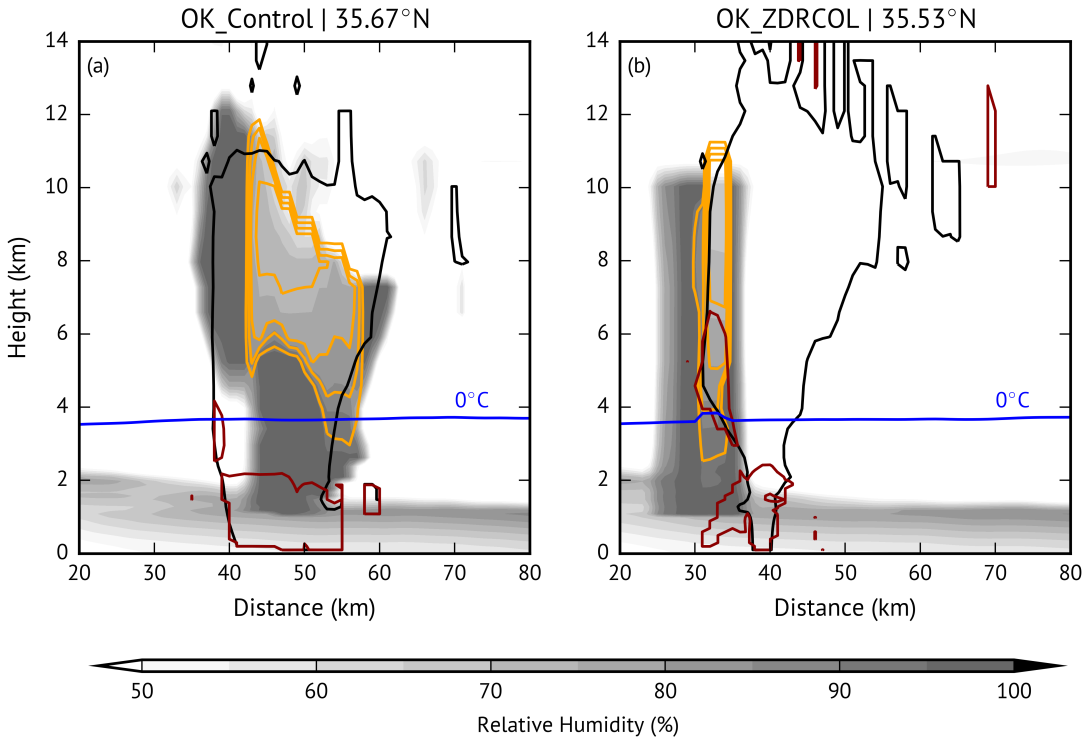

Figure 6.3: Vertical cross sections of the 20:00 UTC analysis increments of relative humidity (shading, %), perturbation potential temperature (orange contours every 1 K), the 15-dBZ Z contour (black), and the 1.0-dB Z_{DR} contour (red) for (a) the traditional cloud analysis (taken through 35.67°N) and (b) the modified cloud analysis (taken through 35.53°N) for the 19 May 2013 Oklahoma case. The environmental 0°C level is shown in blue.

To further demonstrate the differences between the analysis increments and confirm that the changes to the cloud analysis were providing the desired outcome, vertical cross sections are shown for the same time in Figure 6.3 and compared to the Z and Z_{DR}

at 20:00 UTC, analogous to Figure 6.1 from the HUCM. The cross sections are taken approximately through the perturbation potential temperature maximum in each case and subsequently are not through the same point. As in Figure 6.1, the areal extent of moistening in the OK_Control case based on Z (Fig. 6.3a) is more extensive than in OK_ZDRCOL (Fig. 6.3b). The extent of heating is also more extensive and within the area of Z in OK_Control than in OK_ZDRCOL, where it is placed on the left flank of the storm directly above the detected Z_{DR} column, which already extends approximately 2 km above the environmental 0°C level. While the differences in analysis increments between the traditional and modified cloud analyses vary with time, Figures 6.2 and 6.3 provide a demonstrative example of the typical differences seen between the methods.

6.3 Experimental setup

To investigate the impact of the modified cloud analysis, two tornadic supercell events are studied: the 19 May 2013 tornado outbreak in central Oklahoma (the "OK case") and the tornadic supercell of 25 May 2016 in north-central Kansas (the "KS case").

6.3.1 Case descriptions

Around 20:00 UTC on 19 May 2013, thunderstorms initiated near a dryline just west of the Oklahoma City metropolitan area in an environment characterized by strong vertical wind shear and high potential convective instability (i.e., CAPE). These storms developed quickly into three supercells that moved toward the east-northeast; two of the supercells produced a total of eight tornadoes, whereas the third supercell was nontornadic. The northernmost supercell produced two brief tornadoes north and northeast of Oklahoma City, Oklahoma, before producing a long-lived tornado that produced EF3 damage near Carney, Oklahoma between 21:41-22:24 UTC that resulted in 4 injuries; the southernmost supercell spawned a tornado that produced EF4 damage near Shawnee,

Oklahoma between 23:00-23:50 UTC that resulted in 2 fatalities and 10 injuries (National Weather Service 2017a).

In the KS case, an isolated supercell formed in north-central Kansas just north of a warm front around 22:00 UTC on 25 May 2016 and moved slowly east-southeastward. The storm produced a total of four tornadoes, including a long-track tornado just east-northeast of Salina, Kansas that lasted over 1.5 h (00:07-01:40 UTC) (National Weather Service 2017b).

For both cases, observed tornado tracks were retrieved from shapefiles created from damage survey reports.

6.3.2 Model setup

The ARPS (see section 3.1.4) was used in this study. Terrain data were derived from the U.S. Geological Survey 3-s dataset. Subgrid-scale turbulence was parameterized using a 1.5-order TKE turbulence scheme, with the evolution of the planetary boundary layer using the formulation of Sun and Chang (1986). Cloud microphysics were parameterized using the Milbrandt-Yau double-moment scheme (Milbrandt and Yau 2005a,b), and both short- and longwave radiation were parameterized using the NASA Goddard schemes (Chou 1990, 1992). A two-layer force-restore soil model based on Noilhan and Planton (1989) was used with surface fluxes based on stability-dependent drag coefficients using surface temperature and volumetric water content. More information about the full ARPS physics suite can be found in Xue et al. (2001).

Experiments were conducted using a one-way nested grid configuration. The parent domain was 1200 x 1200 km with a horizontal grid spacing of 4 km whereas the inner nest was 500 x 500 km with a horizontal grid spacing of 1 km. The domains for the OK and KS cases were centered on (35.45°N, 97.25°W) and (38.65°N, 97.55°W), respectively. Both nests used a stretched vertical grid containing 53 vertical levels with an average spacing of 400 m and a minimum spacing of 100 m near the surface. The

model top was rigid with a Rayleigh damping layer above 12 km to absorb vertically propagating waves. Lateral boundary conditions were externally forced. The simulated Z fields were computed using the T-matrix-based algorithm of Jung et al. (2010a). The domains used for each case are shown in Figure 6.4, and a summary of the model setup used for these experiments is provided in Table 6.2.

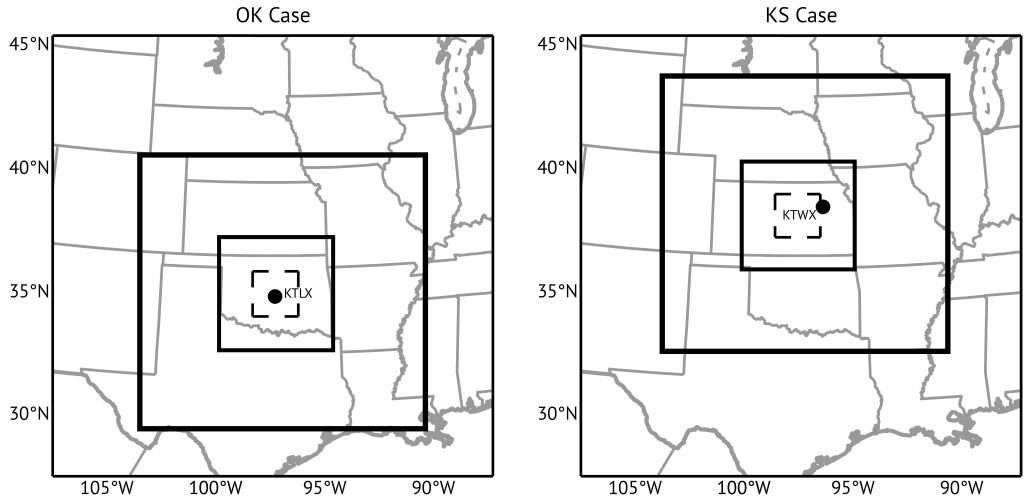

Figure 6.4: Model domains used for the (left) 19 May 2013 Oklahoma case and the (right) 25 May 2016 Kansas case. The larger outer nest is shown in a thick black line, the inner nest is shown in a thin black line, and the zoomed-in domain plotted in subsequent figures is shown with a dotted line. The radar site used for each case is labeled.

6.3.3 Assimilation procedures

The 12-km North American Mesoscale (NAM) model analysis and forecast data were used to initialize the parent domain. For the OK case, the 19 May 2013 18:00 UTC NAM analysis was used, and for the KS case the 2-h forecast from the 25 May 2016 18:00 UTC NAM (valid at 20:00 UTC) was used. The NAM data were interpolated onto the 4-km ARPS grid, which was then integrated forward for 1 h using 3-h lateral boundary conditions derived from the NAM. This forecast was then further interpolated down to the inner nest and integrated forward another 1 h, with boundary conditions on

Table 6.2: Summary of ARPS model setup used for all experiments.

Model Parameter	Value/Description	
	Control	ZDRCOL
Outer horizontal domain size	1200 x 1200	
Outer horizontal grid spacing	$\Delta x = \Delta y = 4$ km	
Inner horizontal domain size	500 x 500	
Inner horizontal grid spacing	$\Delta x = \Delta y = 1$ km	
Vertical grid spacing	Stretched grid with mean $\Delta z = 400$ m and minimum $\Delta z = 100$ m across 53 levels	
Time step	2 s	
Physics	Nonhydrostatic	
Coriolis	On	
Computational mixing	4th-order	
Lateral boundary conditions	Externally forced	
Upper boundary condition	Rigid top with Rayleigh damping layer at $z = 12000$ m	
Microphysics	Milbrandt-Yau double moment scheme (Milbrandt and Yau 2005a,b)	
Radiation	NASA Goddard shortwave and longwave schemes (Chou 1990, 1992)	
Surface	Surface fluxes dependent on stability, temperature, and volumetric water content	
Turbulence	1.5-TKE scheme with Sun and Chang (1986) boundary layer scheme	
Cloud Analysis	Legacy	Modified (see Table 6.1)

the inner nest updated at 30-min intervals from the outer nest, for a total spin-up period of 2 h. This forecast was then used as the background for all assimilation experiments performed.

Assimilation cycles were performed every 10 minutes following Hu and Xue (2007), who found this to be the optimal cycling frequency in their experiments. Radial velocity data were assimilated using the ARPS 3D-Var routine (Gao et al. 2004; Hu et al. 2006b), after which the cloud analysis routine was called. For the OK case, Oklahoma Mesonet data (Brock et al. 1995) were also assimilated using the 3D-Var routine. After 30-min, a separate 1-h forecast was made, with 10-min assimilation cycles continuing. One-hour forecasts were subsequently initiated every 30-min for three hours after the initial analysis time. A diagram of the spin-up, cycling, and assimilation process is shown in Figure 6.5. For the OK case, radar data from the Twin Lakes, Oklahoma WSR-88D (KTLX) were used, whereas the KS case used data from the Topeka, Kansas WSR-88D (KTWX) (Fig. 6.4). For each case, two runs were performed: a control run (hereafter, "Control"), in which the legacy cloud analysis is used (see section 3.1.4.2), and an experimental run (hereafter, "ZDRCOL"), which employed the modified polarimetric cloud analysis described in section 6.2.

Specific nomenclature for each experiment will be referred to hereafter by their case and which cloud analysis method was used (e.g., "KS_ZDRCOL" refers to the 25 May 2016 KS case experiment employing the modified cloud analysis).

6.4 Results

6.4.1 19 May 2013 Case

To investigate the performance of the Z_{DR} column detection algorithm, a composite plot of observed 1-km Z and analyzed Z_{DR} column depth from the KTLX radar observations in 10-min intervals for the assimilation period is shown in Figure 6.6. Each of the three swaths associated with a supercell is labeled and will be used to reference each storm

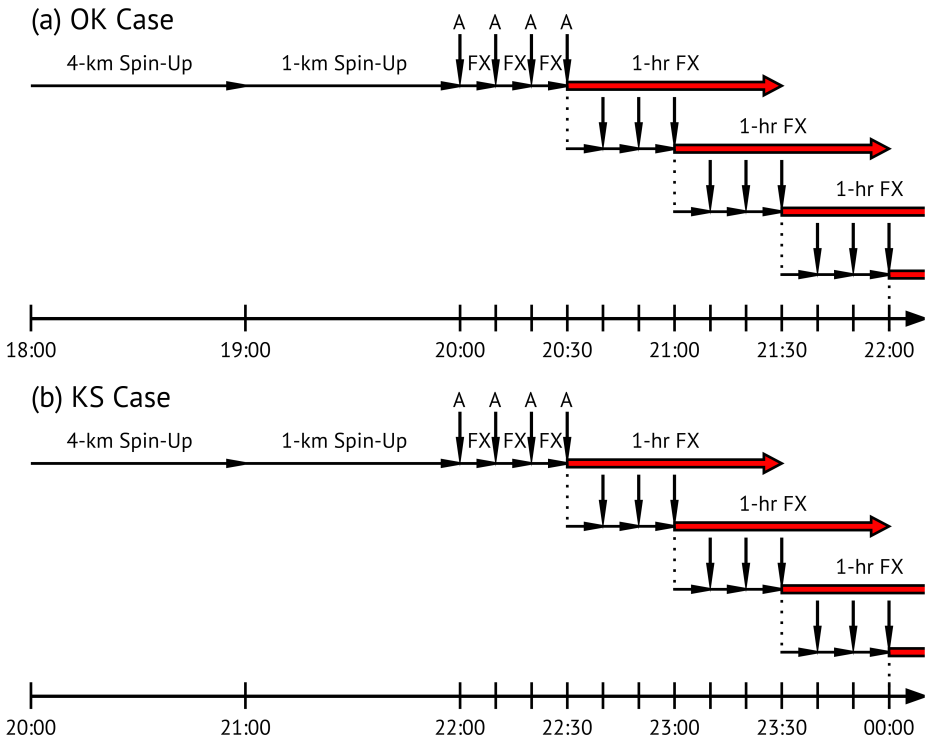

Figure 6.5: Diagram showing the spin-up and assimilation cycles used for the (a) OK Case and the (b) KS Case. 'FX' represents forecasts, whereas 'A' represents assimilation cycles encompassing the ARPS 3D-Var + Cloud Analysis routines. The 0-1 h forecasts initiated every 30-min are denoted by red arrows. The dotted lines indicate a continuation of the 10-min assimilation cycles in addition to the initiated 0-1 h forecast.

in the subsequent discussions. The 15-dBZ contour is also shown as that is the default threshold for saturation in the original cloud analysis routine. Distinct Z_{DR} column tracks are evident for all three primary storms, with all storms exhibiting prominent Z_{DR} columns during their formative stages before becoming more intermittent, supporting the use of Z_{DR} columns for spinning up storms in the model early in their lifecycle. In each case, the Z_{DR} column is found on the southwest flank of the storm where the main updraft is expected to be located. The only exception to this is for the weakening and fast-moving cell north of Oklahoma City that propagates to the left of the mean wind off to the north-northeast. The supercell that begins to the west of Oklahoma City ("Supercell 1" in Fig. 6.6) exhibits a large, deep Z_{DR} column from its inception that travels toward the northeast and then turns to the east-northeast before producing the first tornado. The Z_{DR} column then shrinks and becomes shallower near and after the first tornado dissipates; the Z_{DR} column associated with the main updraft becomes more robust shortly after the genesis of the second tornado east-northeast of Oklahoma City, near the observed track. Two more Z_{DR} column tracks are evident south of Oklahoma City, with the middle track ("Supercell 2") associated with a smaller Z_{DR} column as it tracked northeast. The southernmost storm ("Supercell 3") exhibited a larger and taller Z_{DR} column that suddenly weakened and never fully reappeared. The period analyzed here ends at 23:00 UTC, the approximate start time of the long-track southern tornado southeast of Oklahoma City. However, no clear Z_{DR} column is evident here due to the close proximity of the updraft to the radar (i.e., the Z_{DR} column was likely located within the cone of silence, which extends out to $\approx$12 km from the radar at a height of 4 km AGL), although additional obfuscation by hail or tornadic debris cannot be ruled out. This is a known drawback that should be taken into consideration when using any methods that use vertically integrated data or echo top heights from a single radar.

The areas encompassed by the 15-dBZ threshold are much larger and extend further to the north and east of the analyzed Z_{DR} columns. For this and all subsequent figures

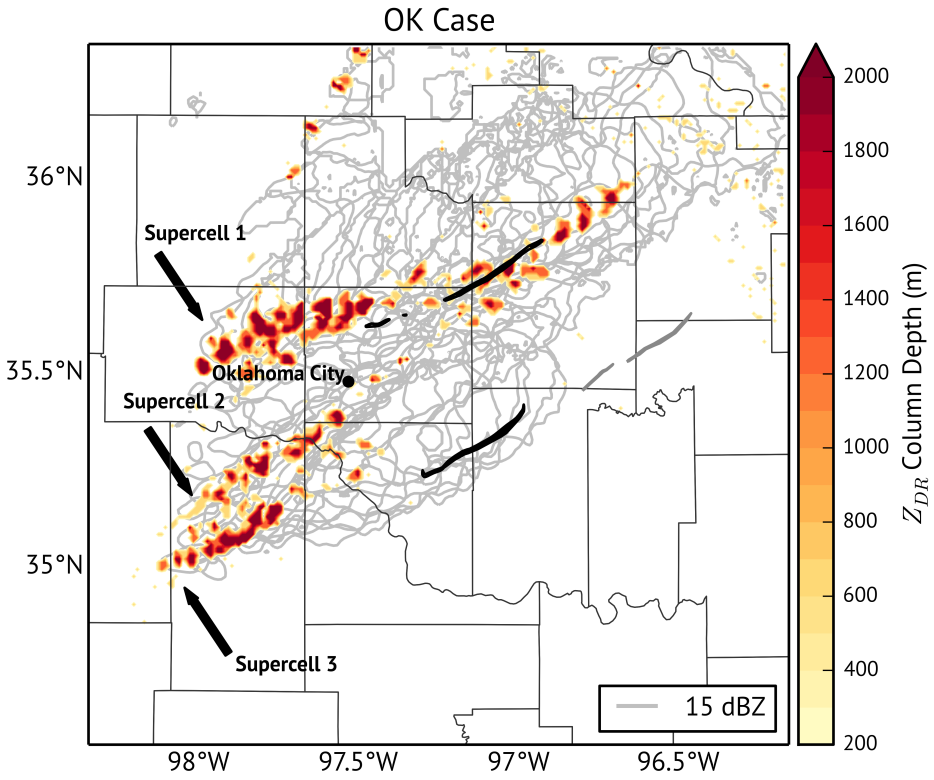

Figure 6.6: Composited remapped Z (15-dBZ contour in gray) and analyzed Z_{DR} column depth (color shaded, in m, and defined as the height of the 1.0-dB surface above the environmental 0°C level) between 20:00-23:00 UTC in 10-min intervals for the 19 May 2013 case using the detection criteria listed in Table 6.1. Observed tornado tracks are shown in black and gray, with gray tracks indicating observed tornadoes that fall outside of the period of study.

for the OK case the two easternmost tornadoes (shown in gray in Fig. 6.6) occurred after the period examined in this experiment.

Composite plots of the maximum analyzed w (contoured at 30 m s^{-1}) at each grid point for both OK_Control and OK_ZDRCOL through the assimilation period (20:00 - 23:00 UTC) are shown in Figure 6.7. OK_Control exhibits a rather noisy w field composed of many spurious updrafts, along with a pronounced northward bias compared to the observed tornado tracks. This northern and positive forward speed bias has been observed in many storm-scale modeling studies (e.g., Potvin et al. 2014; Xue et al. 2014; Stratman and Brewster 2015; Wheatley et al. 2015). In sharp contrast, OK_ZDRCOL features much more consolidated updraft tracks that closely follow the analyzed Z_{DR} column paths (and observed tornado tracks). As in Figure 6.6, the final analysis included is at 23:00 UTC near the beginning of the long-track tornado southeast of Oklahoma City, evident with a large and strong updraft in excess of 40 m s^{-1} near the start of the tornado track that is not as apparent in OK_Control. The 30 m s^{-1} contours also seem to be larger in OK_ZDRCOL than in OK_Control, suggest wider, stronger updrafts.

The composited 1-6 km above-ground-level (AGL) updraft helicity (Kain et al. 2008) swaths for three different forecast periods are shown in Figure 6.8. Model output was saved every 5 minutes and composited over the 1-h forecast, with the maximum for the forecast period shown at each grid point. The 1-6 km updraft helicity provides a reasonable depiction of the path of mesocyclones and overall storm track. To aid in verifying the forecast updraft helicity swaths, rotation tracks derived from the Multi-Radar/Multi-Sensor (MRMS; Smith et al. 2016) system, which are composited maximum values of radar-derived azimuthal shear (Smith and Elmore 2004) in a layer through a given time period, are included in Figure 6.8. While the traditional azimuthal shear product uses 0-2 km or 3-6 km AGL layers, the 1-6 km AGL azimuthal shear was used in this study to better correspond with the 1-6 km updraft helicity derived from the

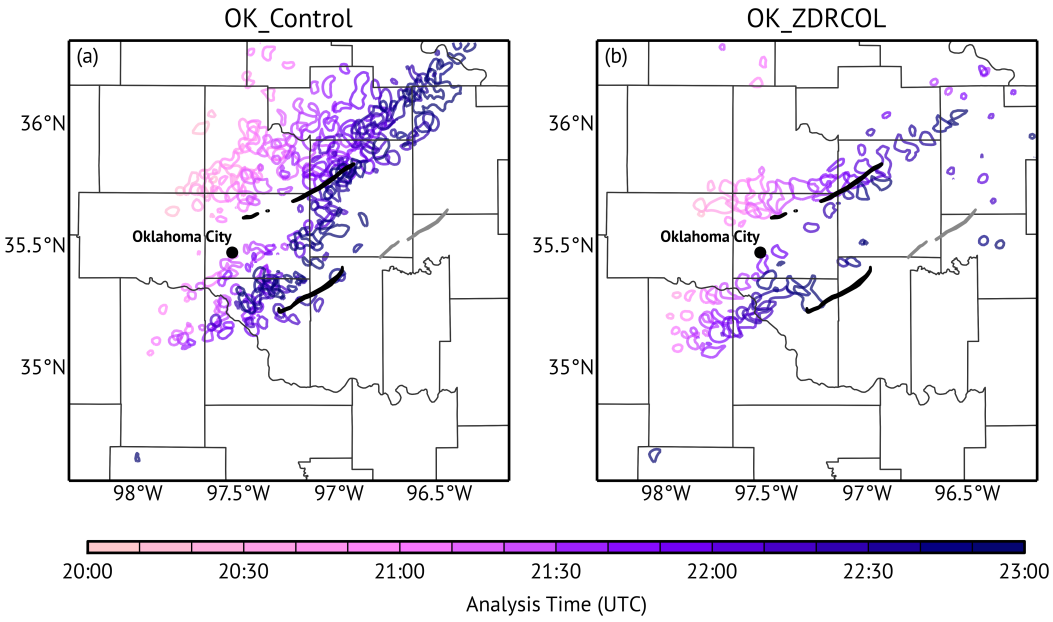

Figure 6.7: Composited maximum vertical velocity in each grid column for each of the post-assimilation analyses from 20:00 UTC through 23:00 UTC for the 19 May 2013 case for the (a) OK_Control case and (b) OK_ZDRCOL case, colored according to their corresponding analysis time and showing the 30 m s^{-1} vertical velocity contour line. Observed tornado tracks are shown in black and gray, with gray tracks indicating observed tornadoes that fall outside of the period of study.

model output. The rotation tracks shown in Figure 6.8 correspond to the 1-h forecast periods shown in each panel.

During the first 0-1 h forecast at 20:30 UTC (Fig. 6.8a,b), both OK_Control and OK_ZDRCOL feature a storm track for Supercell 1 that is located too far north. The updraft helicity swath in OK_ZDRCOL, however, is more consolidated and features a smaller northward bias compared to OK_Control. Supercell 1 in OK_ZDRCOL has a slower mean storm motion, with the center of the updraft helicity swath covering approximately 10 fewer km than OK_Control during the forecast period. Finally, OK_ZDRCOL features a weak updraft helicity swath associated with the second developing storm (Supercell 2, southwest of Oklahoma City) that is absent in the OK_Control run.

The improvements of OK_ZDRCOL over OK_Control are most pronounced in the forecast initiated at 21:30 UTC (Fig. 6.8c,d), approximately 10 minutes before the start of the long-track tornado northeast of Oklahoma City. OK_Control features multiple updraft helicity swaths. There is no identifiable strong updraft helicity swath coincident with the observed rotation track of Supercell 1, with instead a very strong and prominent updraft helicty swath displaced far to the northeast of the observed rotation track and corresponding tornado. Moreover, there are two notable updraft helicity swaths corresponding to the weakening rotation track of Supercell 2 southeast of Oklahoma City, with no updraft helicity swath that clearly corresponds with the rotation track for Supercell 3. In stark contrast, OK_ZDRCOL captures the updraft helicty swath of Supercell 1 well, with the forecast swath nearly coincident with the observed rotation track and with only a slight bias in forward speed. It also correctly captures the updraft helicity swath associated with Supercell 2 that weakens as it moves to the northeast. Finally, the early development of strong rotation in the southernmost supercell (Supercell 3) that would go on to produce the Shawnee tornado is depicted to the south of Oklahoma City while being absent in OK_Control.

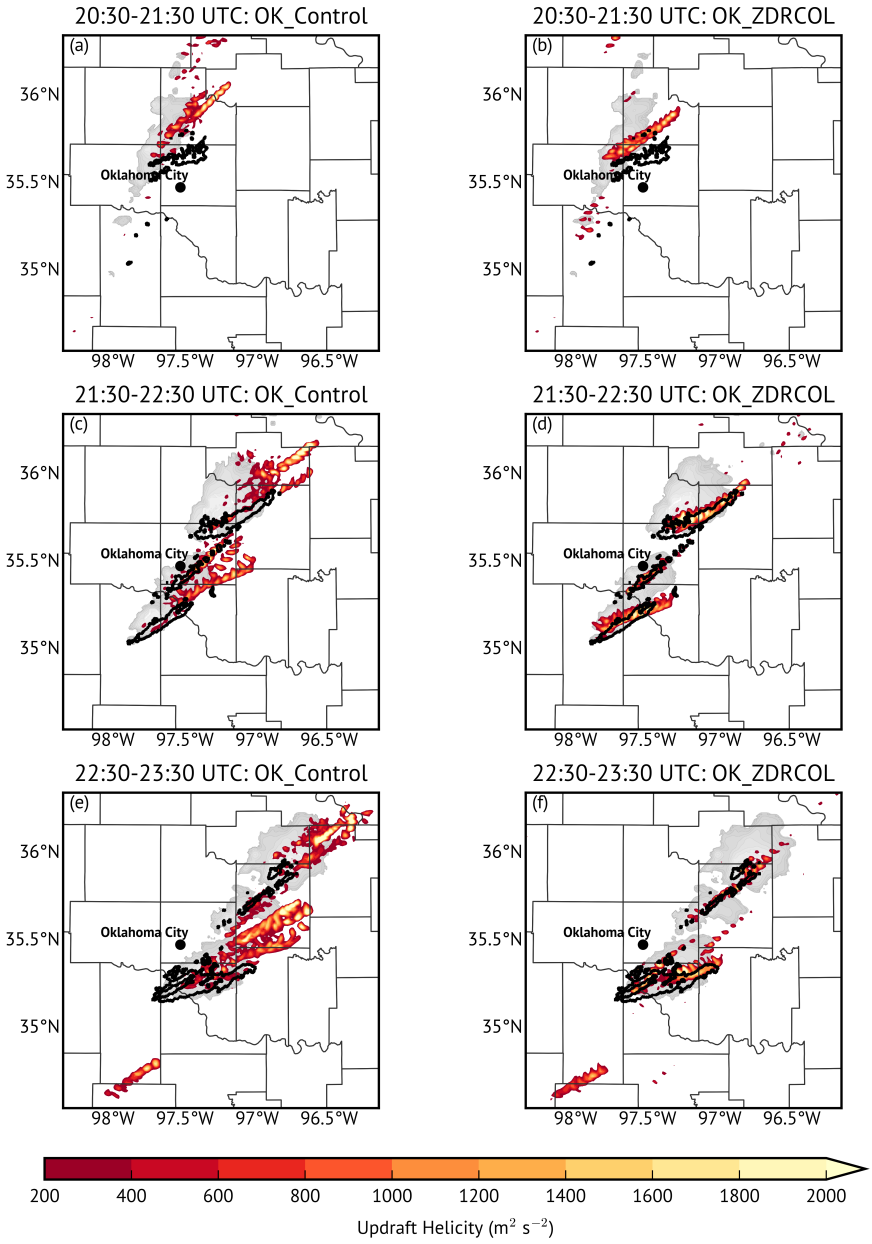

Figure 6.8: Composited 1-6 km AGL updraft helicity (m^2 s^{-2}, red shading) at each grid point for (a,c,e) OK_Control and (b,d,f) OK_ZDRCOL for the 0-1 h forecasts beginning at (a,b) 20:30 UTC, (c,d) 21:30 UTC, (e,f) 22:30 UTC. MRMS-derived 1-6 km AGL rotation tracks (black contours, 0.01 s^{-1} shown) are included for each 1-h period. The initial 1-km *Z* of each 1-h period is shown for reference (grayscale shading).

The 22:30 UTC 0-1 h forecast (Fig. 6.8e,f) show many of the same improvements. Both Supercells 1 and 2 were non-tornadic and beginning to weaken, with less pronounced updraft helicity swaths in OK_ZDRCOL. In contrast, OK_Control has strong but noisy updraft helicity swaths for these storms displaced to the northeast of these storms. For Supercell 3, both OK_Control and OK_ZDRCOL exhibit updraft helicity associated with the strong and broad observed rotation track south of Oklahoma City. However, the updraft helicity swath in OK_Control is primarily north and east of the observed rotation track, whereas OK_ZDRCOL captures the rotation (albeit with a slight north bias) and its timing well.

To further examine the improvements in the OK_ZDRCOL forecasts over OK_Control, the 1-km AGL Z is shown for the forecasts initiated at 21:30 UTC in 20-min increments and compared to the observed radar fields in Figure 6.9. This time period represents the duration of the northern long-track tornado northeast of Oklahoma City, which was on the ground between 21:41 UTC and 22:24 UTC, as well as the lead up period to the long-track tornado produced by Supercell 3, which first touched down at 23:00 UTC. For both the OK_Control and OK_ZDRCOL runs, an adjustment period is seen in the first twenty minutes (Figs. 6.9e,f) with small, yet intense, precipitation cores ($Z \geq 65$ dBZ) present. These high values of Z occur within the core of the middle and northern storms (Supercells 1 and 2) in OK_Control (Fig. 6.9e), whereas in OK_ZDRCOL these high Z values are predominantly near the southern flank of the storms and/or within the hook echoes, where the Z_{DR} columns were analyzed. Later in the forecast period (22:10-22:30 UTC), it is again clear that the OK_Control run features a northward and positive forward speed bias (Fig. 6.9h,k) compared to the observations (Fig. 6.9g,j). Supercell 2 fails to remain distinct, and by 22:30 UTC unobserved banding features are seen in the OK_Control run (Fig. 6.9k). The storms are also larger than those observed, with large areal coverage of $Z \geq 45$ dBZ. In contrast, the OK_ZDRCOL run is much closer to the observations. Although a small northeastward bias does still exist, the forecast

storms are in better agreement with the observations in terms of size and position, with three distinct storms featuring identifiable hook echoes and broad supercellular features present 1-h into the forecast (Fig. 6.9l).

Based on these encouraging qualitative results, the equitable threat scores (ETS) and frequency biases were computed for a quantitative look at the performance of OK_Control and OK_ZDRCOL. The ETS, also known as the Gilbert Skill Score (Gilbert 1884), is given by

$$ETS = \frac{H - H_{rdn}}{M + F + H - H_{rdn}} \tag{6.1}$$

where H is the number of hits, M is the number of misses, F is the number of false alarms, and H_{rdn} is the number of hits expected due to random chance, given by

$$H_{rdn} = \frac{(H+M)(H+F)}{N} \tag{6.2}$$

where N is the total number of forecast points included in the calculation. The ETS is calculated on a gridpoint basis satisfying or exceeding a defined (here Z) threshold, with a value of 1.0 indicating a perfect forecast and 0.0 indicating no forecast skill. The bias is calculated from

$$Bias = \frac{H+F}{H+M} - 1 \tag{6.3}$$

and provides a ratio of the number of forecast grids and the number of observed grids exceeding a threshold, normalized to zero. A bias of zero indicates no bias, whereas a positive bias indicates an overestimate of Z exceeding a threshold. Both the ETS and bias were calculated for the composite Z at 20, 30, and 40 dBZ thresholds and are shown for the OK case in Figure 6.10. Note that the ETS at the analysis time is not necessarily equal to 1.0 due to both smoothing procedures and differences in how Z is calculated: the observations are being compared against simulated Z derived from a T-matrix code for the single-species hydrometeor distribution that was retrieved from the cloud analysis. The ETS for the 20-dBZ threshold (Fig. 6.10a) are comparable between the two experiments, but notable improvements in ETS are seen in OK_ZDRCOL over

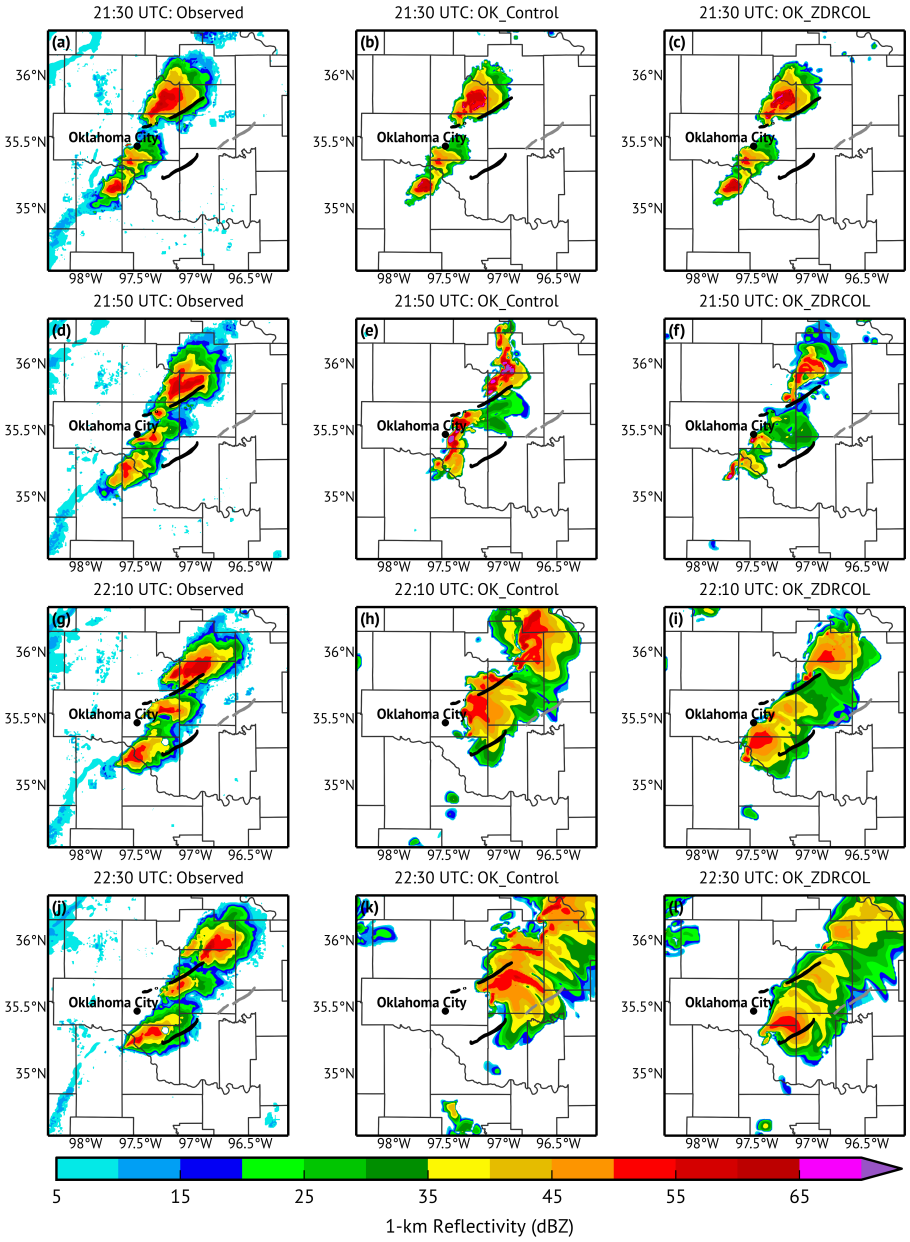

Figure 6.9: Plots of (left) observed 1-km AGL Z from KTLX remapped to the ARPS grid, and corresponding forecasts from the (middle) OK_Control and (right) OK_ZDRCOL runs for the 0-1 h forecast beginning at 21:30 UTC for the 19 May 2013 case. Plots are shown for (a)-(c), the analysis at 21:30 UTC, (d)-(f) 20-min forecast at 21:50 UTC, (g)-(i) 40-min forecast at 22:10 UTC, and (j)-(l) 60-min forecast at 22:30 UTC. Observed tornado tracks are shown in black.

OK_Control for high Z thresholds (Figs. 6.10c,e). The ETS for OK_ZDRCOL remains superior for the entire 1-h duration of every forecast, showing a noteworthy positive impact of Z_{DR} column assimilation. Both OK_Control and OK_ZDRCOL exhibit generally positive biases that increase with time at all three Z thresholds. For all forecasts at all times, however, OK_ZDRCOL features smaller biases (Figs. 6.10b,d,f). This tendency toward smaller Z biases in OK_ZDRCOL is also seen in 1-km Z for the 21:30 UTC forecast (Fig. 6.9).

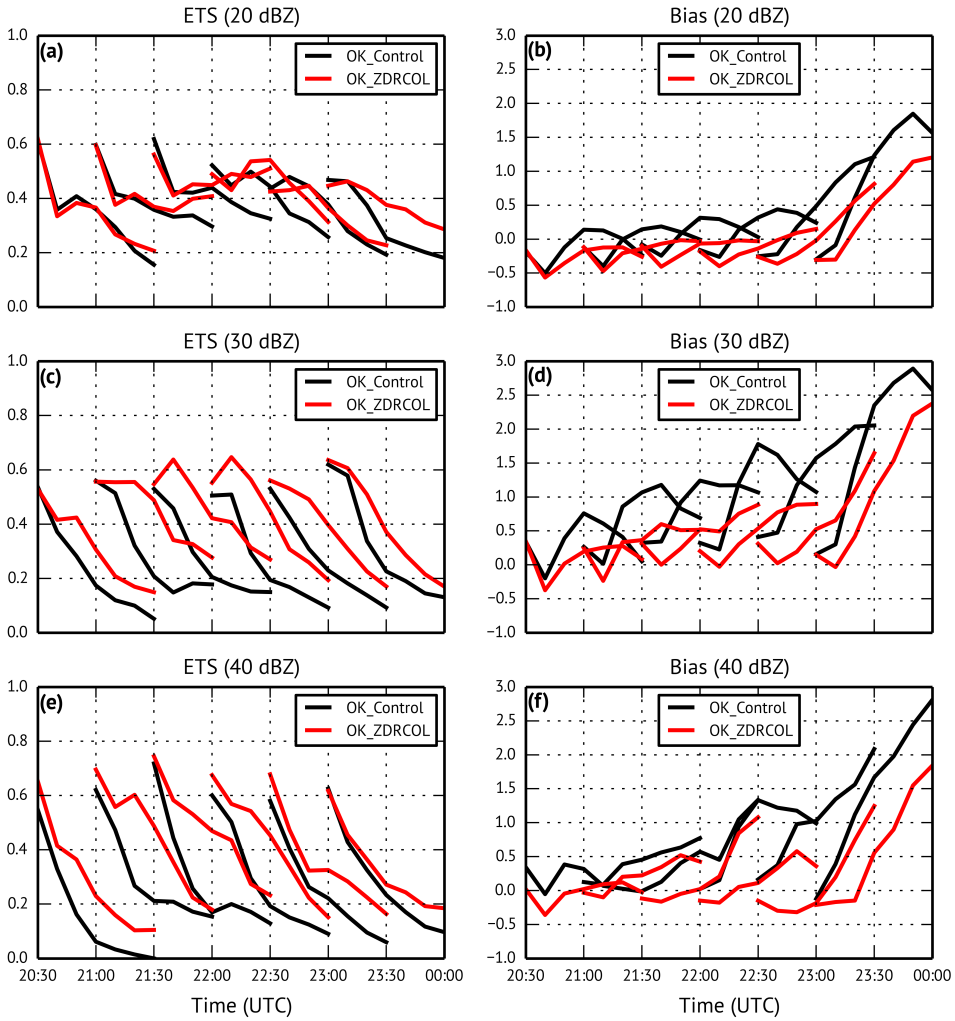

Figure 6.10: Equitable threat score and bias of composite Z at (a,b) 20 dBZ, (c,d) 30 dBZ, and (e,f) 40 dBZ thresholds for each of the 0-1 h forecasts for the OK case.

6.4.2 25 May 2016 Case

The KS case presents a somewhat more challenging forecast scenario owing to a complex evolution of the supercell and the greater distance between the supercell and the radar. After becoming mature, the main supercell began moving slowly to the southeast. A new storm developed to the southwest of the main supercell, which produced a left-moving supercell that moved off to the north-northeast before merging with the primary supercell. Additional convection also formed along, and was absorbed into, the southern flank of the forward flank downdraft in the supercell. This storm was further away from the radar than the storms in the OK case were (initiation occurred approximately 140 km away from the radar compared to 65 km away from the radar in the OK case), resulting in a decrease of the quality of radar data available for assimilation due to both decreased low-level coverage and increasing radar resolution volume ($\approx$0.22 km^3 at a 65 km range vs. $\approx$1.01 km^3 at a 140 km range for a 0.5° elevation angle). Additionally, in contrast to the OK case, this case lacked the assimilation of Mesonet surface observations.

A long, continuous swath of detected Z_{DR} columns are shown for the duration of the period analyzed in the southwest corner of the supercell where the main updraft is expected to be located (Fig. 6.11). The Z_{DR} column's width and depth increases shortly before the start of the long-track tornado northeast of Salina, KS, and the Z_{DR} column remains broad and deep until the end of the tornado, near the end of the assimilation period. A second Z_{DR} column swath is seen with the left split of the supercell as it moves off to the north-northeast. This column weakens near the end of the assimilation period, and the storm weakened shortly thereafter. As in the OK case, the easternmost tornado falls outside the analyzed period for this case.

The composite plot of maximum w in the analyses for the KS case shows many of the same improvements documented in the OK case (Fig. 6.12). The KS_Control case shows a more disorganized and less coherent updraft path, with many spurious updrafts

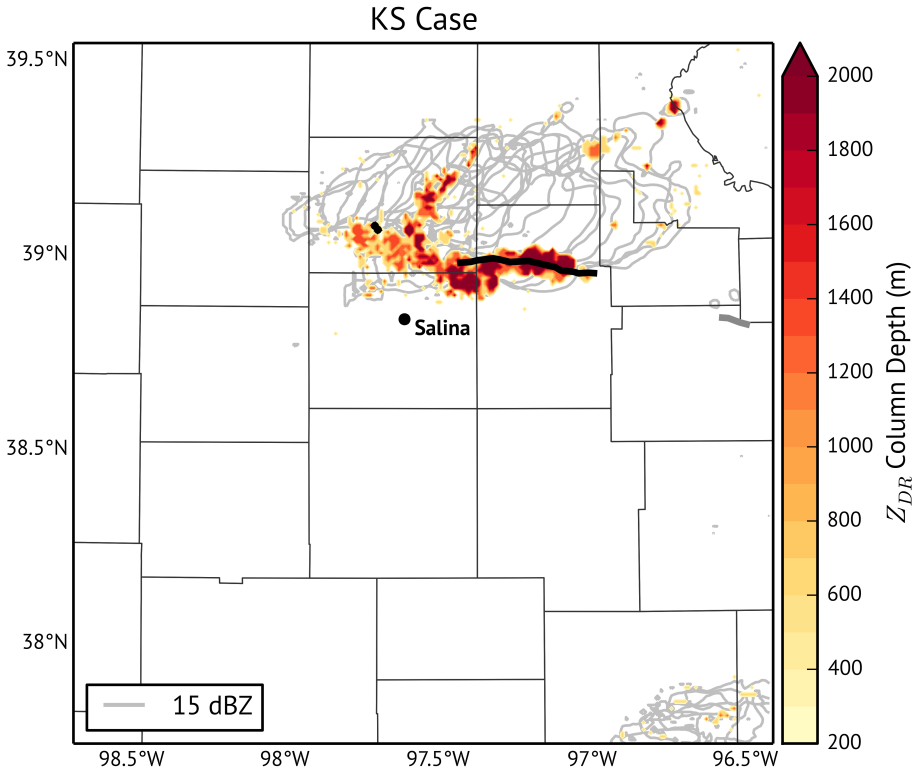

Figure 6.11: Composited remapped Z (15-dBZ contour in gray) and analyzed Z_{DR} column depth (color shaded, in m) between 22:00-01:00 UTC in 10-min intervals for the 25 May 2016 case using the detection criteria listed in Table 6.1. Observed tornado tracks are shown in black and gray, with gray tracks indicating observed tornadoes that fall outside of the period of study.

to the north of the main supercell path and observed tornado tracks (Fig. 6.12a). Considering that the end of the assimilation period is near the ending time of the long-track tornado, the general progression of the analyzed updrafts is also too fast. In contrast, KS_ZDRCOL features a much more coherent updraft swath with a slower forward motion to the east-southeast and a path closer to the observed tornado track (Fig. 6.12b). KS_ZDRCOL also features less spurious convection than KS_Control in the central and southern parts of the domain.

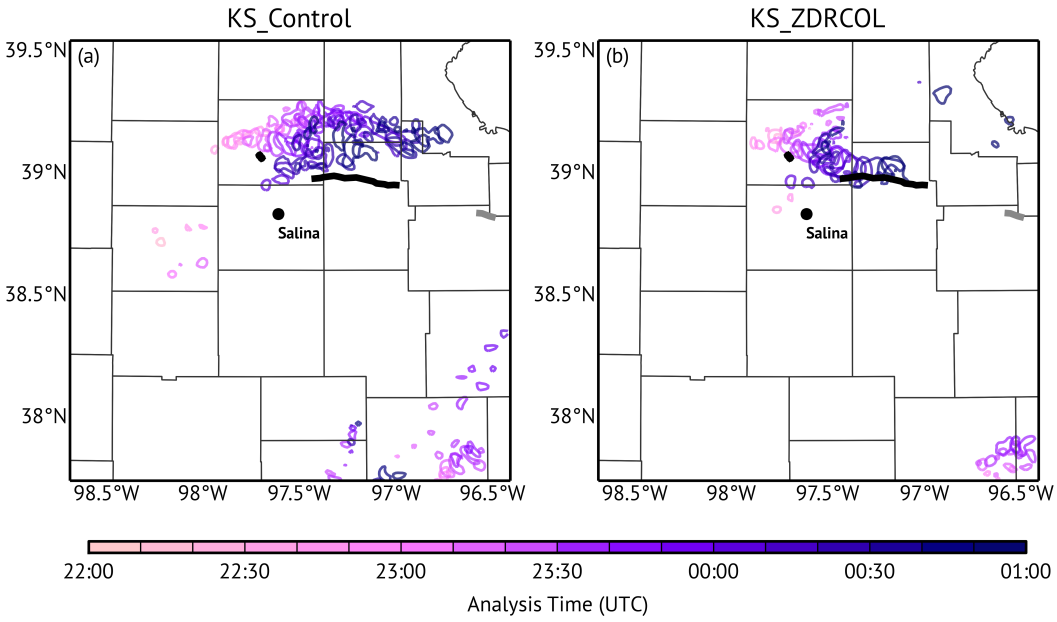

Figure 6.12: Composited maximum vertical velocity in each grid column for each of the post-assimilation analyses from 22:00 UTC through 01:00 UTC for the 25 May 2016 case for the (a) KS_Control case and (b) KS_ZDRCOL case, colored according to their corresponding analysis time and showing the 30 m s^{-1} vertical velocity contour line. Observed tornado tracks are shown in black and gray, with gray tracks indicating observed tornadoes that fall outside of the period of study.

A comparison of 1-6 km updraft helicity with MRMS-derived rotation tracks, similar to Figure 6.8, is shown for the KS case in Figure 6.13. The forecasts selected here were chosen to coincide with the long-track tornado. In the forecast initiated at 23:00

UTC (Fig. 6.13a,b), both KS_Control and KS_ZDRCOL produce a developing supercell north of Salina with an unorganized updraft and an east-northeast motion. The observed rotation tracks show only slight, messy rotation during this period. Starker differences are seen for the 00:00 UTC forecast (Fig. 6.13c,d). KS_Control features a disorganized updraft helicity swath displaced far to the north of the observed rotation track. In contrast, KS_ZDRCOL features a consolidated updraft helicity swath through the duration of the forecast period along and just north of the observed rotation track, although a slight slow bias in forward speed is evident. These same general patterns are also observed for the 01:00 UTC forecast, with a noisy updraft helicity field too far to the northeast in KS_Control; KS_ZDRCOL exhibits a large, southeastward-directed updraft helicity swath displaced slightly southwest of the observed rotation track.

An example of observed and forecast 1-km Z for both KS_Control and KS_ZDRCOL is shown in Figure 6.14 for the 00:00 UTC forecast. This 1-h period begins near the start time of the primary long-track tornado and features a complex evolution involving the secondary storm to the southwest splitting and merging with the main supercell (Figs. 6.14a,d,g,j). As such, both KS_Control and KS_ZDRCOL struggle to accurately predict the evolution of the storm during this period. A very large and elongated forward flank downdraft not seen in the observed Z quickly develops and extends to the east-southeast and east-northeast in KS_Control and KS_ZDRCOL, respectively. This forward flank precipitation seems to stem from weak upper-level Z in the anvil in the observations. Despite this, KS_ZDRCOL features a more realistic supercell structure 20-min into the forecast (Fig. 6.14f) compared to KS_Control (Fig. 6.14e), with a well defined hook echo and rear flank downdraft near the observed tornado track. Neither KS_Control nor KS_ZDRCOL clearly capture the left-splitting supercell. An erroneous region of moderate Z (i.e., 25-35 dBZ) within the inflow region of the supercell is also seen in the KS_Control run (Fig. 6.14e) that is not seen in the KS_ZDRCOL run. Both KS_Control and KS_ZDRCOL generally feature Z values that are too low (by $\approx$5-10 dBZ) compared

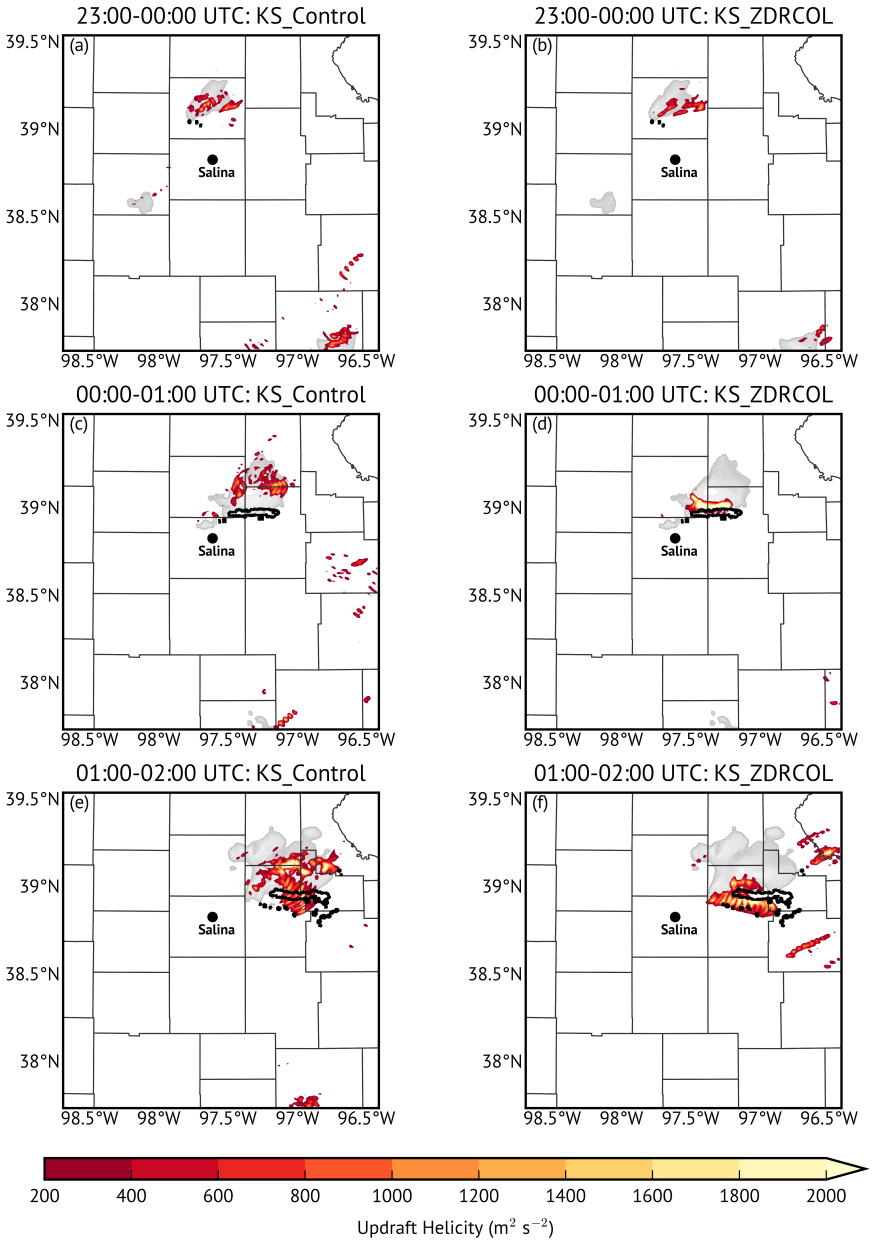

Figure 6.13: Composited 1-6 km AGL updraft helicity (m^2 s^{-2}, red shading) at each grid point for (a,c,e) KS_Control and (b,d,f) KS_ZDRCOL for the 0-1 h forecasts beginning at (a,b) 23:00 UTC, (c,d) 00:00 UTC, (e,f) 01:00 UTC. MRMS-derived 1-6 km AGL rotation tracks (black contours, 0.01 s^{-1} shown) are included for each 1-h period. The initial 1-km *Z* of each 1-h period is shown for reference (grayscale shading).

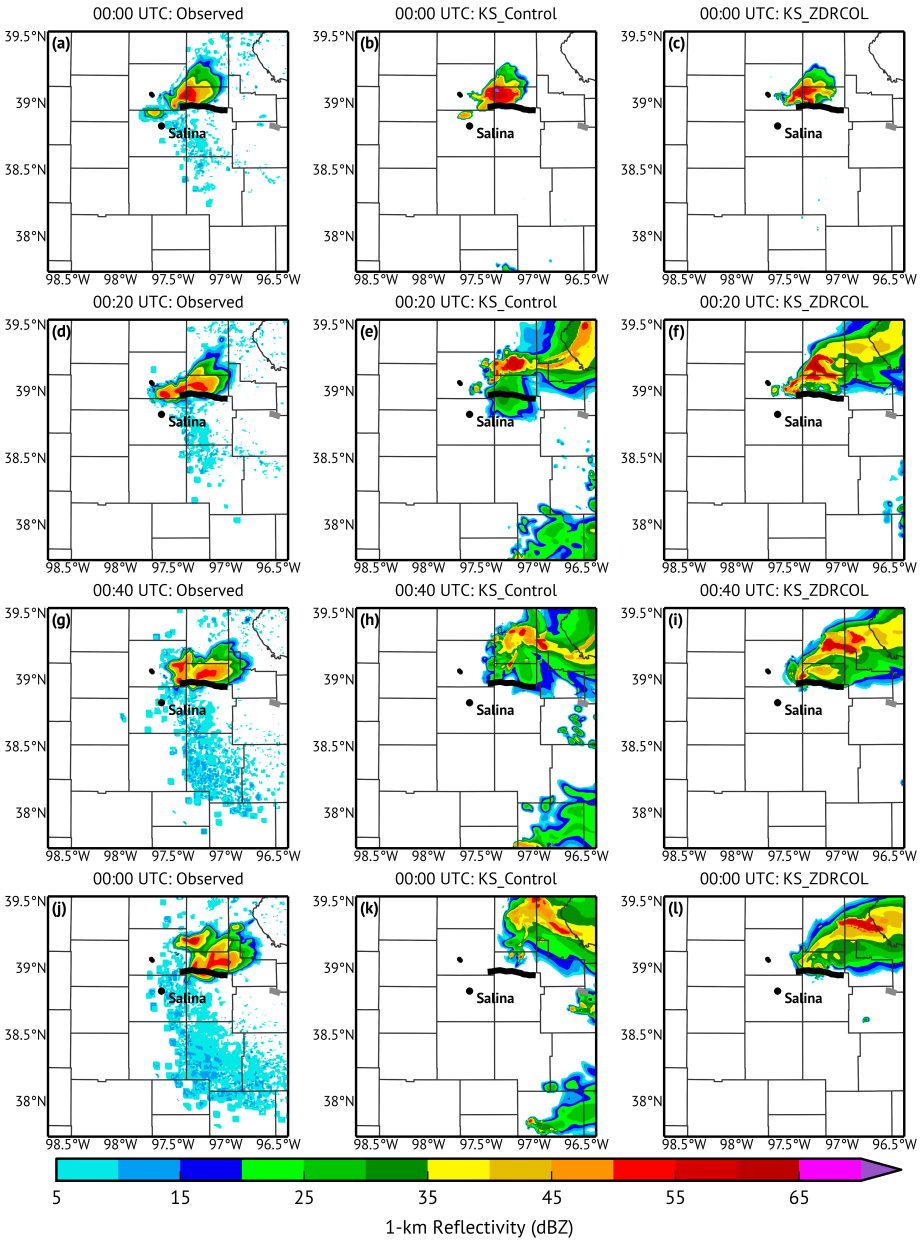

Figure 6.14: Plots of (left) observed 1-km AGL Z from KTWX remapped to the ARPS grid, and corresponding forecasts from the (middle) KS_Control and (right) KS_ZDRCOL runs for the 0-1 h forecast beginning at 00:00 UTC (on 26 May) for the 25 May 2016 case. Plots are shown for (a)-(c), the analysis at 00:00 UTC, (d)-(f) 20-min forecast at 00:20 UTC, (g)-(i) 40-min forecast at 00:40 UTC, and (j)-(l) 60-min forecast at 1:00 UTC. Observed tornado tracks are shown in black and gray, with gray tracks indicating observed tornadoes that fall outside of the period of study.

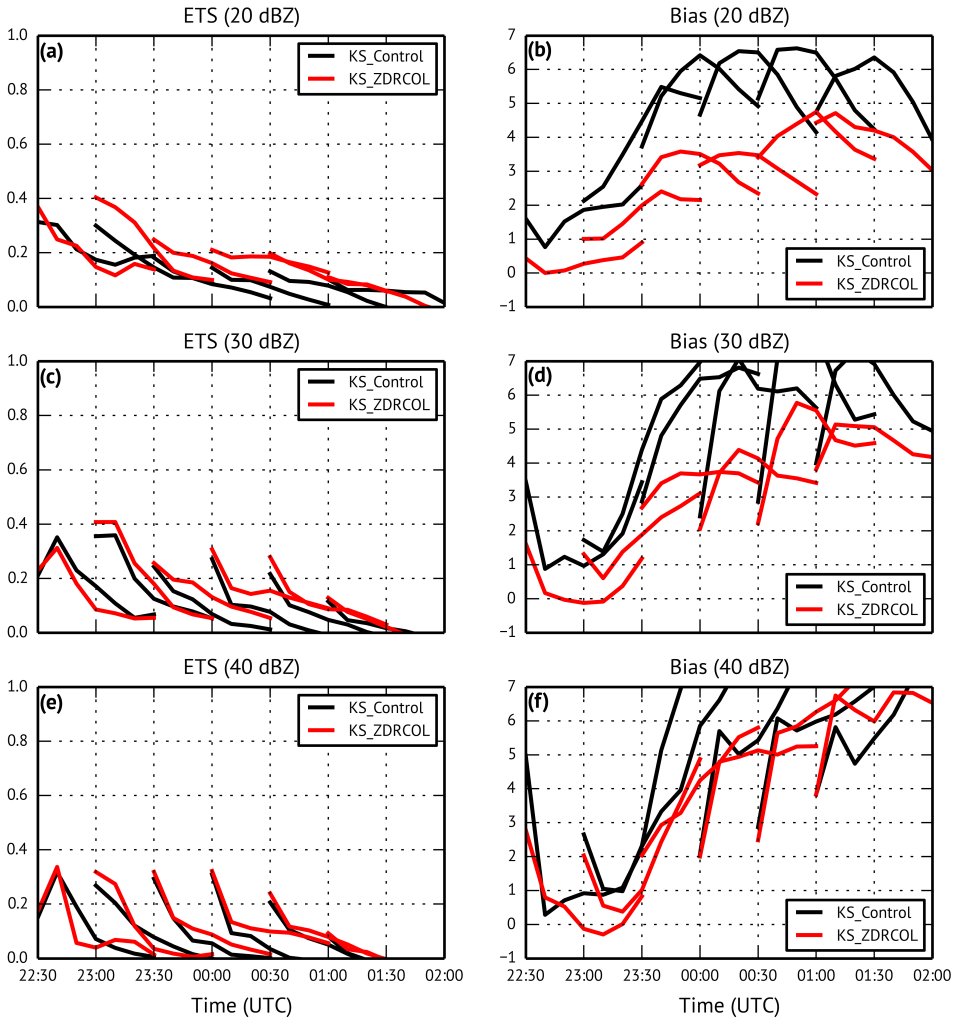

Figure 6.15: As in Fig. 6.10, but for the KS case.

to observations outside of the forward flank downdraft. Overall, KS_ZDRCOL features a slower and noticeably more accurate forecast track of the hook echo than KS_Control (as also seen Figs. 6.13c,d), as well as a more realistic looking hook echo (Fig. 6.14i,l vs. Fig. 6.14h,k) .

Quantitatively, KS_ZDRCOL generally exhibits improvements over KS_Control with larger ETS scores and smaller biases, although the improvements in ETS scores are more mixed than in the OK case, with lower scores for the first two forecasts in the period (Fig. 6.15). Overall scores are lower in the KS case compared to the OK case, in part due to the challenging nature of the forecast and in part due to the aforementioned biases in Z (e.g., Fig. 6.15b,d,f) and the extensive forward flank downdrafts, which generally exceed the biases seen for the OK case, particularly for later forecasts.

6.5 Summary and Future Work

In this work, the potential for the assimilation of polarimetric radar data observations via a cloud analysis technique to aid in the spin-up and forecast of convection in storm-scale NWP models is examined. Z_{DR} columns are ubiquitous features of deep moist convection that are coincident with updrafts and, thus, with areas of saturation and latent heat release. Based on this premise, a Z_{DR} column detection algorithm is developed to identify Z_{DR} columns and (1) insert positive temperature and moisture perturbations at these locations and (2) remove modest amounts of moisture outside of these locations where Z exceeds 15 dBZ. To evaluate this method, two cases are analyzed: the 19 May 2013 tornadic supercells in central Oklahoma and the 25 May 2016 tornadic supercell in north-central Kansas. For each case, two runs were performed to gauge the impact of these changes: a "Control" run using the original cloud analysis, and a "ZDRCOL" run using the newly-modified cloud analysis that incorporates dual-polarization radar data. The general conclusions are that:

1. The Z_{DR} column detection algorithm is shown to reliably identify Z_{DR} columns associated with convective updrafts. Z_{DR} columns are shown to be coincident with plumes of diabatic heating and saturation within updrafts, which occupy a much smaller region than the 15-dBZ contour, the default threshold for saturation with the cloud analysis.

2. The use of Z_{DR} columns in the cloud analysis results in more coherent and consolidated analyzed updraft tracks, with less spurious convection compared to the traditional cloud analysis analyses.

3. Short-term forecasts from analyses that assimilated Z_{DR} columns in the cloud analysis show a reduction in forward speed and northward position bias of the modeled storms than those using the traditional cloud analysis, a bias encountered in many storm-scale modeling experiments. Forecast 1-6 km AGL updraft helicity swaths agree better with radar-derived rotation tracks, and forecast Z fields agree better with observations both in terms of placement and general characteristics.

4. Quantitative verification scores bear out these qualitative conclusions, with generally improved ETS scores for large Z thresholds and reduced biases when using Z_{DR} columns in the cloud analysis than the traditional version.

These experiments represent a basic proof-of-concept investigation of the potential for assimilating Z_{DR} columns into storm-scale models and warrant further study. However, drawbacks to the method examined here exist that have yet to be addressed. First, although Z_{DR} columns are fairly ubiquitous in deep convection and are generally collocated with updrafts, they can be masked by the presence of hail or tornadic debris (Snyder et al. 2015) in the updraft, resulting in the intermittent appearance (or complete disappearance) of Z_{DR} columns; in some cases, Z_{DR} columns may not be observed in deep convection at all. Future work should examine the potential of using K_{DP} columns in a similar manner to alleviate these issues (van Lier-Walqui et al. 2016), although the

use of K_{DP} columns bears its own shortcomings (e.g., poor estimation of K_{DP} in areas of limited precipitation). The polarimetric version of the newly-developed Storm Labeling in Three Dimensions (SL3D) algorithm (Starzec et al. 2017), which has demonstrated success in identifying convective updrafts using a combination of weak-echo regions, Z_{DR} columns, and K_{DP} columns, may also prove particularly useful going forward. Figure 6.16 demonstrates the benefits of combining multiple forms of polarimetric updraft detection (e.g., Z_{DR} and K_{DP} columns) for the two cases presented in this chapter. The added benefit of K_{DP} columns is particularly evident for the OK case, which features intermittent Z_{DR} columns, particularly in the lead up to each of the long-track tornadoes. When combined with K_{DP} columns, a more continuous swath of detected updraft signatures is now available.

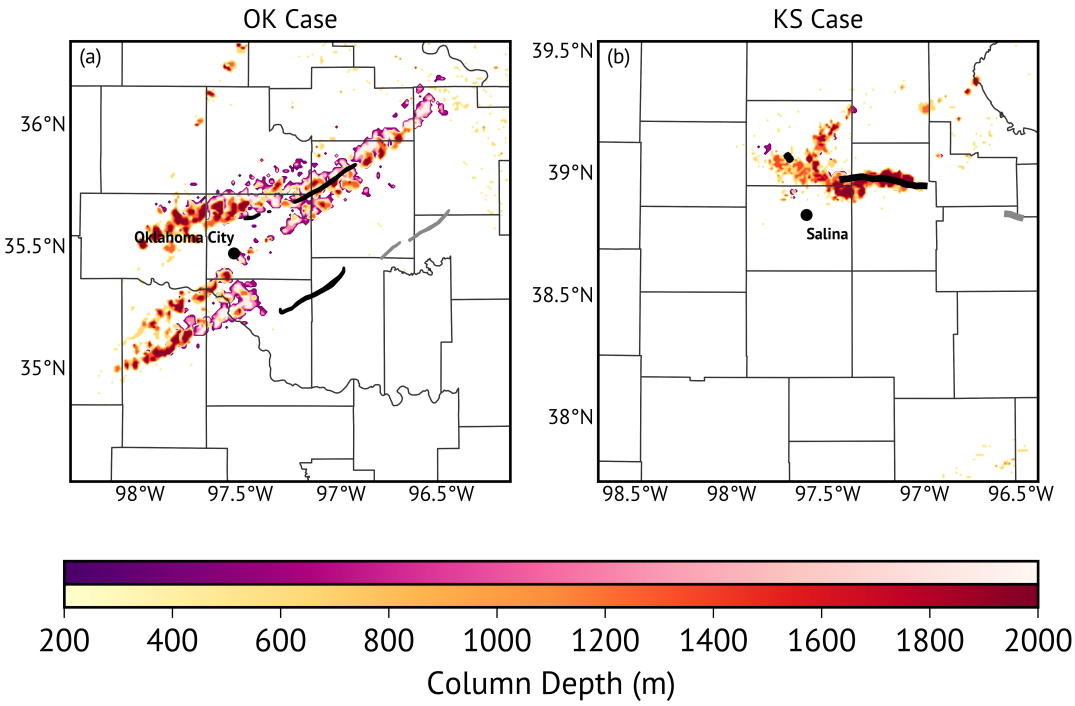

Figure 6.16: As in Figs. 6.6 and 6.11, but including K_{DP} column depth (purples, in m, and defined as the height of the 0.75-$^{\circ}$ km^{-1} surface above the environmental 0°C level in areas where $Z > 30$ dBZ, following Starzec et al. (2017)).

In addition to the aforementioned issues about intermittency, the use of Z_{DR} columns to aid the spin-up of precipitation in a NWP model may not be appropriate for weak convective storms and stratiform rain where Z_{DR} columns are ill defined or may not exist. Only two cases were analyzed in this study, with each being an archetypal case of very strong convection with good radar coverage and prominent Z_{DR} columns. Additional microphysics schemes should be testing to study whether the impacts observed in this study are consistent across schemes. The parameters both for detecting Z_{DR} columns and for applying moisture and temperature increments were subjectively determined and should undergo further refinement. Finally, for this work, only a single radar was assimilated in each case, which may limit the efficacy of assimilating radial velocity observations in conjunction with the cloud analysis. Assimilating data from multiple radars may enhance the impact of radial velocity on the spin-up and analysis of storms examined in this work, as well as alleviate radar coverage concerns for detecting Z_{DR} columns.

While being a relatively simple and efficient method for assimilating Z, cloud analysis techniques may not be optimal owing to their inherent empirical relationships that can compromise initial adjustments in the model. As temperature and moisture increments seem to play a large role in aiding the spin-up of observed storms in storm-scale models, future work should seek to explore the possibility of assimilating cloud analysis-derived temperature and moisture increments based on detected Z_{DR} columns as "pseudo-observations" in a 3D-Var framework, similar to the work of Fierro et al. (2016) for lightning data assimilation. Using a variational framework to assimilate Z_{DR} columns should result in a more balanced analysis between the kinematic and thermodynamic fields and, hence, for a smoother cycling process.

Chapter 7

Summary and Outlook

The increasingly widespread adoption of dual-polarization radar has revolutionized both operational radar meteorology, with improvements in the detection of dangerous phenomena such as hail, tornadoes, and heavy rain, as well as research meteorology, with improved insight into storm microphysical content and processes. As such, the potential for dual-polarization radar data to inform storm-scale NWP models has long been acknowledged, with the few studies done in this area primarily focused on improving the representation of precipitation hydrometeors. The first part of this dissertation is centered here, exploring the deficiencies of current methods for retrieving hydrometeors from Z and to what extent dual-polarization radar can improve upon these estimates. The rest of the work presented here, however, lays the groundwork for a paradigm shift in how dual-polarization radar data is utilized for storm-scale NWP models by investigating its potential to offer information about thermodynamic fields. A one-dimensional model is developed and used to study the polarimetric characteristics of the melting layer in stratiform precipitation, and whether information about the cooling rate in this layer can be retrieved from these characteristics. The heating rate within convective updrafts is also investigated by way of Z_{DR} columns, with a novel method of assimilation into storm-scale NWP models developed that results in positive impacts on the forecast for two real data cases. These results are encouraging, and should promote further study into how dual-polarization radar data can inform not only the hydrometeor content of precipitation systems but their thermodynamic and dynamic components, as well.

The use of Z_{DR} columns to pinpoint the location of latent heating in deep moist convection has been met with interest in the convective-scale modeling community. A procedure predicated on this work is now being implemented and researched for use

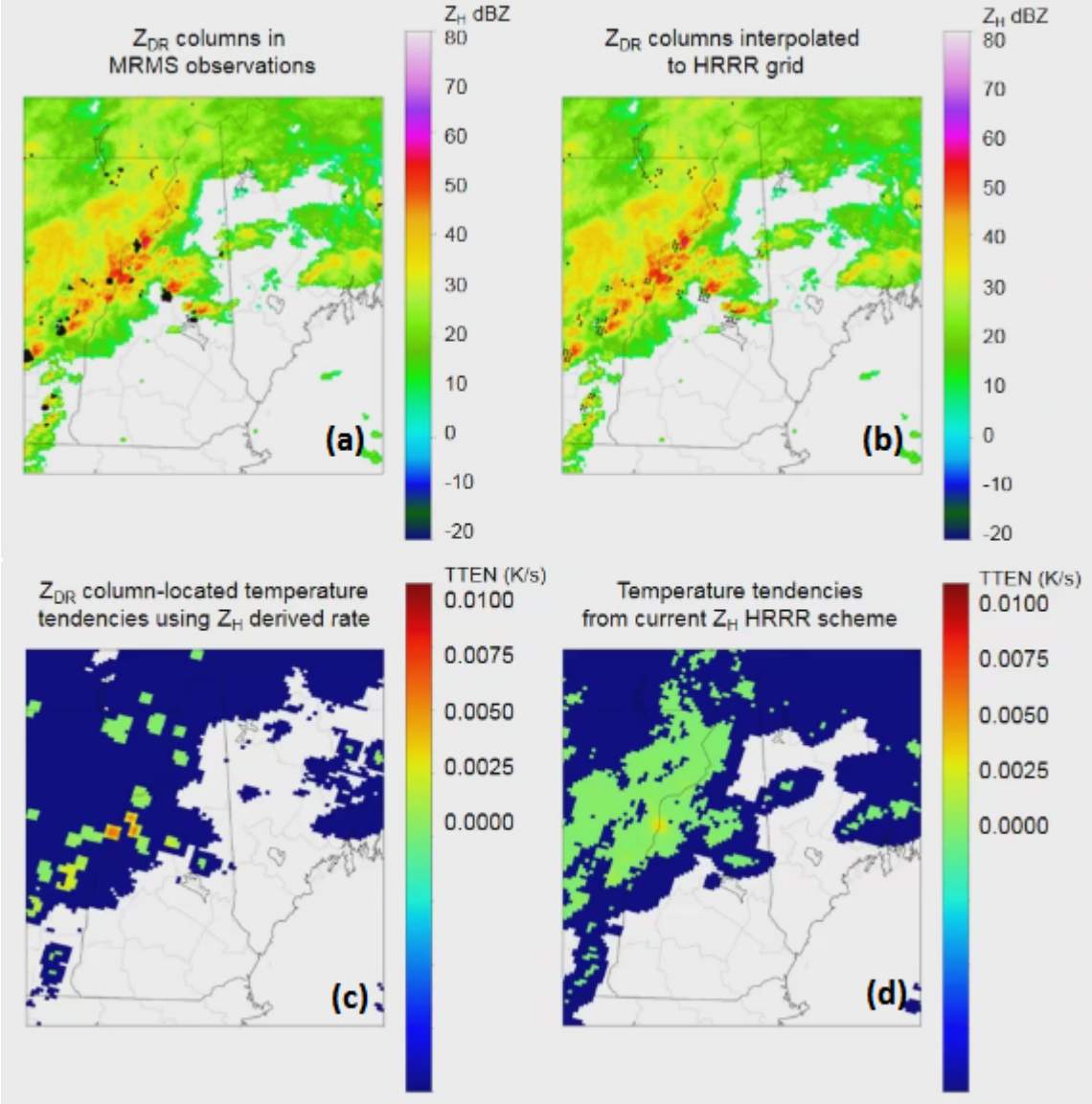

Figure 7.1: A demonstration of ongoing research into the implementation of latent heating rates based on Z_{DR} columns in the HRRR model showing (a) detected Z_{DR} columns (where $Z_{DR} \geq 1.0$ dB and $Z \geq 30$ dBZ above the 0° level), (b) the detected columns interpolated to the model grid, (c) latent heating rate applied at interpolated Z_{DR} column locations, and (d) the latent heating rate from the current Z-based approach. Taken and adapted from Alexander et al. (2017).

in the High-Resolution Rapid Refresh (HRRR) model at the Earth System Research Laboratory (Alexander et al. 2017; Murdzek et al. 2018), with encouraging preliminary results. An example of this implementation in shown in Figure 7.1, which compares the latent heating rate derived from Z_{DR} columns compared to the current procedure based on Z. In addition, the modified polarimetric cloud analysis has now been interfaced to be compatible with the Weather Research and Forecasting (WRF) model (Yunheng Wang, personal communication), which will permit testing and development in a community model with a larger user base. Preliminary work has begun using a three-dimensional polarimetric mosaic of multiple radars (John Krause, personal communication) using the compositing method put forth in Homeyer and Kumjian (2015), as well as assimilating the temperature and moisture increments determined from Z_{DR} columns variationally, as suggested in section 6.5.

Beyond the novel approaches presented here, there are a number of ways dual-polarization radar could also be used to improve upon existing Z-based techniques for utilizing radar data for storm-scale NWP models. Nudging techniques, including latent heat nudging, divergence nudging, and moisture nudging, all rely on the difference between the predicted and observed rainfall at the surface. Dual-polarization radar can improve the quality of radar-derived rainfall estimates, which will directly impact the amount of nudging performed by such schemes. Although somewhat crude, the budgeting techniques for the estimation of diabatic heating within storms discussed in section 2.2.3.1 could be revisited with improved estimates of hydrometeor q from dual-polarization radar. The Bayesian method for estimating the vertical profile of latent heating put forth in Nelson et al. (2016) would benefit from additional radar moments to better constrain the drop size distributions, and Penide et al. (2013) showed the improvement in the partitioning of convective and stratiform precipitation when employing dual-polarization data. Polarimetric radars can also improve the discrimination of

non-meteorological echoes and help with attenuation correction, often a necessary component of using radar observations in any capacity.

As radar technology continues to evolve, the need for studying the potential benefits and effects of these changes will remain present. The next leap forward for weather radar technology may be phased array radar, which is currently being studied as a potential replacement for the aging WSR-88D network. Unlike the WSR-88D radars, which rely on mechanical beam steering and obtain full radar volumes every $\approx$5 minutes, phased-array radars operate using electronic beam steering and can achieve full radar volumes every $\approx$1 minute. Studies have shown that forecaster warning performance is improved when using these faster updates (Heinselman et al. 2012, 2015; Bowden et al. 2015; Wilson et al. 2017b) and that forecasters derived more qualitative value from the enhanced temporal resolution (Bowden and Heinselman 2016; Wilson et al. 2017a). Limited studies have also examined the impact of assimilating such rapid updates of radar data compared to the WSR-88D, with both simulated data in observing system simulation experiments (Lei et al. 2007; Yussouf and Stensrud 2010) and real phased-array radar observations (Supinie et al. 2017) showing positive impacts that warrant further exploration in the future. Thus far, research into the feasibility of phased-array radar has been done with single-polarization data. However, the potential for a dual-polarization phased-array radar system is being investigated (Torres 2017), which would mark another pivotal step forward for the weather radar community. How best to assimilate rapid updates of polarimetic radar data, and whether similar or better improvements can be obtained as with existing polarimetric radar technology, will almost certainly remain a research priority in the coming years.

Bibliography

Aksoy, A., D. C. Dowell, and C. Snyder, 2009: A multicase comparative assessment of the ensemble Kalman filter for assimilation of radar observations. Part I: Storm-scale analyses. *Mon. Wea. Rev.*, **137**, 1805–1824, doi:10.1175/2008MWR2691.1.

Al-Sakka, H., A.-A. Boumahmoud, B. Fradon, S. J. Frasier, and P. Tabary, 2013: A new fuzzy logic hydrometeor classification scheme applied to the french X-, C-, and S-Band polarimetric radars. *J. Appl. Meteor. Climatol.*, **52**, 2328–2344, doi:10.1175/JAMC-D-12-0236.1.

Albers, S. C., J. A. McGinley, D. L. Birkenheuer, and J. R. Smart, 1996: The Local Analysis and Prediction System (LAPS): Analyses of clouds, precipitation, and temperature. *Wea. Forecasting*, **11**, 273–287, doi:10.1175/1520-0434(1996)011⟨0273%3ATLAAPS⟩2.0.CO%3B2.

Alexander, C., D. Dowell, M. Hu, T. Ladwig, S. Weygandt, and S. G. Benjamin, 2017: Expanding use of radar data in deterministic and ensemble data assimilation for the High-Resolution Rapid Refresh (HRRR). *38th Conf. on Radar Meteorology*, Chicago, IL, Amer. Meteor. Soc., 19B.2.

Anderson, R. S., 1974: Meteorological aspects of radar depolarization at 16.5 GHz. M.S. thesis, Dept. of Meteorology, McGill University, 45 pp.

Andrić, J., M. R. Kumjian, D. S. Zrnić, J. M. Straka, and V. M. Melnikov, 2013: Polarimetric signatures above the melting layer in winter storms: An observational and modeling study. *J. Appl. Meteor. Climatol.*, **52**, 682–700, doi:10.1175/JAMC-D-12-028.1.

Armijo, L., 1969: A theory for the determination of wind and precipitation velocities with Doppler radars. *J. Atmos. Sci.*, **26**, 570–573, doi:10.1175/1520-0469(1969)026⟨0570:ATFTDO⟩2.0.CO;2.

Atlas, D., 1954: The estimation of cloud parameters by radar. *J. Meteor.*, **11**, 309–317, doi:10.1175/1520-0469(1954)011⟨0309:TEOCPB⟩2.0.CO;2.

Atlas, D., and A. C. Chemla, 1957: Physical-synoptic variations of drop-size parameters. *Prof. 6th Wea. Radar Conf.*, Amer. Meteor. Soc., 21-29.

Atlas, D., R. Tatehira, R. C. Srivastava, W. Marker, and R. E. Carbone, 1969: Precipitation-induced mesoscale wind perturbations in the melting layer. *Quart. J. Roy. Meteor. Soc.*, **95**, 544–560, doi:10.1002/qj.49709540508.

Atlas, D., and C. W. Ulbrich, 1974: The physical basis for attenuation-rainfall relationships and the measurements of rainfall parameters by combined attenuation and radar methods. *J. Rech. Atmos.*, **8**, 275–298.

Atlas, D., and C. W. Ulbrich, 1977: Path- and area-integrated rainfall measurement by microwave attenuation in the 1-3 cm band. *J. Appl. Meteor.*, **16**, 1322–1331, doi: 10.1175/1520-0450(1977)016⟨1322:PAAIRM⟩2.0.CO;2.

Aubert, E. J., 1957: On the release of latent heat as a factor in large scale atmospheric motions. *J. Meteor.*, **14**, 527–542, doi:10.1175/1520-0469(1957)014⟨0527:OTROLH⟩2.0.CO;2.

Austin, P. M., 1987: Relation between measured radar reflectivity and surface rainfall. *Mon. Wea. Rev.*, **115**, 1053–1070, doi:10.1175/1520-0493(1987)115⟨1053:RBMRRA⟩2.0.CO;2.

Austin, P. M., and A. C. Bemis, 1950: A quantitative study of the "bright band" in radar precipitation echoes. *J. Meteor.*, **7**, 145–151, doi:10.1175/1520-0469(1950)007⟨0145:AQSOTB⟩2.0.CO;2.

Aydin, K., V. N. Bringi, and L. Liu, 1995: Rain-rate estimation in the presence of hail using S-band specific differential phase and other radar parameters. *J. Appl. Meteor.*, **34**, 404–410, doi:10.1175/1520-0450-34.2.404.

Aydin, K., H. Direskeneli, and T. A. Seliga, 1987: Dual-polarization radar estimation of rainfall parameters compared with ground-based disdrometer measurements: October 29, 1982 Central Illinois experiment. *IEEE Trans. Geosci. Remote Sens.*, **GE-25**, 834–844, doi:10.1109/TGRS.1987.289755.

Aydin, K., and C. Tang, 1995: Estimation of ice water content with 94-GHz millimeter wave radar observables. *27th Conf. on Radar Meteorology*, Vail, CO, Amer. Meteor. Soc., 550-552.

Baedi, R. J. P., J. J. M. de Wit, H. W. J. Russchenberg, J. S. Erkelens, and J. P. V. Poiares Baptista, 2000: Estimating effective radius and liquid wataer content from radar and lidar based on the CLARE'98 data-set. *Phys. Chem. Earth*, **25B**, 1057–1062, doi:10.1016/S1464-1909(00)00152-0.

Balakrishnan, N., and D. S. Zrnić, 1990: Estimation of rain and hail rates in mixed-phase precipitation. *J. Atmos. Sci.*, **47**, 565–583, doi:10.1175/1520-0469(1990)047⟨0565:EORAHR⟩2.0.CO;2.

Barnes, H. C., M. D. Zuluaga, and R. A. Houze Jr., 2015: Latent heating characteristics of the MJO computed from TRMM observations. *J. Geophys. Res. Atmos.*, **120**, 1322–1334, doi:10.1002/2014JD022241.

Barthazy, E., W. Henrich, and A. Waldvogel, 1998: Size distribution of hydrometeors through the melting layer. *Atmos. Res.*, **47-48**, 193–208, doi:10.1016/S0169-8095(98)00065-9.

Battaglia, A., C. D. Kummerow, D.-B. Shin, and C. Williams, 2003: Constaining microwave brightness temperatures by radar brightband observations. *J. Atmos. Oceanic Technol.*, **20**, 856–871, doi:10.1175/1520-0426(2003)020⟨0856:CMBTBR⟩2.0.CO;2.

Battan, L. J., 1973: *Radar observations of the atmosphere.* The University of Chicago Press, 324 pp.

Bauer, P., A. Thorpe, and G. Brunet, 2015: The quiet revolution of numerical weather perdiction. *Nature*, **525**, 47–55, doi:10.1038/nature14956.

Benjamin, S. G., C. Alexander, J. M. Brown, T. G. Smirnova, P. Hofmann, E. James, and G. Dimego, 2011: NOAA's hourly-updated 3km HRRR and RUC/Rapid Refresh—Recent (2010) and upcoming changes toward improving weather guidance for air-traffic management. *Proc. Second Aviation, Range, and Aerospace Meteorology Special Symp. on Weather-Air Traffic Management Integration*, Seattle, WA, Amer. Meteor. Soc., 3.2.

Benjamin, S. G., S. Weygandt, T. G. Smirnova, M. Hu, S. E. Peckham, J. M. Brown, K. Brundage, and G. S. Manikin, 2009: Assimilation of radar reflectivity data using a diabatic digital filter: Applications to the Rapid Update Cycle and Rapid Refresh and initialization of High Resolution Rapid Refresh forecasts with RUC/RR grids. *13th Conf. on Integrated Observing and Assimilation Systems for Atmosphere, Oceans, and Land Surface (IOAS-AOLS)*, Phoenix, AZ, Amer. Meteor. Soc., 7B.3.

Bielli, S., and F. Roux, 1999: Initialization of a cloud-resolving model with airbone Doppler radar observation of an oceanic tropical convection system. *Mon. Wea. Rev.*, **127**, 1038–1055, doi:10.1175/1520-0493(1999)127⟨1038:IOACRM⟩2.0.CO;2.

Bodine, D. J., M. R. Kumjian, R. D. Palmer, P. L. Heinselman, and A. V. Ryzhkov, 2013: Tornado damage estimation using polarimetric radar. *Wea. Forecasting*, **28**, 139–158, doi:10.1175/WAF-D-11-00158.1.

Bodine, D. J., R. D. Palmer, and G. Zhang, 2014: Dual-wavelength polarimetric radar analyses of tornadic debris signatures. *J. Appl. Meteor. Climatol.*, **53**, 242–261, doi:10.1175/JAMC-D-13-0189.1.

Bohren, C. F., and D. R. Huffman, 1983: *Absorption and Scattering of Light by Small Particles*. John Wiley and Sons, 660 pp.

Boudala, F. S., G. A. Isaac, and D. Hudak, 2006: Ice water content and precipitation rate as a function of equivalent radar reflectivity and temperature based on in situ observations. *J. Geophys. Res.*, **111**, D11 202, doi:10.1029/2005JD006499.

Bowden, K. A., and P. L. Heinselman, 2016: A qualitative analysis of NWS forecasters' use of phased-array radar data during severe hail and wind events. *Wea. Forecasting*, **31**, 43–55, doi:10.1175/WAF-D-15-0089.1.

Bowden, K. A., P. L. Heinselman, D. M. Kingfield, and R. P. Thomas, 2015: Impacts of phased-array radar data on forecaster performance during severe hail and wind events. *Wea. Forecasting*, **30**, 389–404, doi:10.1175/WAF-D-14-00101.1.

Bozart, L. F., and F. Sanders, 1991: An early-season coastal storm: Conceptual success and model failure. *Mon. Wea. Rev.*, **119**, 2831–2851, doi:10.1175/1520-0493(1991)119⟨2831:AESCSC⟩2.0.CO;2.

Braham Jr., R. R., 1952: The water and energy budgets of the thunderstorm and their relation to thunderstorm development. *J. Meteor.*, **9**, 227–242, doi:10.1175/1520-0469(1952)009⟨0227:TWAEBO⟩2.0.CO;2.

Brandes, E. A., 1978: Mesocyclone evolution and tornadogenesis: Some observations. *Mon. Wea. Rev.*, **106**, 995–1011, doi:10.1175/1520-0493%281978%29106⟨0995%3AMEATSO⟩2.0.CO;2.

Brandes, E. A., 1984: Relationships between radar-derived thermodynamic variables and tornadogenesis. *Mon. Wea. Rev.*, **112**, 1033–1052, doi:10.1175/1520-0493(1984)112⟨1033:RBRDTV⟩2.0.CO;2.

Brandes, E. A., K. Ikeda, G. Zhang, M. Schönhuber, and R. M. Rasmussen, 2007: A statistical and physical description of hydrometeor distributions in Colorado snowstorms using a video disdrometer. *J. Appl. Meteor. Climatol.*, **46**, 634–650, doi:10.1175/JAM2489.1.

Brandes, E. A., J. Vivekanandan, J. D. Tuttle, and C. J. Kessinger, 1995: A study of thunderstorm microphysics with multiparameter radar and aircraft observations. *Mon. Wea. Rev.*, **123**, 3129–3143, doi:10.1175/1520-0493(1995)123⟨3129:ASOTMW⟩2.0.CO;2.

Brandes, E. A., G. Zhang, and J. Vivekanandan, 2002: Experiments in rainfall estimation with a polarimetric radar in a subtropical environment. *J. Appl. Meteor.*, **41**, 674–685, doi:10.1175/1520-0450(2002)041⟨0674:EIREWA⟩2.0.CO;2.

Brandes, E. A., G. Zhang, and J. Vivekanandan, 2005: Corrigendum. *J. Appl. Meteor.*, **44**, 186, doi:10.1175/1520-0450(2005)44⟨186:C⟩2.0.CO;2.

Brewster, K., 2002: Recent advances in the diabatic initialization of a non-hydrostatic numerical model. *15th Conf. on Numerical Weather Prediction/21st Conf. on Severe Local Storms*, Amer. Meteor. Soc., San Antonio, TX, J6.3.

Brewster, K., M. Hu, M. Xue, and J. Gao, 2005: Efficient assimilation of radar data at high resolution for short range numerical weather prediction. *World Weather Research Program Symposium and Nowcasting and Very Short-range Forecasting WSN05*, WMO World Weather Research Program, Geneva, Switzerland, Toulouse, France, 3.06.

Brewster, K. A., and D. R. Stratman, 2015: An updated high resolution hydrometeor analysis system using radar and other data. *27th Conf. on Weather Analysis and Forecasting/23rd Conf. on Numerical Weather Prediction*, Amer. Meteor. Soc., Chicago, IL, 1-10.

Bringi, V. N., and V. Chandrasekar, 2001: *Polarimetric Doppler weather radar: Principles and applications*. Cambridge University Press, 636 pp.

Bringi, V. N., V. Chandrasekar, N. Balakrishnan, and D. S. Zrnić, 1990: An examination of propagation effects in rainfall on radar measurements at microwave frequencies. *J. Atmos. Oceanic Technol.*, **7**, 829–840, doi:10.1175/1520-0426(1990)007⟨0829:AEOPEI⟩2.0.CO;2.

Bringi, V. N., V. Chandrasekar, J. Hubbert, E. Gorgucci, W. L. Randeu, and M. Schoenhuber, 2003: Raindrop size distribution in different climatic regimes from disdrometer and dual-polarized radar analysis. *J. Atmos. Sci.*, **60**, 354–365, doi:10.1175/1520-0469(2003)060⟨0354:RSDIDC⟩2.0.CO;2.

Bringi, V. N., T. D. Keenan, and V. Chandrasekar, 2001: Correcting C-band radar reflectivity and differential reflectivity data for rain attenuation: A self-consistent method with constraints. *IEEE Trans. Geosci. Remote Sens.*, **39**, 1906–1915, doi:10.1109/36.951081.

Bringi, V. N., T. A. Seliga, M. P. M. Hall, S. M. Cherry, J. W. F. Goddard, and G. R. Kennedy, 1981: Dual polarization radar: Techniques and applications. *"Recent progress in radar meteorology", Atmospheric Technology*, **13**, 33–45.

Brock, F. V., K. C. Crawford, R. L. Elliott, G. W. Cuperus, S. J. Stadler, H. L. Johnson, and M. D. Eilts, 1995: The Oklahoma Mesonet: A technical overview. *J. Atmos. Oceanic Technol.*, **12**, 5–19, doi:10.1175/1520-0426(1995)012⟨0005:TOMATO⟩2.0.CO;2.

Browne, I. C., and N. P. Robinson, 1952: Cross-polarization of the radar melting-band. *Nature*, **170**, 1078–1079, doi:10.1038/1701078b0.

Bukovčić, P., 2017: Polarimetric measurements of ice pellets and aggregated snow. Ph.D. thesis, University of Oklahoma, 136 pp.

Bukovčić, P., A. V. Ryzhkov, D. Zrnić, and G. Zhang, 2018: Polarimetric radar relations for quantification of snow based on disdrometer data. *J. Appl. Meteor. Climatol.*, **57**, 103–120, doi:10.1175/JAMC-D-17-0090.1.

Bukovčić, P., D. Zrnić, and G. Zhang, 2017: Winter precipitation liquid-ice phase transitions revealed with polarimetric radar and 2DVD observations in central Oklahoma. *J. Appl. Meteor. Climatol.*, **56**, 1345–1363, doi:10.1175/JAMC-D-16-0239.1.

Byers, H. R., and R. D. Coons, 1947: The 'bright line' in radar cloud echoes and its probable explanation. *J. Meteor.*, **4**, 78–81, doi:10.1175/1520-0469(1947)004⟨0078:TLIRCE⟩2.0.CO;2.

Cao, Q., G. Zhang, E. Brandes, T. Schuur, A. Ryzhkov, and K. Ikeda, 2008: Analysis of video disdrometer and polarimetric radar data to characterize rain microphysics in Oklahoma. *J. Appl. Meteor. Climatol.*, **47**, 2238–2255, doi:10.1175/2008JAMC1732.1.

Caplan, P. M., 1966: On the evaporation of raindrops in the presence of vertical gradients of temperature and relative humidity. *J. Atmos. Sci.*, **23**, 614–617, doi:10.1175/1520-0469(1966)023⟨0614:OTEORI⟩2.0.CO;2.

Caumont, O., V. Ducrocq, É. Wattrelot, G. Jaubert, and S. Pradier-Vabre, 2010: 1D+3DVar assimilation of radar reflectivity data: A proof of concept. *Tellus*, **62**, 173–187, doi:10.1111/j.1600-0870.2009.00430.x.

Caya, A., J. Sun, and C. Snyder, 2005: A comparison between the 4DVAR and the ensemble Kalman filter techniques for radar data assimilation. *Mon. Wea. Rev.*, **133**, 3081–3094, doi:10.1175/MWR3021.1.

Caylor, I. J., and A. J. Illingworth, 1987: Radar observations and modelling of warm rain initiation. *Quart. J. Roy. Meteor. Soc.*, **113**, 1171–1191, doi:10.1002/qj.49711347806.

Chang, S.-F., Y.-C. Liou, J. Sun, and S.-L. Tai, 2016: The implementation of the ice phase microphysical process into a four-dimensional Variational Doppler Radar Analysis System (VDRAS) and its impact on parameter retrieval and quantitative precipitation nowcasting. *J. Atmos. Sci.*, **73**, 1015–1038, doi:10.1175/JAS-D-15-0184.1.

Cheng, L., M. English, and R. Wong, 1985: Hailstone size distributions and their relationship to storm thermodynamics. *J. Climate Appl. Meteor.*, **24**, 1059–1067, doi:10.1175/1520-0450(1985)024⟨1059:HSDATR⟩2.0.CO;2.

Chou, M.-D., 1990: Parameterizations for the absorption of solar radiation by O_2 and CO_2 with application to climate studies. *J. Climate*, **3**, 209–217, doi:10.1175/1520-0442(1990)003⟨0209:PFTAOS⟩2.0.CO;2.

Chou, M.-D., 1992: A solar radiation model for use in climate studies. *J. Atmos. Sci.*, **49**, 762–772, doi:10.1175/1520-0469(1992)049⟨0762:ASRMFU⟩2.0.CO;2.

Cifelli, R., V. Chandrasekar, S. Lim, K. P. C, Y. Wang, and S. A. Rutledge, 2011: A new dual-polarization radar rainfall algorithm: Application in Colorado precipitation events. *J. Atmos. Oceanic Technol.*, **28**, 352–364, doi:10.1175/2010JTECHA1488.1.

Cunningham, R. M., 1947: A different explanation of the "bright line.". *J. Meteor.*, **4**, 163, doi:10.1175/1520-0469(1947)004⟨0163:ADEOTB⟩2.0.CO;2.

D'Amico, M., A. Holt, and C. C, 1998: An anisotropic model of the melting layer. *Radio Science*, **1998**, 535–552, doi:10.1029/97RS03049.

Davolio, S., and A. Buzzi, 2004: A nudging scheme for the assimilation of precipitation data into a mesoscale model. *Wea. Forecasting*, **19**, 855–871, doi:10.1175/1520-0434(2004)019⟨0855:ANSFTA⟩2.0.CO;2.

Dawson, D. T., and M. Xue, 2006: Numerical forecasts of the 15-16 June 2002 Southern Plains mesoscale convective system: Impact of mesoscale data and cloud analysis. *Mon. Wea. Rev.*, **134**, 1607–1629, doi:10.1175/MWR3141.1.

Dawson, D. T., M. Xue, J. A. Milbrandt, and A. Shapiro, 2015: Sensitivity of real-data simulations of the 3 May 1999 Oklahoma City tornadic supercell and associated tornadoes to multimoment microphysics. Part I: Storm- and tornado-scale numerical forecasts. *Mon. Wea. Rev.*, **143**, 2241–2265, doi:10.1175/MWR-D-14-00279.1.

Dawson, D. T., M. Xue, J. A. Milbrandt, and M. K. Yau, 2010: Comparison of evaporation and cold pool development between single-moment and multimoment bulk microphysics schemes in idealized simulations of tornadic thunderstorms. *Mon. Wea. Rev.*, **138**, 1152–1171, doi:10.1175/2009MWR2956.1.

Dawson II, D. T., E. R. Mansell, Y. Jung, L. J. Wicker, M. R. Kumjian, and M. Xue, 2014: Low-level $z_{\rm dr}$ signatures in supercell forward flanks: The role of size sorting and melting hail. *J. Atmos. Sci.*, **71**, 276–299, doi:10.1175/JAS-D-13-0118.1.

Dawson II, D. T., L. J. Wicker, E. R. Mansell, Y. Jung, and M. Xue, 2013: Low-level polarimetric radar signatures in EnKF analyses and forecasts of the May 8, 2003 Oklahoma City tornadic supercell: Impact of multimoment microphysics and comparisons with observation. *Adv. Meteor.*, **2013**, 1–13, doi:10.1155/2013/818394.

Dixon, M., Z. Li, H. Lean, N. Roberts, and S. Ballard, 2009: Impact of data assimilation on forecasting convection over the United Kingdom using a high-resolution version of the Met Office Unified Model. *Mon. Wea. Rev.*, **137**, 1562–1584, doi:10.1175/2008MWR2561.1.

Doviak, R. J., and D. S. Zrnić, 1993: *Doppler Radar and Weather Observations*. Dover Publications, 562 pp.

Dowell, D. C., and H. B. Bluestein, 2002: The 8 June 1995 McLean, Texas, storm: Part I: Observations of cyclic tornadogenesis. *Mon. Wea. Rev.*, **130**, 2626–2648, doi:10.1175/1520-0493(2002)130⟨2626:TJMTSP⟩2.0.CO;2.

Dowell, D. C., L. J. Wicker, and C. Snyder, 2011: Ensemble Kalman filter assimilation of radar observations of the 8 May 2003 Oklahoma City supercell: Influences of reflectivity observations on storm-scale analyses. *Mon. Wea. Rev.*, **139**, 272–294, doi:10.1175/2010MWR3438.1.

Dowell, D. C., F. Zhang, L. J. Wicker, C. Snyder, and N. A. Crook, 2004: Wind and temperature retrievals in the 17 May 1981 Arcadia, Oklahoma, supercell: Ensemble Kalman filter experiments. *Mon. Wea. Rev.*, **132**, 1982–2005, doi:10.1175/1520-0493(2004)132⟨1982%3AWATRIT⟩2.0.CO;2.

Ducrocq, V., P.-J. Lafore, J.-L. Redelsperger, and F. Orain, 2000: Initialization of a fine-scale model for convective-system prediction: A case study. *Quart. J. Roy. Meteor. Soc.*, **126**, 3041–3065, doi:10.1002/qj.49712657004.

Ducrocq, V., D. Ricard, J.-P. Lafore, and F. Orain, 2002: Storm-scale numerical rainfall prediction for five precipitating events over France: On the importance of the initial humidity field. *Wea. Forecasting*, **17**, 1236–1256, doi:10.1175/1520-0434(2002)017⟨1236:SSNRPF⟩2.0.CO;2.

Erlingis, J. M., J. J. Gourley, P.-E. Kirstetter, E. N. Anagnostou, J. Kalogiros, M. Anagnostou, and W. Petersen, 2018: Evaluation of operational and experimental precipitation algorithms and microphysical insights during IPHEx. *J. Hydrometeor.*, **113**, 113–125, doi:10.1175/JHM-D-17-0080.1.

Evensen, G., 1994: Sequential data assimilation with a nonlinear quasi-geostrophic model using Monte Carlo methods to forecast error statistics. *J. Geophys. Res.*, **99**, 10 143–10 162, doi:10.1029/94JC00572.

Fabry, F., and W. Szyrmer, 1999: Modeling of the melting layer. Part II: Electromagnetic. *J. Atmos. Sci.*, **56**, 3593–3600, doi:10.1175/1520-0469(1999)056⟨3573:MOTMLP⟩2.0.CO;2.

Fabry, F., and I. Zawadzki, 1995: Long-term radar obsevations of the melting layer of precipitation and their interpretation. *J. Atmos. Sci.*, **52**, 838–851, doi:10.1175/1520-0469(1995)052⟨0838:LTROOT⟩2.0.CO;2.

Federer, B., and A. Waldvogel, 1975: Hail and raindrop size distributions from a Swiss multicell storm. *J. Appl. Meteor.*, **14**, 91–97, doi:10.1175/1520-0450(1975)014⟨0091:HARSDF⟩2.0.CO;2.

Field, P. R., R. Wood, P. R. A. Brown, P. H. Kaye, E. Hirst, R. Greenaway, and J. A. Smith, 2003: Ice particle interarrival times measured with a fast FSSP. *J. Atmos. Oceanic Technol.*, **20**, 249–261, doi:10.1175/1520-0426(2003)020⟨0249:IPITMW⟩2.0.CO;2.

Fierro, A. O., A. Clark, E. R. Mansell, D. R. MacGorman, S. R. Dembek, and C. L. Ziegler, 2015: Impact of storm-scale lightning data assimilation on WRF-ARW precipitation forecasts during the 2013 warm season over the contiguous United States. *Mon. Wea. Rev.*, **143**, 757–777, doi:10.1175/MWR-D-14-00183.1.

Fierro, A. O., J. Gao, C. L. Ziegler, K. M. Calhoun, E. R. Mansell, and D. R. MacGorman, 2016: Assimilation of flash extent data in the variational framework at

convection-allowing scales: Proof-of-concept and evaluation for the short-term forecast of the 24 May 2011 tornado outbreak. *Mon. Wea. Rev.*, **144**, 4373–4393, doi:10.1175/MWR-D-16-0053.1.

Fierro, A. O., J. Gao, C. L. Ziegler, E. R. Mansell, D. R. MacGorman, and S. R. Dembek, 2014: Evaluation of a cloud-scale lightning data assimilation technique and a 3DVAR method for the analysis and short-term forecast of the 29 June 2012 derecho event. *Mon. Wea. Rev.*, **142**, 183–202, doi:10.1175/MWR-D-13-00142.1.

Fierro, A. O., E. R. Mansell, C. L. Ziegler, and D. R. MacGorman, 2012: Application of a lightning data assimilation technique in the WRF-ARW model at cloud-resolving scales for the tornado outbreak of 24 May 2011. *Mon. Wea. Rev.*, **140**, 2609–2627, doi:10.1175/MWR-D-11-00299.1.

Findeisen, W., 1940: The formation of the 0°c-isothermal layer and fractocumulus under nimbostratus. *Meteor. Z.*, **76**, 49–54.

Foote, G. B., and P. S. du Toit, 1969: Terminal velocity of raindrops aloft. *J. Appl. Meteor.*, **8**, 249–253, doi:10.1175/1520-0450(1969)008⟨0249:TVORA⟩2.0.CO;2.

French, M. M., D. W. Burgess, E. R. Mansell, and L. J. Wicker, 2015: Bulk hook echo raindrop sizes retrieved using mobile, polarimetric Doppler radar observations. *J. Appl. Meteor. Climatol.*, **54**, 423–450, doi:10.1175/JAMC-D-14-0171.1.

French, M. M., and J. C. Snyder, 2016: Intercomparison between polarimetric radar, lightning, and satellite indicators of storm severity in a tornadic supercell. *28th Conf. on Severe Local Storms*, Portland, OR, Amer. Meteor. Soc., 180.

Frisch, A. S., L. J. Miller, and R. G. Strauch, 1974: Three-dimensional air motion measured in snow. *Geophys. Res. Lett.*, **1**, 86–89.

Gal-Chen, T., 1978: A method for the initialization of the anelastic equations: Implications for matching models with observations. *Mon. Wea. Rev.*, **106**, 587–606, doi:10.1175/1520-0493(1978)106⟨0587:AMFTIO⟩2.0.CO;2.

Gallus, W. A., and M. Preifer, 2008: Intercomparison of simulations using 5 WRF microphysical schemes with dual-polarization data for a German squall line. *Adv. Geosci.*, **16**, 109–115, doi:10.5194/adgeo-16-109-2008.

Gao, J., C. Fu, D. J. Stensrud, and J. S. Kain, 2016: OSSEs for an ensemble 3DVAR data assimilation system with radar observations of convective storms. *J. Atmos. Sci.*, **73**, 2403–2426, doi:10.1175/JAS-D-15-0311.1.

Gao, J., and D. J. Stensrud, 2012: Assimilation of reflectivity data in a convective-scale, cycled 3DVAR framework with hydrometeor classification. *J. Atmos. Sci.*, **69**, 1054–1065, doi:10.1175/JAS-D-11-0162.1.

Gao, J., and D. J. Stensrud, 2014: Some observing system simulation experiments with a hybrid 3DEnVAR system for storm-scale radar data assimilation. *Mon. Wea. Rev.*, **142**, 3326–2246, doi:10.1175/MWR-D-14-00025.1.

Gao, J., D. J. Stensrud, L. Wicker, M. Xue, and K. Zhao, 2014: Storm-scale radar data assimilation and high resolution NWP. *Adv. Meteor.*, **2014**, 1–3, doi:10.1155/2014/213579.

Gao, J., M. Xue, K. Brewster, and K. K. Droegemeier, 2004: A three-dimensional variational data analysis method with recursive filter for Doppler radars. *J. Atmos. Oceanic Technol.*, **21**, 457–469, doi:10.1175/1520-0426(2004)021⟨0457%3AATVDAM⟩2.0.CO%3B2.

Gao, J., M. Xue, A. Shapiro, and K. K. Droegemeier, 1999: A variational method for the analysis of three-dimensional wind fields from two Doppler radars. *Mon. Wea. Rev.*, **127**, 2128–2142, doi:10.1175/1520-0493(1999)127⟨2128:AVMFTA⟩2.0.CO;2.

Gao, J., M. Xue, A. Shapiro, Q. Xu, and K. K. Droegemeier, 2001: Three-dimensional simple adjoint velocity retrievals from single-Doppler radar. *J. Atmos. Oceanic Technol.*, **18**, 26–38, doi:10.1175/1520-0426(2001)018⟨0026:TDSAVR⟩2.0.CO;2.

Gao, J., M. Xue, and D. J. Stensrud, 2013: The development of a hybrid EnKF-3DVAR algorithm for storm-scale data assimilation. *Adv. Meteor.*, **2013**, 1–12, doi:10.1155/2013/512656.

Garrett, T. J., S. E. Yuter, C. Fallgatter, K. Shkurko, S. R. Rhodes, and J. L. Endries, 2015: Orientations and aspect ratios of falling snow. *Geophys. Res. Lett.*, **42**, 4617–4622, doi:10.1002/2015GL064040.

Ge, G., J. Gao, and M. Xue, 2013: Impacts of assimilating measurements of different state variables with a simulated supercell storm and three-dimensional variational method. *Mon. Wea. Rev.*, **141**, 2759–2777, doi:10.1175/MWR-D-12-00193.1.

Giangrande, S. E., 2007: Investigation of polarimetric measurements of rainfall at close and distant ranges. Ph.D. thesis, University of Oklahoma, 227 pp.

Giangrande, S. E., and A. V. Ryzhkov, 2008: Estimation of rainfall based on the results of polarimetric echo classification. *J. Appl. Meteor. Climatol.*, **47**, 2445–2462, doi:10.1175/2008JAMC1753.1.

Gilbert, G. K., 1884: Finley's tornado predictions. *Amer. Meteor. J.*, **1**, 166–172.

Golestani, Y., V. Chandrasekar, and V. N. Bringi, 1989: Intercomparison of multiparameter radar measurements. *24th Conf. on Radar Meteorology*, Amer. Meteor. Soc., Tallahassee, FL, 309-313.

Gorgucci, E., V. Chandrasekar, V. N. Bringi, and G. Scarchilli, 2002: Estimation of raindrop size distribution parameters from polarimetric radar measurements. *J. Atmos. Sci.*, **59**, 2373–2384, doi:10.1175/1520-0469(2002)059⟨2373:EORSDP⟩2.0.CO;2.

Gray, W. M., 1968: Global view of the origin of tropical disturbances and storms. *Mon. Wea. Rev.*, **96**, 669–700, doi:10.1175/1520-0493(1968)096⟨0669:GVOTOO⟩2.0.CO;2.

Gray, W. R., I. D. Cluckie, and R. J. Griffith, 2001: Aspects of melting and the radar bright band. *Meteor. Appl.*, **8**, 371–379, doi:10.1017/S1350482701003139.

Griffin, E., T. Schuur, and A. Ryzhkov, 2018: A polarimetric analysis of ice microphysical processes in snow, using quasi-vertical profiles. *J. Appl. Meteor. Climatol.*, **57**, 31–50, doi:10.1175/JAMC-D-17-0033.1.

Grim, J. A., G. M. McFarquhar, R. M. Rauber, A. M. Smith, and B. F. Jewett, 2009: Microphysical and thermodynamic structure and evolution of the trailing stratiform regions of mesoscale convective systems during BAMEX. Part II: Column model simulations. *Mon. Wea. Rev.*, **137**, 1186–1205, doi:10.1175/2008MWR2505.1.

Guimond, S. R., M. A. Bourassa, and P. D. Reasor, 2011: A latent heat retrieval and its effects on the intensity and structure change of Hurricane Guillermo (1997): Part I: The algorithm and observations. *J. Atmos. Sci.*, **68**, 1549–1567, doi:10.1175/2011JAS3700.1.

Guimond, S. R., and J. M. Reisner, 2012: A latent heat retrieval and its effects on the intensity and structure change of Hurricane Guillermo (1997): Part II: Numerical simulations. *J. Atmos. Sci.*, **69**, 3128–3146, doi:10.1175/JAS-D-11-0201.1.

Gunn, K., and J. Marshall, 1958: The distribution with size of aggregate snowflakes. *J. Meteor.*, **15**, 452–461, doi:10.1175/1520-0469(1958)015⟨0452:TDWSOA⟩2.0.CO;2.

Haines, P. A., J. K. Luers, and C. A. Cerbus, 1989: The role of the Smith-Feddes model in improving the forecasting of aircraft icing. *Third Conf. on the Aviation Weather System*, Amer. Meteor. Soc., Anaheim, CA, 258-263.

Hall, M. P. M., J. W. F. Goddard, and S. M. Cherry, 1984: Identification of hydrometeors and other targets by dual-polarization radar. *Radio Sci.*, **19**, 132–140, doi:10.1029/RS019i001p00132.

Hall, W. D., and H. R. Pruppacher, 1976: The survival of ice particles falling from cirrus clouds in subsaturated air. *J. Atmos. Sci.*, **33**, 1995–2006, doi:10.1175/1520-0469(1976)033⟨1995:TSOIPF⟩2.0.CO;2.

Hallett, J., and S. C. Mossop, 1974: Production of secondary ice particles during the riming process. *Nature*, **249**, 26–28, doi:10.1038/249026a0.

Hane, C. E., and P. S. Ray, 1985: Pressure and buoyancy fields derived from Doppler radar in a tornadic thunderstorm. *J. Atmos. Sci.*, **42**, 18–35, doi:10.1175/1520-0469(1985)042⟨0018:PABFDF⟩2.0.CO;2.

Hane, C. E., and B. C. Scott, 1978: Temperature and pressure perturbations within convective clouds derived from detailed air motion information: Preliminary testing. *Mon. Wea. Rev.*, **106**, 654–661, doi:10.1175/1520-0493(1978)106⟨0654:TAPPWC⟩2.0.CO;2.

Hardaker, P. J., A. R. Holt, and C. G. Collier, 1995: A melting-layer model and its use in correcting for the bright band in single-polarization radar echoes. *Quart. J. Roy. Meteor. Soc.*, **121**, 494–525, doi:10.1002/qj.49712152303.

Hartmann, D. L., H. H. Hendon, and R. A. Houze Jr., 1984: Some implications of the mesoscale circulations in tropical cloud clusters for large-scale dynamics and climate. *J. Atmos. Sci.*, **41**, 113–121, doi:10.1175/1520-0469(1984)041⟨0113:SIOTMC⟩2.0.CO;2.

Hauser, D., F. Roux, and P. Amayenc, 1988: Comparison of two methods for the retrieval of thermodynamic and microphysical variables from Doppler radar measuremnets: Application to the case of a tropical squall line. *J. Atmos. Sci.*, **45**, 1285–1303, doi:10.1175/1520-0469(1988)045⟨1285:COTMFT⟩2.0.CO;2.

Heinselman, P. L., D. S. LaDue, D. M. Kingfield, and R. Hoffman, 2015: Tornado warning decisions using phased-array radar data. *Wea. Forecasting*, **30**, 57–78, doi:10.1175/WAF-D-14-00042.1.

Heinselman, P. L., D. S. LaDue, and H. Lazrus, 2012: Exploring impacts of rapid-scan radar data on NWS warning decisions. *Wea. Forecasting*, **27**, 1031–1044, doi:10.1175/WAF-D-11-00145.1.

Heinselman, P. L., and A. V. Ryzhkov, 2006: Validation of polarimetric hail detection. *Wea. Forecasting*, **21**, 839–850, doi:10.1175/WAF956.1.

Heymsfield, A. J., 1977: Precipitation development in stratiform ice clouds: A microphysical and dynamical study. *J. Atmos. Sci.*, **34**, 367–381, doi:10.1175/1520-0469(1977)034⟨0367:PDISIC⟩2.0.CO;2.

Heymsfield, A. J., 2007: On measurements of small ice particles in clouds. *Geophys. Res. Lett.*, **34**, L23 812, doi::10.1029/2007GL030951.

Heymsfield, A. J., A. Bansemer, P. R. Field, S. L. Durden, J. L. Stith, J. E. Dye, W. Hall, and C. A. Grainger, 2002: Observations and parameterizations of particle size distributions in deep tropical cirrus and stratiform precipitation clouds: Results from in situ observations in TRMM field campaigns. *J. Atmos. Sci.*, **59**, 3457–3491, doi:10.1175/1520-0469(2002)059⟨3457:OAPOPS⟩2.0.CO;2.

Heymsfield, A. J., A. Bansemer, M. R. Poellot, and N. Wood, 2015: Observations of ice microphysics through the melting layer. *J. Atmos. Sci.*, **72**, 2902–2928, doi:10.1175/JAS-D-14-0363.1.

Heymsfield, A. J., S. Y. Matrosov, and N. B. Wood, 2016: Toward improving ice water content and snow-rate retrievals from radars. Part I: X and W bands, emphasizing *cloudsat*. *J. Appl. Meteor. Climatol.*, **55**, 2063–2090, doi:10.1175/JAMC-D-15-0290.1.

Heymsfield, A. J., C. Schmitt, and A. Bansemer, 2013: Ice cloud particle size distributions and pressure-dependent terminal velocities from in situ observations at temperatures from 0° to -86°C. *J. Atmos. Sci.*, **70**, 4123–4154, doi:10.1175/JAS-D-12-0124.1.

Heymsfield, G. M., 1979: Doppler radar study of a warm frontal region. *J. Atmos. Sci.*, **136**, 2093–2107, doi:10.1002/qj.49712152303.

Hitschfeld, W., and J. Bordan, 1954: Errors inherent in the radar measurement of rainfall at attenuation wavelengths. *J. Atmos. Sci.*, **11**, 58–67, doi:10.1175/1520-0469(1954)011⟨0058:EIITRM⟩2.0.CO;2.

Hoekstra, S., K. Klockow, R. Riley, J. Brotzge, H. Brooks, and S. Erickson, 2011: A preliminary look at the social perspective of Warn-on-Forecast: Preferred tornado warning lead time and the general public's perceptions of weather risks. *Wea. Climate Soc.*, **3**, 128–140, doi:10.1175/2011WCAS1076.1.

Hogan, R. J., L. Tian, P. R. A. Brown, C. D. Westbrook, A. J. Heymsfield, and J. D. Eastment, 2012: Radar scattering from ice aggregates using the horizontally aligned oblate spheroid approximation. *J. Appl. Meteor. Climatol.*, **51**, 655–671, doi:10.1175/JAMC-D-11-074.1.

Homeyer, C. R., and M. R. Kumjian, 2015: Microphysical characteristics of overshooting convection from polarimetric radar observations. *J. Atmos. Sci.*, **72**, 870–891, doi:10.1175/JAS-D-13-0388.1.

Houze Jr., R. A., 1982: Cloud clusters and large-scale vertical motions in the Tropics. *J. Meteor. Soc. Japan*, **60**, 396–409, doi:10.2151/jmsj1965.60.1_396.

Houze Jr., R. A., 1989: Observed structure of mesoscale convective systems and implications for large-scale heating. *Quart. J. Roy. Meteor. Soc.*, **115**, 425–461, doi:10.1002/qj.49711548702.

Houze Jr., R. A., 1994: Mesoscale convective systems. *Rev. Geophys.*, **42**, RG4003, doi:10.1029/2004RH000150.

Hu, M., and M. Xue, 2007: Impact of configurations of rapid intermittent assimilation of WSR-88D radar data fro the 8 May 2003 Oklahoma City tornadic thunderstorm case. *Mon. Wea. Rev.*, **135**, 507–525, doi:10.1175/MWR3313.1.

Hu, M., M. Xue, and K. Brewster, 2006a: 3DVAR and cloud analysis with WSR-88D level-II data for the prediction of the Fort Worth, Texas, tornadic thunderstorms. Part I: Cloud analysis and its impact. *Mon. Wea. Rev.*, **134**, 675–698, doi:10.1175/MWR3092.1.

Hu, M., M. Xue, J. Gao, and K. Brewster, 2006b: 3DVAR and cloud analysis with WSR-88D level-II data for the prediction of the Fort Worth, Texas, tornadic thunderstorms. Part II: Impact of radial velocity analysis via 3DVAR. *Mon. Wea. Rev.*, **134**, 699–721, doi:10.1175/MWR3093.1.

Hubbert, J., V. N. Bringi, L. D. Carley, and S. Bolen, 1998: CSU-CHILL polarimetric radar measurements from a severe hail storm in eastern Colorado. *J. Appl. Meteor.*, **37**, 749–775, doi:10.1175/1520-0450(1998)037⟨0749:CCPRMF⟩2.0.CO;2.

Humphries, R. G., 1974: Depolarization effects at 3 GHz due to precipitation. Ph.D. thesis, McGill University, 81 pp.

Humphries, R. G., and B. L. Barge, 1979: Polarization and dual-wavelength radar observations of the bright band. *IEEE Trans. Geosci. Electron.*, **GE-17**, 190–195, doi:10.1109/TGE.1979.294648.

Iguchi, T., and Coauthors, 2014: WRF-SBM simulations of melting-layer structure in mixed-phase precipitation events observed during LPVEx. *J. Appl. Meteor. Climatol.*, **53**, 2710–2731, doi:10.1175/JAMC-D-13-0334.1.

Illingworth, A. J., 1988: The formation of rain in convective clouds. *Nature*, **336**, 754–756, doi:10.1038/336754a0.

Illingworth, A. J., and I. J. Caylor, 1989: Cross polar observations of the bright band. *24th Conf. on Radar Meteorology*, Tallahassee, Florida, American Meteorological Society, 323-327.

Illingworth, A. J., J. W. F. Goddard, and S. M. Cherry, 1987: Polarization radar studies of precipitation development in convective storms. *Quart. J. Roy. Meteor. Soc.*, **113**, 469–489, doi:10.1002/qj.49711347604.

Illingworth, A. J., and R. J. Thompson, 2005: The estimation of moderate rain rates with operational polarisation radar. *32nd International Conference on Radar Meteorology*, Albuquerque, NM, American Meteorological Society, P9R.1, [Available online at https://ams.confex.com/ams/pdfpapers/96204.pdf.].

Ilotoviz, E., A. P. Khain, N. Benmoshe, V. T. J. Phillips, and A. V. Ryzhkov, 2016: Effect of aerosols on freezing drops, hail and precipitation in a mid-latitude storm. *J. Atmos. Sci.*, **73**, 109–144, doi:10.1175/JAS-D-14-0155.1.

Johnson, M., Y. Jung, D. Dawson, and M. Xue, 2016: Comparison of simulated polarimetric signatures in idealized supercell storms using two-moment bulk microphysics schemes in WRF. *Mon. Wea. Rev.*, **144**, 971–996, doi:10.1175/MWR-D-15-0233.1.

Johnson, R. H., 1984: Partitioning tropical heat and moisture budgets into cumulus and mesoscale components: Implications for cumulus parameterization. *Mon. Wea. Rev.*, **112**, 1590–1601, doi:10.1175/1520-0493(1984)112⟨1590:PTHAMB⟩2.0.CO;2.

Jones, C. D., and B. Macpherson, 1997: A latent heat nudging scheme for the assimilation of precipitation data into an operational mesoscale model. *Meteorol. Appl.*, **4**, 269–277, doi:10.1017/S1350482797000522.

Jones, T. A., K. Knopfmeier, D. Wheatley, G. Creager, P. Minnis, and R. Palikonda, 2016: Storm-scale data assimilation and ensemble forecasting with the NSSL experimental Warn-on-Forecast system. Part II: Combined radar and satellite data experiments. *Wea. Forecasting*, **31**, 297–327, doi:10.1175/WAF-D-15-0107.1.

Jorgensen, D. P., and B. F. Smull, 1993: Mesovortex circulations seen by airborne Doppler radar within a bow-echo mesoscale convective system. *Bull. Amer. Meteor. Soc.*, **74**, 2146–2158, doi:10.1175/1520-0477(1993)074⟨2146:MCSBAD⟩2.0.CO;2.

Jung, Y., M. Xue, and M. Tong, 2012: Ensemble Kalman filter analyses of the 29-30 May 2004 Oklahoma tornadic thunderstorm using one- and two-moment bulk microphysics schemes, and verification against polarimetric radar data. *Mon. Wea. Rev.*, **140**, 1457–1475, doi:10.1175/MWR-D-11-00032.1.

Jung, Y., M. Xue, and G. Zhang, 2010a: Simulations of polarimetric radar signatures of a supercell storm using a two-moment bulk microphysics scheme. *J. Appl. Meteor. Climatol.*, **49**, 146–163, doi:10.1175/2009JAMC2178.1.

Jung, Y., M. Xue, and G. Zhang, 2010b: Simultaneous estimation of microphysical parameters and the atmospheric state using simulated polarimetric radar data and an ensemble Kalman filter in the presence of an observation operator error. *Mon. Wea. Rev.*, **138**, 539–562, doi:10.1175/2009MWR2748.1.

Jung, Y., G. Zhang, and M. Xue, 2008a: Assimilation of simulated polarimetric radar data for a convective storm using the ensemble Kalman filter. Part I: Observation operators for reflectivity and polarimetric variables. *Mon. Wea. Rev.*, **136**, 2228–2245, doi:10.1175/2007MWR2083.1.

Jung, Y., G. Zhang, M. Xue, and J. M. Straka, 2008b: Assimilation of simulated polarimetric radar data for a convective storm using the ensemble Kalman filter. Part II: Impact of polarimetric data on storm analysis. *Mon. Wea. Rev.*, **136**, 2246–2260, doi:10.1175/2007MWR2288.1.

Kain, J. S., S. M. Goss, and M. E. Baldwin, 2000: The melting effect as a factor in precipitation-type forecasting. *Wea. Forecasting*, **15**, 700–714, doi:10.1175/1520-0434(2000)015⟨0700:TMEAAF⟩2.0.CO;2.

Kain, J. S., and Coauthors, 2008: Some practical considerations regarding horizontal resolution in the first generation of operational convection-allowing NWP. *Wea. Forecasting*, **23**, 931–952, doi:10.1175/WAF2007106.1.

Kain, J. S., and Coauthors, 2010: Assessing advances in the assimilation of radar data and other mesoscale observations within a collaborative forecasting–research environment. *Wea. Forecasting*, **25**, 1510–1521, doi:10.1175/2010WAF2222405.1.

Kamra, A. K., R. V. Bhalwankar, and A. B. Sathe, 1991: Spontaneous breakup of charged and uncharged water drops freely suspended in a wind tunnel. *J. Geophys. Res.*, **96**, 17 159–17 168, doi:10.1029/91JD01475.

Kennedy, P. C., and S. A. Rutledge, 2011: S-band dual-polarization radar observations of winter storms. *J. Appl. Meteor. Climatol.*, **50**, 844–858, doi:10.1175/2010JAMC2558.1.

Kessler, E., Ed., 1969: *On the distribution and continuity of water substance in atmospheric circulations*. No. 32, *Meteor. Monogr.*, Amer. Meteor. Soc., 84 pp.

Khain, A., M. Pinsky, L. Magaritz, O. Krasnov, and H. W. J. Russchenberg, 2008: Combined observational and model investigations of the *Z*-LWC relationship in stratocumulus clouds. *J. Appl. Meteor. Climatol.*, **47**, 591–606, doi:10.1175/2007JAMC1701.1.

Khain, A., A. Pokrovsky, M. Pinsky, A. Seifert, and V. Phillips, 2004: Simulation of effects of atmospheric aerosols on deep turbulent convective clouds using a spectral microphysics mixed-phase cumulus cloud model. Part I: Model description and possible applications. *J. Atmos. Sci.*, **61**, 2963–2982, doi:10.1175/JAS-3350.1.

Khain, A., T. Prabha, N. Benmoshe, G. Pandithurai, and M. Ovchinnikov, 2013: The mechanism of first raindrops formation in deep convective clouds. *J. Geophys. Res.*, **118**, 9123–9140, doi:10.1002/jgrd.50641.

Khain, A., D. Rosenfeld, A. Pokrovsky, U. Blahak, and A. Ryzhkov, 2011: The role of CCN in precipitation and hail in a mid-latitude storm as seen in simulations using a spectral (bin) microphysics model in a 2D dynamic frame. *Atmospheric Research*, **99**, 129–146.

Khain, A. P., 2009: Notes on state-of-the-art investigations of aerosol effects on precipitation: a critical review. *Env. Res. Let.*, **4**, 1–20, doi:10.1088/1748-9326/4/1/015004.

Klaasen, W., 1988: Radar observations and simulation of the melting layer of precipitation. *J. Atmos. Sci.*, **45**, 3741–3753, doi:10.1175/1520-0469(1988)045⟨3741:ROASOT⟩2.0.CO;2.

Klemp, J. B., and R. B. Wilhelmson, 1978: The simulation of three-dimensional convective storm dynamics. *J. Atmos. Sci.*, **35**, 1070–1096, doi:10.1175/1520-0469(1978)035⟨1070:TSOTDC⟩2.0.CO;2.

Klemp, J. B., R. B. Wilhelmson, and P. S. Ray, 1981: Observed and numerically simulated structure of a mature supercell thunderstorm. *J. Atmos. Sci.*, **38**, 1558–1580, doi:10.1175/1520-0469(1981)038⟨1558:OANSSO⟩2.0.CO;2.

Knight, C. A., 2006: Very early formation of big, liquid drops revealed by Z_{DR} in continental cumulus. *J. Atmos. Sci.*, **63**, 1939–1953, doi:10.1175/JAS3721.1.

Knight, C. A., J. Vivekanandan, and S. Lasher-Trapp, 2002: First radar echoes and the early z_{dr} history of florida cumulus. *J. Atmos. Sci.*, **59**, 1454–1472, doi:10.1175/1520-0469(2002)059⟨1454:FREATE⟩2.0.CO;2.

Koch, S. E., A. Aksakal, and J. T. McQueen, 1997: The influence of mesoscale humidity and evapotranspiration fields on a model forecast of a cold-frontal squall line. *Mon. Wea. Rev.*, **125**, 384–409, doi:10.1175/1520-0493(1997)125⟨0384:TIOMHA⟩2.0.CO;2.

Korolev, A., and G. Isaac, 2003: Roundness and aspect ratio of particles in ice clouds. *J. Atmos. Sci.*, **60**, 1795–1808, doi:10.1175/1520-0469(2003)060⟨1795:RAAROP⟩2.0.CO;2.

Korsholm, U., C. Petersen, B. H. Sass, N. Woetman, and D. G. Jensen, 2015: A new approach for assimilation of two-dimensional radar precipitation in a high resolution NWP model. *Meteor. Appl.*, **22**, 48–59, doi:10.1002/met.1466.

Krishnamurti, T. N., J. Xue, H. S. Bedi, K. Kingles, and D. Oosterhof, 1991: Physical initialization for numerical weather prediction over the tropics. *Tellus*, **43A**, 53–81, doi:10.1034/j.1600-0870.1991.t01-3-00007.x.

Kumjian, M., 2012: The impact of precipitation physical processes on the polarimetric radar variables. Ph.D. thesis, University of Oklahoma, 248 pp.

Kumjian, M. R., 2011: Precipitation properties of supercell hook echoes. *Electron. J. Severe Storms Meteor.*, **6**, 1–21.

Kumjian, M. R., 2013a: Principles and applications of dual-polarization weather radar. Part I: Description of the polarimetric radar variables. *J. Operational Meteor.*, **1**, 226–242, doi:10.15191/nwajom.2013.0119.

Kumjian, M. R., 2013b: Principles and applications of dual-polarization weather radar. Part II: Warm- and cold-season applications. *J. Operational Meteor.*, **1**, 243–264, doi:10.15191/nwajom.2013.0120.

Kumjian, M. R., 2013c: Principles and applications of dual-polarization weather radar. Part III: Artifacts. *J. Operational Meteor.*, **1**, 265–274, doi:10.15191/nwajom.2013.0121.

Kumjian, M. R., S. M. Ganson, and A. V. Ryzhkov, 2012: Freezing of raindrops in deep convective updrafts: A microphysical and polarimetric model. *J. Atmos. Sci.*, **69**, 3471–3490, doi:10.1175/JAS-D-12-067.1.

Kumjian, M. R., A. P. Khain, N. Benmoshe, E. Ilotoviz, A. V. Ryzhkov, and V. T. Phillips, 2014: The anatomy and physics of Z_{DR} columns: Investigating a polarimetric radar signature with a spectral bin microphysical model. *J. Appl. Meteor. Climatol.*, **53**, 1820–1843, doi:10.1175/JAMC-D-13-0354.1.

Kumjian, M. R., and K. A. Lombardo, 2017: Insights into the evolving microphysical and kinematic structure of northeastern U.S. winter storms from dual-polarization Doppler radar. *Mon. Wea. Rev.*, **145**, 1033–1061, doi:10.1175/MWR-D-15-0451.1.

Kumjian, M. R., S. Mishra, S. E. Giangrande, T. Toto, A. V. Ryzhkov, and A. Bansemer, 2016: Polarimetric radar and aircraft observations of saggy bright bands during MC3E. *J. Geophys. Res. Atmos.*, **121**, 3584–3607, doi:10.1002/2015JD024446.

Kumjian, M. R., and A. V. Ryzhkov, 2008: Polarimetric signatures in supercell thunderstorms. *J. Appl. Meteor. Climatol.*, **47**, 1940–1961, doi:10.1175/2007JAMC1874.1.

Kumjian, M. R., and A. V. Ryzhkov, 2010: The impact of evaporation on polarimetric characteristics of rain: Theoretical model and practical implications. *J. Appl. Meteor. Climatol.*, **49**, 1247–1267, doi:10.1175/2010JAMC2243.1.

Kumjian, M. R., and A. V. Ryzhkov, 2012: The impact of size sorting on the polarimetric radar variables. *J. Atmos. Sci.*, **69**, 2042–2060, doi:10.1175/JAS-D-11-0125.1.

Kumjian, M. R., A. V. Ryzhkov, H. D. Reeves, and T. J. Schuur, 2013: A dual-polarization radar signature of hydrometeor refreezing in winter storms. *J. Appl. Meteor. Climatol.*, **52**, 2549–2566, doi:10.1175/JAMC-D-12-0311.1.

Lang, S., W.-K. Tao, J. Simpson, and B. Ferrier, 2003: Modeling of convective-stratiform precipitation processes: Sensitivity to partitioning methods. *J. Appl. Meteor.*, **42**, 505–527, doi:10.1175/1520-0450(2003)042⟨0505:MOCSPP⟩2.0.CO;2.

Leary, C. A., and R. A. House Jr., 1979: Melting and evaporation of hydrometeors in precipitation from the anvil clouds of deep tropical convection. *J. Atmos. Sci.*, **36**, 669–679, doi:10.1175/1520-0469(1979)036⟨0669:MAEOHI⟩2.0.CO;2.

Lee, W.-C., R. E. Carbone, and R. M. Wakimoto, 1992: The evolution and structure of a "bow-echo-microburst" event. Part I: The microburst. *Mon. Wea. Rev.*, **120**, 2188–2210, doi:10.1175/1520-0493%281992%29120⟨2188%3ATEASOA⟩2.0.CO;2.

Lei, T., M. Xue, T. Yu, and M. Teshiba, 2007: Study on the optimal scanning strategies of phase-array radar through ensemble Kalman filter assimilation of simulated data. *33rd Conf. on Radar Meteorology*, Cairns, Australia, Amer. Meteor. Soc., P7.1.

Leinonen, J., 2014: High-level interface to T-matrix scattering calculations: architecture, capabilities, and limitations. *Opt. Express*, **22**, 1655–1660, doi:10.1364/OE.22.001655.

Leinonen, J., B. Slavko, A. Seifert, A. von Lerber, and M. Lebsock, 2017: Snowflake models for ice microphysics retrievals with multi-frequency radars. *38th Conf. on Radar Meteorology*, Chicago, IL, American Meteorological Society, KS2.1.

Leuenberger, D., and A. Rossa, 2007: Revisiting the latent heat nudging scheme for the rainfall assimilation of a simulated convective storm. *Meteor. Atmos. Phys.*, **98**, 195–215, doi:10.1007/s00703-007-0260-9.

Lhermitte, R., 1970: Dual-Doppler radar observations of convective storm circulation. *14th Radar Meteorology Conference*, Tucson, AZ, Amer. Meteor. Soc., 139-144.

Li, X., and J. Mecikalski, 2010: Assimilation of the dual-polarization Doppler radar data for a convective storm with a warm-rain radar forward operator. *J. Geophys. Res.*, **115**, 1–16, doi:10.1029/2009JD013666.

Li, X., and J. Mecikalski, 2012: Impact of the dual-polarization Doppler radar data on two convective storms with a warm-rain radar forward operator. *Mon. Wea. Rev.*, **140**, 2147–2167, doi:10.1175/MWR-D-11-00090.1.

Li, X., W.-K. Tao, A. P. Khain, J. Simpson, and D. E. Johnson, 2008: Sensitivity of a cloud-resolving model to bulk and explicit bin microphysics schemes. Part I: Comparisons. *J. Atmos. Sci.*, **66**, 3–21, doi:10.1175/2008JAS2646.1.

Lilly, D. K., 1990: Numerical prediction of thunderstorms——has its time come? *Quart. J. Roy. Meteor. Soc.*, **116**, 779–798, doi:10.1002/qj.49711649402.

Lim, S., V. Chandrasekar, and V. N. Bringi, 2005: Hydrometeor classification system using dual-polarization radar measurements: Model improvements and in situ verification. *IEEE Trans. Geosci. Remote Sens.*, **43**, 792–801, doi:10.1109/TGRS.2004.843077.

Lin, Y., P. S. Ray, and K. W. Johnson, 1993: Initialization of a modeled convective storm using Doppler radar-derived fields. *Mon. Wea. Rev.*, **121**, 2757–2775, doi:10.1175/1520-0493(1993)121⟨2757:IOAMCS⟩2.0.CO;2.

Lin, Y.-L., R. D. Farley, and H. D. Orville, 1983: Bulk parameterization of the snow field in a cloud model. *J. Climate Appl. Meteor.*, **22**, 1065–1092, doi:10.1175/1520-0450(1983)022⟨1065%3ABPOTSF⟩2.0.CO%3B2.

Liu, C.-L., and A. J. Illingworth, 2000: Toward more accurate retrievals of ice water content from radar measurements of clouds. *J. Appl. Meteor.*, **39**, 1130–1146, doi:10.1175/1520-0450(2000)039⟨1130:TMAROI⟩2.0.CO;2.

Lo, K. K., and R. E. Passarelli Jr., 1982: The growth of snow in winter storms: An airborne observational study. *J. Atmos. Sci.*, **39**, 697–706, doi:10.1175/1520-0469(1982)039⟨0697:TGOSIW⟩2.0.CO;2.

Loney, M. L., D. S. Zrnić, J. M. Straka, and A. V. Ryzhkov, 2002: Enhanced polarimetric radar signatures above the melting level in a supercell storm. *J. Appl. Meteor.*, **41**, 1179–1194, doi:10.1175/1520-0450(2002)041⟨1179:EPRSAT⟩2.0.CO;2.

Macpherson, B., 2001: Operational experience with assimilation of rainfall data in the Met Office Mesoscale model. *Meteor. Atmos. Phys.*, **76**, 3–8, doi:10.1007/s007030170035.

Marchand, M. R., and H. E. Fuelberg, 2014: Assimilation of lightning data using a nudging method involving low-level warming. *Mon. Wea. Rev.*, **142**, 4850–4871, doi:10.1175/MWR-D-14-00076.1.

Marécel, V., D. Hauser, and F. Roux, 1993: The 12/13 January 1988 narrow cold-frontal rainband observed during MFDP/FRONTS 87. Part II: Microphysics. *J. Atmos. Sci.*, **50**, 975–998, doi:10.1175/1520-0469(1993)050⟨0975:TJNCFR⟩2.0.CO;2.

Markowski, P. M., J. M. Straka, and E. N. Rasmussen, 2002: Direct surface thermodynamic observations within the rear-flank downdrafts of nontornadic and tornadic supercells. *Mon. Wea. Rev.*, **130**, 1692–1721, doi:10.1175/1520-0493(2002)130⟨1692:DSTOWT⟩2.0.CO;2.

Markowski, P. M., J. M. Straka, and E. N. Rasmussen, 2003: Tornadogenesis resulting from the transport of circulation by a downdraft: Idealized numerical simulations. *J. Atmos. Sci.*, **60**, 795–823, doi:10.1175/1520-0469(2003)060⟨0795:TRFTTO⟩2.0.CO;2.

Marshall, J. S., and W. M. K. Palmer, 1948: The distribution of raindrops with size. *J. Meteor.*, **5**, 165–166, doi:10.1175/1520-0469(1948)005⟨0165:TDORWS⟩2.0.CO;2.

Matrosov, S. Y., 2005: Attenuation-based estimates of rainfall rates aloft with vertically pointing K_a-band radars. *J. Atmos. Oceanic Technol.*, **22**, 43–54, doi:10.1175/JTECH-1677.1.

Matrosov, S. Y., 2006: Modeling backscatter properties of snowfall at millimeter wavelengths. *J. Atmos. Sci.*, **64**, 1727–1736, doi:10.1175/JAS3904.1.

Matrosov, S. Y., and A. J. Heymsfield, 2017: Empirical relations between size parameters of ice hydrometeor populations and radar reflectivity. *J. Appl. Meteor. Climatol.*, **56**, 2479–2488, doi:10.1175/JAMC-D-17-0076.1.

Matrosov, S. Y., A. J. Heymsfield, and Z. Wang, 2005: Dual-frequency radar ratio of nonspherical atmospheric hydrometeors. *Geophys. Res. Lett.*, **32**, L13 816, doi:10.1029/2005GL023210.

Matrosov, S. Y., R. Reinking, R. A. Kropfli, and B. W. Bartram, 1996: Estimation of ice hydrometeor types and shapes from radar polarization measurements. *J. Atmos. Oceanic Technol.*, **13**, 85–96, doi:10.1175/1520-0426(1996)013⟨0085:EOIHTA⟩2.0.CO;2.

Matsuo, T., and Y. Sasyo, 1981: Melting of snowflakes below freezing level in the atmosphere. *J. Meteor. Soc. Japan*, **59**, 10–25, doi:10.2151/jmsj1965.59.1_10.

Maxwell Garnett, J. C., 1904: Color in metal glasses and in metallic films. *Philos. Trans. Roy. Soc. London*, **A203**, 385–420, doi:10.1098/rsta.1904.0024.

McDonald, J. E., 1963: Use of the electrostatic analogy in studies of ice crystal growth. *Z. Angew. Math. Phys.*, **14**, 610–620, doi:10.1007/BF01601268.

McFarquhar, G. M., M. S. Timlin, R. M. Rauber, B. F. Jewett, and J. A. Grim, 2007: Vertical variability of cloud hydrometeors in the stratiform region of mesoscale convective systems and bow echoes. *Mon. Wea. Rev.*, **135**, 3405–3428, doi:10.1175/MWR3444.1.

Meneghini, R., and L. Liao, 1996: Comparisons for cross sections for melting hydrometeors as derived from dielectric mixing formulas and a numerical method. *J. Appl. Meteor.*, **35**, 1658–1670, doi:10.1175/1520-0450(1996)035⟨1658:COCSFM⟩2.0.CO;2.

Mie, G., 1908: Beiträge zur Optik trüber Medien speziell kollaidaler Metallösungen. *Ann. Phys.*, **25**, 377–445.

Milbrandt, J. A., J. Thériault, and R. Mo, 2014: Modeling the phase transition associated with melting snow in a 1D kinematic framework: Sensitivity to the microphysics. *R. Pure Appl. Geophys.*, **171**, 303–322, doi:10.1007/s00024-012-0552-y.

Milbrandt, J. A., and M. K. Yau, 2005a: A multimoment bulk microphysics parameterization. Part I: Analysis of the role of the spectral shape parameter. *J. Atmos. Sci.*, **62**, 3051–3064, doi:10.1175/JAS3534.1.

Milbrandt, J. A., and M. K. Yau, 2005b: A multimoment bulk microphysics parameterization. Part II: A proposed three-moment closure and scheme description. *J. Atmos. Sci.*, **62**, 3065–3081, doi:10.1175/JAS3535.1.

Miller, M. J., and R. P. Pearce, 1974: A three-dimensional primitive equation model of cumulonimbus convection. *Quart. J. Roy. Meteor. Soc.*, **100**, 133–154, doi:10.1002/qj.49710042402.

Mishchenko, M. I., 2000: Calculation of the amplitude matrix for a nonspherical particle in a fixed orientation. *Appl. Optics*, **39**, 1026–1031, doi:10.1364/AO.39.001026.

Mitchell, D., R. Zhang, and R. Pitter, 1990: Mass-dimensional relationships for ice particles and the influence of riming on snowfall rates. *J. Appl. Meteor.*, **29**, 153–163, doi:10.1175/1520-0450(1990)029⟨0153:MDRFIP⟩2.0.CO;2.

Mitra, S. K., O. Vohl, M. Ahr, and H. R. Pruppacher, 1990: A wind tunel and theoretical study of the melting behavior of atmospheric ice particles. IV: Experiment and theory for snow flakes. *J. Atmos. Sci.*, **47**, 584–591, doi:10.1175/1520-0469(1990)047⟨0584:AWTATS⟩2.0.CO;2.

Morrison, H., and W. W. Grabowski, 2013: Response of tropical deep convection to localized heating perturbations: Implications for aerosol-induced convective invigoration. *J. Atmos. Sci.*, **70**, 3533–3555, doi:10.1175/JAS-D-13-027.1.

Murdzek, S., D. Dowell, T. Ladwig, M. Hu, C. R. Alexander, and J. M. Brown, 2018: Assimilating differential reflectivity columns into the High Resolution Rapid Refresh using latent heating forcing. *22nd Conf. on Integrated Observing and Assimilation Systems for the Atmosphere, Oceans, and Land Surface*, Amer. Meteor. Soc., Austin, TX, 172.

Murphy, A. M., A. V. Ryzhkov, P. Zhang, G. M. McFarquhar, W. Wu, and D. M. Stechman, 2018: A polarimetric and microphysical analysis of the stratiform rain region of MCSs. *19th Symposium on Meteorological Observation and Instrumentation*, Amer. Meteor. Soc., Austin, TX, 682.

National Oceanic and Atmospheric Administration, 2017: Experimental model predicted tornado's path hours, not minutes, before it formed. [Available online at http://www.noaa.gov/stories/experimental-model-predicted-tornados-path-hours-not-minutes-before-it-formed.].

National Weather Service, 2017a: The tornado outbreak of May 19, 2013. National Weather Service Forecast Office, Norman, OK. [Available online at http://www.weather.gov/oun/events-20130519].

National Weather Service, 2017b: Wednesday, May 25th, 2016: Long track tornado hits north central Kansas. National Weather Service Forecast Office, Topeka, KS. [Available online at http://www.weather.gov/top/LongTrackTornadoHitsNorthCentralKS].

Nelson, E. L., T. S. L'Ecuyer, S. M. Saleeby, W. Berg, S. R. Herbener, and S. C. van den Heever, 2016: Toward an algorithm for estimating latent heat release in warm rain systems. *J. Atmos. Oceanic Technol.*, **33**, 1309–1329, doi:10.1175/JTECH-D-15-0205.1.

Neumann, A. J., 2016: Investigating evaporation of melting ice particles within a bin melting layer model. Ph.D. thesis, University of North Dakota, 98 pp.

Noilhan, J., and S. Planton, 1989: A simple parameterization of land surface processes for meteorological models. *Mon. Wea. Rev.*, **117**, 536–549, doi:10.1175/1520-0493(1989)117⟨0536:ASPOLS⟩2.0.CO;2.

Noppel, H., U. Blahak, A. Seifert, and K. D. Beheng, 2010: Simulations of a hailstorm and the impact of CCN using an advanced two-moment cloud microphysical scheme. *Atmos. Res.*, **96**, 286–301, doi:10.1016/j.atmosres.2009.09.008.

Ogura, Y., 1963: The evolution of a moist convective element in a shallow conditional unstable atmosphere: A numerical calculation. *J. Atmos. Sci.*, **20**, 407–424, doi:10.1175/1520-0469(1963)020⟨0407:TEOAMC⟩2.0.CO;2.

Ohtake, T., 1969: Observations of size distributions of hydrometeors through the melting layer. *J. Atmos. Sci.*, **26**, 545–557, doi:10.1175/1520-0469(1969)026⟨0545:OOSDOH⟩2.0.CO;2.

Olson, W. S., P. Bauer, N. F. Viltard, D. E. Johnson, W.-K. Tao, R. Meneghini, and L. Liao, 2001: A melting-layer model for passive/active microwave remote sensing applications. Part I: Model formulation and comparison with observations. *J. Appl. Meteor.*, **40**, 1145–1163, doi:10.1175/1520-0450(2001)040⟨1145:AMLMFP⟩2.0.CO;2.

Ortega, K. L., J. M. Krause, and A. V. Ryzhkov, 2016: Polarimetric radar characteristics of melting hail. Part III: Validation of the algorithm for hail size discrimination. *J. Appl. Meteor. Climatol.*, **55**, 829–848, doi:10.1175/JAMC-D-15-0203.1.

Orville, H. D., 1965: A numerical sutdy of the initiation of cumulus clouds over mountainous terrain. *J. Atmos. Sci.*, **22**, 431–451, doi:10.1175/1520-0469(1965)022⟨0684:ANSOTI⟩2.0.CO;2.

Pan, S., J. Gao, D. J. Stensrud, X. Wang, and T. A. Jones, 2017: Assimilation of radar radial velocity and reflectivity, satellite Cloud Water Path and Total Precipitable Water for convective scale NWP in OSSEs. *J. Atmos. Oceanic Technol.*, doi:10.1175/JTECH-D-17-0081.1.

Pan, Y., M. Xue, and G. Ge, 2016: Incorporating diagnosed intercept parameters and the graupel category within the ARPS cloud analysis system for the initialization of double-moment microphysics: Testing with a squall line over South China. *Mon. Wea. Rev.*, **144**, 371–392, doi:10.1175/MWR-D-15-0008.1.

Pandya, R. E., and D. R. Durran, 1996: The influence of convective generated thermal forcing on the mesoscale circulation around squall lines. *J. Atmos. Sci.*, **53**, 2924–2951, doi:10.1175/1520-0469(1996)053⟨2924:TIOCGT⟩2.0.CO;2.

Park, H., A. V. Ryzhkov, D. S. Zrnić, and K.-E. Kim, 2009: The hydrometeor classification algorithm for the polarimetric WSR-88D: Description and application to an MCS. *Wea. Forecasting*, **24**, 730–748, doi:10.1175/2008WAF2222205.1.

Park, M.-S., and R. L. Elsberry, 2013: Latent heating and cooling rates in developing and nondeveloping tropical disturbances during TCS-08: TRMM PR versus ELDORA retrievals. *J. Atmos. Sci.*, **70**, 15–35, doi:10.1175/JAS-D-12-083.1.

Parsons, D. B., C. G. Mohr, and T. Gal-Chen, 1987: A severe frontal rainband. Part III: Derived thermodynamic structure. *J. Atmos. Sci.*, **44**, 1615–1631, doi:10.1175/1520-0469(1987)044⟨1615:ASFRPI⟩2.0.CO;2.

Patade, S., T. V. Prabha, D. Axisa, K. Gayatri, and A. Heymsfield, 2015: Particle size distribution properties in mixed-phase monsoon clouds from in situ measurements during CAIPEEX. *J. Geophys. Res. Atmos.*, **120**, 10 418–10 440, doi:10.1002/2015JD023375.

Penide, G., A. Protat, V. V. Kumar, and P. T. May, 2013: Comparison of two convective/stratiform precipitation classification techniques: Radar reflectivity texture versus

drop size distribution-based approach. *J. Atmos. Oceanic Technol.*, **30**, 2788–2797, doi:10.1175/JTECH-D-13-00019.1.

Pfeifer, M., G. C. Craig, M. Hagen, and C. Keil, 2008: A polarimetric radar forward operator for model evaluation. *J. Appl. Meteor. Climatol.*, **47**, 3202–3220, doi:10.1175/2008JAMC1793.1.

Phillips, V. T. J., A. P. Khain, N. Benmoshe, A. V. Ryzhkov, and E. Ilotovish, 2014: Theory of time-dependent freezing. Part I: Description of scheme for wet growth of hail. *J. Atmos. Sci.*, **71**, 4527–4557, doi:10.1175/JAS-D-13-0375.1.

Phillips, V. T. J., A. P. Khain, N. Benmoshe, A. V. Ryzhkov, and E. Ilotovish, 2015: Theory of time-dependent freezing. Part II: Scheme for freezing raindrops and simulations by a cloud model with spectral bin microphysics. *J. Atmos. Sci.*, **72**, 262–286, doi:10.1175/JAS-D-13-0376.1.

Phillips, V. T. J., A. Pokrovsky, and A. P. Khain, 2007: The influence of time-dependent melting on the dynamics and precipitation production in maritime and continental storm clouds. *J. Atmos. Sci.*, **64**, 338–359, doi:10.1175/JAS3832.1.

Picca, J. C., D. M. Kingfield, and A. V. Ryzhkov, 2017: Utilizing a polarimetric size sorting signature to develop a convective nowcasting algorithm. *18th Conf. on Aviation, Range, and Aerospace Meteorology*, Amer. Meteor. Soc., Seattle, WA, 14.5.

Picca, J. C., M. Kumjian, and A. Ryzhkov, 2010: Z_{DR} columns as a predictive tool for hail growth and storm evolution. *25th Conference on Severe Local Storms*, Amer. Meteor. Soc., Denver, CO, 11.3, [Available online at https://ams.confex.com/ams/25SLS/techprogram/paper_175750.htm.].

Picca, J. C., J. C. Snyder, and A. V. Ryzhkov, 2015: An observational analysis of z_{dr} column trends in tornadic supercells. *37th Conf. on Radar Meteorology*, Amer. Meteor. Soc., Norman, OK, 5A.5.

Planche, C., W. Wobrock, and A. I. Flossmann, 2014: The continuous melting process in a cloud-scale model using a bin microphysics scheme. *Quart. J. Roy. Meteor. Soc.*, **140**, 1986–1996, doi:10.1002/qj.2265.

Polder, D., and J. H. van Santen, 1946: The effective permeability of mixtures of solids. *Physica*, **12**, 257–271, doi:10.1016/S0031-8914(46)80066-1.

Posselt, D. J., X. Li, S. A. Tushaus, and J. R. Mecikalski, 2015: Assimilation of dual-polarization radar observations in mixed- and ice-phase regions of convective storms: Information content and forward model errors. *Mon. Wea. Rev.*, **143**, 2611–2636, doi:10.1175/MWR-D-14-00347.1.

Potvin, C., and M. Flora, 2015: Sensitivity of idealized supercell simulations to horizontal grid spacing: Implications for Warn-on-Forecast. *Mon. Wea. Rev.*, **143**, 2998–3024, doi:10.1175/MWR-D-14-00416.1.

Potvin, C. K., L. J. Wicker, M. M. French, and D. D. Burgess, 2014: Warn-on-Forecast sensitivity experiments with the 19 May 2013 Norman-Shawnee, OK, tornadic supercell. *27th Conf. on Severe Local Storms*, Amer. Meteor. Soc., Madison, WI, 8A.3.

Pruppacher, H. R., and J. D. Klett, 1997: *Microphysics of Clouds and Precipitation*. 2nd ed., Kluwer Academic Publishers, 954 pp.

Putnam, B. J., M. Xue, Y. Jung, N. A. Snook, and G. Zhang, 2014: The analysis and prediction of microphysical states and polarimetric radar variables in a mesoscale convective system using double-moment microphysics, multinetwork radar data, and the ensemble Kalman filter. *Mon. Wea. Rev.*, **142**, 141–162, doi: 10.1175/MWR-D-13-00042.1.

Qiu, C.-J., and Q. Xu, 1992: A simple adjoint method of wind analysis for single-Doppler data. *J. Atmos. Oceanic Technol.*, **9**, 588–598, doi:10.1175/1520-0426(1992)009⟨0588:ASAMOW⟩2.0.CO;2.

Rabier, F., 2005: Overview of global data assimilation developments in numerical weather-prediction centres. *Quart. J. Roy. Meteor. Soc.*, **131**, 3215–3233, doi: 10.1256/qj.05.129.

Rasmussen, R. M., and A. J. Heymsfield, 1987a: Melting and shedding of graupel and hail. Part I: Model physics. *J. Atmos. Sci.*, **44**, 2754–2763, doi:10.1175/1520-0469(1987)044⟨2754:MASOGA⟩2.0.CO;2.

Rasmussen, R. M., and A. J. Heymsfield, 1987b: Melting and shedding of graupel and hail. Part II: Sensitivity study. *J. Atmos. Sci.*, **44**, 2764–2782, doi:10.1175/1520-0469(1987)044⟨2764:MASOGA⟩2.0.CO;2.

Rasmussen, R. M., V. Levizzani, and H. R. Pruppacher, 1984: A wind tunnel study on the melting behavior of atmospheric ice particles. III: Experiment and theory for spherical ice particles of radius >500 μm. *J. Atmos. Sci.*, **41**, 381–388, doi:10.1175/1520-0469(1984)041⟨0381:AWTATS⟩2.0.CO;2.

Rasmussen, R. M., and H. R. Pruppacher, 1982: A wind tunnel study on the melting behavior of atmospheric ice particles. III: Experiment and theory for spherical ice particles of radius <500 μm. *J. Atmos. Sci.*, **39**, 152–158, doi:10.1175/1520-0469(1982)039⟨0152:AWTATS⟩2.0.CO;2.

Ray, P., 1972: Broadband complex refractive indices of ice and water. *Appl. Opt.*, **11**, 1836–1844, doi:10.1364/AO.11.001836.

Ray, P. S., 1976: Vorticity and divergence fields within tornadic storms from dual-Doppler observations. *J. Appl. Meteor.*, **15**, 879–890, doi:10.1175/1520-0450%281976%29015⟨0879%3AVADFWT⟩2.0.CO;2.

Ray, P. S., R. J. Doviak, G. B. Walker, D. Sirmans, J. Carter, and B. Bumgarner, 1975: Dual-Doppler observation of a tornadic storm. *J. Appl. Meteor.*, **14**, 1521–1530, doi:10.1175/1520-0450%281975%29014⟨1521%3ADDOOAT⟩2.0.CO;2.

Rennie, S. J., S. L. Dance, A. J. Illingworth, S. P. Ballard, and D. Simonin, 2011: 3D-Var assimilation of insect-derived Doppler radar radial winds in convective cases using a high-resolution model. *Mon. Wea. Rev.*, **139**, 1148–1163, doi:10.1175/2010MWR3482.1.

Ridal, M., and M. Dahlbom, 2017: Assimilation of multinational radar reflectivity data in a mesoscale model: A proof of concept. *J. Appl. Meteor. Climatol.*, **56**, 1739–1751, doi:10.1175/JAMC-D-16-0247.1.

Riehl, H., and J. S. Malkus, 1958: On the heat balance in the equatorial trough zone. *Geophysica*, **6**, 503–538.

Rogers, R. F., J. M. Fritsch, and W. C. Lambert, 2000: A simple technique for using radar data in the dynamic initialization of a mesoscale model. *Mon. Wea. Rev.*, **128**, 2560–2574, doi:10.1175/1520-0493(2000)128⟨2560:ASTFUR⟩2.0.CO;2.

Rogers, R. R., and M. K. Yau, 1989: *A Short Course in Cloud Physics*. 3rd ed., Elsevier Press, 290 pp.

Rotunno, R., J. B. Klemp, and M. L. Weisman, 1988: A theory for strong, long-lived squall lines. *J. Atmos. Sci.*, **45**, 463–485.

Roux, F., 1985: Retrieval of thermodynamic fields from multiple-Doppler radar data using the equations of motion and the thermodynamic equation. *Mon. Wea. Rev.*, **113**, 2142–2157, doi:10.1175/1520-0493(1985)113⟨2142:ROTFFM⟩2.0.CO;2.

Roux, F., and S. Ju, 1990: Single-Doppler observations of a west African squall line on 27-28 May 1981 during COPT 81: Kinematics, thermodynamics, and water budget. *Mon. Wea. Rev.*, **118**, 1826–1854, doi:10.1175/1520-0493(1990)118⟨1826:SDOOAW⟩2.0.CO;2.

Roux, F., V. Marecal, and D. Hauser, 1993: The 12/13 January 1988 narrow cold-frontal rainband observed during MFDP/FRONTS 87. Part I: Kinematics and thermodynamics. *J. Atmos. Sci.*, **50**, 951–974, doi:10.1175/1520-0469%281993%29050⟨0951%3ATJNCFR⟩2.0.CO;2.

Roux, F., J. Testud, M. Payen, and B. Pinty, 1984: West african squall-line thermodynamic structure retrieved from dual-Doppler radar observations. *J. Atmos. Sci.*, **41**, 3104–3121, doi:10.1175/1520-0469(1984)041⟨3104:WASLTS⟩2.0.CO;2.

Russchenberg, H. W. J., and L. P. Ligthart, 1996: Backscattering by and propagation through the melting layer of precipitation: A new polarimetric model. *IEEE Trans. Geosci. Remote Sens.*, **34**, 3–14, doi:10.1109/36.481885.

Rutledge, S. A., and P. V. Hobbs, 1984: The mesoscale and microscale structure and organization of clouds and precipitation in midlatitude cyclones. VII: A diagnostic modeling study of precipitation development in narrow cold-frontal rainbands. *J. Atmos. Sci.*, **41**, 2949–2972, doi:10.1175/1520-0469(1984)041⟨2949:TMAMSA⟩2.0.CO;2.

Ryzhkov, A., M. Diederich, P. Zhang, and C. Simmer, 2014: Potential utilization of specific attenuation for rainfall estimation, mitigation of partial beam blockage, and radar networking. *J. Atmos. Oceanic Technol.*, **31**, 599–619, doi:10.1175/JTECH-D-13-00038.1.

Ryzhkov, A., M. Pinsky, A. Pokrovsky, and A. Khain, 2011: Polarimetric radar observation operator for a cloud model with spectral microphysics. *J. Appl. Meteor. Climatol.*, **50**, 873–894, doi:10.1175/2010JAMC2363.1.

Ryzhkov, A. V., S. Ganson, M. Pinsky, and A. Pokrovsky, 2009: Polarimetric characteristics of melting hail at S and C bands. *34th Conf. on Radar Meteorology*, Williamsburg, VA, Finnish Meteorological Institute, 4A.6, [Available online at http://ams.confex.com/ams/pdfpapers/155571.pdf.].

Ryzhkov, A. V., S. E. Giangrande, and T. J. Schuur, 2005a: Rainfall estimation with a polarimetric prototype of WSR-88D. *J. Appl. Meteor.*, **44**, 502–515, doi:10.1175/JAM2213.1.

Ryzhkov, A. V., M. R. Kumjian, S. M. Ganson, and A. P. Khain, 2013a: Polarimetric radar characteristics of melting hail. Part I: Theoretical simulations using spectral microphysical modeling. *J. Appl. Meteor. Climatol.*, **52**, 2849–2869, doi:10.1175/JAMC-D-13-073.1.

Ryzhkov, A. V., M. R. Kumjian, S. M. Ganson, and P. Zhang, 2013b: Polarimetric radar characteristics of melting hail. Part II: Practical implications. *J. Appl. Meteor. Climatol.*, **52**, 2871–2886, doi:10.1175/JAMC-D-13-074.1.

Ryzhkov, A. V., T. J. Schuur, D. W. Burgess, P. L. Heinselman, S. E. Giangrande, and D. S. Zrnić, 2005b: The Joint Polarization Experiment: Polarimetric rainfall measurements and hydrometeor classification. *Bull. Amer. Meteor. Soc.*, **86**, 809–824, doi:10.1175/BAMS-86-6-809.

Ryzhkov, A. V., T. J. Schuur, D. W. Burgess, and D. S. Zrnić, 2005c: Polarimetric tornado detection. *J. Appl. Meteor.*, **44**, 557–570, doi:10.1175/JAM2235.1.

Ryzhkov, A. V., P. Zhang, H. Reeves, M. Kumjian, T. Tschallener, S. Trömel, and C. Simmar, 2016: Quasi-vertical profiles—A new way to look at polarimetric radar data. *J. Atmos. Oceanic Technol.*, **33**, 551–562, doi:10.1175/JTECH-D-15-0020.1.

Ryzhkov, A. V., V. B. Zhuravlyov, and N. A. Rybakova, 1994: Preliminary results of X-band polarization radar studies of clouds and precipitation. *J. Atmos. Oceanic Technol.*, **11**, 132–139, doi:10.1175/1520-0426(1994)011,0132:PROXBP.2.0.CO;2.

Ryzhkov, A. V., and D. S. Zrnić, 1995: Comparison of dual-polarization radar estimators of rain. *J. Atmos. Oceanic Technol.*, **12**, 249–256, doi:10.1175/1520-0426(1995)012⟨0249:CODPRE⟩2.0.CO;2.

Ryzhkov, A. V., D. S. Zrnić, and B. A. Gordon, 1998: Polarimetric method for ice water content determination. *J. Appl. Meteor.*, **37**, 125–134, doi:10.1175/1520-0450(1998)037⟨0125:PMFIWC⟩2.0.CO;2.

Sachidananda, M., and D. S. Zrnić, 1986: Differential propagation phase shift and rainfall rate estimation. *Radio Sci.*, **21**, 235–247, doi:10.1029/RS021i002p00235.

Sachidananda, M., and D. S. Zrnić, 1987: Rain rate estimates from differential polarization measurements. *J. Atmos. Oceanic Technol.*, **4**, 588–598, doi:10.1175/1520-0426(1987)004⟨0588:RREFDP⟩2.0.CO;2.

Sassen, K., 1987: Ice cloud content from radar reflectivity. *J. Climate Appl. Meteor.*, **26**, 1050–1053, doi:10.1175/1520-0450(1987)026⟨1050:ICCFRR⟩2.0.CO;2.

Sauvageot, H., and J. Omar, 1987: Radar reflectivity of cumulus clouds. *J. Atmos. Oceanic Technol.*, **4**, 264–272, doi:10.1175/1520-0426(1987)004⟨0264:RROCC⟩2.0.CO;2.

Scharfenberg, K. A., 2003: Polarimetric radar signatures in microburst-producing thunderstorms. *31st Int. Conf. on Radar Meteorology*, Seattle, WA, Amer. Meteor. Soc., 8B.4.

Schenkman, A. D., 2012: Exploring tornadogenesis with high-resolution simulations initialized with real data. Ph.D. thesis, University of Oklahoma, 186 pp.

Schenkman, A. D., X. Ming, A. Shapiro, K. Brewster, and J. Gao, 2011a: The analysis and prediction of the 8-9 May 2007 Oklahoma tornadic mesoscale convective system by assimilation WSR-88D and CASA radar data using 3DVAR. *Mon. Wea. Rev.*, **139**, 224–246, doi:10.1175/2010MWR3336.1.

Schenkman, A. D., M. Xue, A. Shapiro, K. A. Brewster, and J. Gao, 2011b: Impact of CASA radar and Oklahoma mesonet data assimilation on the analysis and prediction of tornadic mesovortices in an MCS. *Mon. Wea. Rev.*, **139**, 3422–3445, doi:10.1175/MWR-D-10-05051.1.

Schultz, C. J., and Coauthors, 2012a: Dual-polarization tornadic debris signatures. Part I: Examples and utility in an operational setting. *Electron. J. Oper. Meteor.*, **13**, 120–137, [Available online at http://nwafiles.nwas.org/ej/pdf/2012-EJ9.pdf].

Schultz, C. J., and Coauthors, 2012b: Dual-polarization tornadic debris signatures. Part II: Comparisons and caveats. *Electron. J. Oper. Meteor.*, **13**, 138–150, [Available online at http://nwafiles.nwas.org/ej/pdf/2012-EJ10.pdf].

Schumacher, C., R. A. Houze, and I. Kraucunas, 2004: The tropical dynamical response to latent heating estimates derived from the TRMM Precipitation Radar. *J. Atmos. Sci.*, **61**, 1341–1358, doi:10.1175/1520-0469(2004)061⟨1341:TTDRTL⟩2.0.CO;2.

Schumacher, R. S., and J. M. Peters, 2017: Near-surface thermodynamic sensitivities in simulated extreme-rain-producing mesoscale convective systems. *Mon. Wea. Rev.*, **145**, 2177–2200, doi:10.1175/MWR-D-16-0255.1.

Schuur, T. J., and S. A. Rutledge, 2000: Electrification of stratiform regions in mesoscale convevctive systems. Part I: An observational comparison of symmetric and asymmetric MCSs. *J. Atmos. Sci.*, **57**, 1961–1982, doi:10.1175/1520-0450(2001)040⟨1019:DSDMBA⟩2.0.CO;2.

Schuur, T. J., A. V. Ryzhkov, and D. R. Clabo, 2005: Climatological analysis of DSDs in Oklahoma as revealed by 2D-video disdrometer and polarimetric WSR-88D. *32nd Conf. on Radar Meteorology*, Albuquerque, NM, Amer. Meteor. Soc., 15R.4.

Sekhon, R., and R. Srivastava, 1970: Snow size spectra and radar reflectivity. *J. Atmos. Sci.*, **27**, 299–307, doi:10.1175/1520-0469(1970)027⟨0299:SSSARR⟩2.0.CO;2.

Seliga, T. A., K. Aydin, and H. Direskeneli, 1986: Disdrometer measurements during an intense rainfall event in Central Illinois: Implications for differential reflectivity radar observations. *J. Climate Appl. Meteor.*, **25**, 835–846, doi:10.1175/1520-0450(1986)025⟨0835:DMDAIR⟩2.0.CO;2.

Seliga, T. A., and V. N. Bringi, 1976: Potential use of radar differential reflectivity measurements at orthogonal polarizations for measuring precipitation. *J. Appl. Meteor.*, **15**, 69–76, doi:10.1175/1520-0450(1976)015⟨0069:PUORDR⟩2.0.CO;2.

Seliga, T. A., and V. N. Bringi, 1978: Differential reflectivity and differential phase shift: Applications in radar meteorology. *Radio Science*, **13**, 271–275, doi:10.1029/RS013i002p00271.

Seliga, T. A., V. N. Bringi, and H. H. Al-Khatib, 1981: A preliminary study of comparative measurements of rainfall rate using the differential reflectivity radar technique and a raingage network. *J. Appl. Meteor.*, **20**, 1362–1368, doi:10.1175/1520-0450(1981)020⟨1362:APSOCM⟩2.0.CO;2.

Shapiro, A., S. Ellis, and J. Shaw, 1995: Single-Doppler velocity retrievals with Phoenix II data: Clear air and microburst wind retrievals in the planetary boundary layer. *J. Atmos. Sci.*, **52**, 1265–1287, doi:10.1175/1520-0469(1995)052⟨1265:SDVRWP⟩2.0.CO;2.

Shapiro, A., C. K. Potvin, and J. Gao, 2009: Use of a vertical vorticity equation in variational dual-Doppler wind analysis. *J. Atmos. Oceanic Technol.*, **26**, 2089–2106, doi:10.1175/2009JTECHA1256.1.

Shige, S., Y. N. Takayabu, S. Kida, W.-K. Tao, X. Zeng, C. Yokoyama, and T. L'Ecuyer, 2009: Spectral retrieval of latent heating profiles from TRMM PR data. Part IV: Comparisons of lookup tables from two- and three-dimensional simulations. *J. Climate*, **22**, 5577–5594, doi:10.1175/2009JCLI2919.1.

Shige, S., Y. N. Takayabu, W.-K. Tao, and D. E. Johnson, 2004: Spectral retrieval of latent heating profiles from TRMM PR data. Part I: Development of a model-based algorithm. *J. Appl. Meteor.*, **43**, 1095–1113, doi:10.1175/1520-0450(2004)043⟨1095:SROLHP⟩2.0.CO;2.

Shige, S., Y. N. Takayabu, W.-K. Tao, and D. E. Johnson, 2007: Spectral retrieval of latent heating profiles from TRMM PR data. Part II: Algorithm improvement and heating estimates over tropical ocean regions. *J. Appl. Meteor. Climatol.*, **46**, 1098–1124, doi:10.1175/JAM2510.1.

Sikdar, R. E., D N Schlesinger, and C. E. Anderson, 1974: Severe storm latent heat release: Comparison of radar estimate versus a numerical experiment. *Mon. Wea. Rev.*, **102**, 455–465, doi:10.1175/1520-0493(1974)102⟨0455:SSLHRC⟩2.0.CO;2.

Simmons, K. M., and D. Sutter, 2005: WSR-88D radar, tornado warnings, and tornado casualties. *Wea. Forecasting*, **20**, 301–310, doi:10.1175/WAF857.1.

Simpson, J., R. F. Adler, W.-K. Tao, and R. Adler, 1996: On the Tropical Rainfall Measuring Mission (TRMM). *Meteor. Atmos. Phys.*, **60**, 19–36, doi:10.1007/BF01029783.

Skamarock, W. C., J. B. Klemp, J. Dudhia, D. O. Gill, D. M. Barker, W. Wang, and J. G. Power, 2005: A description of the advanced research WRF version 2. NCAR Tech. Note NCAR/TN-468+STR, 88 pp. [Available from UCAR Communications, P.O. Box 3000, Boulder, CO, 80307.].

Smith, P. L., 1984: Equivalent radar reflectivity factors for snow and ice particles. *J. Climate Appl. Meteor.*, **23**, 1258–1260, doi:10.1175/1520-0450(1984)023⟨1258:ERRFFS⟩2.0.CO;2.

Smith, P. L., D. J. Musil, S. F. Weber, J. F. Spahn, G. N. Johnson, and W. R. Sand, 1976: Raindrop and hailstone distributions inside hailstorms. *17th Int. Conf. on Cloud Physics*, Boulder, CO, American Meteorological Society, 252-257.

Smith, P. L., C. G. Myers, and H. D. Orville, 1975: Radar reflectivity factor calculations in numerical cloud models using bulk parameterization of precipitation. *J. Appl. Meteor.*, **14**, 1156–1165, doi:10.1175/1520-0450(1975)014⟨1156:RRFCIN⟩2.0.CO%3B2.

Smith, T. M., and K. M. Elmore, 2004: The use of radial velocity derivatives to diagnose rotation and divergence. *11th Conf. on Aviation, Range, and Aerospace*, Amer. Meteor. Soc., Hyannis, MA, P5.6, [Available online at https://ams.confex.com/ams/pdfpapers/81827.pdf].

Smith, T. M., and Coauthors, 2016: Multi-Radar Multi-Sensor (MRMS) severe weather and aviation products: Initial operating capabilities. *Bull. Amer. Meteor. Soc.*, **97**, 1617–1630, doi:10.1175/BAMS-D-14-00173.1.

Snook, N., and M. Xue, 2008: Effects of microphysical drop size distribution on tornadogenesis in supercell thunderstorms. *Geophys. Res. Lett.*, **35**, 1–5, doi:10.1029/2008GL035866.

Snook, N., M. Xue, and Y. Jung, 2011: Analysis of a tornadic mesoscale convective vortex based on ensemble Kalman filter assimilation of CASA X-band and WSR-88D radar data. *Mon. Wea. Rev.*, **139**, 3446–3468, doi:10.1175/MWR-D-10-05053.1.

Snook, N., M. Xue, and Y. Jung, 2012: Ensemble probabilistic forecasts of a tornadic mesoscale convective system from ensemble Kalman filter analyses using WSR-88D and CASA radar data. *Mon. Wea. Rev.*, **140**, 2126–2146, doi:10.1175/MWR-D-11-00117.1.

Snyder, C., and F. Zhang, 2003: Assimilation of simulated Doppler radar observations with an ensemble Kalman filter. *Mon. Wea. Rev.*, **131**, 1663–1677, doi:10.1175/2555.1.

Snyder, J. C., H. B. Bluestein, D. T. Dawson, and Y. Jung, 2017a: Simulations of polarimetric, X-band radar signatures in supercells. Part I: Description of experiment and simulated ρ_{hv} rings. *J. Appl. Meteor. Climatol.*, **56**, 2001–2026, doi:10.1175/JAMC-D-16-0139.1.

Snyder, J. C., H. B. Bluestein, D. T. Dawson, and Y. Jung, 2017b: Simulations of polarimetric, X-band radar signatures in supercells. Part II: z_{dr} columns and rings and k_{dp} columns. *J. Appl. Meteor. Climatol.*, **56**, 1977–1999, doi:10.1175/JAMC-D-16-0138.1.

Snyder, J. C., H. B. Bluestein, G. Zhang, and S. J. Frasier, 2010: Attenuation correction and hydrometeor classification of high-resolution, X-band, dual-polarized mobile radar measurements in severe convective storms. *J. Atmos. Oceanic Technol.*, **27**, 1979–2001, doi:10.1175/2010JTECHA1356.1.

Snyder, J. C., and A. V. Ryzhkov, 2015: Automated detection of polarimetric tornadic debris signatures using a hydrometeor classification algorithm. *J. Appl. Meteor. Climatol.*, **54**, 1861–1870, doi:10.1175/JAMC-D-15-0138.1.

Snyder, J. C., A. V. Ryzhkov, M. R. Kumjian, A. P. Khain, and J. Picca, 2015: A z_{dr} column detection algorithm to examine convective storm updrafts. *Wea. Forecasting*, **30**, 1819–1844, doi:10.1175/WAF-D-15-0068.1.

Sokol, Z., and D. Rezacova, 2009: Assimilation of the radar-derived water vapour mixing ratio into the LM COSMO model with a high horizontal resolution. *Atmos. Res.*, **92**, 331–342, doi:10.1016/j.atmosres.2009.01.012.

Souto, M. J., C. F. Balseiro, V. Pérez-Muñuzuri, M. Xue, and K. Brewster, 2003: Impact of cloud analysis on numerical weather prediction in the Galician region of Spain. *J. Appl. Meteor.*, **42**, 129–140, doi:10.1175/1520-0450(2003)042⟨0129:IOCAON⟩2.0.CO;2.

Srivastava, R. C., 1985: A simple model of evaporatively driven downdraft: Application to microburst downdraft. *J. Atmos. Sci.*, **42**, 1004–1023, doi:10.1175/1520-0469(1985)042⟨1004:ASMOED⟩2.0.CO;2.

Srivastava, R. C., 1987: A model of intense downdrafts driven by the melting and evaporation of precipitation. *J. Atmos. Sci.*, **44**, 1752–1774, doi:10.1175/1520-0469(1987)044⟨1752:AMOIDD⟩2.0.CO;2.

Starzec, M., C. R. Homeyer, and G. L. Mullendore, 2017: Storm Labeling in Three Dimensions (SLD3): A volumetric radar echo and dual-polarization updraft classification algorithm. *Mon. Wea. Rev.*, **145**, 1127–1145, doi:10.1175/MWR-D-16-0089.1.

Steiner, J. T., 1973: A three-dimensional model of cumulus cloud development. *J. Atmos. Sci.*, **30**, 414–435, doi:10.1175/1520-0469(1973)030⟨0414:ATDMOC⟩2.0.CO;2.

Stensrud, D. J., and J. Gao, 2010: Importance of horizontally inhomogeneous environmental initial conditions to ensemble storm-scale radar data assimilation and very short-range forecasts. *Mon. Wea. Rev.*, **138**, 1250–1272, doi:10.1175/2009MWR3027.1.

Stensrud, D. J., and Coauthors, 2009: Convective-scale Warn-on-Forecast system: A vision for 2020. *Bull. Amer. Meteor. Soc.*, **90**, 1487–1499, doi:10.1175/2009BAMS2795.1.

Stensrud, D. J., and Coauthors, 2013: Progress and challenges with Warn-on-Forecast. *Atmos. Res.*, **123**, 2–16, doi:10.1016/j.atmosres.2012.04.004.

Stephan, K., S. Klink, and C. Schraff, 2008: Assimilation of radar-derived rain rates into the convective-scale model COSMO-DE at DWD. *Quart. J. Roy. Meteor. Soc.*, **134**, 1315–1326, doi:10.1002/qj.269.

Stewart, R. E., and S. R. Macpherson, 1989: Winter storm structure and melting-induced circulations. *Atmos.-Ocean*, **27**, 5–23, doi:10.1080/07055900.1989.9649326.

Stewart, R. E., J. D. Marwitz, and J. C. Pace, 1984: Characteristics through the melting layer of stratiform clouds. *J. Atmos. Sci.*, **41**, 3227–3237, doi:10.1175/1520-0469(1984)041⟨3227:CTTMLO⟩2.0.CO;2.

Straka, J. M., D. S. Zrnić, and A. V. Ryzhkov, 2000: Bulk hydrometeor classification using polarimetric radar data: Synthesis of relations. *J. Appl. Meteor.*, **39**, 1341–1372, doi:10.1175/1520-0450(2000)039⟨1341:BHCAQU⟩2.0.CO;2.

Stratman, D. R., and K. A. Brewster, 2015: Verification of 24 May 2011 simulated mesocyclones using various microphysics schemes at 1-km grid resolution. *27th Conf. on Weather Analysis and Forecasting/23rd Conf. on Numerical Weather Prediction*, Amer. Meteor. Soc., Chicago, IL, 13A.6, [Available online at https://ams.confex.com/ams/27WAF23NWP/webprogram/Manuscript/Paper273795/stratman_wafnwp_2015.pdf].

Sugimoto, S., N. A. Crook, J. Sun, Q. Xiao, and D. M. Barker, 2009: An examination of WRF 3DVAR radar data assimilation on its capability in retrieving unobserved variables and forecasting precipitation thruogh Observing System Simulation Experiments. *Mon. Wea. Rev.*, **137**, 4011–4029, doi:10.1175/2009MWR2839.1.

Sun, J., 2005a: Convective-scale assimilation of radar data: Progress and challenges. *Quart. J. Roy. Meteor. Soc.*, **131**, 3439–3463, doi:10.1256/qj.05.149.

Sun, J., 2005b: Initialization and numerical forecasting of a supercell storm observed during STEPS. *Mon. Wea. Rev.*, **133**, 793–813, doi:10.1175/MWR2887.1.

Sun, J., and A. Crook, 1994: Wind and thermodynamic retrieval from single-Doppler measurements of a gust front observed during Phoenix II. *Mon. Wea. Rev.*, **122**, 1075–1091, doi:10.1175/1520-0493(1994)122⟨1075:WATRFS⟩2.0.CO;2.

Sun, J., and A. N. Crook, 1997: Dynamical and microphysical retrieval from Doppler radar observations using a cloud model and its adjoint. Part I: Model development and simulated data experiments. *J. Atmos. Sci.*, **54**, 1642–1661, doi:10.1175/1520-0469(1997)054⟨1642%3ADAMRFD⟩2.0.CO%3B2.

Sun, J., and A. N. Crook, 1998: Dynamical and microphysical retrieval from Doppler radar observations using a cloud model and its adjoint. Part II: Retrieval experiments of an observed Florida convective storm. *J. Atmos. Sci.*, **55**, 835–852, doi:10.1175/1520-0469(1998)055⟨0835%3ADAMRFD⟩2.0.CO%3B2.

Sun, J., D. W. Flicker, and D. K. Lilly, 1991: Recovery of three-dimensional wind and temperature fields from simulated single-Doppler radar data. *J. Atmos. Sci.*, **48**, 876–890, doi:10.1175/1520-0469(1991)048⟨0876:ROTDWA⟩2.0.CO;2.

Sun, J., S. B. Trier, Q. Xiao, M. L. Weisman, H. Wang, Z. Ying, M. Xu, and Y. Zhang, 2012: Sensitivity of 0—12-h warm-season precipitation forecasts over the central United States to model initialization. *Wea. Forecasting*, **27**, 832–855, doi:10.1175/WAF-D-11-00075.1.

Sun, J., and H. Wang, 2013: Radar data assimilation with WRF 4D-Var: Part II: Comparison with 3D-Var for a squall line over the U.S. Great Plains. *Mon. Wea. Rev.*, **141**, 2245–2264, doi:10.1175/MWR-D-12-00169.1.

Sun, J., and Y. Zhang, 2008: Analysis and prediction of a squall line observed during IHOP using multiple WSR-88D observations. *Mon. Wea. Rev.*, **136**, 2364–2388, doi:10.1175/2007MWR2205.1.

Sun, W.-Y., and C.-Z. Chang, 1986: Diffusion model for a convective layer. Part I: Numerical simulation of convective boundary layer. *J. Climate Appl. Meteor.*, **25**, 1445–1453, doi:10.1175/1520-0450(1986)025⟨1445:DMFACL⟩2.0.CO;2.

Supinie, T. A., N. Yussouf, Y. Jung, M. Xue, J. Cheng, and S. Wang, 2017: Comparison of the analyses and forecasts of a tornadic supercell storm from assimilating phased-array radar and WSR-88D observations. *Wea. Forecasting*, **32**, 1379–1401, doi:10.1175/WAF-D-16-0159.1.

Szeto, K. K., C. A. Lin, and R. E. Stewart, 1988: Mesoscale circulations forced by melting snow. Part I: Basic simulations and dynamics. *J. Atmos. Sci.*, **45**, 1629–1641, doi:10.1175/1520-0469(1988)045⟨1629:MCFBMS⟩2.0.CO;2.

Szyrmer, W., and I. Zawadzki, 1999: Modeling of the melting layer. Part I: Dynamics and microphysics. *J. Atmos. Sci.*, **56**, 3573–3592, doi:10.1175/1520-0469(1999)056⟨3573:MOTMLP⟩2.0.CO;2.

Szyrmer, W., and I. Zawadzki, 2010: Snow studies. Part II: Average relationship between mass of snowflakes and their terminal fall velocity. *J. Atmos. Sci.*, **67**, 3320–3335, doi:10.1175/2010JAS3390.1.

Tabary, P., A.-A. Boumahmoud, H. Andrieu, R. J. Thompson, A. J. Ilingworth, E. Le Bouar, and J. Testud, 2011: Evaluation of two "integrated" polarimetric quantitative precipitation estimation (QPE) algorithms at C-band. *J. Hydrology*, **405**, 248–260, doi:10.1016/j.jhydrol.2011.05.021.

Tao, W., and Coauthors, 2006: Retrieval of latent heating from TRMM measurements. *Bull. Amer. Meteor. Soc.*, **87**, 1555–1572, doi:10.1175/BAMS-87-11-1555.

Tao, W.-K., S. Lang, J. Simpson, and R. Adler, 1993: Retrieval algorithms for estimating the vertical profiles of latent heat release: Their applications for TRMM. *J. Meteor. Soc. Japan*, **71**, 685–700, doi:10.2151/jmsj1965.71.6_685.

Tao, W.-K., S. Lang, X. Zeng, S. Shige, and Y. Takayabu, 2010: Relating convective and stratiform rain to latent heating. *J. Climate*, **23**, 1874–1893, doi:10.1175/2009JCLI3278.1.

Tao, W.-K., and J. Simpson, 1993: Goddard Cumulus Ensemble model. Part I: Model description. *Terr. Atmos. Oceanic Sci.*, **4**, 35–72.

Tardif, R., and R. S. Rasmussen, 2010: Evaporation of nonequilibrium raindrops as a fog formation mechanism. *J. Atmos. Sci.*, **67**, 345–364, doi:10.1175/2009JAS3149.1.

Taylor, K. E., 2001: Summarizing multiple aspects of model performance in a single diagram. *J. Geophys. Res.*, **106**, 7183–7192, doi:10.1029/2000JD900719.

Testud, J., E. L. Bouar, E. Obligis, and M. Ali-Mehenni, 2000: The rain profiling algorithm applied to polarimetric weather radar. *J. Atmos. Oceanic Technol.*, **17**, 332–356, doi:10.1175/1520-0426(2000)017⟨0332:TRPAAT⟩2.0.CO;2.

Testud, J., S. Oury, R. A. Black, P. Amayenc, and X. Dou, 2001: The concept of "normalized" distribution to describe raindrop spectra: A tool for cloud physics and cloud remote sensing. *J. Appl. Meteor.*, **40**, 1118–1140, doi:10.1175/1520-0450(2001)040⟨1118:TCONDT⟩2.0.CO;2.

Thériault, J. M., and Coauthors, 2012: A case study of processes impacting precipitation phase and intensity during the Vancouver 2010 Winter Olympics. *Wea. Forecasting*, **27**, 1301–1325, doi:10.1175/WAF-D-11-00114.1.

Thompson, E., S. Rutledge, B. Dolan, V. Chandrasekar, and B. Cheong, 2014: A dual-polarization radar hydrometeor classification algorithm for winter precipitation. *J. Atmos. Oceanic Technol.*, **31**, 1457–1481, doi:10.1175/JTECH-D-13-00119.1.

Thurai, M., V. Bringi, M. Szakáll, S. Mitra, K. Beard, and S. Borrmann, 2009: Drop shapes and axis ratio distributions: Comparison between 2D video disdrometer and wind-tunnel measurements. *J. Atmos. Oceanic Technol.*, **26**, 1427–1432, doi:10.1175/2009JTECHA1244.1.

Tong, C.-C., 2015: Limitations and potential of complex cloud analysis and its improvement for radar reflectivity data assimilation using OSSEs. Ph.D. thesis, University of Oklahoma, 174 pp.

Tong, H., V. Chandrasekar, K. R. Knupp, and J. Stalker, 1998: Multiparameter radar observations of time evolution of convective storms: Evaluation of water budgets and latent heating rates. *J. Atmos. Oceanic Technol.*, **15**, 1097–1109, doi:10.1175/1520-0426(1998)015⟨1097:MROOTE⟩2.0.CO;2.

Tong, M., and M. Xue, 2005: Ensemble Kalman filter assimilation of Doppler radar data with a compressible nonhydrostatic model: OSS experiments. *Mon. Wea. Rev.*, **133**, 1789–1807, doi:10.1175/1520-0426(1996)013⟨0454:AORMUS⟩2.0.CO;2.

Torres, S. M., 2017: The future is here: Capabilities and plans for the Advanced Technology Demonstrator at the National Severe Storms Laboratory. *38th Conf. on Radar Meteorology*, Amer. Meteor. Soc., Chicago, IL, 122.

Trapp, R., S. Nesbitt, S. Lasher-Trapp, P. Borque, G. Marion, and H. Mallinson, 2018: Inter-relationships between convectively generated cold pools, updraft/downdraft characteristics, and microphysical processes. *9th Atmos. System Research Science Team Meeting*, U.S. Dept. of Energy, Tysons, VA, 33.

Trömel, S., A. V. Ryzhkov, B. Hickman, and C. Simmer, 2017: Climatology of the vertical profiles of polarimetric radar variables at X band in stratiform clouds. *38th Conf. on Radar Meteorology*, Amer. Meteor. Soc., Chicago, IL, 5.

Trömel, S., A. V. Ryzhkov, P. Zhang, and C. Simmer, 2014: Investigations of backscatter differential phase in the melting layer. *J. Appl. Meteor. Climatol.*, **53**, 2344–2359, doi:10.1175/JAMC-D-14-0050.1.

Tuttle, J. D., V. N. Bringi, H. D. Orville, and F. J. Kopp, 1989: Preliminary results of X-band polarization radar studies of clouds and precipitation. *J. Atmos. Sci.*, **46**, 601–620, doi:10.1175/1520-0469(1989)046,0601:MRSOAM.2.0.CO;2.

Ulbrich, C. W., 1983: Natural variations in the analytical form of the raindrop size distribution. *J. Climate Appl. Meteor.*, **22**, 1764–1775, doi:10.1175/1520-0450(1983)022⟨1764:NVITAF⟩2.0.CO;2.

Ulbrich, C. W., and D. Atlas, 1982: Hail parameter relations: A comprehensive digest. *J. Appl. Meteor.*, **21**, 22–43, doi:10.1175/1520-0450(1982)021⟨0022:HPRACD⟩2.0.CO;2.

Ulbrich, C. W., and D. Atlas, 1984: Assessment of the contribution of differential polarization to improved rainfall measurements. *Radio Sci.*, **19**, 49–57, doi:10.1029/RS019i001p00049.

van den Broeke, M. S., 2016: Polarimetric variability of classic supercell storms as a function of environment. *J. Appl. Meteor. Climatol.*, **55**, 1908–1925, doi:10.1175/JAMC-D-15-0346.1.

van den Broeke, M. S., 2017: Polarimetric radar metrics related to tornado life cycles and intensity in supercell storms. *Mon. Wea. Rev.*, **145**, 3671–3686, doi:10.1175/MWR-D-16-0453.1.

van den Broeke, M. S., and S. T. Jauernic, 2014: Spatial and temporal characteristics of polarimetric tornadic debris signatures. *J. Appl. Meteor. Climatol.*, **53**, 2217–2231, doi:10.1175/JAMC-D-14-0094.1.

van den Heever, S. C., G. G. Carrio, W. R. Cotton, P. J. DeMott, and A. J. Prenni, 2006: Impacts of nucleating aerosol on Florida storms. Part I: Mesoscale simulations. *J. Atmos. Sci.*, **63**, 1752–1775, doi:10.1175/JAS3713.1.

van Lier-Walqui, M., and Coauthors, 2016: On polarimetric radar signatures of deep convection for model evaluation: Columns of specific differential phase observed during MC3E. *Mon. Wea. Rev.*, **144**, 737–758, doi:10.1175/MWR-D-15-0100.1.

Vivekanandan, J., V. N. Bringi, M. Hagen, and P. Meischner, 1994: Polarimetric radar studies of atmospheric ice particles. *IEEE Trans. Geosci. Remote Sens.*, **32**, 1–10, doi:10.1109/36.285183.

Vogel, J., F. Fabry, and I. Zawadzki, 2015: Attempts to observe polarimetric signatures of riming in stratiform precipitation. *37th Conf. on Radar Meteorology*, Amer. Meteor. Soc., Norman, OK, 6B.6.

Wainwright, C. E., D. T. Dawson II, M. Xue, and G. Zhang, 2014: Diagnosing the intercept parameters of the exponential drop size distributions in a single-moment microphysics scheme and impact on supercell storm simulations. *J. Appl. Meteor. Climatol.*, **53**, 2072–2090, doi:10.1175/JAMC-D-13-0251.1.

Wakimoto, R. M., and V. N. Bringi, 1988: Dual polarization observations of microbursts associated with intense convection: The 20 July storm during the MIST project. *Mon. Wea. Rev.*, **116**, 1521–1539, doi:10.1175/1520-0493(1988)116⟨1521:DPOOMA⟩2.0.CO;2.

Wang, H., J. Sun, S. Fan, and X.-Y. Huang, 2013: Indirect assimilation of radar reflectivity with WRF 3D-Var and its impact on prediction of four summertime convective events. *J. Appl. Meteor. Climatol.*, **52**, 889–902, doi:10.1175/JAMC-D-12-0120.1.

Wang, X., D. M. Barker, C. Snyder, and T. M. Hamill, 2008a: A hybrid ETKF–3DVAR data assimilation scheme for the WRF model. Part I: Observing system simulation sxperiment. *Mon. Wea. Rev.*, **136**, 5116–5131, doi:10.1175/2008MWR2444.1.

Wang, X., D. M. Barker, C. Snyder, and T. M. Hamill, 2008b: A hybrid ETKF–3DVAR data assimilation scheme for the WRF model. Part II: Real observation experiments. *Mon. Wea. Rev.*, **136**, 5132–5147, doi:10.1175/2008MWR2445.1.

Wattrelot, E., O. Caumont, and J.-F. Mahfouf, 2014: Implementation of the 1D+3D-Var assimilation method of radar reflectivity data in the AROME model. *Mon. Wea. Rev.*, **142**, 1852–1873, doi:10.1175/MWR-D-13-00230.1.

Weisman, M. L., and J. B. Klemp, 1982: The dependence of numerical simulated convective storms on vertical wind shear and buoyancy. *Mon. Wea. Rev.*, **110**, 504–520, doi:10.1175/1520-0493(1982)110⟨0504:TDONSC⟩2.0.CO;2.

Wexler, R., 1955: An evaluation of the physical effects in the melting layer. *Prof. Fifth Weather Radar Conf.*, Fort Monmouth, New Jersey, 329-334.

Weygandt, S. S., S. G. Benjamin, T. G. Smirnova, and J. M. Brown, 2008: Assimilation of radar reflectivity data using a diabatic digital filter within the Rapid Udate Cycle. *12th Conf. on IOAS-AOLS*, Amer. Meteor. Soc., New Orleans, LA, 8.4.

Weygandt, S. S., A. Shapiro, and K. K. Droegemeier, 2002a: Retrieval of model initial fields from single-Doppler observations of a supercell thunderstorm. Part I: Single-Doppler velocity retrieval. *Mon. Wea. Rev.*, **130**, 433–453, doi:10.1175/1520-0493(2002)130⟨0454:ROMIFF⟩2.0.CO;2.

Weygandt, S. S., A. Shapiro, and K. K. Droegemeier, 2002b: Retrieval of model initial fields from single-Doppler observations of a supercell thunderstorm. Part II: Thermodynamic retrieval and numerical prediction. *Mon. Wea. Rev.*, **130**, 454–476, doi:10.1175/1520-0493(2002)130⟨0454:ROMIFF⟩2.0.CO;2.

Wheatley, D. M., K. H. Knopfmeier, T. A. Jones, and G. J. Creager, 2015: Storm-scale data assimilation and ensemble forecasting with the NSSL experimental Warn-on-Forecast system. Part 1: Radar data experiments. *Wea. Forecasting*, **30**, 1795–1817, doi:10.1175/WAF-D-15-0043.1.

Wheatley, D. M., N. Yussouf, and D. J. Stensrud, 2014: Ensemble Kalman filter analyses and forecasts of a severe mesoscale convective system using different choices of microphysics schemes. *Mon. Wea. Rev.*, **142**, 3243–3263, doi:10.1175/MWR-D-13-00260.1.

Wilhelmson, R. B., and J. B. Klemp, 1981: A three-dimensional numerical simulation of splitting severe storms on 3 April 1964. *J. Atmos. Sci.*, **38**, 1581–1600.

Willis, P. T., and A. J. Heymsfield, 1989: Structure of the melting layer in mesoscale convective system stratiform precipitation. *J. Atmos. Sci.*, **46**, 2008–2025, doi:10.1175/1520-0469(1989)046⟨2008:SOTMLI⟩2.0.CO;2.

Wilson, K. A., P. L. Heinselman, and C. M. Kuster, 2017a: Considerations for phased-array radar data use within the National Weather Service. *Wea. Forecasting*, **32**, 1959–1965, doi:10.1175/WAF-D-17-0084.1.

Wilson, K. A., P. L. Heinselman, C. M. Kuster, D. M. Kingfield, and Z. Kang, 2017b: Forecaster performance and workload: Does radar update time matter? *Wea. Forecasting*, **32**, 253–274, doi:10.1175/WAF-D-16-0157.1.

Wolfensberger, D., D. Scipion, and A. Berne, 2016: Detection and characterization of the melting layer based on polarimetric radar scans. *Quart. J. Roy. Meteor. Soc.*, **142**, 108–124, doi:10.1002/qj.2672.

Woods, C. P., M. T. Stoelinga, and J. D. Locatelli, 2008: Size spectra of snow particles measured in wintertime precipitation in the Pacific Northwest. *J. Atmos. Sci.*, **65**, 189–205, doi:10.1175/2007JAS2243.1.

Wu, B., J. Verlinde, and J. Sun, 2000: Dynamical and microphysical retrievals from Doppler radar observations of a deep convective cloud. *J. Atmos. Sci.*, **57**, 262–283, doi:10.1175/1520-0469(2000)057⟨0262:DAMRFD⟩2.0.CO;2.

Wurman, J., Y. Richardson, C. Alexander, S. Weygandt, and P. F. Zhang, 2007: Dual-Doppler and single-Doppler analysis of a tornadic storm undergoing mergers and repeated tornadogenesis. *Mon. Wea. Rev.*, **135**, 736–758, doi:10.1175/MWR3276.1.

Xiao, Q., Y.-H. Kuo, J. Sun, W.-C. Lee, D. M. Barker, and E. Lim, 2007: An approach of radar reflectivity data assimilation and its assessment with the inland QPE of Typhoon Rusa (2002) at landfall. *J. Appl. Meteor. Climatol.*, **46**, 14–22, doi:10.1175/JAM2439.1.

Xiao, Q., Y.-H. Kuo, J. Sun, W.-C. Lee, E. Lim, Y.-R. Guo, and D. M. Barker, 2005: Assimilation of Doppler radar observations with a regional 3DVAR system: Impact of Doppler velocities on forecasts of a heavy rainfall case. *J. Appl. Meteor.*, **44**, 768–788, doi:10.1175/JAM2248.1.

Xie, X., R. Evaristo, S. Trömel, P. Saavedra, C. Simmer, and A. V. Ryzhkov, 2016: Radar observation of evaporation and implications for quantitative precipitation and cooling rate estimation. *J. Atmos. Oceanic Technol.*, **33**, 454–476, doi:10.1175/JTECH-D-15-0244.1.

Xue, M., K. K. Droegemeier, and V. Wong, 2000: The Advanced Regional Prediction System (ARPS) - a multi-scale nonhydrostatic atmospheric simulation and prediction tool. Part I: Model dynamics and verification. *Meteor. Atmos. Phys.*, **75**, 161–193, doi:10.1007/s007030170027.

Xue, M., K. K. Droegemeier, and V. Wong, 2001: The Advanced Regional Prediction System (ARPS) - a multi-scale nonhydrostatic atmospheric simulation and prediction tool. Part II: Model physics and applications. *Meteor. Atmos. Phys.*, **76**, 143–165, doi:10.1007/s007030170027.

Xue, M., M. Hu, and A. D. Schenkman, 2014: Numerical prediction of the 8 May 2003 Oklahoma City tornadic supercell and embedded tornado using ARPS with the assimilation of WSR-88D data. *Wea. Forecasting*, **29**, 39–62, doi:10.1175/WAF-D-13-00029.1.

Xue, M., M. Tong, and K. K. Droegemeier, 2006: An OSSE framework based on the ensemble square root Kalman filter for evaluating the impact of data from radar networks on thunderstorm analysis and forecasting. *J. Atmos. Oceanic Technol.*, **23**, 46–66, doi:10.1175/JTECH1835.1.

Xue, M., D. Wang, J. Gao, K. Brewster, and K. K. Droegemeier, 2003: The Advanced Regional Prediction System (ARPS), storm-scale numerical weather prediction and data assimilation. *Meteor. Atmos. Phys.*, **82**, 139–170, doi:10.1007/s00703-001-0595-6.

Yang, M.-J., and R. A. Houze Jr., 1995a: Multicell squall-line structure as a manifestation of vertically trapped gravity waves. *Mon. Wea. Rev.*, **123**, 641–661, doi:10.1175/1520-0493(1995)123⟨0641:MSLSAA⟩2.0.CO;2.

Yang, M.-J., and R. A. Houze Jr., 1995b: Sensitivity of squall-line rear inflow to ice microphysics and environmental humidity. *Mon. Wea. Rev.*, **123**, 3175–3193, doi:10.1175/1520-0493(1995)123⟨3175:SOSLRI⟩2.0.CO;2.

Yokota, S., H. Seko, M. Kunii, H. Yamauchi, and H. Niino, 2016: The tornadic supercell on the Kanto Plain on 6 May 2012: Polarimetric radar and surface data assimilation with EnKF and ensemble-based sensitivity analysis. *Mon. Wea. Rev.*, **144**, 3133–3157, doi:10.1175/MWR-D-15-0365.1.

Yokoyama, T., and H. Tanaka, 1984: Microphysical processes of melting snowflakes detected by two-wavelength radar. Part I: Principle of measurement based on model calculation. *J. Meteor. Soc. Japan*, **62**, 650–667, doi:10.2151/jmsj1965.62.4_650.

Yussouf, N., E. R. Mansell, L. J. Wicker, D. M. Wheatley, and D. J. Stensrud, 2013: The ensemble Kalman filter analyses and forecasts of the 8 May 2003 Oklahoma City tornadic supercell storm using single- and double-moment microphysics schemes. *Mon. Wea. Rev.*, **141**, 3388–3412, doi:10.1175/MWR-D-12-00237.1.

Yussouf, N., and D. J. Stensrud, 2010: Impact of phased-array radar observations over a short assimilation period: Observing system simulation experiments using an ensemble Kalman filter. *Mon. Wea. Rev.*, **138**, 517–538, doi:10.1175/2009MWR2925.1.

Zawadzki, I., W. Szyrmer, C. Bell, and F. Fabry, 2005: Modeling of the melting layer. Part III: The density effect. *J. Atmos. Sci.*, **62**, 3705–3723, doi:10.1175/JAS3563.1.

Zhang, G., 2016: *Weather Radar Polarimetry*. CRC Press, 304 pp.

Zhang, G., J. Vivekanandan, and E. Brandes, 2001: A method for estimating rain rate and drop size distribution from polarimetric radar measurements. *IEEE Trans. Geosci. Remote Sens.*, **39**, 830–841, doi:10.1109/36.917906.

Zhang, G., M. Xue, Q. Cao, and D. Dawson, 2008: Diagnosing the intercept parameter for exponential raindrop size distribution based on video disdrometer observations: Model development. *J. Appl. Meteor. Climatol.*, **47**, 2983–2992, doi:10.1175/2008JAMC1876.1.

Zhang, J., 1999: Moisture and diabatic initialization based on radar and satellite observation. Ph.D. thesis, University of Oklahoma, 194 pp.

Zhang, J., F. Carr, and K. Brewster, 1998: ADAS cloud analysis. *12th Conf. on Numerical Weather Prediction*, Amer. Meteor. Soc., Phoenix, AZ, 185-188.

Zhao, K., and M. Xue, 2009: Assimilation of coastal Doppler radar data with the ARPS 3DVAR and cloud analysis for the prediction of Hurricane Ike (2008). *Geophys. Res. Lett.*, **36**, 1–6, doi:10.1029/2009GL038658.

Zhuang, Z., N. Yussouf, and J. Gao, 2016: Analyses and forecasts of a tornadic supercell outbreak using a 3DVAR system ensemble. *Adv. Atmos. Sci.*, **33**, 544–558, doi:10.1007/s00376-015-5072-0.

Ziegler, C. L., 1978: A dual Doppler variational objective analysis as applied to studies of convective storms. M.S. thesis, University of Oklahoma, 116 pp.

Ziegler, C. L., 1985: Retrieval of thermal and microphysical variables in observed convective storms. Part I: Model development and preliminary testing. *J. Atmos. Sci.*, **42**, 1487–1509, doi:10.1175/1520-0469(1985)042⟨1487:ROTAMV⟩2.0.CO;2.

Ziegler, C. L., 1988: Retrieval of thermal and microphysical variables in observed convective storms. Part II: Sensitivity of cloud processes to variation of the microphysical parameterization. *J. Atmos. Sci.*, **45**, 1072–1090, doi:10.1175/1520-0469(1988)045⟨1072:ROTAMV⟩2.0.CO;2.

Ziegler, C. L., 2013a: A diabatic Lagrangian technique for the analysis of convective storms. Part I: Description and validation via an Obseving System Simulation Experiment. *J. Atmos. Oceanic Technol.*, **30**, 2248–2265, doi:10.1175/JTECH-D-12-00194.1.

Ziegler, C. L., 2013b: A diabatic Lagrangian technique for the analysis of convective storms. Part II: Application to a radar-observed storm. *J. Atmos. Oceanic Technol.*, **30**, 2266–2280, doi:10.1175/JTECH-D-13-00036.1.

Zrnić, D. S., N. Balakrishnan, C. L. Zeigler, V. N. Bringi, K. Aydin, and T. Matejka, 1993: Polarimetric signatures in the stratiform region of a mesoscale convective system. *J. Appl. Meteor.*, **32**, 678–693, doi:10.1175/1520-0450(1993)032⟨0678:PSITSR⟩2.0.CO;2.

Zrnić, D. S., and A. V. Ryzhkov, 1996: Advantages of rain measurements using specific differential phase. *J. Atmos. Oceanic Technol.*, **13**, 454–464, doi:10.1175/1520-0426(1996)013⟨0454%3AAORMUS⟩2.0.CO%3B2.

Zrnić, D. S., and A. V. Ryzhkov, 1999: Polarimetry for weather surveillance radars. *Bull. Amer. Meteor. Soc.*, **80**, 389–406.